Matrix Effects in Differential Scanning Calorimetry

Thesis

MATRIX EFFECTS IN DIFFERENTIAL SCANNING CALORIMETRY (VOLUME 1 OF 3)

by

M. THOMPSON M.Sc., C.Chem., MRSC.

Submitted to

THE OPEN UNIVERSITY

for the degree

DOCTOR OF PHILOSOPHY

FACULTY OF SCIENCE

1991

Date of submission : 13th February 1991
Date of award : 12th April 1991

ProQuest LLC.
789 East Eisenhower Parkway
P.O. Box 1346
Ann Arbor, MI 48106 – 1346

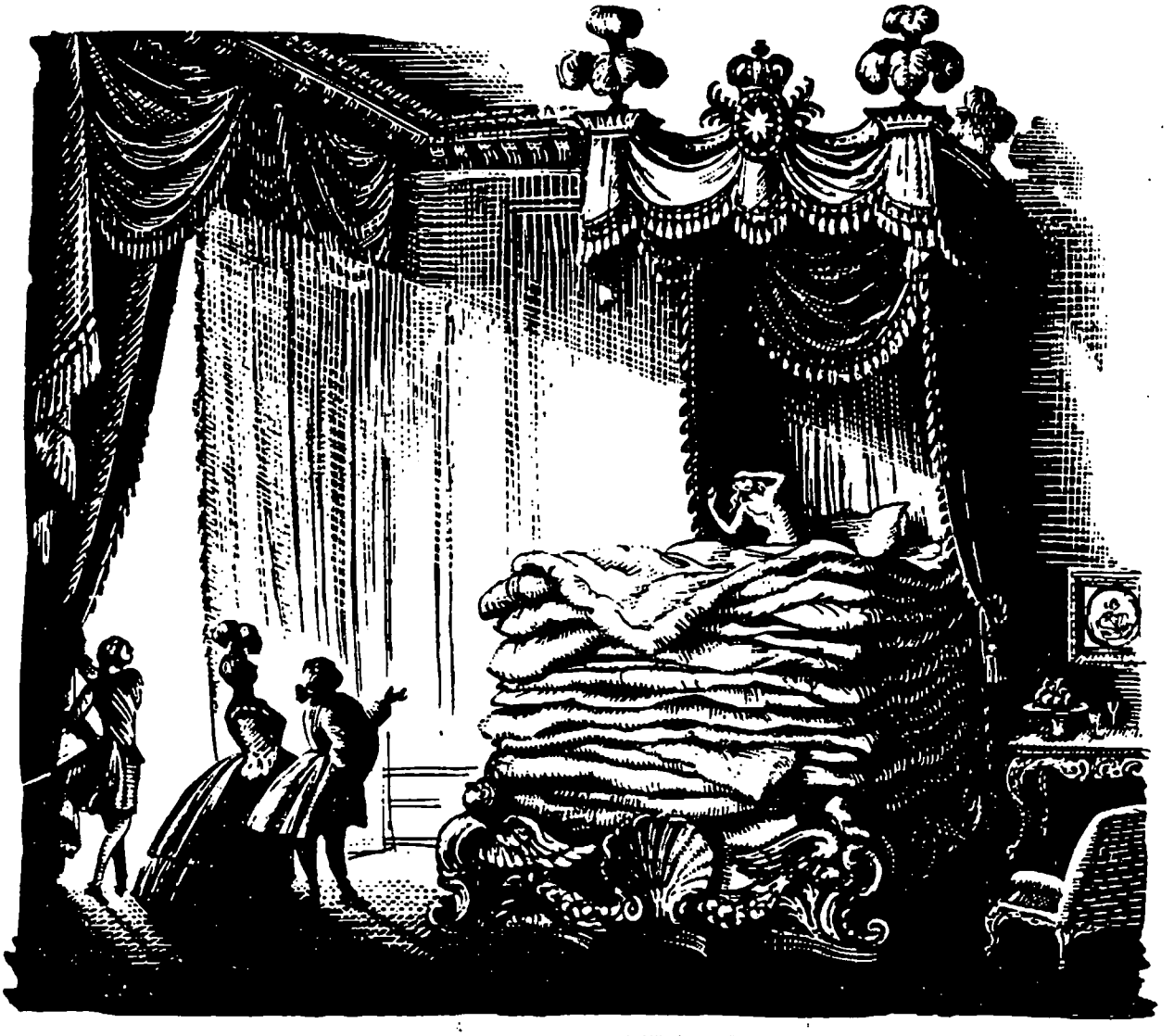

There once was a prince who wished to marry, but there were so many make-believe princesses around that he was unable to find one who was suitable. One evening a fearful storm arose, with thunder clouds streaked by lightning. The sky was black as pitch and rain poured down in torrents. There came a loud knocking at the palace doors and the Prince went to see who was without. The figure outside was a sorry sight, with water running from her hair and her soaking wet dress clinging tightly to her body. She claimed to be a princess. The prince was impressed, but the old Queen-mother was not so easily convinced and decided to set the girl a test. She went to her chamber, removed the bedclothes from her bed and placed a hard dry pea on the bare bedstead. Onto this she laid twenty mattresses, one atop the other, and on top of them twenty eiderdowns. The young girl spent a night on this bed, but when asked next day if she had spent a restful night replied "No, I was so uncomfortable that I hardly slept a wink. My whole body is black and blue with bruises". They knew then that she was what she claimed, for only a real princess would be so sensitive that she could detect a tiny pea through so many intervening layers.

Adapted from 'The Princess on the Pea' by Hans Christian Andersen.

Illustration by Rex Whistler in 'Fairy Tales and Legends by Hans Andersen', Cobden-Sanderson (1935).

The method of pelletising composites for DSC analysis, using a hydraulic die, was conceived during previous work by this author [1]. None of the work described in this thesis was carried out at that time, nor has it previously been submitted in whole or in part to The Open University or any other institution. The work is that of the author except for the following, which were carried out by colleagues at Thornton Research Centre:

Barry Jones constructed the centring tool and modified the DSC cell.
Jim Milner prepared the silica discs (thermal conductivity standards).
Dave Park and **Karen Horsley** carried out the electron microscopy.
Steve Garner made the surface profile measurements.
Keith Titchener carried out the X-ray diffraction.
Karen Dunne analysed the aqueous nickel oxide extracts for anions.
Dick Heather synthesised the β-octaethylporphyrin.

The invaluable contribution made by each of these is gratefully acknowledged.

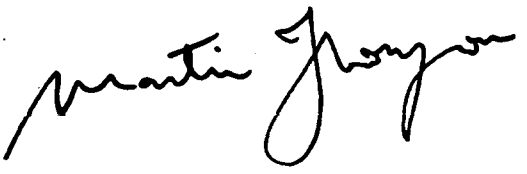

Martin Thompson, February 1991.

ACKNOWLEDGEMENTS

I am indebted to Alan Quayle and Charles Milne, without whose initial support this work could never have begun, and also to Shell Research Ltd. for providing facilities to carry out the research. The continued interest shown by Alan and Charles, long after their formal involvement with the work had ended, was also much appreciated.
I would particularly like to thank my supervisors Jack Pearce and Charlie Harding for their advice, encouragement and patience (Oh no! - not another experiment?) and of course Liz, for putting up with it for so long and also for making the sandwiches. Special thanks go to two close friends: Rob Wetton (perhaps the most like-minded* of all?) for morale support, staying awake through hours of tedious proof-reading and for many pints in the Swan; Jezz Leckenby (formerly of Du Pont) for reams of scientific information, his critical observations and several jugs of wine in a dubious Italian restaurant. I would also like to thank the many other friends and colleagues at Thornton Research Centre and in the outside world of thermal analysis, who contributed their scientific expertise and morale support. In addition to those detailed on the previous page, these include: Phil Barnes (Leeds Polytechnic), Jim Botterill, Graham Clark (Angus College), Ray Cooke, Simon O'Connor, Rod Davies, Richard Heins, Irene Hughes, Charlie Kenwright, Steve Lett, Trevor Lever (Perkin-Elmer, UK), Albert Lynes, Thomas McKarns (Mettler, Switzerland), Euan McKerrell, Alan McNab, Geoff Morris, Richard Selfe, Kate Smith and Alan Smithers.

If anyone has been missed out - Sorry, and thanks anyway!

* With acknowledgements to Survival Aids, Cumbria.

ABSTRACT

Problems arise in differential scanning calorimetry (DSC) when large samples and high levels of amplification are used to enhance sensitivity. Artifact peaks are generated by the instrument, calorimetric sensitivity is reduced and DSC peaks are distorted as the transition interface passes through the specimen. These effects have been investigated by peak shape analysis for fusion, crystallisation and a polymorphic transition occurring in model DSC specimens. The results were used to develop two techniques for studying interactions in solid composites by means of heat-flux DSC. These novel techniques were applied to solid composites containing porphyrins and nickel(II) oxide.

One of the techniques utilised an improved procedure for measuring the thermal conductivity (λ) of small samples. Values of λ were measured for several pure porphyrins and composites, and the results compared with calculated values from various mathematical models which predict transport properties. This allowed structural changes at the interface between the solid phases to be inferred. The occurrence of these changes was supported by electron microscopy.

The second technique was designed to isolate relatively weak DSC peaks from background interference. A fully reacted composite specimen was used to generate a reference DSC curve, which was subtracted from the initial DSC scan. This compensated for the varying heat capacity and Néel transition in nickel(II) oxide, and allowed two types of event to be detected. One of these appeared to be a general feature for free-base porphyrins, corresponding to formation of a nickel-porphyrin complex and water. Reaction began at 0.5-0.6 of the fusion temperature (T/K) for the porphyrin, which Tammann's rule identifies as the region where lattice mobility becomes significant. The second type of event appeared as a very sharp exothermic peak, whose onset corresponded to decomposition of carbonate and hydroxide functions associated with nickel. Rapid acceleration of the process occurred at the Néel transition point in nickel(II) oxide. Both events are believed to represent interactions at the interface between the solid phases.

CONTENTS

CHAPTER 1

INTRODUCTION

CHAPTER 2

DEVELOPMENT OF EXPERIMENTAL TECHNIQUES

CHAPTER 3

INVESTIGATION OF MATRIX EFFECTS FOR ENDOTHERMIC EVENTS

CHAPTER 4

INVESTIGATION OF MATRIX EFFECTS FOR AN EXOTHERMIC EVENT

CHAPTER 5

THERMAL CONDUCTIVITY OF PORPHYRINS AND BINARY MIXTURES

CHAPTER 6

THE USE OF DSC TO DETECT INTERACTIONS BETWEEN PORPHYRINS AND NICKEL(II) OXIDE

CHAPTER 7

CONCLUSIONS

CHAPTER 1

INTRODUCTION

1.1 BACKGROUND

Differential scanning calorimetry (DSC) is a versatile analytical technique which can be used to study enthalpy and heat capacity changes in a variety of materials over a wide range of temperature. It was found during previous work by this author [1] that DSC could detect reactions occurring between the separate phases in heterogeneous solids. Preliminary studies were carried out on composites containing free-base porphyrins and clays, which had been compacted under high pressure. In the work described here, this method of preparing specimens for DSC analysis was developed further. It was then used as the basis for an improved procedure for measuring thermal conductivity and a technique for detecting small energy changes resulting from interactions between solids. These techniques have been applied to a study of interactions between nickel(II) oxide and several free-base porphyrins (structures shown in Figure 1.1):

meso-Tetraphenylporphyrin (TPP)
meso-Tetrakis(pentafluorophenyl)porphyrin (T(PFP)P)
meso-Tetrakis(*p*-methoxyphenyl)porphyrin (T(*p*-MP)P)
β-Octaethylporphyrin (OEP)
Phthalocyanine (PTC)

The last of these is not a true porphyrin, because the bridging (*meso*) carbon atoms are replaced by nitrogen, but its structure is analogous to that of tetrabenzoporphyrin. PTC is used in similar catalytic applications to porphyrins and was included in this study because of its exceptionally high melting point and thermal stability. The nickel complexes of PTC and TPP were also included as being representative of the organic products from reaction between the free-bases and nickel oxide.

Almost all of the calorimetric studies were carried out using a Du Pont model 910 DSC cell with a model 1090 control unit. The latter was also used for storage, manipulation and analysis of data. Some archive data is also referred to, obtained using the same type of cell with a model 990 controller which had no facility for data storage.

1.1.1 Catalytic behaviour of porphyrins

Transition-metal complexes of porphyrins and phthalocyanines are used as photo- and electro-chemical catalysts [2] and have a wide range of applications. These include power generation, use in organic synthesis and as selective gas sensors. A diversity of chemical reactions may be catalysed in this way, for example: cleavage of water molecules by visible light [3]; reduction of oxygen in air batteries [4]; selective production of epoxides [5]; oxidation of sulphur dioxide to sulphuric acid [6]. The central metal atom plays an essential role in determining the reactivity and specificity of the complex. Nickel(II), as its phthalocyanine [7] or tetraphenyl-porphyrin [8] complex, is the most effective first row transition metal in the catalytic reduction of nitric oxide. Interactions between a metallo-porphyrin catalyst and the substrate used to support it are also important. The activity of tetraphenylporphyrinato-cobalt(II) towards decomposition of hydrogen peroxide was more than doubled when it was supported on green nickel oxide and increased by almost thirty times on black nickel oxide [9]. Nickel and oxo-vanadium porphyrin complexes also occur in petroleum [10], where they cause problems in recovery, refining and utilisation. Some of these 'petroporphyrins' are surface active [11] and influence the mobility of petroleum in the reservoir and its water-shedding ability after recovery. High molecular weight metallo-porphyrins associate strongly with asphaltenes and tend to concentrate in residues from distillation of petroleum. Heavy fuel oil, which has a high metals content, can cause serious damage to components of a furnace in which it is burned. Refinery catalysts, especially those used for high temperature cracking, are sensitive to contamination by heavy metals and may be poisoned by those metals which are bound as porphyrin complexes.

Knowledge of the mechanisms by which porphyrins interact with inorganic surfaces is important in understanding their catalytic behaviour. Catalytic complexes might also be produced *in situ*, by reacting a free-base porphyrin directly with the inorganic substrate. This type of interaction between solids is also of mechanistic interest, since a solvent is usually required to dissolve the starting materials in the synthesis of metallo-porphyrins. A particularly

interesting reaction is the formation of a nickel-porphyrin from the free-base and nickel(II) oxide:

$$PORPH{\cdot}H_2 + NiO \rightarrow PORPH{\cdot}Ni + H_2O\uparrow$$

(Where 'PORPH' is a porphyrin di-anion ligand)

This appears to be a simple acid/oxide reaction, but reactions occurring in the solid state are invariably complex and involve at least four processes: physical interaction, chemical reaction, transport of products away from the interface and replacement by fresh reactant molecules. The energy changes detected by DSC are very small because the degree of reaction is restricted by the limited interfacial area between the solid phases. Analysis by DSC is further hindered by a phase transition in nickel(II) oxide, which lies in the temperature region where the above reaction is expected to take place.

1.1.2 Problems due to thermal resistance in DSC

It is well established that the response of a DSC is influenced by the thermal contact resistance between the sample thermocouple and the base of the sample pan [12,13]. Many authors have noted that the calorimeter response is also affected by the physical properties of the specimen. In fact the measured rate of heat flow depends on the total resistance between the sample thermocouple and the site of the thermal event within the sample. Resistances within the bulk of the sample and at its contact with the sample container all contribute to the overall resistance of this conduction path. If the change of heat flux associated with a particular thermal event in the DSC is very small, it is tempting to use a large sample in order to achieve an acceptable signal:noise ratio. This generally results in the specimen having a high thermal resistance, which can have serious consequences in applications where shape analysis of the peak is carried out, such as in purity determination [14] or kinetic measurements [15]. Even when formal shape analysis is not required, visual comparison between DSC curves from different samples is often used to infer structural or chemical differences. It is implicitly assumed that any experimental variables which affect the peak shape have been kept constant, but the thermal resistance of the sample is frequently overlooked. Almost every possible variable in the DSC experiment has some effect on the output DSC curve and these are not always systematic [16,17,18]. It is

therefore important to recognise the particular factors which may influence the experiment being undertaken.

1.1.3 Objectives

The approach used in this work was to consider the DSC specimen, its container and the calorimeter cell as being intimately connected parts of a matrix of thermal resistances. Each of these three components was then investigated to determine its contribution to the overall measuring system. The factors investigated were:

(1) Response of the DSC to a range of heat-flux signal levels, when operated at high electrical gain.

(2) Influence of the type of sample container in coupling the DSC specimen to the measuring element of the calorimeter.

(3) Effects of the internal thermal resistance of the specimen on detection of both endothermic and exothermic processes.

Experiments for investigating interactions between porphyrins and nickel oxide were then based on these findings, with the particular aims of:

(4) Measuring the thermal conductivity (λ) of the specimens in order to identify possible anomalies in the DSC results due to variations of λ,

(5) Detecting interactions between solid porphyrins and nickel oxide in the presence of background interference from other events.

(6) Identifying any mechanistic contribution by the Néel transition in nickel(II) oxide, such as initiation of reaction or a change of reaction rate.

1.2 HISTORY OF DIFFERENTIAL SCANNING CALORIMETRY

Calorimeters are generally classified according to the degree of heat transfer between the sample and the surrounding body of the calorimeter. Isothermal calorimeters allow heat to flow freely into or out of the specimen while the temperature of the surrounding body remains constant. Adiabatic calorimeters lie at the other extreme of the classification range, where heat exchanges are minimised by insulating the sample container. Both types suffer problems due to the

effects of spurious heat leakage between the calorimeter and its surroundings. This caused severe degradation of both the measurement precision and signal/noise ratio in early instruments. Consequently sample sizes tended to be fairly large (several grams or more) and the overall sensitivity was poor. Thermal stability is still a significant source of error in calorimetry, which means that high precision systems tend to have a limited range of accessible temperatures. In spite of this, classical techniques such as isothermal or adiabatic calorimetry are still preferred where specific data is required on known systems. DSC sacrifices some calorimetric accuracy, but it can provide far more information than the other techniques. Its applicability over a wide temperature range means that it is better suited to exploratory studies on novel materials.

The history of DSC is not altogether clear because it appears to have evolved along two almost independent paths.

1.2.1 Tian's heat leakage calorimeter

Tian [19] developed a novel type of calorimeter which helped to overcome many of the problems inherent in trying to totally insulate a calorimeter from its surroundings. The sample container was surrounded by two thermopiles, each of which had alternate junctions connected to the sample container and a massive heat-sink. The first thermopile was used to measure the temperature difference between the inner and outer boundaries of the calorimeter as shown in Figure 1.2. Use of a thermopile made this measurement very sensitive because even a small temperature difference gave rise to a relatively large EMF. The second thermopile (not shown in Figure 1.2) was used to compensate for most of this temperature difference, by means of the Peltier effect, and to measure the amount of energy required. The remaining energy balance was calculated from the temperature difference across the heat leakage path formed by the thermopile wires.

1.2.2 Calvet's work

Tian's apparatus was probably the first example of a true 'heat-leakage' or 'heat-flux' calorimeter. From about 1932, Calvet and his co-workers continued to develop calorimeters from Tian's design in order to improve the sensitivity and accuracy [20]. Probably one of the most significant developments in their work (at least as far as modern thermal analysis is concerned) was the mounting of two identical Tian calorimeters in a common heat sink [21]. By connecting the electrical outputs from the measuring thermopiles in opposition, the differential heat-flux between the sample and reference calorimeters was recorded. This corrected for variations in ambient temperature and also allowed small transitions to be detected more easily because of the stable instrument background. This differential arrangement was so effective in correcting for changes in the external temperature of the calorimeter that the temperature could actually be altered as an experimental variable. The function of this temperature scanning calorimeter was identical to heat-flux DSC in the sense that it is known today.

1.2.3 Boersma's work

Heat-flux DSC of a slightly different type evolved in parallel with the work of Tian and Calvet. This began in the late 19th century, with Le Chatelier's heating curve experiments [22]. Roberts-Austen [23] suggested the use of a dual thermocouple system to simplify recording of thermal events in heating curves. This approach formed the basis of differential thermal analysis (DTA) and had the same aim as Calvet's dual calorimeter system - to eliminate the complex instrument background. A matched pair of thermocouples was used to measure the temperature difference (ΔT) between the sample and a thermally inert reference material, both of which were heated or cooled simultaneously (Figure 1.3a). This experiment produced simple curves in which thermal events were represented by peaks on a nominally flat baseline. Many attempts were made to interpret DTA curves quantitatively and in 1948 Kerr and Kulp [24] published a theory to describe the shape and area of DTA peaks. This work assumed that the temperature of the specimen was uniform, which would only be true for a well-stirred fluid. Smyth

[25] studied the temperature gradients within a heated specimen and showed how altering the position of thermocouples in the test and reference samples would affect the shape of a DTA peak. It was evident from this work that repeatable qualitative results would be difficult to achieve using a conventional DTA apparatus, and that quantification would inevitably be poor. These problems were successfully overcome by Boersma [26] who devised a 'quantitative DTA'. Boersma's system differed from classical DTA in that the thermocouples were fixed outside the sample and reference containers, and formed part of the heat conduction path to them (Figure 1.3b). This meant that the ΔT signal, and consequently the shape and area of the DTA peak, should not be affected by temperature gradients within the sample and reference materials. The main advantages of Boersma's apparatus were that sample preparation was simpler than in classical DTA, but repeatable and quantitative data could be obtained more easily.

A calorimeter operating on an identical principle was described later by de Waal [27], but no reference was made to Boersma's work. Although the materials of construction differed between the two instruments the overall designs were very similar. The most significant difference was that de Waal employed thermopiles, rather than discrete thermocouples, to measure ΔT. These consisted of constantan wire wound into rectangular coils, with one side of each loop silver plated. The coiled wire was then wound into a flat spiral which was used to support a sample container. Two of these arrays were mounted on a common aluminium or copper block to form a differential element, which was quite different in design from that in the Tian-Calvet DSC. Although thermopiles offer improved sensitivity over single junctions, no commercially available system has been based on de Waal's design.

1.3 COMMERCIAL APPARATUS FOR DSC

Virtually all manufacturers of thermal analysis equipment supply some form of DSC apparatus, all of which have broadly similar specifications. They can be operated isothermally or under controlled heating or cooling programmes. Most can be used over a wide temperature range, typically between about −150°C and +700°C.

1.3.1 Setaram's Tian-Calvet system

A DSC based on the Tian-Calvet design was described by Mercier [28] and is produced commercially by the French company Setaram. In this instrument the sample and reference containers are inserted into two tubes, each surrounded by a single thermopile which measures the temperature difference between the tube and heat-sink. Peltier-compensation is not used but the heat-sink block can be resistively heated or cooled by water or some other cryogenic fluid. The physical arrangement, in which the sample is contained in an open tube and surrounded by a cylindrical heat flow sensor, has many practical advantages: aggressive atmospheres are isolated from the thermopile; automatic sample handling and flow-through experiments, such as evolved gas analysis, are easy to set up; vertical alignment of the sample/reference tubes allows the specimen to be supported by an electrobalance, in order to carry out thermogravimetry simultaneously with the DSC experiment. Setaram offer many different types of sample containers which allow experiments to be carried out under a wide range of conditions.

1.3.2 Systems based on the Boersma design

The majority of commercial DSC systems are variations on Boersma's design. One of the most important factors which has led to this widespread adoption is its simplicity, particularly in the use of a pair of relatively cheap thermocouples as the heat-flow sensor. The Boersma-type heat-flux DSCs marketed in Europe are produced by six companies: Du Pont (USA), Mettler (Switzerland), Netzsch (Germany), Seiko Instruments (Japan), Setaram (France) and PL Thermal Sciences (UK). Setaram produce a Boersma system as an alternative to their long standing, but expensive, range of Tian-Calvet calorimeters.

The Mettler design is unique among the Boersma derivatives in that it employs a differential thermopile to measure ΔT between the sample and reference containers. The conduction element is a ceramic plate (as in the original Boersma design) on which a series of vapour-deposited nickel and gold conductors form a thermopile with five junctions under both the sample and reference containers. Figure 1.3c shows how the

sample and reference junctions are connected alternately, in contrast to both the Tian-Calvet and de Waal approaches where the thermopiles are discrete and the two complete elements connected in opposition. Another unusual feature is Mettler's approach to measuring the sample temperature. Most DSCs employ a thermocouple in contact with the sample container to measure its temperature, but the Mettler thermopile arrangement does not allow a separate sample thermocouple to be incorporated readily. The easiest way to measure temperature is by means of the control thermocouple mounted in the surrounding furnace, but the thermal resistance between the furnace and sample is high, owing to the relatively low conductivity of the ceramic disc and a physical break between it and the furnace. This high resistance would give rise to serious problems if the thermal lag between the furnace and the sample position were assumed to be constant: DSC curves would actually be time-based, even when plotted on a temperature axis; the large temperature lag would lead to a substantial error in temperature measurement when the heat flow was reversed during a strongly exothermic event. To overcome these potential errors, the sample temperature is calculated from the furnace temperature and the difference in temperature between sample and reference positions (measured by the ΔT thermopile). This approach assumes that the thermal lag between the furnace and reference position is constant for a particular programme rate and is therefore corrected for by the conventional calibration procedure. It is interesting to note that Mettler's DSC sales literature makes no mention of their approach to temperature measurement. This has led to a widespread belief that problems related to thermal lag <u>are</u> inherent in this design. The above information only became available through personal communication with Thomas McKarns of Mettler (Switzerland).

Development of Mettler's original thermopile DSC does not appear to have been publicised in the literature, but a new design has recently been announced [29]. This employs <u>forty</u> gold|gold-palladium thermocouples under both the sample and reference pans, which are insulated by a thin ceramic layer. Specifications for this sensor are impressive: Sensitivity 1.5 $mV \cdot K^{-1}$; Contact resistance 30 $K \cdot W^{-1}$; Thermal noise 1 μW peak-peak. The method of measuring sample temperature is as before.

1.3.3 The power-compensation approach

There is another type of DSC which does not follow either of the above heat-flux designs, but operates on an entirely different principle known as 'power-compensation' [12,30]. This type of instrument is claimed by its manufacturers, Perkin-Elmer (USA), to be the only true DSC (all others being quantitative DTAs). In reality, this is semantic hair-splitting and the International Confederation for Thermal Analysis (ICTA) has defined two categories of DSC [31] according to their operating principle: 'heat-flux' and 'power-compensation'. Perkin-Elmer systems occupy a major section of the DSC market and are a serious contender in exactly the same application areas as their competitors. Although the principle of power-compensation is quite different from the heat-flux systems described in the rest of this thesis, it is included here for comparison.

Sample and reference materials are contained in discrete, thermally isolated micro-furnaces, each of which has a heater and a platinum resistance thermometer (PRT) (Figure 1.3d). Both furnaces are contained in a single heat-sink, which is cooled by either water or liquid nitrogen depending on the temperature range and cooling rate required. Electrical power is supplied to the heaters at such a rate as to keep the temperatures of the two furnaces as closely matched as possible, and following the chosen temperature programme. During an endothermic event, more power will be fed to the sample furnace in order to maintain its rate of temperature rise. The heat released during an exothermic event could be balanced either by supplying more power to the reference furnace or less to that containing the sample. The former approach would always lead to a deviation from the temperature programme during an event, as occurs with heat-flux designs. The manufacturers claim that the leakage rate from the furnaces to the heat-sink is so high that any normally accessible temperature ramp can maintained, even during a pyrotechnic reaction, simply by reducing the sample-furnace power. This is difficult to prove because the indicated sample temperature is in fact the value calculated from the programme rate, not that measured by the PRT. The analytical signal in this case is the difference in power input to the furnaces, rather than a differential temperature. In spite of the

difference in operating principle between heat-flux and power compensation designs, the results from each type of instrument are generally very similar.

1.4 THE Du PONT DSC SYSTEM

Instrument manufacturers differ in their approach to construction of the DSC and signal manipulation but the widely used Du Pont 910 [32] is typical of those systems based on Boersma's design. The following description of Du Pont's system illustrates the major features of a typical commercial DSC.

The calorimeter cell is mounted on an electronics module (the 'cell-base') which contains thermocouple reference cold-junctions, signal amplifier and, in older instruments, a calorimetric linearisation circuit. The lineariser corrects the ΔT signal so that it becomes proportional to the rate of heat flow (Φ) into or out of the sample. The analog Φ signal is digitised and stored on disk, by a remote microprocessor, along with the incremented time, temperature and an optional second analytical signal. Disk files can then be plotted and analysed for characteristic parameters such as extrapolated onset temperature, peak coordinates and specific area. The processor or computer is also used to control the temperature of the cell according to a pre-defined temperature programme. This programme may contain combinations of isothermal, heating and cooling stages, provided that these are within the temperature and controllable rate limits of the cell.

1.4.1 Construction of the 910 DSC cell

Boersma's original design is compared with the construction of the Du Pont 910 DSC cell in Figure 1.4. The latter cell consists of a cylindrical silver block containing a circular well which is bridged by a constantan disc. The circumference of the silver block acts as the former for a wire-wound furnace which is used to heat it. A Platinel II thermocouple embedded in the furnace block is used for temperature control, but this temperature is not recorded as a characteristic signal for the experiment (*cf.* Mettler design). Two

raised portions of the constantan disc have circular chromel plates welded to their undersides, and these are connected by chromel wires to a plug which mates with the electronics module. The chromel/constantan/chromel junctions are used to measure the temperature difference between the raised platforms on which the sample and reference pans are located. An alumel wire welded to the sample position forms a thermocouple junction with the chromel wire and this is used to measure the temperature of the platform under the sample. This probably represents the best approximation to measuring the actual sample temperature which can be readily achieved in this type of instrument.

Purge gas is passed through the furnace block before entering the sample chamber. This brings the temperature of the gas as close as possible to that of the cell in order to minimise thermal disturbance in the region of the heat flow sensor. Gas then escapes via a vent in the silver cover plate. The latter is in contact with the furnace block so that the constantan disc is completely surrounded by walls which have a high thermal conductivity. This means that temperature gradients around the boundary are small and consequently that undetected heat leakage through the atmosphere in the sample chamber ('parasitic' heat exchanges) should be minimal. Thermal stability is further increased by enclosing the furnace in two concentric metal radiation shields and a glass bell-jar. The shields are heated by conduction through their contact points and by radiation from the outside of the furnace. They act as intermediate temperature barriers between the sensitive measuring region of the cell and the outside environment, whose temperature may vary erratically. The behaviour of this shield arrangement may be compared to a system used in adiabatic calorimetry, whereby the temperature of a screen is servo-controlled to follow changes in the sample temperature [33]. This means that the largest fluctuations in heat transfer take place outside the shield rather than between the sample and its immediate surroundings.

1.4.2 Signal processing in the cell-base

The electrical elements of the DSC cell, and their connections to the block components of the cell-base module, are shown in Figure 1.5.

Analog amplification

The small signal levels produced by a differential thermocouple are incompatible with DC amplifiers, which are generally prone to drift. Consequently, the ΔT signal from the DSC cell is converted to AC, by a 103 Hz chopper, amplified by means of a conventional AC amplifier, and then reverted to DC by a second chopper which is synchronised with the first. Early models of the Du Pont amplifier were based on discrete electronic components, but the current system uses two operational amplifiers ('op-amps') in tandem. This gives an overall gain of approximately x3,000 or x30,000, the value being selected manually by switching between two pre-set feed-back levels in the second op-amp.

Calorimetric linearisation

An inevitable consequence of the Boersma design is that the relationship between ΔT and heat flow into (or out of) the sample is not linear (see next section). In the early Du Pont systems (up to and including the Model 1090) the variation in sensitivity of the cell with temperature was corrected by attenuating the amplified ΔT signal with a resistive shunt. This function was carried out by the 'E*(error)*-curve lineariser' circuit in the cell-base. The effective resistance of the lineariser varies with temperature, and is controlled by the signal from the temperature-programmer as follows. The reference voltage which controls the furnace temperature is also used to switch a chain of transistors at regular temperature intervals. These in turn connect resistors in parallel with the ΔT amplifier and thereby attenuate its output. The characteristics of the changeover points can be altered by varying the amplitude of a 40 Hz square wave, which is superimposed on the voltage ramp from the temperature-programmer. This 'overlap matching' is controlled by a potentiometer (R9) mounted on the lineariser circuit board, but optimum matching can only be achieved over a limited temperature range. Mis-matching at these crossover points leads to spurious steps on the output DSC curve which may resemble second order transitions in the specimen.

The microcomputer-based Du Pont systems which followed the Model 1090 employ software linearisation of the ΔT signal, which avoids introducing electronic artifacts. A correction factor is applied to

the amplified signal from the DSC cell as it passes through the computer interface. The factor used depends on the sample temperature, and is taken either directly from a 'look-up table' or calculated by polynomial interpolation between these values. The correction factors have values which follow a smooth curve (Figure 1.6), with a similar form to that derived from the resistive lineariser [34].

1.5 THEORY OF HEAT-FLUX DSC

1.5.1 Heat flow in the DSC cell

The DSC cell consists of a matrix of thermal resistances in which heat flows between the furnace and sample (Figure 1.7). The behaviour of this array is analogous to an electrical circuit, in which electrical potential is replaced by temperature and electrical current by heat flux. It is convenient to consider the two plate thermocouples as temperature nodes and analyse the heat flow relative to these fixed points. Applying the thermal equivalent of Kirchhoff's first law *('The algebraic sum of the currents which meet at any point is zero')* and using symbols defined in Figure 1.7:

For the sample node;

$$([T_p - T_s]/R_a) + ([T_p - T_s]/R_g) + ([T_r - T_s]/R_b) - \Phi_s = 0 \quad ...(1.1)$$

For the reference node;

$$([T_p - T_r]/R_a) + ([T_p - T_r]/R_g) - ([T_r - T_s]/R_b) - \Phi_r = 0 \quad ...(1.2)$$

Subtracting (1.1) − (1.2) to eliminate T_p, and substituting $T_r - T_s = \Delta T$:

$$\Delta T = (\Phi_r - \Phi_s)/([1/R_a] + [1/R_g] + [2/R_b]) \quad ...(1.3)$$

Equation 1.3 shows that the differential heat flow into the sample and reference is related to the temperature difference between the corresponding thermal nodes, i.e. the parameter measured by the differential thermocouple. It is also evident that the measured temperature difference depends strongly on the thermal resistance of the atmosphere in the cell (R_g) and of the constantan disc (R_a and R_b). Any change in these resistances, due to altering the temperature

of the cell or the composition/pressure of the atmosphere in it, will result in a change in thermal sensitivity ($\Delta T/[\Phi_r - \Phi_s]$).

One of the reasons given by Du Pont [13] for choosing constantan for the conductive plate of the DSC cell is that 'since its electrical conductivity is *very constant (sic)* as a function of temperature, one expects its thermal conductivity to be equally constant according to the Wiedemann-Franz law'. This assumption seems to be at variance with the law*, and in fact the thermal conductivity of constantan increases from 20 $W \cdot m^{-1} \cdot K^{-1}$ at 100 K to 30 $W \cdot m^{-1} \cdot K^{-1}$ at 500 K, with corresponding decreases in R_a and R_b. Over the same temperature range, R_s decreases by a factor of about three. The effect of these resistance changes is to decrease the sensitivity of ΔT to changes in the differential heat flux ($\Phi_r - \Phi_s$) as temperature increases. However, the sensitivity of the differential thermocouple used to measure ΔT actually increases with temperature (by a factor of about two in the above temperature range). The overall effect is that the electrical sensitivity ($V/\Delta\Phi$) of the cell displays a maximum at ~ 35°C, decreasing rapidly at lower temperatures and more gradually above this temperature, i.e. the inverse of the curve in Figure 1.6. In spite of the above comments, constantan is a good choice of material for the cell for the following reasons.

Constantan has:

- a fairly low thermal conductivity (compared to most metals) which means that R_a and R_b are high (*cf.* use of a ceramic plate in Boersma's original design). This leads to a high sensitivity ($\Delta T/[\Phi_r - \Phi_s]$).
- a low coefficient of expansion, which minimises the tendency of the disc to distort as the cell is heated.
- good chemical resistance to most common atmospheres and sample decomposition products.

---

*Wiedemann-Franz law:
The ratio of the thermal conductivity of a metal to its electrical conductivity is a constant (independent of the metal) times its absolute temperature.

Type E (chromel/constantan) thermocouples have:

- higher thermoelectric voltages than most common thermocouples.
- a Seebeck coefficient which varies smoothly with temperature, having no sharp inflections or troughs.

In order to achieve the best sensitivity with this type of cell R_g should be large, and therefore argon or nitrogen should be used as an inert purge gas rather than helium. If the conductivity of the cell atmosphere is different from that when the E-curve linearisor was set up, significant calorimetric errors may be introduced. This highlights a potential problem with more recent Du Pont DSC systems, namely that the sensitivity factors in the look-up table are not accessible. Consequently a universal correction curve is applied to the ΔT signal, no matter what the experimental conditions.

1.5.2 Measurement of heat capacity

As the temperature of the DSC cell is increased, heat will flow from each of the temperature nodes of the thermal bridge (Figure 1.7) at a rate which depends both on the heating rate of the cell (dT_p/dt) and on the heat capacity of the specimen container (C_h) + contents (C_s). Part of the constantan plate will lie between the notional position of the thermal node and the sample container. Consequently, this region of the platform supporting the pan will make a contribution (C_d) to the heat capacity C_h.

For the reference node:

$$\Phi_r = (C_h + C_d) \cdot dT_p/dt \qquad \ldots(1.4)$$

For the sample node:

$$\Phi_s = (C_s + C_h + C_d) \cdot dT_p/dt \qquad \ldots(1.5)$$

Subtracting (1.5) − (1.4) gives:

$$\Phi_s - \Phi_r = C_s \cdot dT_p/dt \qquad \ldots(1.6)$$

Thus the heat capacities of the constantan disc and the pans cancel between sample and reference positions. This means that, provided the sample container and thermocouple are matched to those on the reference side of the bridge, the DSC baseline will be offset from

electrical zero by an amount ($\Phi_s - \Phi_r$) which is proportional to the heat capacity of the specimen in the sample container (Figure 1.8). Similarly, a second order transition in the specimen, during which its heat capacity changes, will appear as a step on the baseline.

1.5.3 Response to a sharp first-order transition

Consider a specimen of a pure material being heated in the DSC. The initial baseline offset (Figure 1.8, up to point 'a') represents the heat flux required to raise its temperature at the programme rate. If a sharp first order transition, such as fusion, occurs in the sample its temperature will remain constant while the transition is taking place. Meanwhile, the temperature of the furnace (T_p) continues to rise at a linear rate and consequently the heat flux Φ_s increases (a→b). The slope of this region of the curve depends on the temperature programme rate, and also on the thermal contact resistance (R_c) between the sample and its associated node:

$$\text{Slope(ab)} = \left|\Delta\Phi_s/\Delta t\right| = (1/R_c)\cdot(dT_p/dt) \qquad \ldots(1.7)$$

(Note: the modulus of the slope has been used here because the negative sign convention for endothermic heat flux is not universally accepted.)

This contact resistance will be affected by the conductivity of the atmosphere in the DSC cell. Although the absolute sensitivity of the calorimeter is improved by use of a low conductivity atmosphere (equation 1.3) the *resolution* of overlapping peaks is improved by the use of helium as a purge gas [35]. This is because R_c is reduced and the peaks become correspondingly sharper.

Returning to Figure 1.8, all of the heat flow Φ_s in the interval t(a)→t(b) is used to transform solid sample to liquid at the same temperature. Therefore, the heat capacities of the isothermal parts of the system (i.e. $C_s + C_h + C_d$) make no contribution to the heat flow. The total area under this region of the curve represents the enthalpy of fusion of the specimen:

$$\int_{t(a)}^{t(b)} \Phi_s \, dt = (A+C) = \Delta H_{fus} \qquad \ldots(1.8)$$

At point 'b' on the curve, the sample has just completely melted and its temperature is still T_{fus}. However, the temperature of the sample node is:

$$T_s = [T_{fus} + (dT_p/dt) \cdot (t(b) - t(a))] \quad \ldots(1.9)$$

The sample, its container and the associated part of the constantan plate undergo ballistic heating to catch up with the temperature programme. Lee and Levey [13] analysed the shape of the peak trailing edge and showed it to have an exponential form. If we consider the melted sample to have reached the temperature equivalent to its initial rate of heating at point 'c', then the area under the curve in the region b→c, i.e. {B+D}, represents the energy required to raise the temperature of the specimen from $T_s(a)$ (= $T_s(b)$) to $T_s(c)$. However, if no transition occurred in the specimen, the energy required to heat it from $T_s(a)$ to $T_s(c)$ would be represented by the area {C+D}. This means that the enthalpy of fusion is equivalent to:

$$\{A+C\} + \{B+D\} - \{C+D\} = \{A+B\}$$

which is the area of the peak below the 'sample baseline' (ac).

The baseline construction for integrating the peak area in this case is a simple extrapolation from the sample baseline before the peak to that after it. Significant errors can arise when the baselines differ between the two sides of the DSC peak, as happens when the heat capacities of the corresponding phases are different. The problem is compounded when the slopes of the baselines also differ, owing to a difference in the temperature coefficients of heat capacity of the two phases. Sandu and Singh [36] discussed baseline construction in these cases and analysed the shape of DSC peaks by partial areas in a similar manner to that shown for a simple baseline in Figure 1.8. It was shown that the error in peak integration increases with heating rate and extrapolation to zero rate was suggested as a means of improving measurement accuracy.

1.6 MEASUREMENT OF THERMAL CONDUCTIVITY

In the previous section, equation 1.7 indicated that the rate of change of heat flow during a transition is determined by the thermal contact resistance R_c. This arises because DSC involves measurement of heat-flux under conditions of varying temperature. Limitation of heat

transfer rates in the calorimeter can be exploited to measure the thermal conductivity (λ) of a small specimen. Although this is not one of the 'classical' applications of DSC, it is becoming increasingly popular for measurements where only a limited amount of sample is available.

1.6.1 Experimental approaches

Several authors have reported measurement of λ using modified Du Pont and Perkin-Elmer DSC cells [37-41]. In all these cases a relatively large specimen was surmounted by a thermostatic heat sink. The temperature difference between the two faces of the test specimen was then related to the rate of heat flow through it, measured by the DSC. The experiment may be carried out isothermally or with a temperature ramp. Two distinct modes of measurement have been reported: single sided experiments - involving an absolute measurement for a single specimen on the sample platform; double sided experiments - in which heat flow through the test specimen was compared with that through a reference material occupying the other DSC position. These methods have two disadvantages, in that ancillary apparatus (a heat sink fitted with thermocouples) is required and the specimen dimensions are relatively large (albeit smaller than for most classical conductivity methods).

An alternative method [42-44] utilises the change of peak shape for an endothermic event, where increasing resistance broadens the DSC peak and reduces the slope of its leading edge. The experimental arrangement (Figure 1.9a) is analogous to the single-sided case of the modified DSC except that a layer of pure material (usually a metal) undergoing fusion acts as an isothermal heat sink. In this experiment the temperature of the top face of the specimen is fixed at the melting point of the fusible standard, while the bottom face is subjected to a linear temperature ramp. The slope of the DSC peak leading edge is inversely proportional to the total resistance of the heat flow path, i.e. the sum of the test resistance and contact resistances. This method does not require any modification to the calorimeter cell and uses relatively small samples, of similar size to normal DSC specimens.

1.6.2 Theory of the fusion onset slope method

Consider the experimental arrangement shown in Figure 1.9a where the furnace is being heated using a linear temperature programme. Two parameters are measured by the DSC - the rate of heat flow into the sample (Φ) and the temperature of the sample platform (T_s). At the melting point of the fusible metal disc, the temperature of the top surface of the sample ceases to rise and remains at T_{fus} until all of the metal is liquid. During this interval the temperature difference between the two faces of the sample increases at the programme rate and the heat flux increases accordingly. This corresponds to the leading edge of the DSC fusion endotherm as described in section 1.5.3, except that the sample resistance has been added to the thermocouple/pan contact resistance. The exact form of the temperature profile along the conduction path will be affected by heat leakage to the sides and top of the specimen (Figure 1.9b). However, if this is considered to be a relatively small effect, the heat flow path can be broken down into two parts as shown in Figure 1.9c.

Under steady state conditions, heat flux along the axis of a cylinder in which there is no radial temperature gradient is given by the one-dimensional form of Fourier's law:

$$\Phi = \lambda \cdot A \cdot (dT/h) \qquad \ldots(1.10)$$

Where Φ = heat flux (W)
λ = thermal conductivity ($W \cdot m^{-1} \cdot K^{-1}$)
A = cross sectional area of the specimen (m^2)
dT/h = temperature gradient ($K \cdot m^{-1}$) in a specimen of length h.

The absolute values of temperature and heat flux are difficult to measure accurately, but the change of each with respect to time can be measured easily from the DSC output as shown in Figure 1.10. It is important to note that this plot is temperature-based rather than time-based (*cf.* Figure 1.8) and that the significance of onset slope and partial areas are not the same in the two cases.

If Φ_1 is the measured heat flux when $T_s = T_1$ and Φ_2 is the measured heat flux at some time later when $T_s = T_2$, then from equation 1.10:

$$\Phi_1 - \Phi_2 = \lambda \cdot A \cdot (T_2 - T_1)/h \qquad \ldots(1.11)$$

The slope of the leading edge of the DSC peak is then:

$$\frac{\Phi_1 - \Phi_2}{T_2 - T_1} = \frac{\Delta\Phi}{\Delta T} = \frac{\lambda \cdot A}{h} = \frac{1}{R} \qquad \ldots(1.12)$$

Where R is the <u>total</u> resistance of the heat flow path between the sample thermocouple and fusible metal. The contact resistances (Figure 1.9c) are independent of sample thickness and should be constant between experiments provided that the surface finish of the sample and flatness of the pan are repeatable. If measured resistance is plotted against sample thickness the Y-intercept should correspond to the sum of the contact and pan resistances. The slope will then be the resistance per unit thickness for pellets of this diameter.

The temperatures at which measurements of λ can be made depends on the availability of pure, well characterised, reference materials. Metals are the best choice, because their high conductivity (relative to the test specimen) means that only a small change in resistance occurs as the melt interface passes through the fusible layer. Various organic materials have been suggested as fusible standards for this technique [43] but these would not be applicable to any test material which dissolves in or reacts with the molten phase.

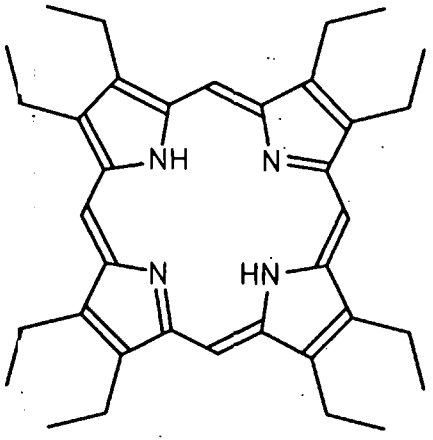

OCTAETHYLPORPHYRIN [OEP]

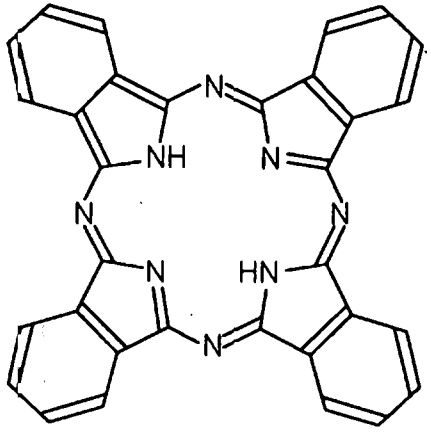

PHTHALOCYANINE [PTC]

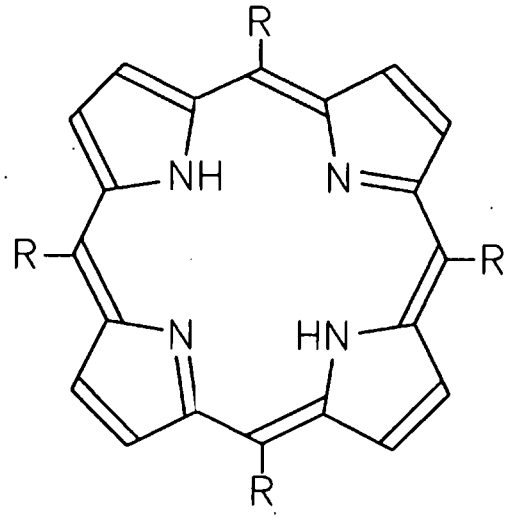

meso–TETRA–ARYLPORPHYRINS

R = 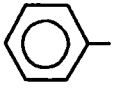 (phenyl) [TPP]

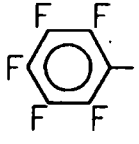

(pentafluorophenyl) [T(PFP)P]

CH_3O 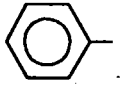 (p–methoxyphenyl) [T(pMP)P]

Figure 1.1 – Structures of the free–base porphyrins.

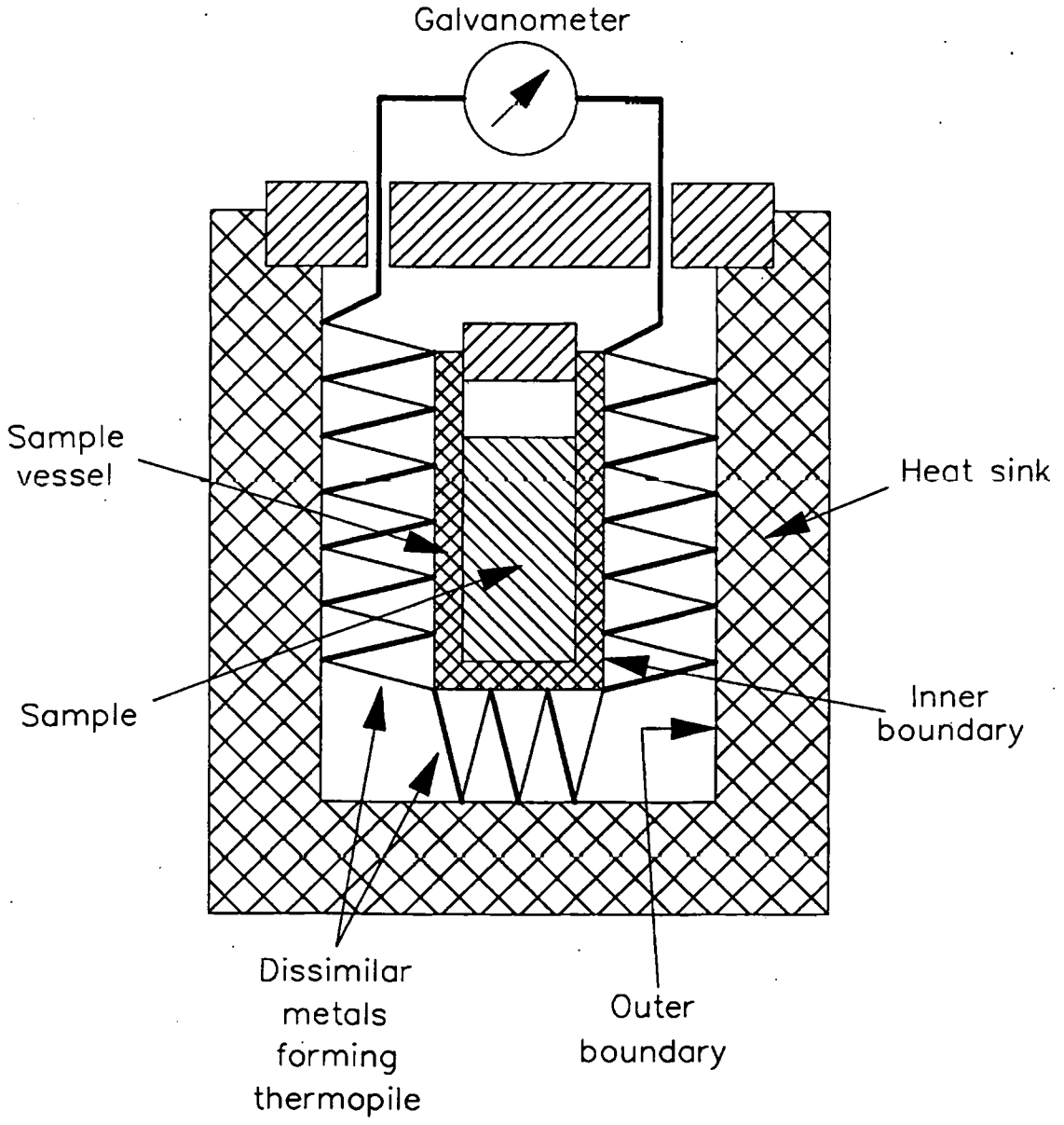

Figure 1.2 – Schematic diagram of Tian's heat–leakage calorimeter.

(compensating thermopile omitted for clarity)

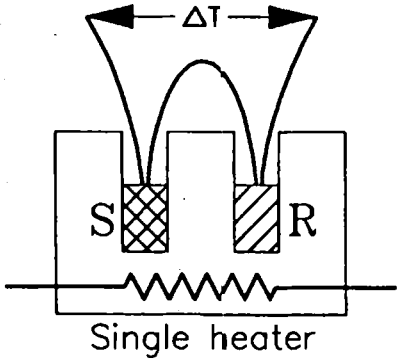

(a) Classical DTA

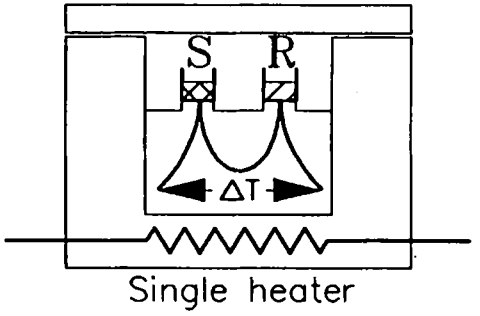

(b) 'Boersma' heat–flux DSC

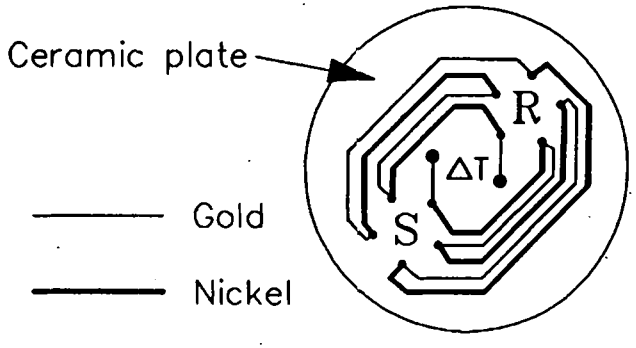

(c) Mettler DSC thermopile

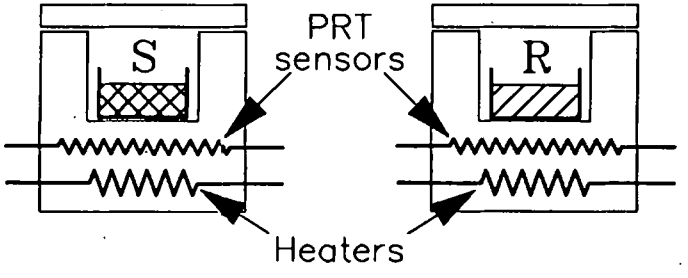

(d) Power–compensation DSC

Figure 1.3 – Some differential temperature sensors which are used in thermal analysis.

(S = sample position R = reference position)

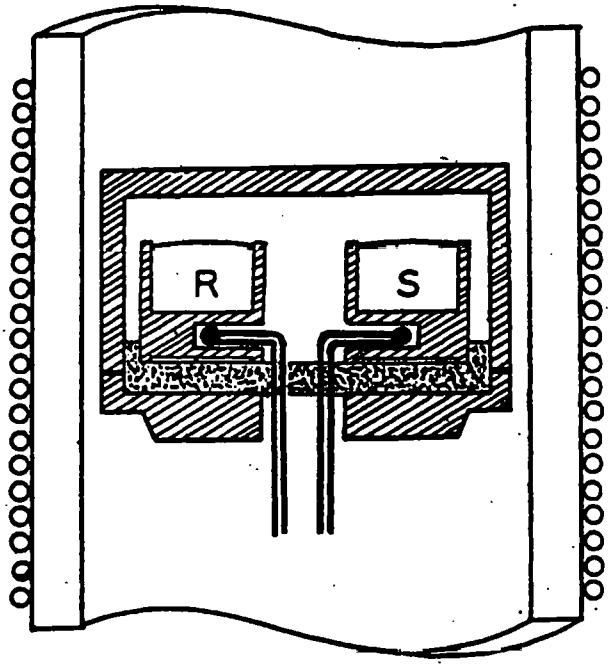

Nickel.

Ceramic plate.

Boersma's original design

(reproduced from J. Am. Ceram. Soc. Vol. 38 1955)

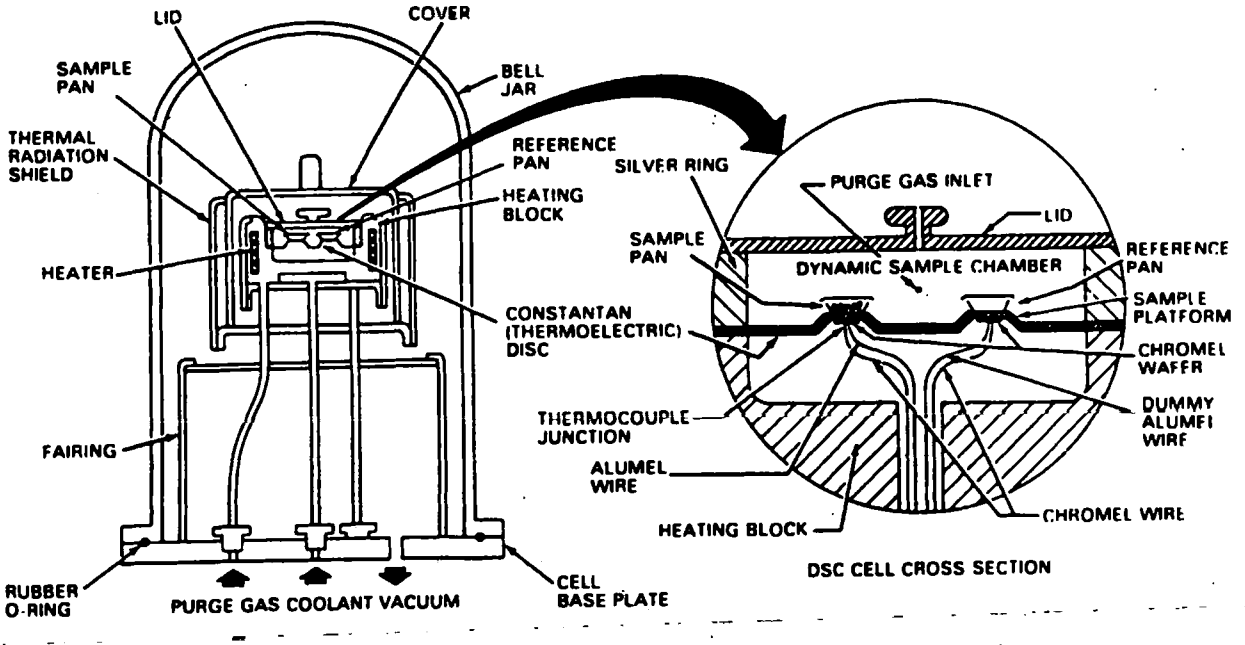

Du Pont 910 (based on the above)

Figure 1.4 – Construction of two heat–flux DSC cells.

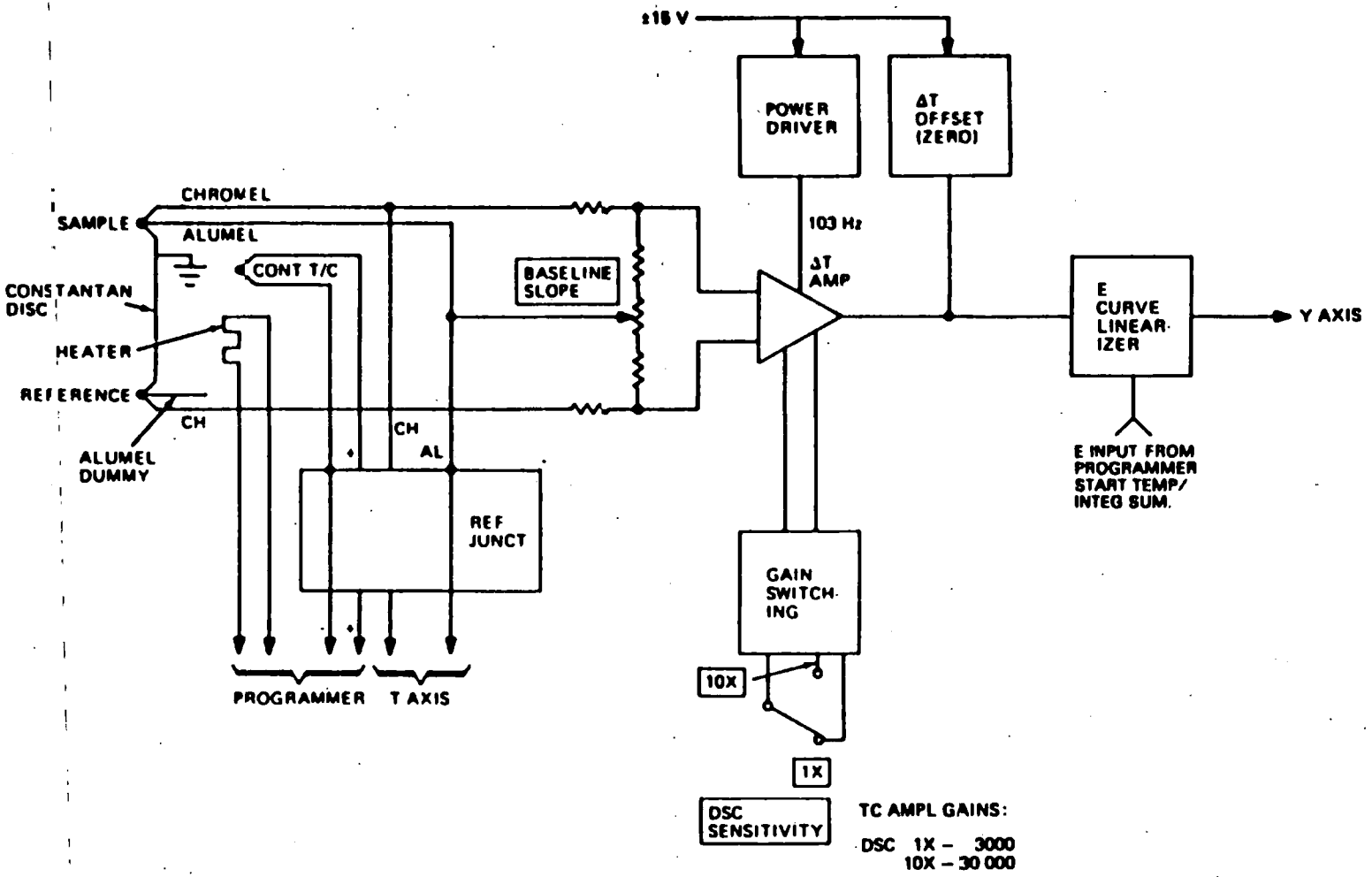

Figure 1.5 – Block functions of the Du Pont DSC cell–base module.
(adapted from Du Pont 910 DSC instruction manual PN 910037–000)

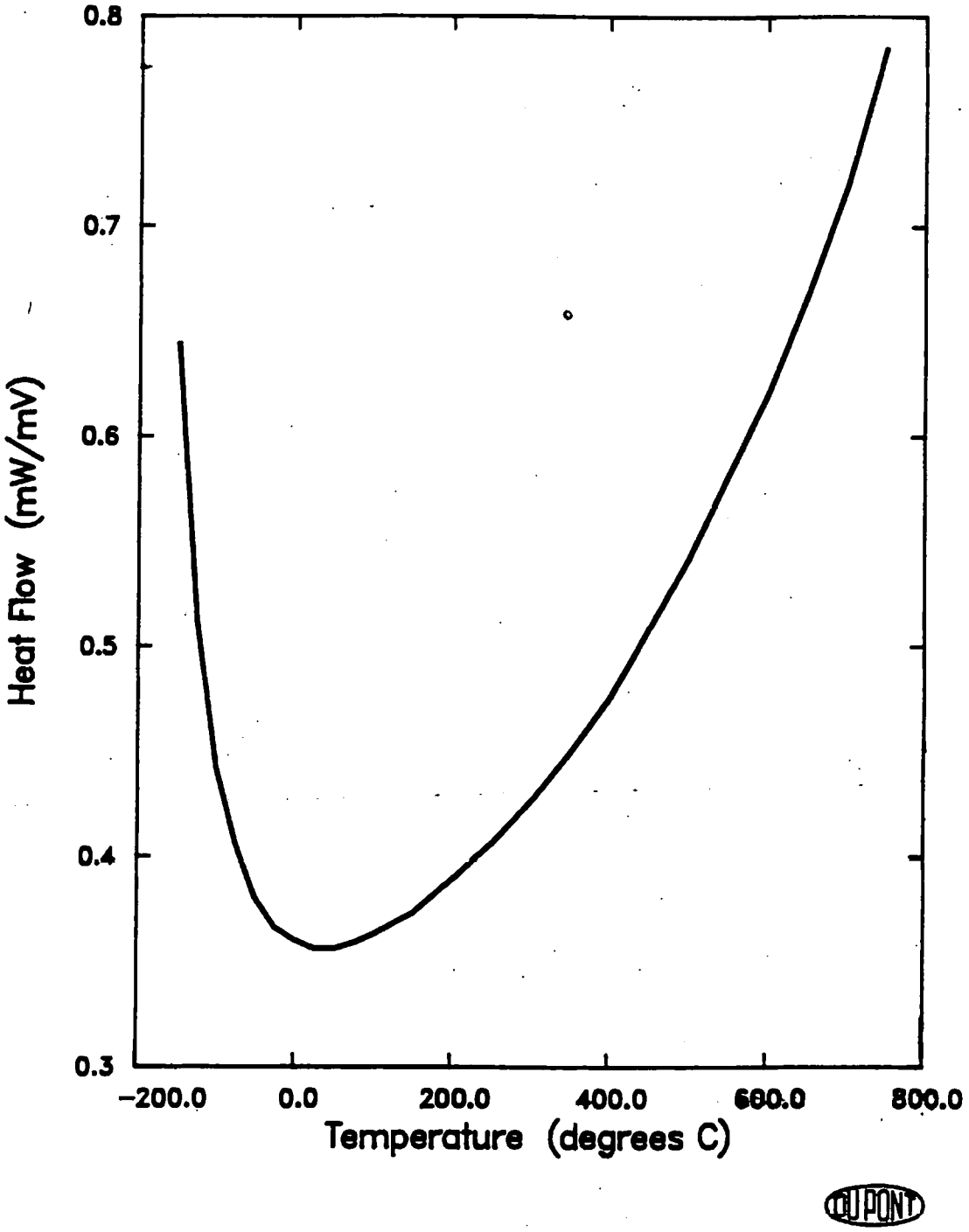

Figure 1.6 – 'Error-curve' function applied to the output from the Du Pont DSC cell.

Note: this is the inverse of the calorimetric sensitivity curve (reproduced from 912 Operator's manual PN 912027-001)

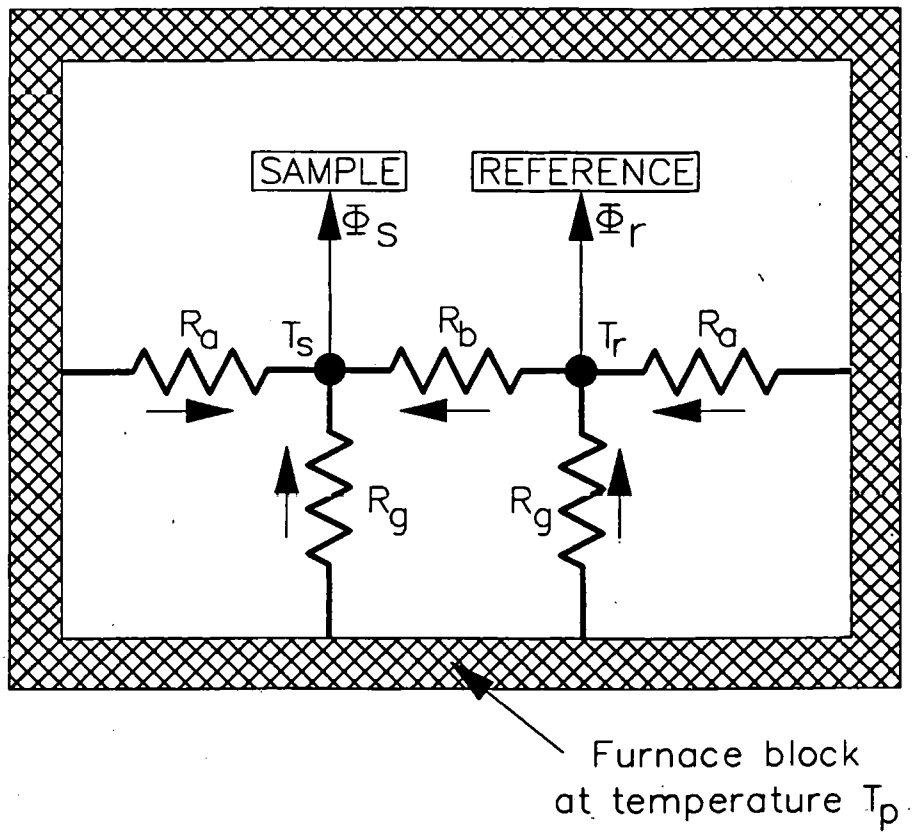

R_a = sample/reference arm resistance
R_b = bridging resistance
R_g = leakage resistance through atmosphere
Φ_s = heat flux into sample
Φ_r = heat flux into reference
T_s = temperature of sample node
T_r = temperature of reference node
→ = heat flow paths during an endothermic transition

Figure 1.7 – Representation of the DSC cell as a resistive network for the Kirchhoff treatment.

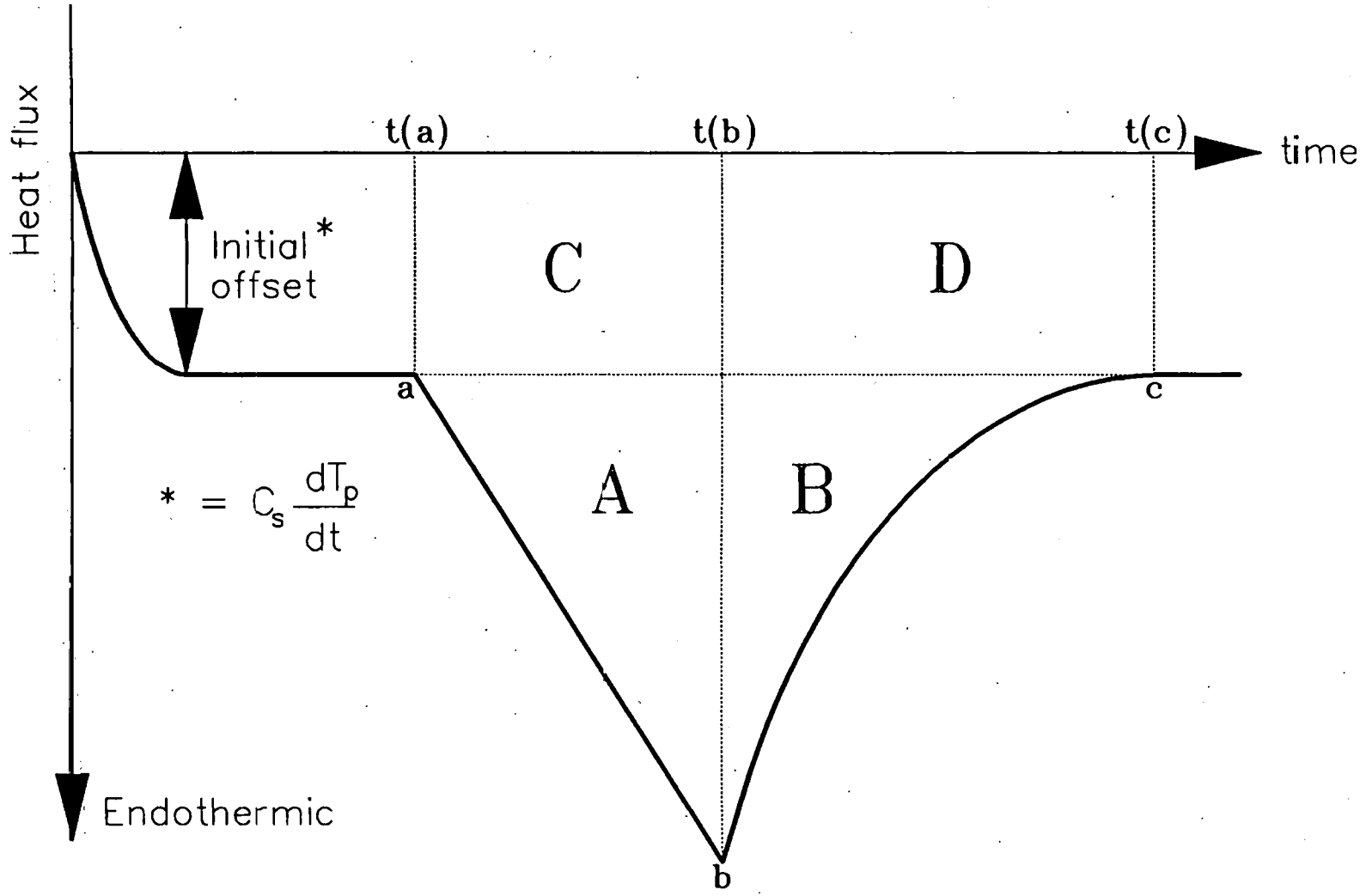

Figure 1.8 – Characteristics of a time–based DSC curve.

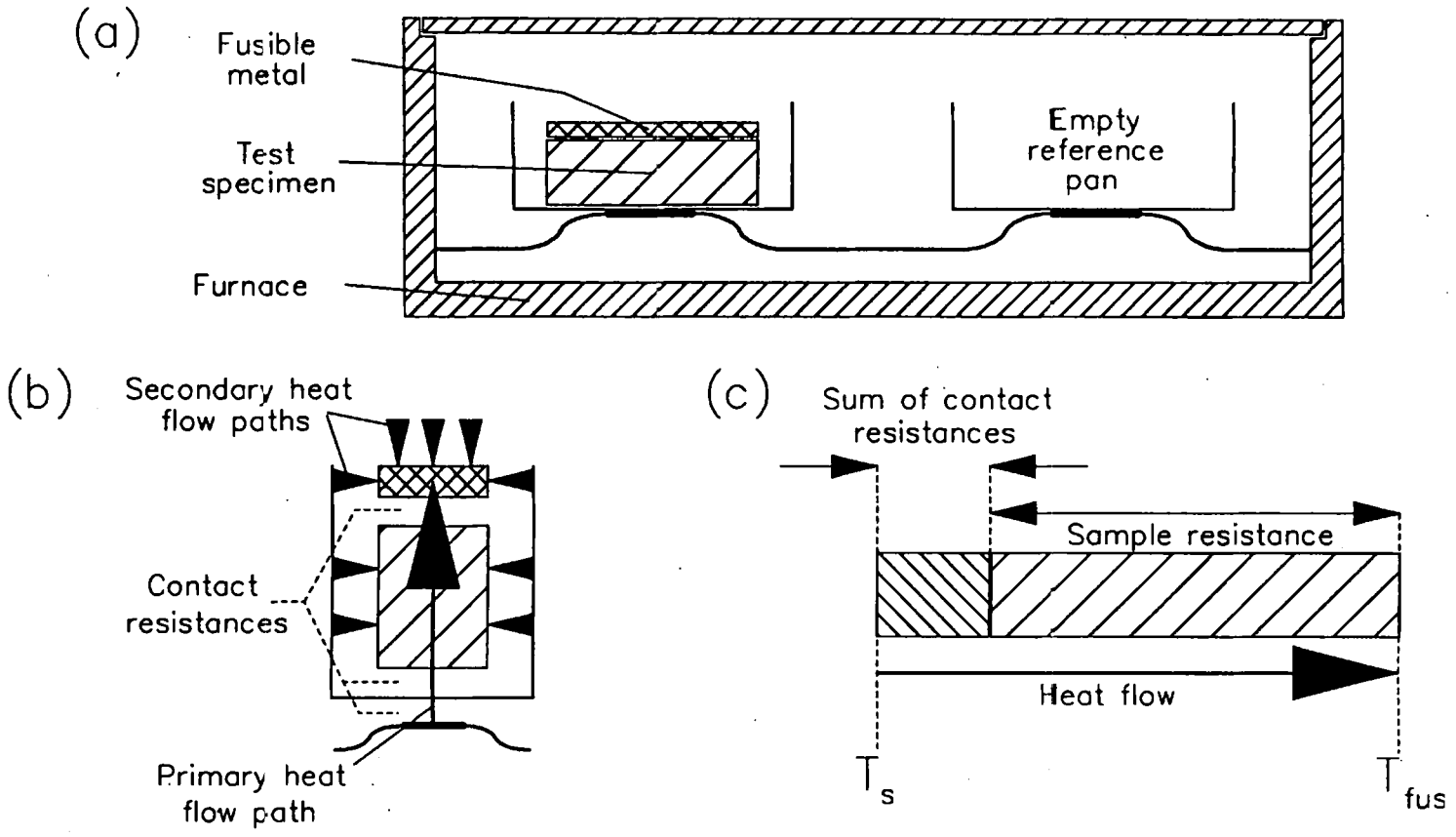

Figure 1.9 – Measurement of thermal conductivity by the fusion onset slope method:
(a) Experimental arrangement.
(b) Heat flow elements.
(c) Equivalent structure for the Fourier model.

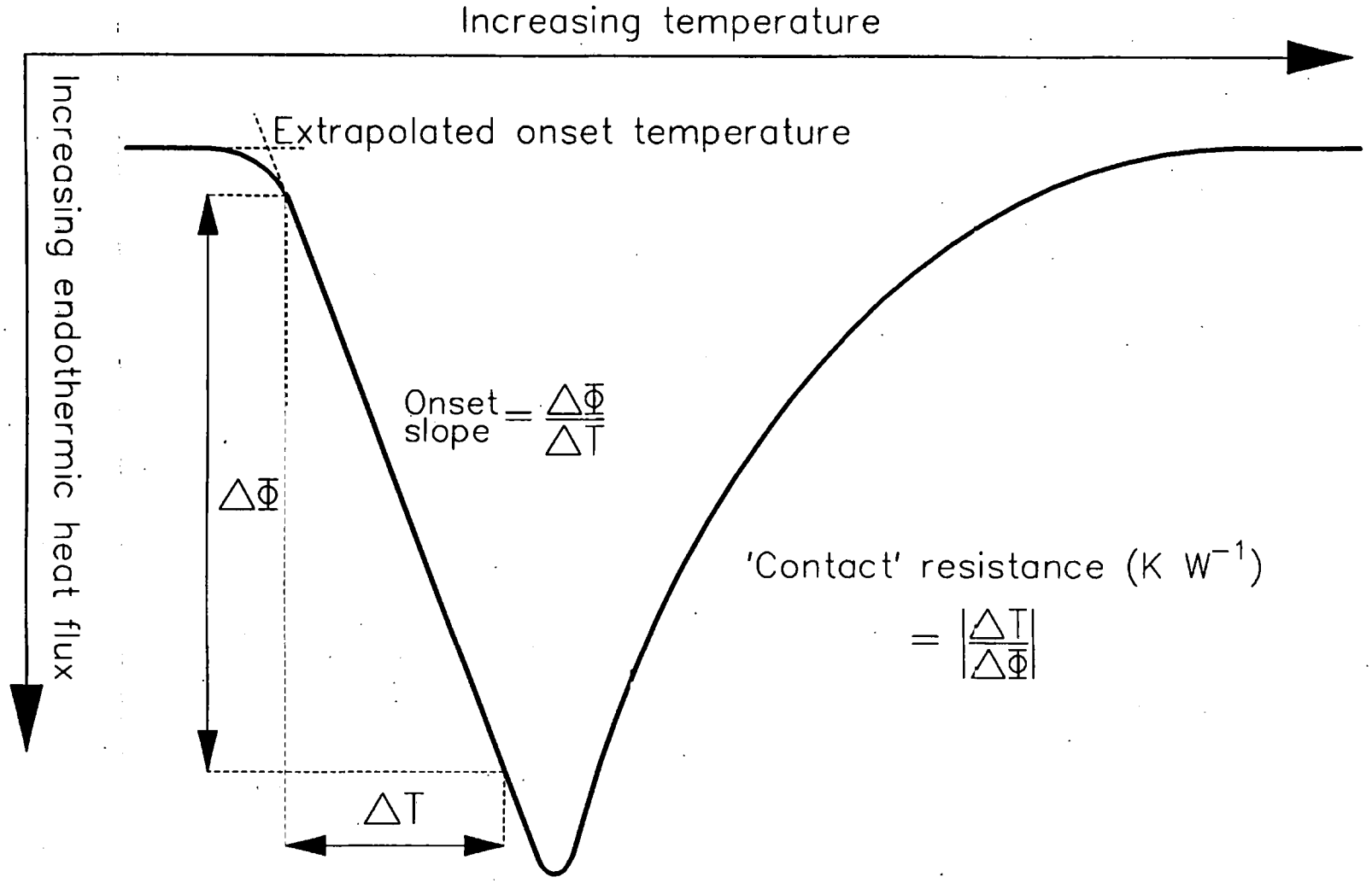

Figure 1.10 – Calculation of thermal resistance from a DSC fusion curve.

CHAPTER 2

DEVELOPMENT OF EXPERIMENTAL TECHNIQUES

2.1 INTRODUCTION

In order to detect small energy changes occurring in a DSC sample it may be necessary to operate the signal (ΔT) amplifier at a high level of gain. This helps to minimise interference by electronic noise and also the limitation of digitisation steps. The latter arise because the heat flux signal is broken down into a finite number of fixed levels for storage as digital data. At very low signal levels, these steps become noticeable on the DSC curve. The amplifier gain should therefore be such that the step height is less than or equal to the baseline noise level on the DSC curve, otherwise information will be lost. The dynamic range of the amplifier may become a limiting factor at high signal levels, which often result from the use of very large samples. Even though the superimposed events (which are of primary interest) may be small, the background signal level may drive the amplifier into saturation. Another undesirable consequence of operating at high gain is that spurious thermal and electronic events are amplified along with the events of interest. If these are not eliminated, or at least identified and discounted, they may be interpreted as being significant properties of the sample. The objectives of the work described in this chapter were to identify: (i) experimental techniques which can improve data quality, and (ii) sources of error and interference. This was specifically intended to assist in the study of matrix effects and its application to detection of interactions between porphyrins and nickel oxide.

If used with caution, software manipulation of data files can be a valuable way of improving data quality. Addition of the DSC curves from several replicate experiments will reduce random effects such as noise and sample variability. Subtraction of an appropriate reference file can remove systematic interferences by the instrument or components of the sample. In DSC, these techniques rely on good temperature stability and baseline repeatability. If the temperature scale shifts between DSC scans, the resulting offset of a sharp event can actually create an artifact and therefore stability is particularly important. Another common technique is smoothing of DSC curves, which may be carried out either by averaging clusters of data points or by polynomial interpolation between overlapping groups of

points. Some electrical smoothing is built into the DSC signal amplifier but this is not usually accessible to the operator. In the work described here, software smoothing of the stored data was not used because this would prevent the benefits of improved experimental techniques from being recognised.

The factors which were found to affect sensitivity and repeatability have been grouped into two sets according to whether they influence detection of enthalpy changes or heat capacity measurements. These have been termed **first order** and **second order** effects respectively, from the thermodynamic classification of a pure enthalpy change as a first order transition and a change in heat capacity as a second order transition. Throughout this thesis where results are quoted with confidence limits, or differences between data have been tested for significance, the 95% confidence level was used.

2.2 BASIC PRECAUTIONS

Many spurious events in DSC are caused by contamination of the cell or sample containers by material which can undergo phase transitions or reactions in the temperature range of interest. Du Pont non-hermetic pans are supplied with a coating of metal-working oil which can oxidise or evaporate on heating. This results in broad shallow peaks which have the overall appearance of baseline curvature. Aggressive atmospheres can cause oxidation of the constantan thermocouple plate, resulting in formation of a layer of scale on which volatile products from the sample may adsorb and undergo reaction. To avoid these problems, all sample containers were washed in dichloromethane, acetone and pentane, dried for two hours at 140°C, and stored in a desiccator over silica gel. The thermocouple plate and DSC sample chamber walls were polished using a glass fibre brush at the start of the experiments but no further cleaning was required between runs. The sample chamber was purged with dry nitrogen at a flow rate of 25 $cm^3 \cdot min^{-1}$ during experiments. Most experiments were carried out at a heating rate of $10°C \cdot min^{-1}$. This is a compromise which sacrifices some thermal resolution of adjacent events (which require a slow heating rate in order to give narrow peaks) for sensitivity and high through-put of samples. The heating rate was increased to $20°C \cdot min^{-1}$

in a few cases where resolution was not important but even higher sensitivity was required.

2.3 FIRST ORDER EFFECTS

Isothermal absorption of heat takes place when a material undergoes a structural or phase transformation. This type of event, which is known as a first order transition, appears as a sharp peak on the DSC curve of a pure material. The narrow form of these peaks tends to accentuate experimental errors, particularly those which lead to a shift of temperature or peak distortion. Spurious sharp peaks are also less likely to be overlooked in the baseline noise than are steps or changes of slope. This makes them liable to optimistic 'over-interpretation' when minor thermal events are being sought.

2.3.1 Temperature measurement stability

Temperature shifts in DSC may be caused by instrumental or experimental factors such as electronic instability, changes in conductivity of the sample chamber atmosphere or the contact resistances between the thermocouple and pan or the pan and sample. Any shift which does not reflect a real change in the intensive properties of the sample (i.e. those which are independent of the dimensions of the specimen) is likely to invalidate addition or subtraction of data files.

The DSC system used in this work was left switched on constantly, so as to ensure that the electronics were as stable as possible. In spite of this precaution, it was noted that repeated calibrations at the start of a series of experiments showed a systematic drift of the measured onset temperature, even though a fresh specimen was used for each scan. Indium powder was contained in a covered Du Pont non-hermetic aluminium pan and heated using a temperature programme 120-180°C @ 10°C•min^{-1}. Starting with a cell at room temperature, it was found that the measured values of extrapolated onset temperature drifted by about 1°C over the first 12 scans, before reaching a constant value (Figure 2.1). In a separate experiment, the system was cycled automatically for 24 hours, over the temperature range

120-180°C, before carrying out calibration scans. In this case drift was not detectable and the repeatability of the measured onset temperature was better than ± 0.1°C. If the DSC cell was heated to 250°C in a single step, the initial offset of measured heat flux ($\Delta\Phi$) was virtually complete within about 2 minutes, but a gradual drift continued for a long time afterwards. The change of offset decayed exponentially with time and eventually reached a stable level - 1.5 mW beyond the value at the instrument settling time of 2 minutes. The output was stable to within 0.1 mW of its ultimate value after about 50 minutes. In order to overcome the drift of measured temperature and $\Delta\Phi$, the cell was heated isothermally at the highest programme temperature for at least one hour before carrying out DSC experiments. This eliminated detectable temperature drift and had the same effect as cycling the DSC through the chosen temperature programme for 24 hours.

2.3.2 Distortion of the sample container

Variation of the thermal contact resistance (R_c) between the pan and thermocouple will affect the shape of a DSC peak. In order to make the contact area more repeatable, it is normal to flatten the base of a DSC pan before use. A sudden change of contact area during an experiment is normally distinguished by a sharp spike on the DSC curve. This occurs if for example the cell is accidentally knocked, or the pans disturbed by a surge of gas. Spurious events of this type are readily distinguished from normal DSC peaks by their shape. Dimensional changes in the sample, or evolution of gas from it, may cause gradual distortion of the pan and hence alter its contact resistance in such a way as to generate a broader, less obvious artifact.

The effect of pan distortion on a DSC curve was investigated by heating a moderately volatile material, contained in a hermetically sealed pan (see Appendix I for details), over a temperature range in which its increasing vapour pressure would be expected to cause dilation of the container. A DSC cell contained in a high pressure housing (PDSC) was used, with the following experimental conditions:

Sample; 2 μl paraffinic mineral oil (HVI 160-B).
Container; Du Pont hermetically sealed pan.
Atmosphere; Nitrogen at 150 psig.
Gas flow rate; 50 $cm^3 \cdot min^{-1}$ at vent.
Amplifier range; x10.
Temperature programme; 25-400°C @ 20°C$\cdot min^{-1}$.

The DSC curve from this experiment displayed an exothermic shift of approximately 1.3 mW in the region 180-220°C (Figure 2.2), which was attributed to an increase in thermal contact resistance caused by 'ballooning' of the pan (Note: indicated peak height is 13 mW because Y-range is x10). The offset then decayed back to approximately the original baseline, presumably due to failure of the seal and release of internal pressure. This event had the appearance of a broad exotherm, followed by an erratic endothermic peak which continued up to ~ 350°C. After the cell had cooled the pan was removed and weighed, which showed that the sample had completely evaporated.

These results showed that Du Pont hermetic pans should be used with caution and a different type of sample container used whenever possible. Other problems associated with this design of pan were also identified (see section 2.4.3).

2.3.3 Condensation of moisture in the DSC cell

In order to ensure a steady baseline, it is normal to begin a DSC temperature programme ~ 10-50°C below the temperature from which data is required. This means that many experiments require initial cooling below ambient temperature before the heating cycle. There are several ways of achieving this, including accessories which bolt on to the DSC head, such as Du Pont's Mechanical Cooling Accessory (MCA) or Liquid Nitrogen Cooling Accessory (LNCA). These have the disadvantage that they remain in contact with the cell head during the DSC experiment, which reduces the upper temperature limit of the system and tends to increase thermal noise levels. An alternative method is to use a 'quenching can', filled with liquid nitrogen, which is removed before heating so that the convection and radiation shields can be replaced. Unfortunately, the close fit of this accessory tends to make it grip

the cell head and cause vibration as it is withdrawn. If the cell cover is then removed, in order to check that the pans have not been disturbed, atmospheric moisture may condense in the cell. Ice can form if the cell is cooled to below 0°C and spurious peaks are produced on heating as the ice melts and capillary water film evaporates.

A DSC cell containing two empty aluminium pans was purged with dry nitrogen, at a flow rate of 25 $cm^3 \cdot min^{-1}$, and cooled to −50°C using a quenching can. The can was then removed and the cell opened to the atmosphere (~ 40% relative humidity) for 5 seconds, to represent the time taken to relocate displaced pans. The cover and shields were then replaced and the cell heated at $20°C \cdot min^{-1}$ to 150°C. Peaks produced by water which had condensed under these conditions were found to be variable, but frequently had a form similar to that shown in Figure 2.3. Each event has a characteristic 'S' shape which is believed to result from thermal asymmetry in the cell and may be explained as follows. The first peak results from ice melting in the vicinity of the reference thermocouple and is followed by a rapid endothermic swing as ice around the sample thermocouple reaches its fusion temperature. The capillary film of liquid water on the surface of the constantan thermocouple plate then evaporates in the stream of dry purge gas. As for the first event, evaporation does not take place symmetrically around the differential thermocouple and the phase transition is recorded as a sigmoid curve. The second event was assigned to evaporation because there was no evidence of moisture in the cell when it was opened at 20°C, and no further events were detected up to 150°C.

In order to cool the DSC cell without exposing it to the atmosphere, and to avoid increasing the thermal noise level, a cooling system was constructed (Figure 2.4) which did not require extra hardware to be fixed to the measuring head. This consisted of a coil of copper tubing immersed in liquid nitrogen, through which dry nitrogen gas was passed. The cold exhaust stream was connected to the cooling port on the cell base by insulated silicone tubing. A second stream of dry nitrogen, at room temperature, was used to purge the sample chamber. The cooling flow was switched off before starting programmed heating, as the insulation of the cell was sufficient to prevent it heating up

faster than the programme rate. This approach allowed the cell to be cooled rapidly to −100°C without disturbing the pans and with no evidence of contamination by moisture.

2.3.4 Saturation of the signal amplifier

Some sources of interference, such as contamination of the DSC cell by moisture, are readily identified from the shape of the events which they produce. The greatest threat to reliable results lies in slight, but significant, distortion of existing events as these may be overlooked. Instrumental distortion is most likely to result from working beyond the linear response range of the system. The dynamic range of a DSC system may be limited by the cell itself [45], the analog amplifier or the analog-digital converter (ADC). If the response of the system is limited by the cell or amplifier, the sensitivity (as indicated by specific peak area) will gradually decrease as the linear range is exceeded. Conversely, clipping by the ADC will result in flat-topped peaks and a clearly defined point beyond which sensitivity declines. The linear dynamic range, and the type of distortion produced by exceeding it, were investigated for both endothermic and exothermic events.

Endothermic distortion

Fusion of indium and zinc, carried out in non-hermetic aluminium pans, were used as model endothermic events. Indium specimens covering a range of mass were heated at $10°C \cdot min^{-1}$ using amplifier range x10. This showed that saturation and severe peak distortion occurred as an indicated heat flux of approximately −170 mW was exceeded. The shape of the distorted peaks was rather surprising (Figure 2.5), with rounding-off of the peak top and two regions of curvature on the peak tail. A plot of specific peak area vs. sample mass (Figure 2.6) showed a sharp change of response at ~ 6 mg, above which mass a linear decrease of sensitivity occurred. The amplifier range was changed to x1 in order to reduce the indicated heat flux by a factor of 10. In this case no loss of calorimetric sensitivity was detected up to 110 mg of indium, which was the largest mass which could be accommodated in a covered non-hermetic pan. This gave a peak heat flux of −80 mW, which would be equivalent to an indicated −800 mW on range x10, with

no evidence of saturation. The absence of saturation at true endothermic heat flux values > 17 mW (= 170 mW on range x10) showed that thermal limitation by the cell was not responsible for the observed peak distortion.

A further series of experiments was carried out using specimens cut from 0.5 mm thick zinc foil. Zinc has a similar density to that of indium but a much higher specific enthalpy of fusion. The peak heat flux during fusion was further increased by doubling the scanning rate to $20°C \cdot min^{-1}$. The saturation level was slightly different from that found previously (Figure 2.7), but the ΔT offset may well have been adjusted between carrying out the two sets of experiments. The overall shapes of the distorted peaks were very similar for the two metals using range x10. Saturation was achieved for range x1 using zinc at the higher scan rate. The indicated heat flux at the saturation plateau was almost identical for the two amplifier ranges, but the shape of the distorted peaks was slightly different (Figure 2.8). A similar experiment was carried out using an old model of cell-base, which differed from the one used for all other experiments in that the ΔT amplifier was based on discrete electronic components rather than operational amplifiers ('op-amps'). This older system was found to have quite different saturation behaviour (Figure 2.9) from its more modern equivalent.

Exothermic distortion

Three metallic alloys were considered as candidates for the study of exothermic saturation. These were cold-rolled beryllium-copper, which contains regions of work-induced stress, and two metallic glass ribbons of nominal compositions $Fe_{80}B_{20}$ and $Fe_{72}Al_{11}P_9C_8$. The copper alloy displayed a very broad stress relaxation exotherm, which was almost 200°C wide at a heating rate of $20°C \cdot min^{-1}$. The enthalpy change for this event was ~ 25 $J \cdot g^{-1}$, which gave a peak height of 2.3 mW for a 25 mg specimen. This would not be sufficient to cause saturation within the limited capacity of the sample pan. The simpler ferrous alloy appeared to have completely crystallised during six years storage. Only the multi-component alloy had a sufficiently large enthalpy of crystallisation (~ 120 $J \cdot g^{-1}$) for this work.

The metal ribbon was cut into short lengths (< 6 mm) which were placed in a non-hermetic aluminium pan and covered with a lightly crimped lid to improve thermal contact. A temperature programme of 400-520°C @ $10°C \cdot min^{-1}$ was used. Distortion of the exothermic crystallisation peak for $Fe_{72}Al_{11}P_9C_8$ was found to have a slightly different form to that observed for endothermic peaks. This was because the limit of linear response occurred in the same region of sample mass as peak skewing due to temperature overshoot (Figure 2.10). In the absence of overshoot, the distortion would probably be of a similar form to that observed for endothermic events. Exothermic saturation occurred at an indicated heat flux of +270 mW, but the difference between this and the endothermic limit is probably arbitrary and depends on the setting of the ΔT offset. The specific area vs. sample mass relationship for crystallisation of the metallic glass (Figure 2.11) had a similar form to that observed for fusion of indium.

2.4 SECOND ORDER EFFECTS

The baseline offset in DSC is caused by a difference in thermal lag between the sample and reference thermocouples, during temperature programming, and is proportional to the heat capacity of the sample (equation 1.6). There are many potential sources of error which influence baseline repeatability. These cause particular problems in heat capacity measurements, but can also affect other applications of DSC in which data file subtraction is carried out.

2.4.1 Errors due to asymmetry in pan placement

The design of the Du Pont DSC cell makes no provision for rigid location of the sample and reference pans, even though the operating principle makes accurate centring critical for baseline repeatability. Problems associated with measurement of heat capacity using this type of equipment are well recognised and several modifications have been suggested to improve precision. The ASTM test method for measuring specific heat of aircraft turbine lubricants [46] involves the use of a silicone heat sink compound between the pan and thermocouple. It is difficult to imagine that this would improve accuracy, because the amount of compound applied is large (20-30 mg) and this is not

weighed. The contact is cleaned between runs and a fresh application of heat sink compound used. This will make a substantial but poorly characterised contribution to the measured heat capacity of the sample. Du Pont recommend increasing the pan/thermocouple contact area by attaching silver or aluminium discs to the thermocouple platforms by means of Dow Corning #340 heat-sink compound [47]. This approach overcomes some of the limitations of the ASTM method, but Yuen and Yosel [48] have shown that the silicone fluid in #340 compound displays a complex DSC curve and mass loss in the 25-500°C region. This introduces further problems in an already difficult technique. They proposed the use of a cylindrical guide tool [48], which locates on the raised stiffening ribs of the constantan disc and assists in repeatable placement of the two pans.

In an attempt to optimise the baseline performance of the DSC a centring tool was constructed according to the design published by Yuen and Yosel. Although this afforded some improvement over visual placement, it was apparent that the pans tended to be displaced from their seats as the guide cylinder was withdrawn from the cell. This was attributed to two aspects of the design of this tool:
(i) The centring cylinder continued to enclose the pans for a short distance after it had disengaged from the stiffening ribs. If it was inadvertently rotated while being withdrawn form the cell, the pans were displaced.
(ii) DSC pans are never perfectly circular and sometimes have small burrs on the rim. Consequently, they tended to grip the inside of the tool and were picked up by it.
To overcome these limitations, a modified tool was constructed (Figures 2.12 and 2.13) which engaged with two brass pegs protruding vertically from the walls of the DSC furnace (Figure 2.14). A pair of weighted rods was used to hold the pans firmly on their platforms while the guide body was being withdrawn (Plate 1). The dimensions of the tool were chosen such that the pan rims were clear of the perspex cylinder before the rods were lifted away. The locating pegs in the wall of the furnace ensured that both the cylinder and rods were withdrawn vertically until they were clear of the pans. These modifications made the tool much easier to use and improved the repeatability of the baseline dramatically. The degree of baseline

scatter for empty sample and reference pans heated at $10°C \cdot min^{-1}$ is illustrated in Figure 2.15, which shows the improvement over visual centring.

2.4.2 Artifacts produced by the calorimetric lineariser

The heat flux sensing element in the Du Pont DSC cell is a differential thermocouple, which measures the temperature difference (ΔT) between the sample and reference platforms. The output signal is not directly proportional to the heat flux into the sample, which means that the ΔT signal must be corrected to maintain a constant calibration coefficient over a wide temperature range. This is carried out electronically in the DSC cell base, by attenuating the amplified ΔT signal with a variable resistive shunt as described in the previous chapter. Switching points in this lineariser are characterised by steps in the baseline which may resemble changes of heat capacity in the sample (i.e. second order or 'glass' transitions). It was found that these steps could be located by carrying out a rising temperature scan at a large $\Delta\Phi$ offset, using a sample which does not have any characteristic transitions in the temperature range of interest. A 60 mg disc of α-alumina (synthetic sapphire heat-capacity standard) was heated at $20°C \cdot min^{-1}$ using various settings of the overlap adjuster*. The results over a narrow temperature range are shown in Figure 2.16. Curve (d) displays the best matching between the linear response regions, with virtually complete elimination of the steps at ~ 315 and 385°C. This experiment showed that spurious steps occur at intervals of ~ 70°C and that the maximum temperature interval over which the lineariser can be optimised to eliminate these is less than 200°C.

2.4.3 Effects due to parasitic heat exchanges

The sensitivity of a Boersma type of heat flux DSC (equation 1.3) depends on the ratio between heat flowing into the sample via the thermocouple plate (i.e. the measured component) and the unmeasured

---

*Variable resistor R9 on PC board A1 (E-curve lineariser 990295-901), see DSC manual [49].

leakage through the sample chamber atmosphere (the 'parasitic' component). If this ratio is altered, such as by changing the conductivity of the purge gas, then the calorimetric sensitivity of the DSC will also be affected.

The hermetically-sealable pans supplied by Du Pont for use with volatile samples are sealed by folding a raised lip, on the base, over the edge of the lid and compressing it to form a cold weld (Figure 2.17). The sealed area is in the form of a flat rim around the circumference of the pan, which lies parallel to the region of the constantan disc surrounding the plate thermocouple. A larger parasitic heat flow would be expected in this configuration than with an un-crimped pan, whose lip is aligned perpendicular to the constantan surface. It is common practice in heat capacity measurement to carry out three scans on each pan as follows:

(1) un-crimped empty pan.
(2) un-crimped pan containing an involatile reference material such as alumina.
(3) crimped pan containing the volatile sample.

These files are then subtracted, [(2) − (1)] for calibration and [(3) − (1)] for the sample analysis. The first subtraction should be valid because the geometry of the pan is the same for each scan. However, in the second case a scan using an un-crimped pan is subtracted from one after crimping, with the assumption that the measured/parasitic heat flux ratio is not affected by the change of pan geometry. In order to test the validity of this assumption, a series of experiments was carried out using a hermetic pan in three configurations:

(a) un-crimped pan covered by a loose lid.
(b) crimped pan, with its seal broken to allow the sample to be changed.
(c) as for (b), but with an indented base.

Pan configuration (c) had a cruciform indentation in the base such that contact with the thermocouple was limited to four points. This was intended to increase the thermal contact resistance from that of (a) and (b). Consequently the three configurations should have different measured/parasitic heat flux ratios. Assuming that the

crimped lip around the pan decreases the resistance to parasitic heat transfer, the differences between the three configurations will be:

Contact resistance (R_c): (a) = (b) < (c)

Parasitic resistance (R_s): (a) > (b) = (c)

Nickel(II) oxide was used to investigate the effects of pan configuration on the form of the baseline in a rising temperature experiment. Although NiO is not volatile in the operating temperature range of the 910 DSC cell, and would not normally be run in a hermetically sealed pan, it was chosen for this study because its heat capacity shows two distinct regions of temperature dependence. Below 250°C NiO exists as an antiferromagnetic phase whose heat capacity increases fairly rapidly with increasing temperature. At the Néel transition temperature, where its structure changes to give a paramagnetic phase, the heat capacity of NiO falls sharply and then increases gradually. This behaviour allowed the influence of changing heat capacity to be investigated in the same experiment as the effect of crimping the sample pan. Indium (T_{fus} = 156.6°C) and zinc (T_{fus} = 419.4°C) were used to investigate changes of the relative values of measured and parasitic heat flux. The onset slope of the fusion endotherm is a measure of the contact resistance ($R_c \propto slope^{-1}$), while differences in calorimetric sensitivity (i.e. apparent enthalpy of fusion) indicate changes in the heat flux ratio (R_c/R_s). These two metals were chosen because their melting points lie on either side of the Néel transition temperature for NiO, and hence allowed the thermal resistances of the system to be estimated in both regions of heat capacity behaviour. Samples examined were as follows:

(1) 35 mg nickel(II) oxide, which had been heated at 500°C in air for 4 hours and compacted in a 3 mm diameter pellet press.

(2) 60 mg indium wire, pressed to conform to the base of the pan.

(3) 60 mg zinc granules (DSC standard ex. Du Pont)

Each of these was analysed in all three types of hermetic aluminium pan, (a)-(c) above, using a temperature programme of 20-500°C @ 20°C·min^{-1}. Five replicate experiments were carried out for each of the nine sample/pan combinations, with the same NiO specimen being used throughout but a fresh metal specimen for each scan.

The DSC curves for nickel oxide (Figure 2.18) showed a fairly wide scatter of both offset and slope, which was attributable to centring the pans visually (the guide tool described previously having been dimensioned for non-hermetic pans). Comparison of the average DSC curves for each pan configuration (Figure 2.19), obtained by adding each set of five data files together, showed that the slopes were significantly different. The differences were even more evident in the subtracted plots (Figure 2.20), which both showed an increasing change of offset with increasing temperature. It was also evident that the slope was independent of changes in heat capacity of the sample. Differences in sensitivity between the pan configurations also created a residual peak in the region of the Néel point.

Results obtained using the two calibration metals are given in Table 2.1. Inspection of the onset slope data showed that the differences between configurations (a) and (b) were not significant for either metal. This meant that crimping the pan had not caused significant distortion of the base area in contact with the thermocouple. The values of R_c derived from measurements on zinc (~ $90°C \cdot W^{-1}$) were higher than those for indium (~ $75°C \cdot W^{-1}$). This was probably because the zinc was in the form of granules, which make poorer contact with the inside of the pan than does a very malleable metal such as indium. Indenting the base of the pan increased R_c by approximately $55°C \cdot W^{-1}$ for indium and $50°C \cdot W^{-1}$ for zinc. Again, the experimental error in these results meant that the difference between results for the two metals was not significant.

The specific peak area measurements showed decreases of calorimetric sensitivity due both to crimping and to the deliberate increase of R_c. Crimping reduced the calorimetric sensitivity by ~ 3% for indium and ~ 4% for zinc. The effect of increasing R_c was to decrease the calorimetric sensitivity by ~ 15% for indium and ~ 18% for zinc. As with the onset slope measurements, the small differences between results for the two metals were not statistically significant.

2.5 DISCUSSION

These results showed that the Du Pont 910 DSC has several inherent limitations which must be considered when setting up an experiment from which high accuracy and precision are required. Errors may be introduced by the sample container, the calorimeter cell and the electronics associated with processing the analytical signal. Each of these sources of interference may result in a distorted representation of thermal events taking place in the sample. In addition, spurious events may be created, which have a similar magnitude and shape to 'real' thermal events due to the sample.

2.5.1 Sources of error

Sample containers

Problems encountered with sample containers were mainly attributable to the design and construction of Du Pont's hermetic pans. Three aspects were identified:

(i) The contact resistance (R_c) of the hermetic pans was found to be ~ $75°C \cdot W^{-1}$, which is more than twice that of Du Pont non-hermetic aluminium pans. R_c has a major influence on the width of DSC peaks and a high resistance leads to loss of resolution between overlapping events. It also causes loss of calorimetric sensitivity by increasing the contribution of parasitic heat flux relative to that via the measuring thermocouple. The specific peak areas measured for fusion of indium and zinc in crimped hermetic pans were ~ 93% of those for measurements carried out using non-hermetic pans.

(ii) A consequence of crimping these pans is to change the vertical wall of the base, which has a total surface area of ~ 75 mm^2, into a horizontal 'fin' with an area of ~ 46 mm^2. Convective heat transfer is probably dominated by the turbulent jet of pre-heated purge gas which enters via the furnace wall. This would be expected to have more influence on the larger surface area of the un-crimped pan. Radiative heat transfer from the lid of the cell and the region of the constantan disc surrounding the thermocouple should be greater for the crimped configuration. It is difficult to assess the relative contributions of these leakage paths to the total parasitic heat flux, but measurement of heat capacity requires that no overall change takes

place on crimping. The experimental results showed that crimping actually reduced the calorimetric sensitivity by ~ 4%. If the leakage resistance of the sample chamber atmosphere (R_g) is assumed to be ~ 100°C•W^{-1} [13], and R_c ~ 75°C•W^{-1} (as measured above), then treating these as parallel resistances with a fixed net heat flow shows that crimping must have reduced R_g by > 7%. Crimping also altered the baseline slope by ~ 3 μW•°C^{-1}, with the greatest error at higher temperatures. This would make a substantial difference to the measured heat capacity of a small specimen. For example, the heat capacity of eicosane (n-$C_{20}H_{42}$), which is a typical waxy hydrocarbon, increases by ~ 35% in the temperature range 400-600K. However, if a 5 mg specimen were scanned at 20°C•min^{-1} in a hermetically sealed pan, the normal calibration procedure would give data which showed a virtually constant heat capacity over this temperature range. This shows that the file subtraction often carried out in heat capacity determinations can introduce larger errors than those resulting from normal variations in contact resistance.

(iii) These hermetically sealed pans can distort under internal pressure, resulting in an increase in contact resistance and formation of a spurious peak. The most direct way of detecting this distortion would be to compare the expansion of filled and empty pans by thermodilatometry (TD). Alternative methods would be simultaneous thermogravimetry/DSC, which would indicate the point at which leakage and evaporation begin, or by varying the ambient pressure in a PDSC. The latter approach would shift the artifact peak by increasing the temperature at which the sample vapour pressure becomes sufficient to dilate the pan.

Calorimeter cell

Errors introduced by the cell itself were found to result from:

(i) Contamination by atmospheric moisture, which can occur if a cold cell is opened while its temperature is below the atmospheric dew point, or if damp purge gas is used. Condensed water on the surface of the thermocouple plate gives rise to a complex series of artifact peaks as it melts and evaporates in the region above 0°C. Temperature gradients in the cell cause a time lag between arrival of the phase transition interface at the two thermocouples. Consequently each event

appears to have both endothermic and exothermic components, which gives the DSC curve a characteristic sigmoid shape.
(ii) Subjective placement of the sample and reference pans on their thermocouples is not accurate and leads to a wide scatter in the baseline slope and offset. The most serious consequence of inaccurate pan placement is to make precise measurement of heat capacity impossible. It also causes difficulty in detecting the onset of a reaction by first deviation from the baseline. In the worst case, inaccurate centring of the pans can cause an 'elbow' on the baseline which might be interpreted as an onset point.

Electrical/electronic contributions

All of the problems which were encountered with signal processing were associated with circuit boards located in the DSC cell-base or the connection between these and the cell. The factors identified were as follows:
(i) Measured onset temperatures tend to drift over the first few scans when the instrument has been at room temperature for some time. Thermocouples do not normally show hysteresis effects, so this drift is unlikely to be due to instability in the cell itself. The DSC furnace draws a current of approximately 2 amps at 700°C, through wiring contained in the cell base. It is unlikely that the power loss from this wiring would increase the temperature in the (un-ventilated) case sufficiently to affect the reference cold-junction by such a large amount. The most probable source of this interference is the multi-pin connector which allows different types of cell to be mounted on the cell-base. Both the cell/socket and plug/cold junction connections are made using chromel or alumel wire as appropriate, but the pin and socket contact surfaces are silver and gold plated respectively. This means that the two thermocouple leads contain different combinations of dissimilar metal contacts. When the first scan is carried out, the connector will be at room temperature. Conduction of heat from the cell-head will gradually heat up the connection block and consequently alter the overall contact EMF until thermal equilibrium is reached.
(ii) The 'E-curve lineariser', which corrects for the temperature dependence of the ΔT signal, causes steps in the baseline which resemble glass transition events. This type of artifact should not be

observed in systems subsequent to the model 1090, because these use software correction rather than sacrificing sensitivity by signal attenuation.

(iii) The dynamic range limiting factor in the Du Pont DSC system appears to be electronic in nature rather than the physical design of the calorimeter cell itself. Digital clipping is unlikely to be the cause because the peaks are not flat-topped. The most likely cause of peak distortion is saturation of the analog (ΔT) amplifier. Signal amplification is carried out in two steps by operational amplifiers. The gain of the second of these op-amps can be varied to give an overall gain of either 3,000 or 30,000. Saturation occurs at the same output level on each range, even though the input signal varies by an order of magnitude, and therefore the first gain stage cannot be the limiting factor. The difference in shape between saturated peaks for the two gain settings is probably caused by a change in the characteristics of the amplifier, resulting from the difference in feedback level used to alter the gain. Similarly, the older discrete component amplifier would be expected to behave differently from a modern integrated circuit and hence give a rather different form of distortion when driven beyond its linear response range.

2.5.2 Procedures used for subsequent experiments

Most of the sources of error identified above give rise to fairly small artifacts or loss of accuracy, but these were considered to be important in the studies described subsequently. On the basis of these findings, the following precautions were taken:

(1) Du Pont hermetic pans were not used for any DSC experiments.

(2) The calorimeter was stabilised by heating isothermally at the maximum programme temperature for at least one hour before use.

(3) The pan centring tool was used whenever possible (i.e. with Du Pont non-hermetic aluminium pans).

(4) The cooling accessory shown in Figure 2.4 was used for cooling below ambient temperature. A quenching can was only used for rapid cooling down to ~ 25°C.

(5) Addition and subtraction of data files was only used for DSC scans carried out in the same type of sample pan.

(6) DSC curves were scrutinised for artifacts, particularly at temperatures where such interferences had been identified previously, e.g. lineariser cross-over points.

Table 2.1

DSC peak parameters for fusion of pure metals in Du Pont hermetic pans

(Raw data based on five measurements, with no correction for cell sensitivity)

MEASURED PARAMETER [TEST METAL]		PAN CONFIGURATION* (a)	(b)	(c)
ONSET SLOPE ($mW \cdot °C^{-1}$)	In	13.1 ± 0.23	12.8 ± 0.31	7.60 ± 0.25
	Zn	11.1 ± 0.24	11.0 ± 0.46	7.16 ± 0.32
SPECIFIC AREA ($J \cdot g^{-1}$)	In	24.2 ± 0.11	23.5 ± 0.13	19.9 ± 0.60
	Zn	88.3 ± 0.25	84.6 ± 0.10	69.7 ± 0.91

*(a) un-crimped pan covered by loose lid 

(b) crimped pan, with seal broken 

(c) as for (b), but with indented base 

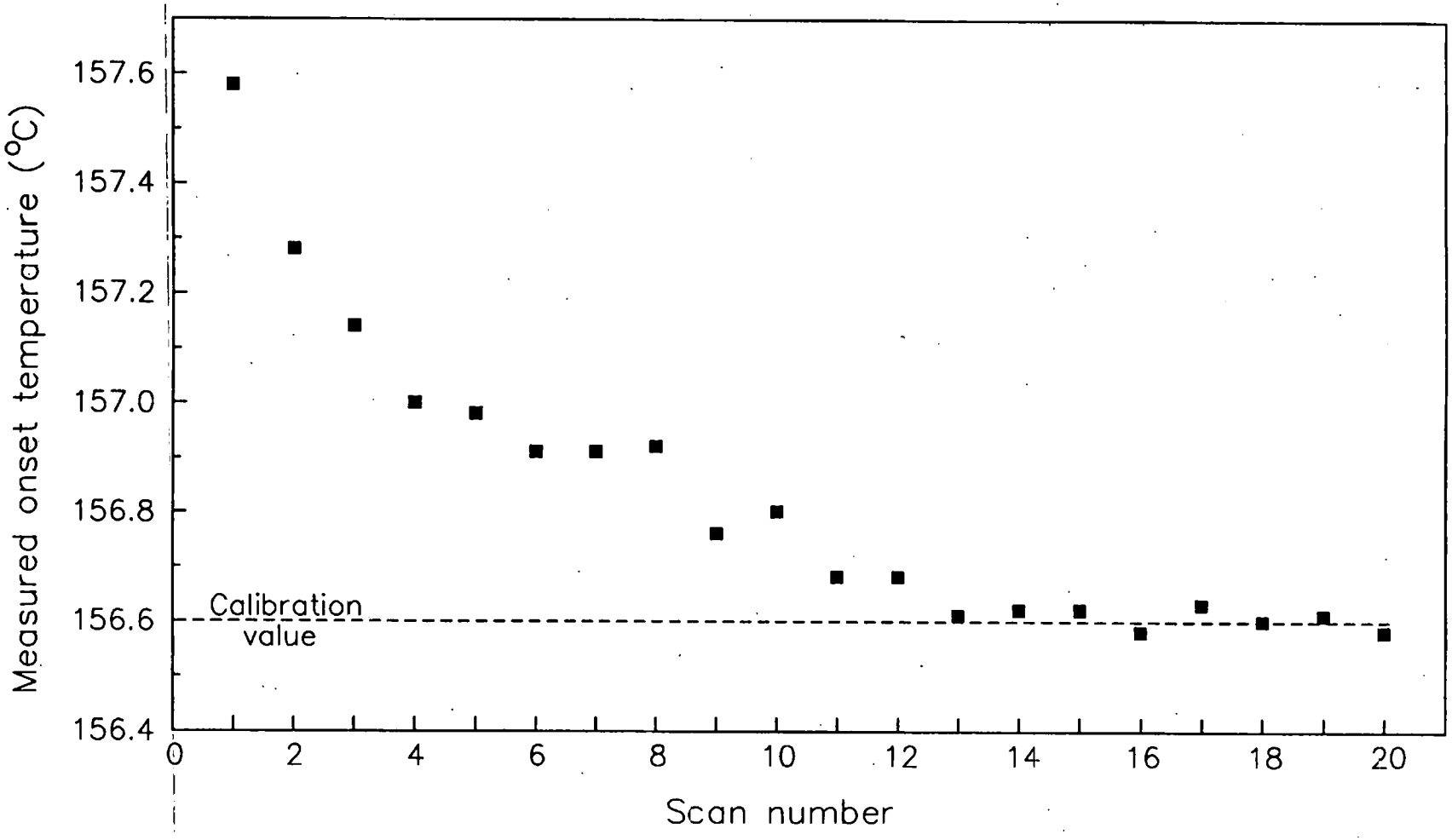

Figure 2.1 – Drift of the measured onset temperature for fusion of indium.
(DSC cell was at room temperature at the start of scan 1)

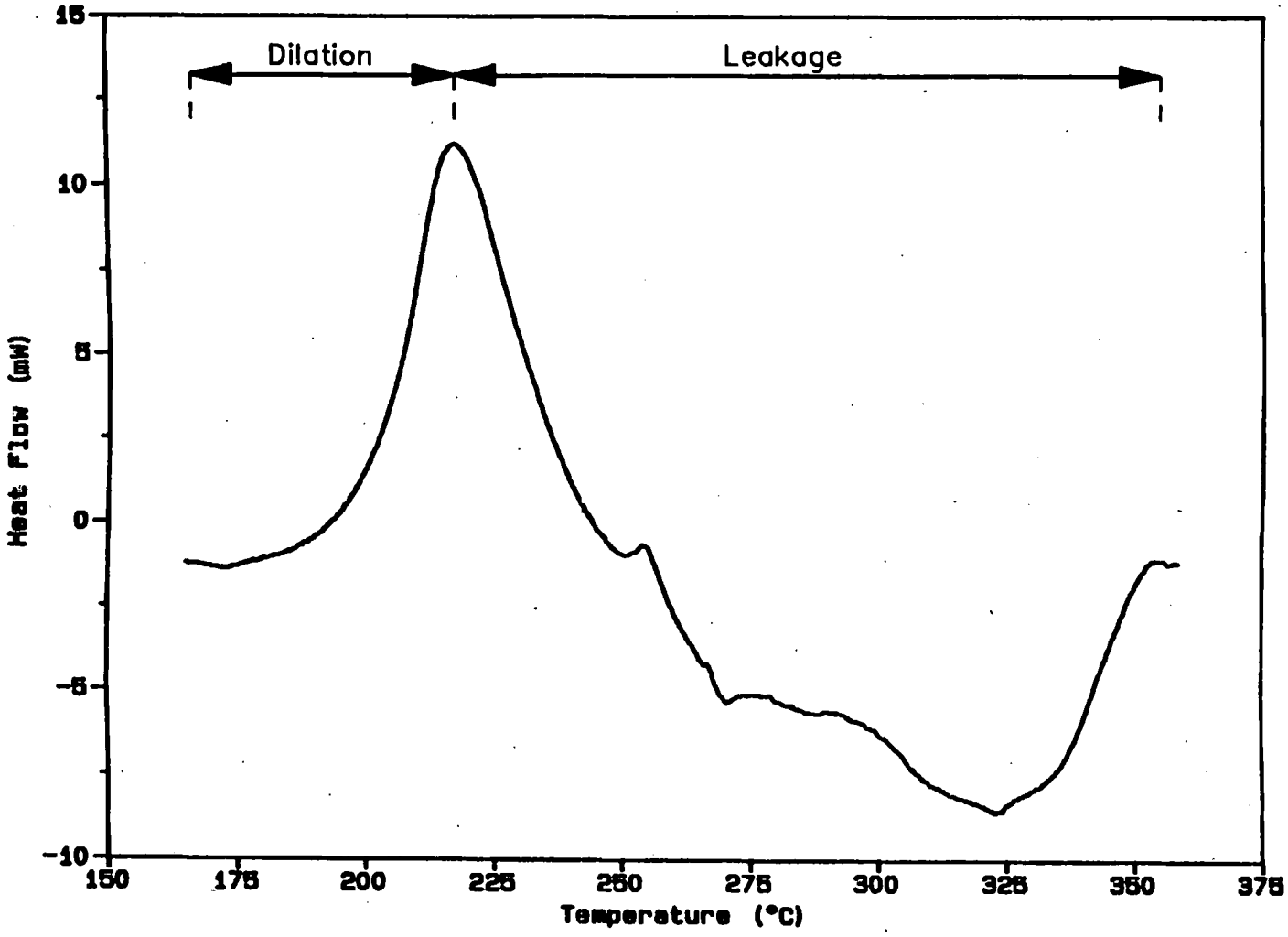

Figure 2.2 – Artifact peaks caused by distortion of the DSC pan.

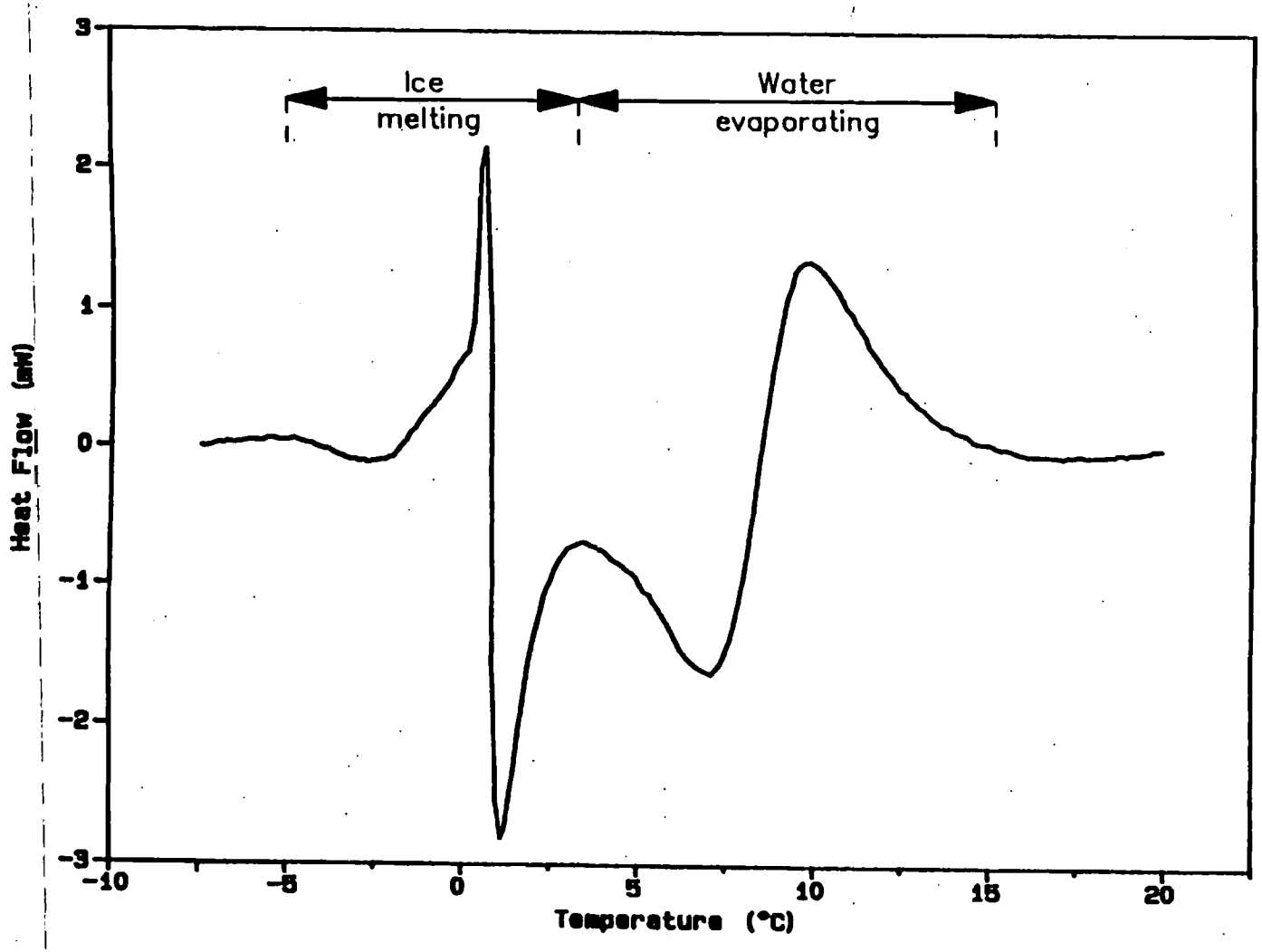

Figure 2.3 – Artifact peaks caused by condensation of atmospheric moisture in the DSC cell.

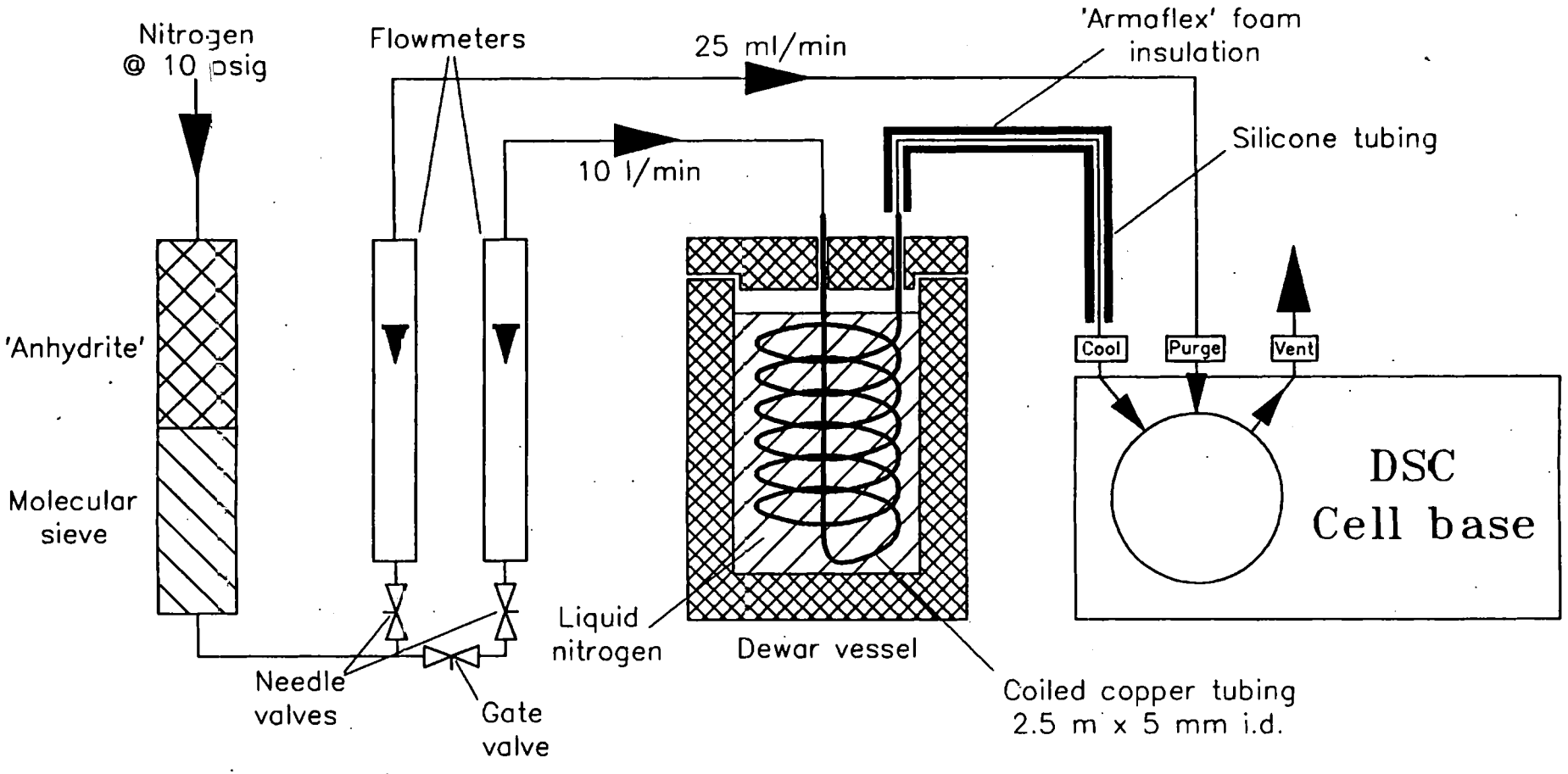

Figure 2.4 – Schematic diagram of the DSC cooling system.

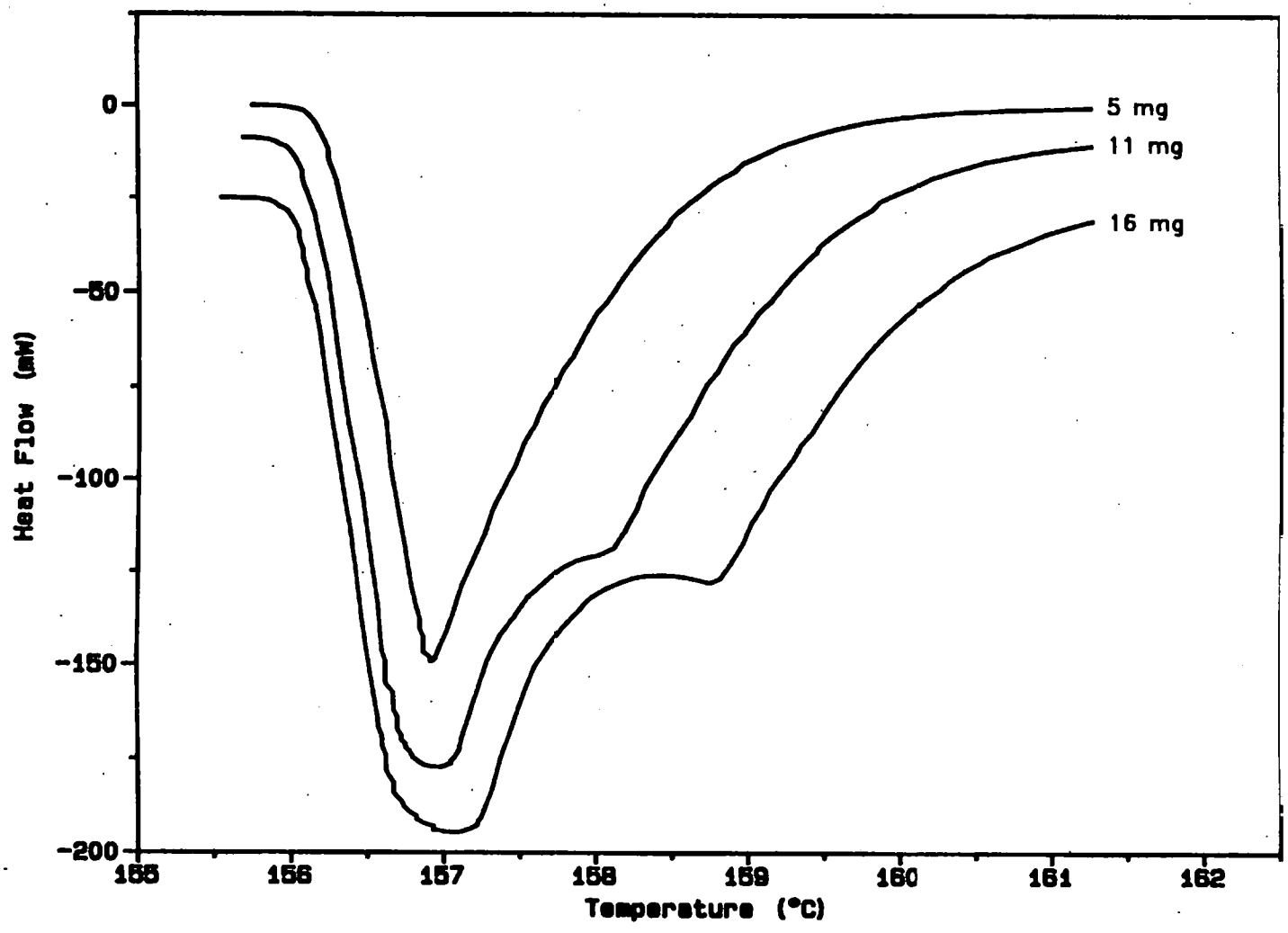

Figure 2.5 – Effect of sample mass on peak shape for fusion of indium.
(Amplifier range = x10)

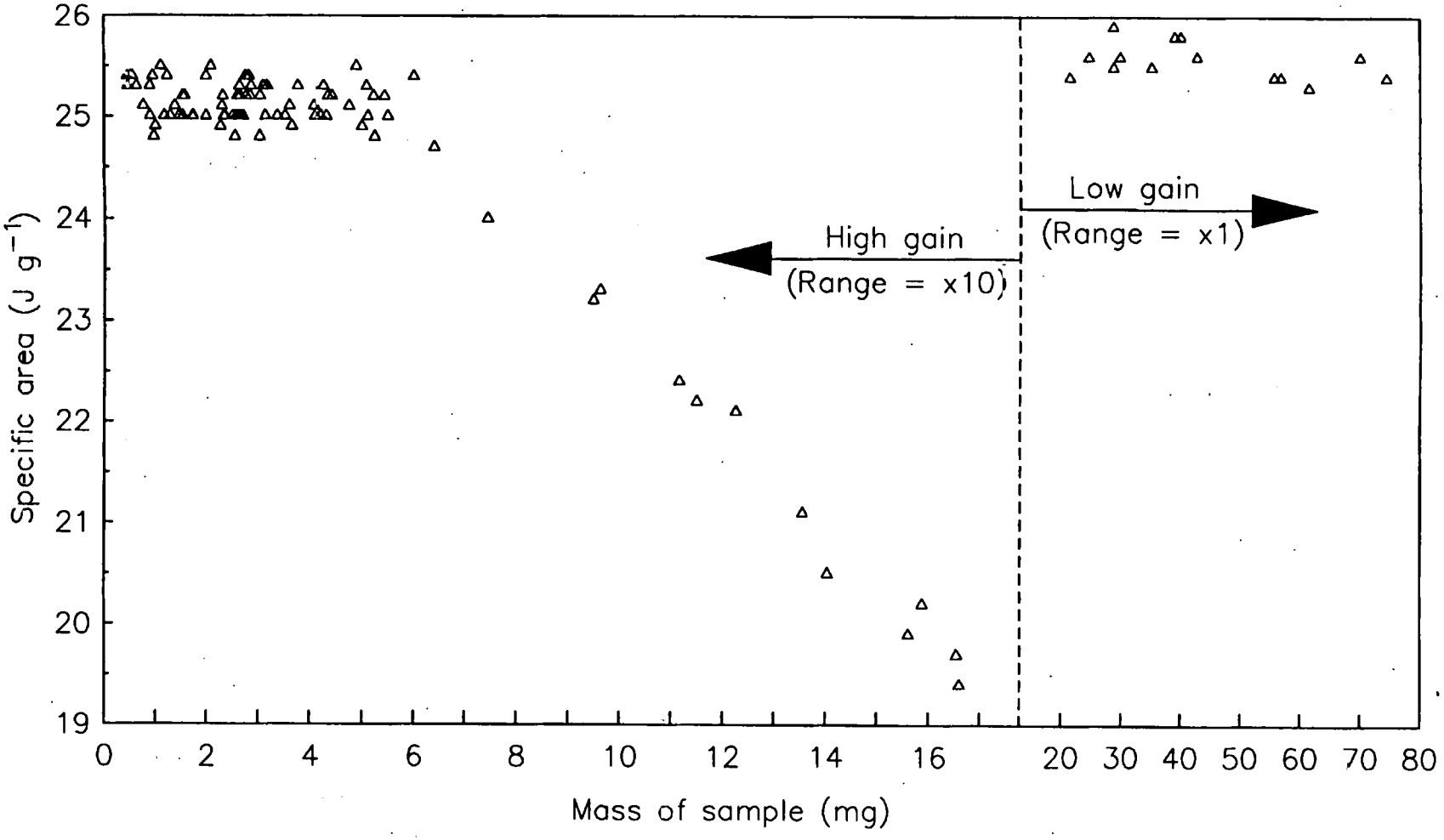

Figure 2.6 – Effect of sample mass and amplifier gain on the measured enthalpy of fusion for indium.

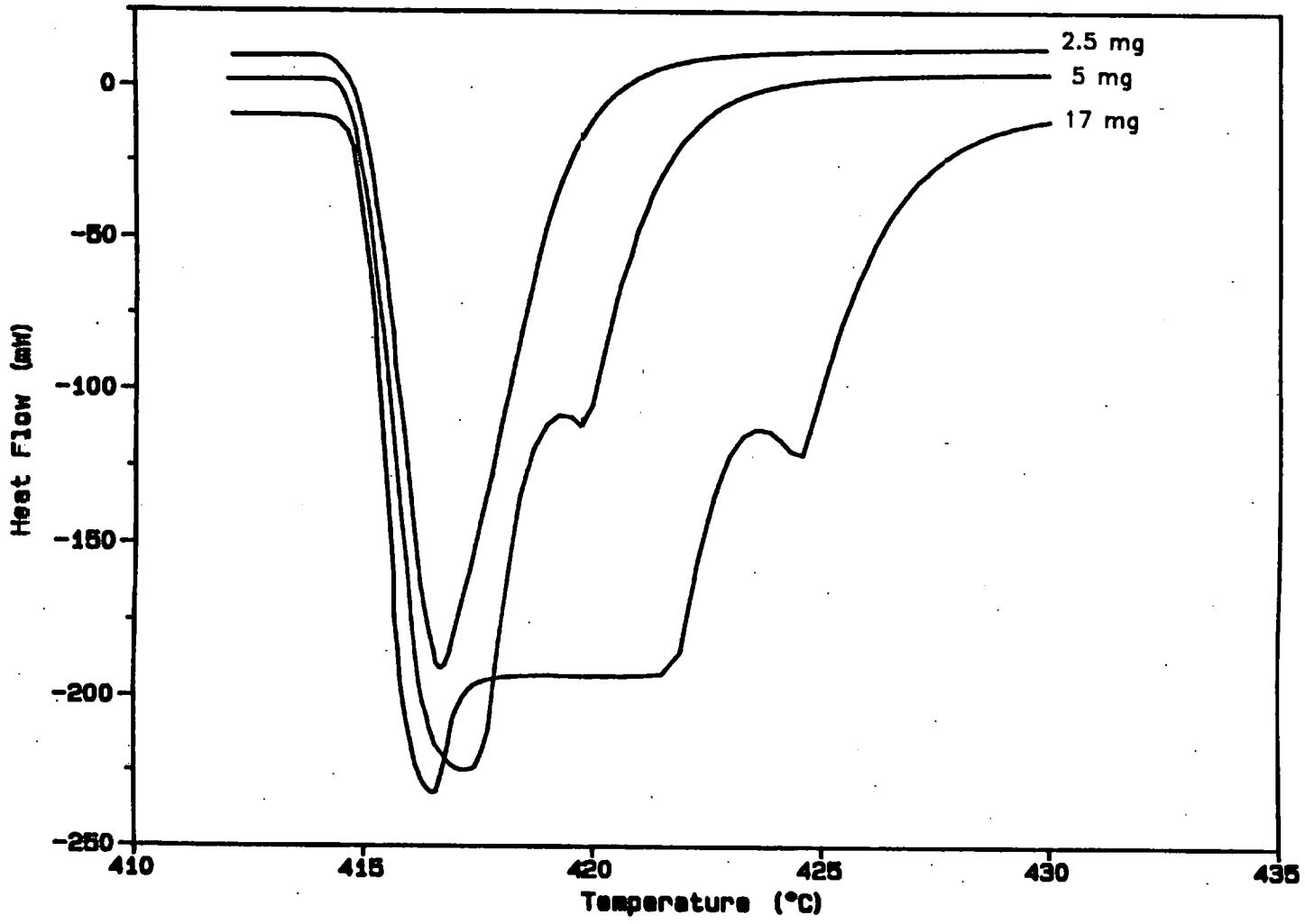

Figure 2.7 – Effect of sample mass on peak shape for fusion of zinc.
(ΔT amplifier based on op–amps: Range = x10)

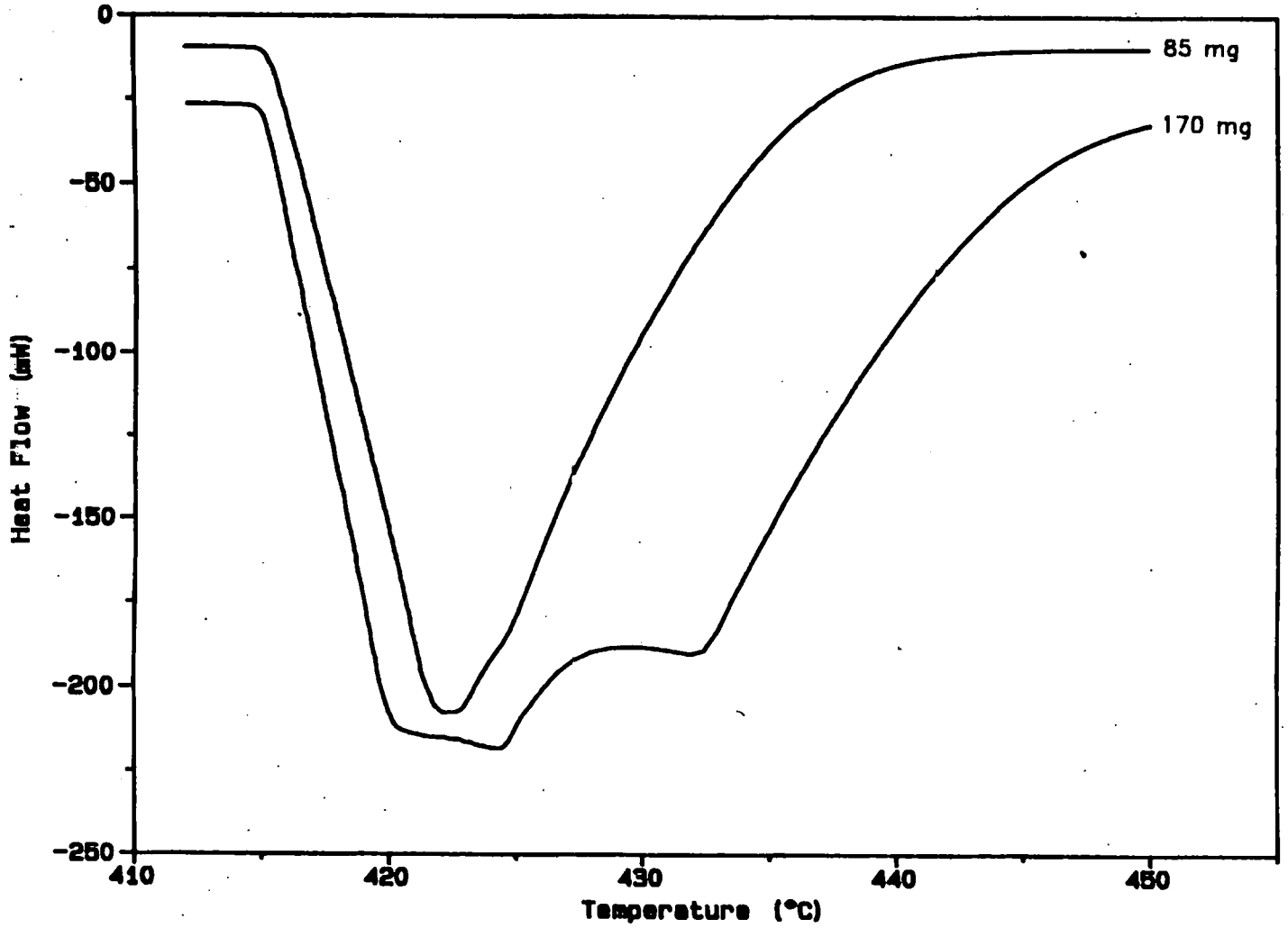

Figure 2.8 – Effect of sample mass on peak shape for fusion of zinc.
(ΔT amplifier based on op-amps: Range = x1)

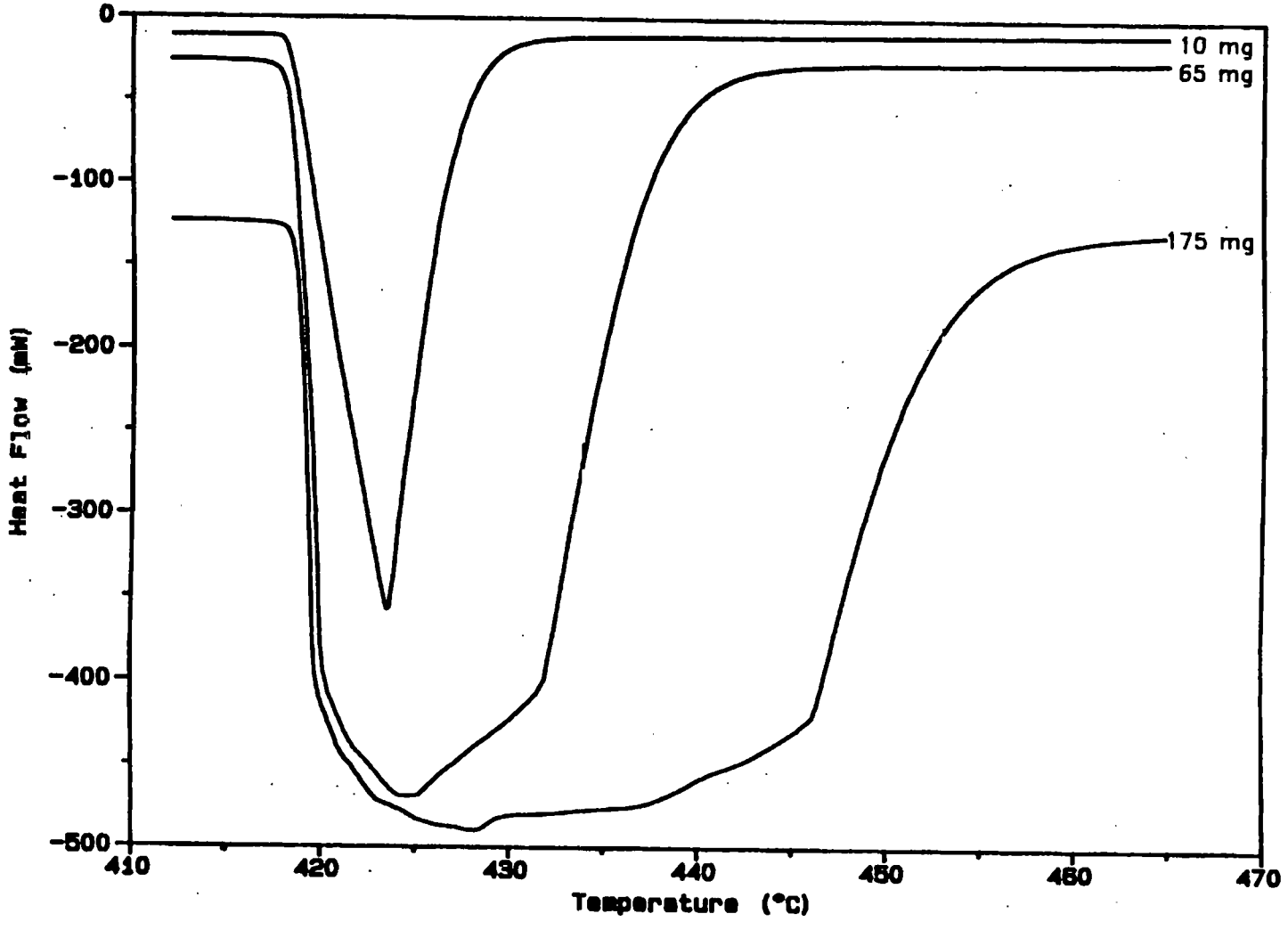

Figure 2.9 – Effect of sample mass on peak shape for fusion of zinc.
(ΔT amplifier based on discrete components: Range = x5)

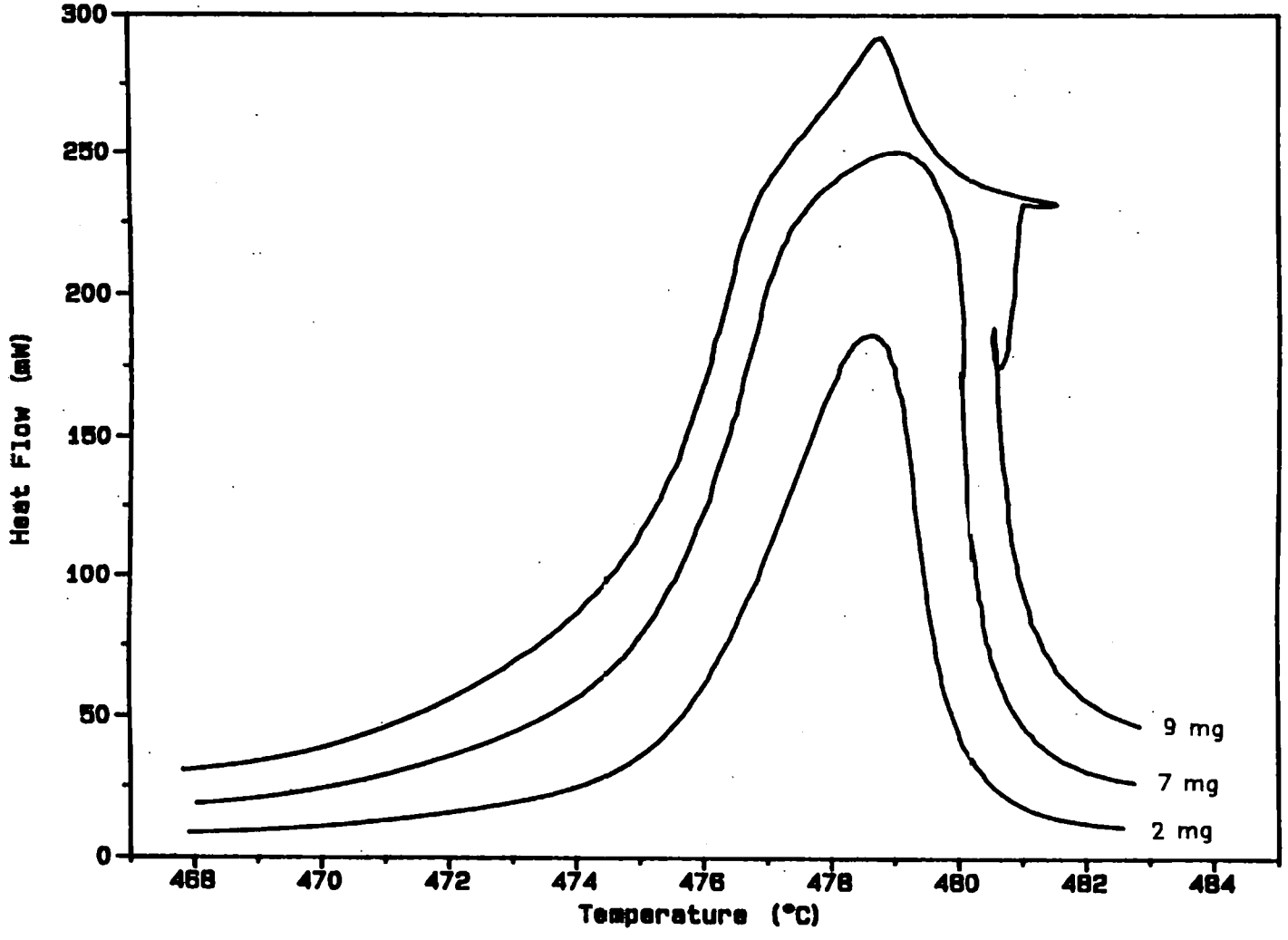

Figure 2.10 – Effect of sample mass on peak shape for crystallisation of an amorphous alloy [$Fe_{72}Al_{11}P_9C_8$] (Amplifier range = x10).

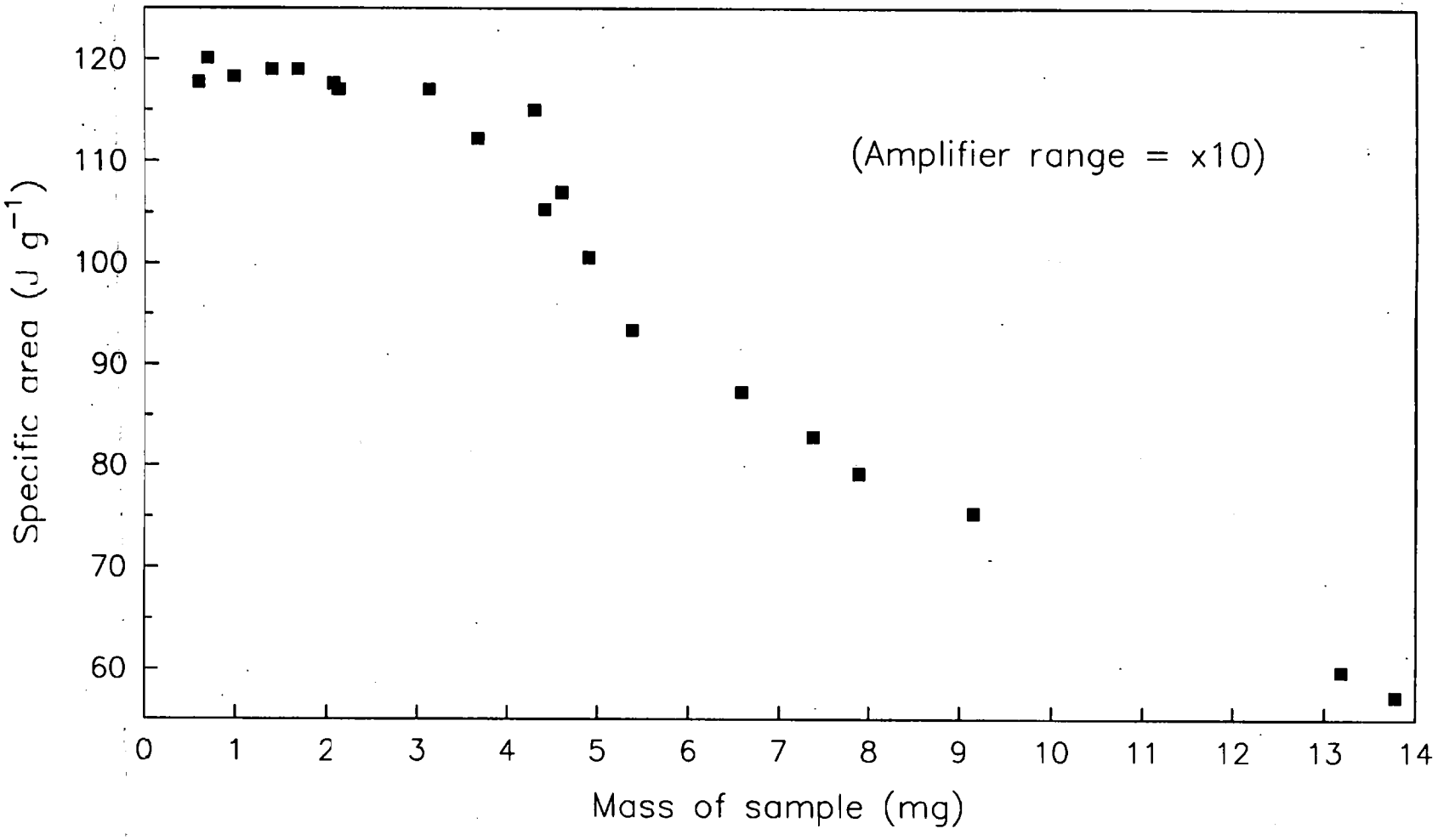

Figure 2.11 – Effect of sample mass on the measured enthalpy of crystallisation for an amorphous alloy [$Fe_{72}Al_{11}P_9C_8$].

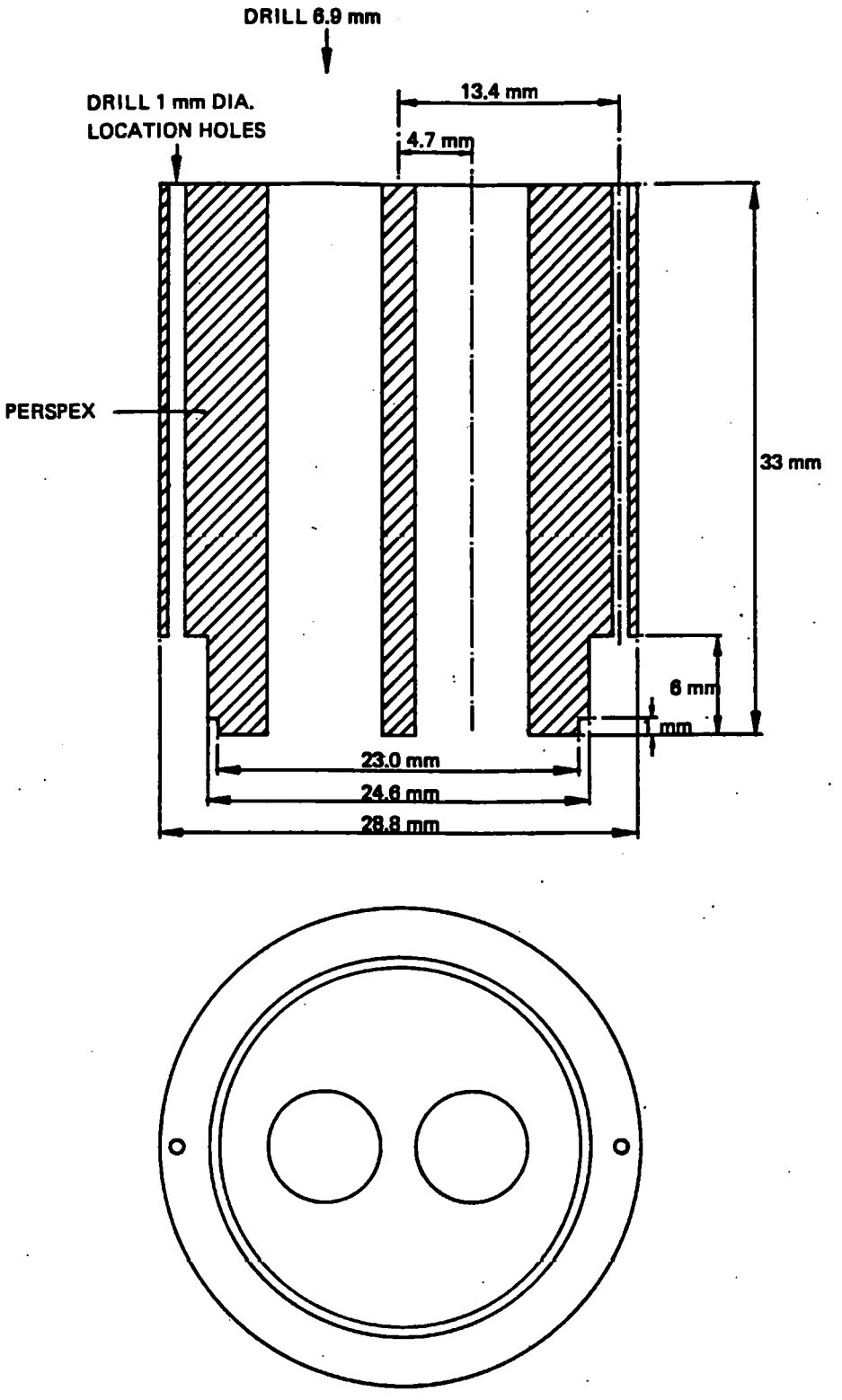

Figure 2.12 – Dimensions for the guide body of the DSC pan centring tool.

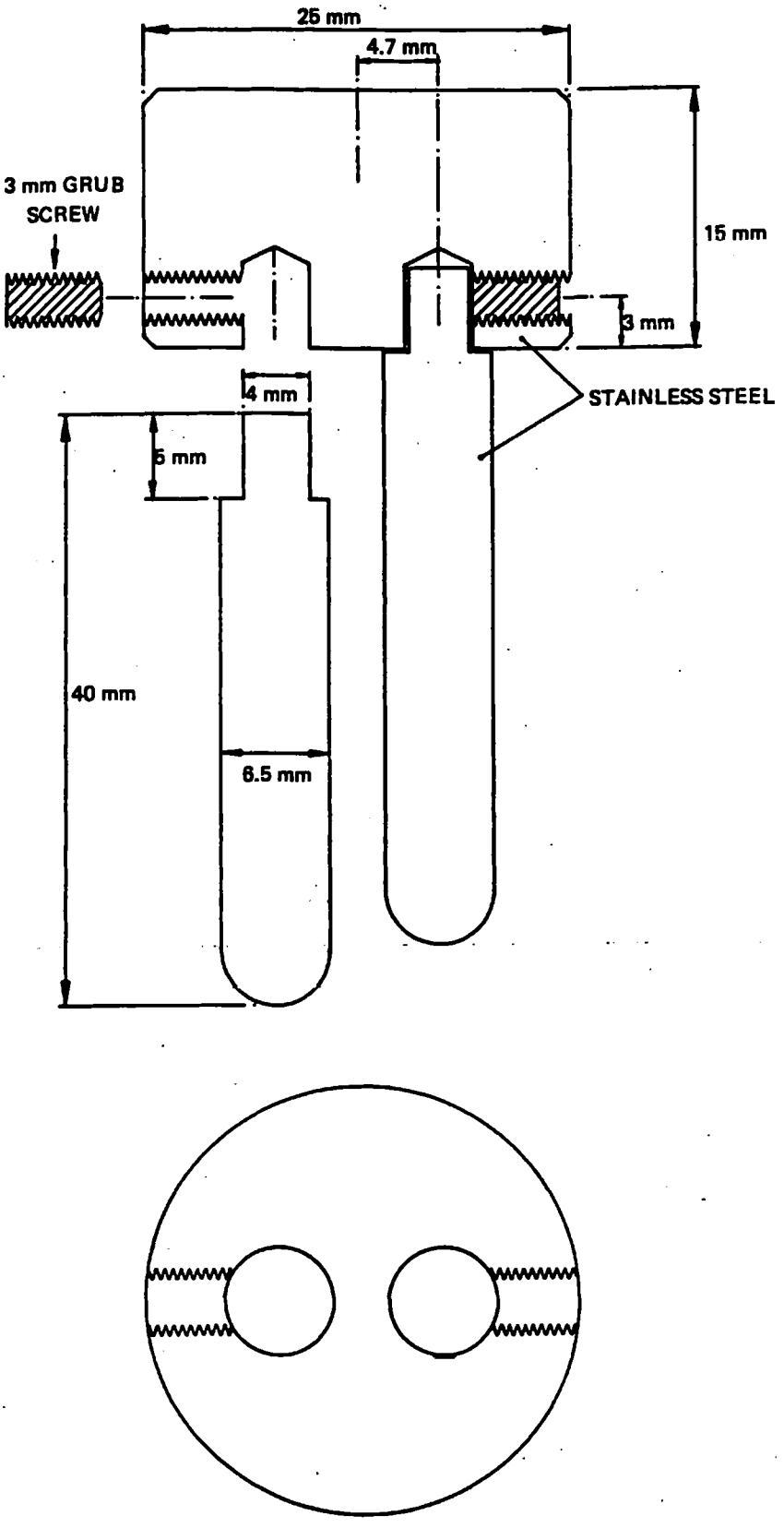

Figure 2.13 – Dimensions for the plunger assembly of the DSC pan centring tool.

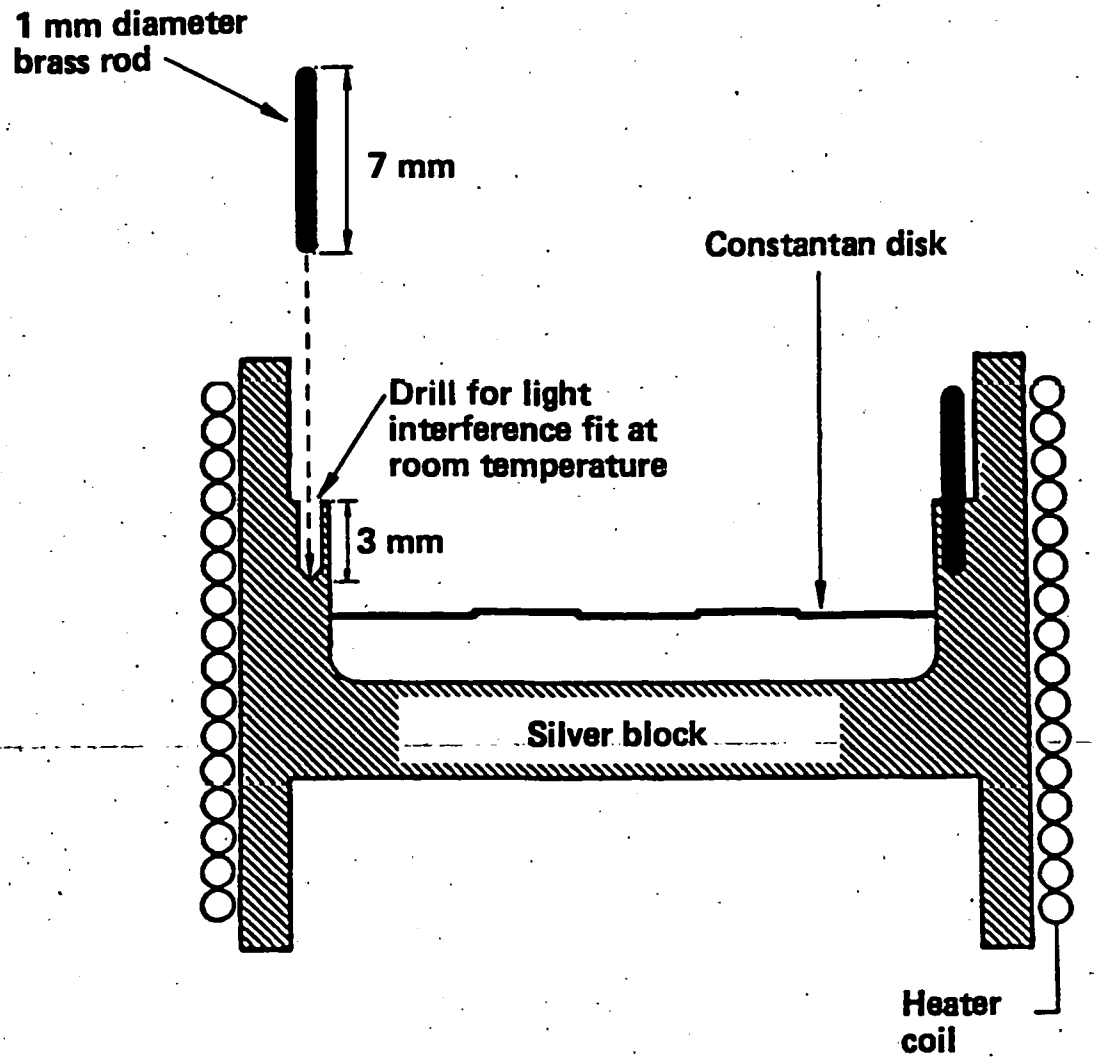

Figure 2.14 – Location of the guide pins in the DSC furnace block.

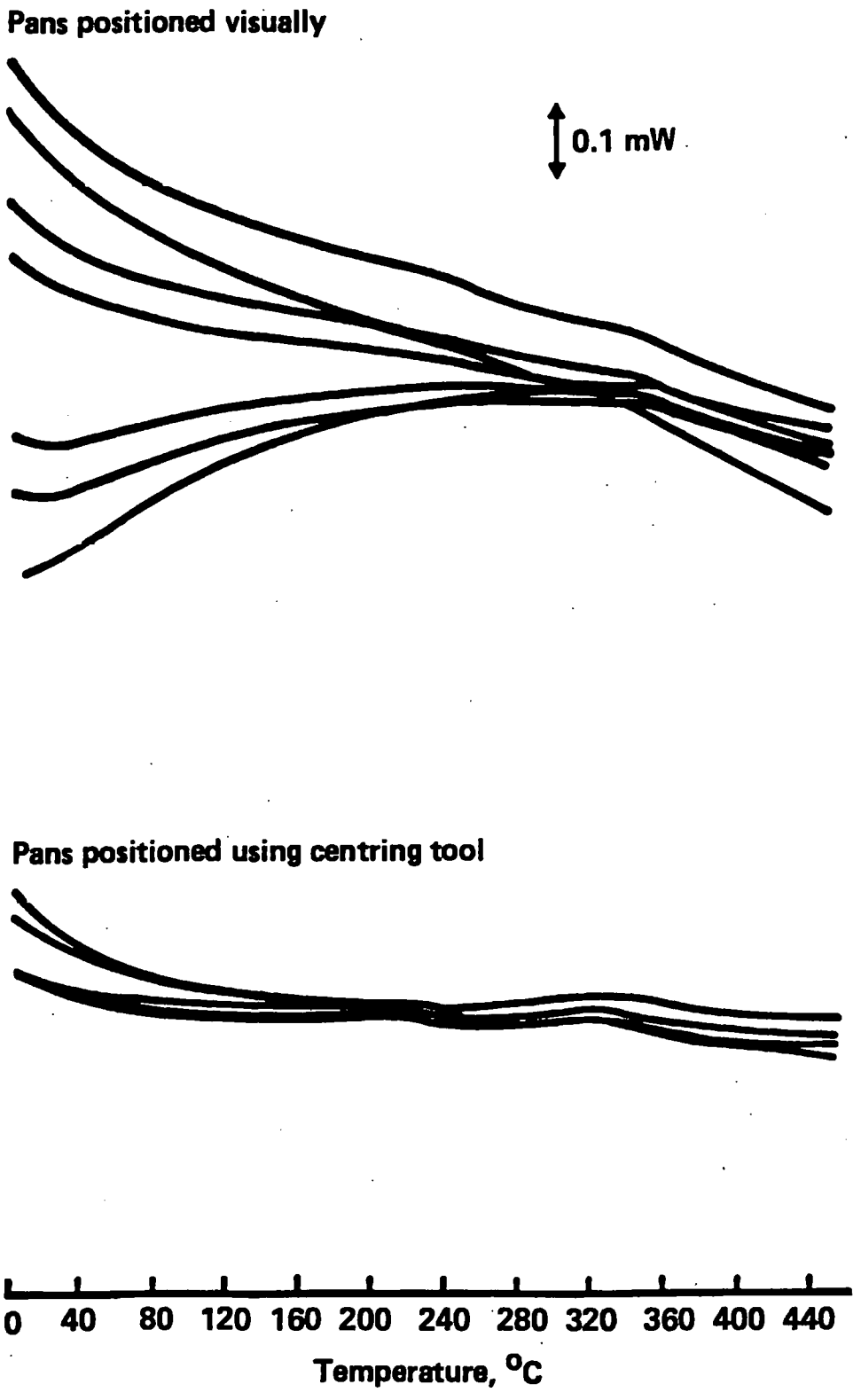

Figure 2.15 – Effect of accurate centring of the DSC pans on baseline repeatability.

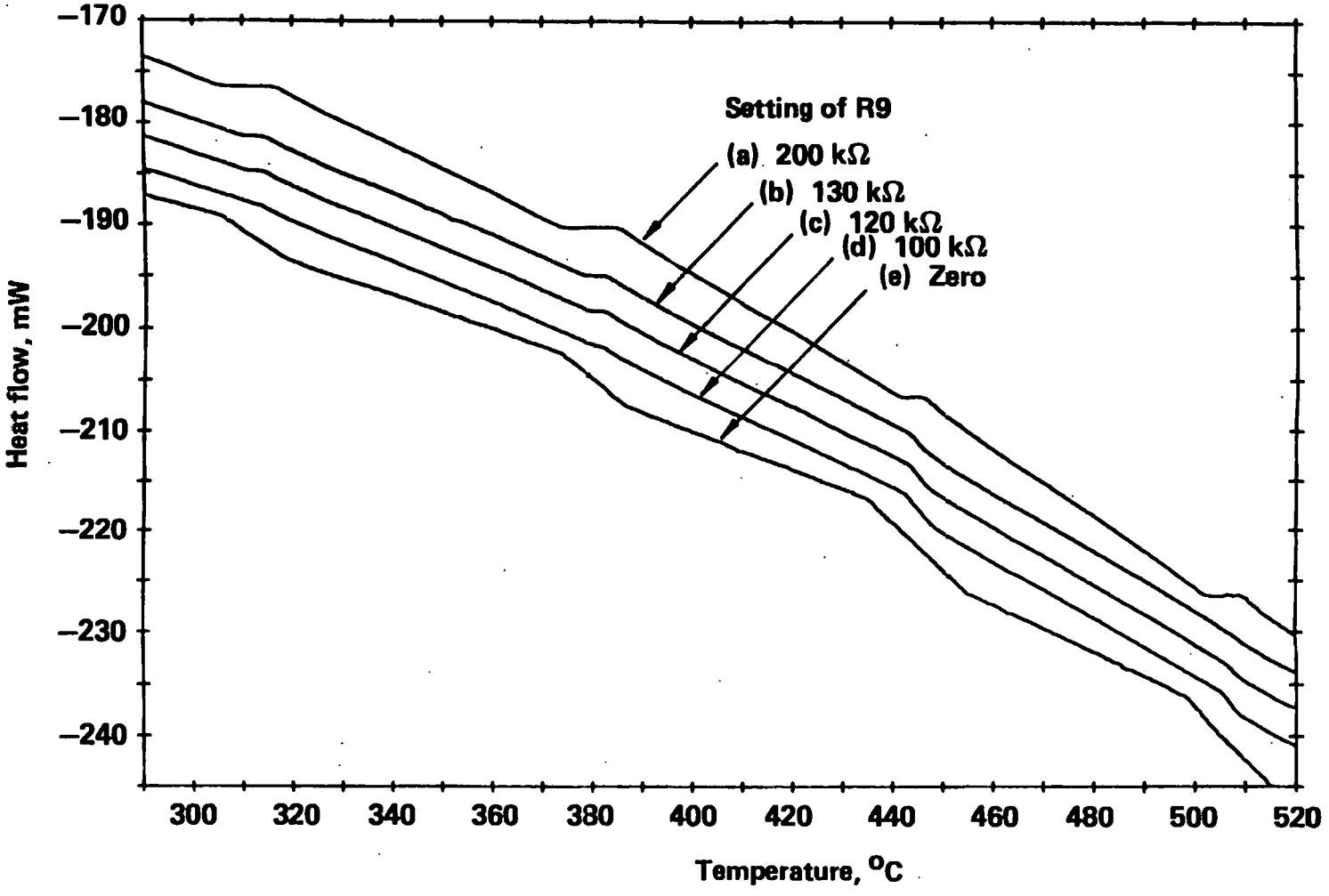

Figure 2.16 – Artifact steps produced by the 'Error–curve' lineariser.

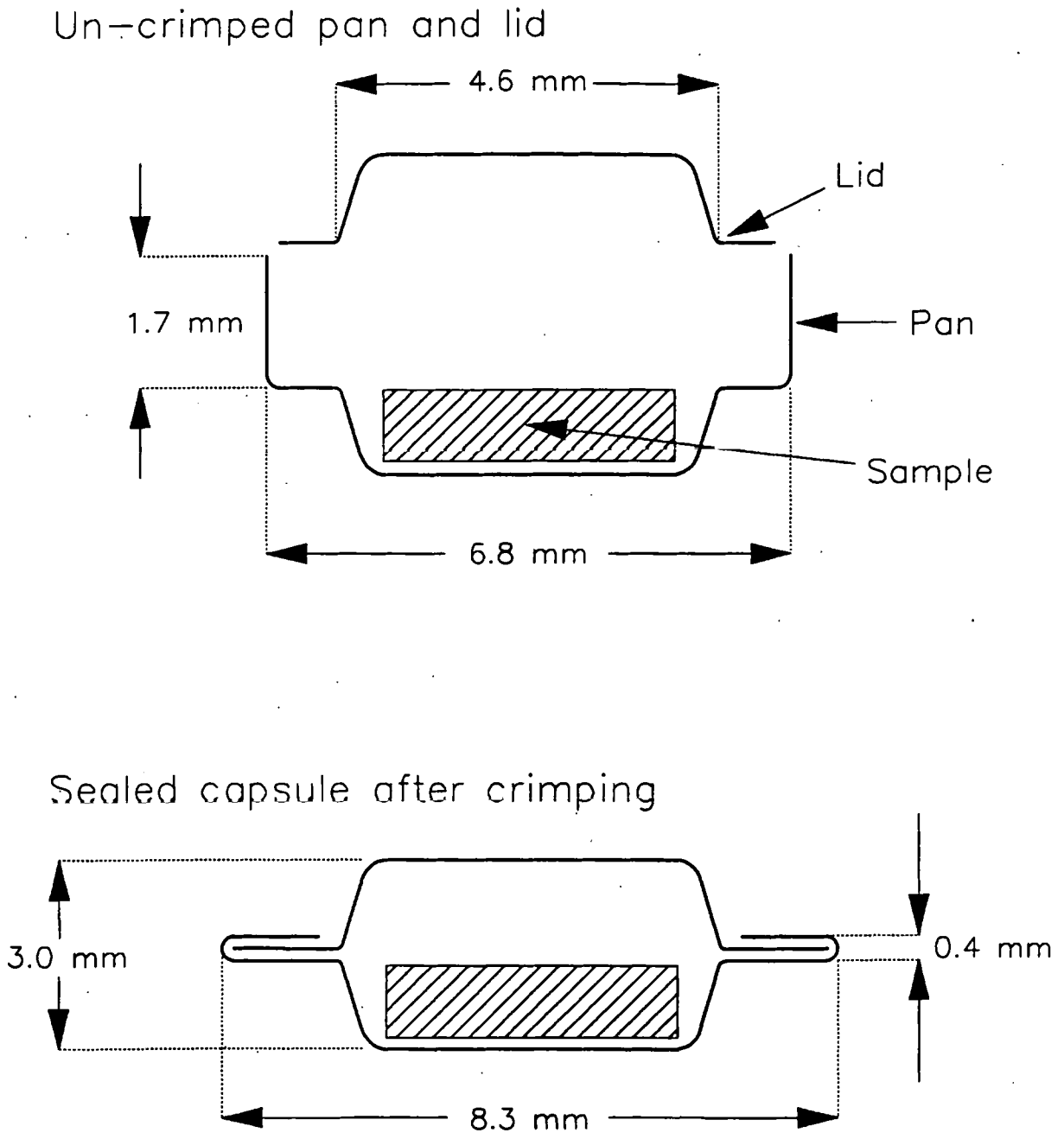

Figure 2.17 – Effect of crimping on the geometry of a Du Pont hermetic DSC pan.

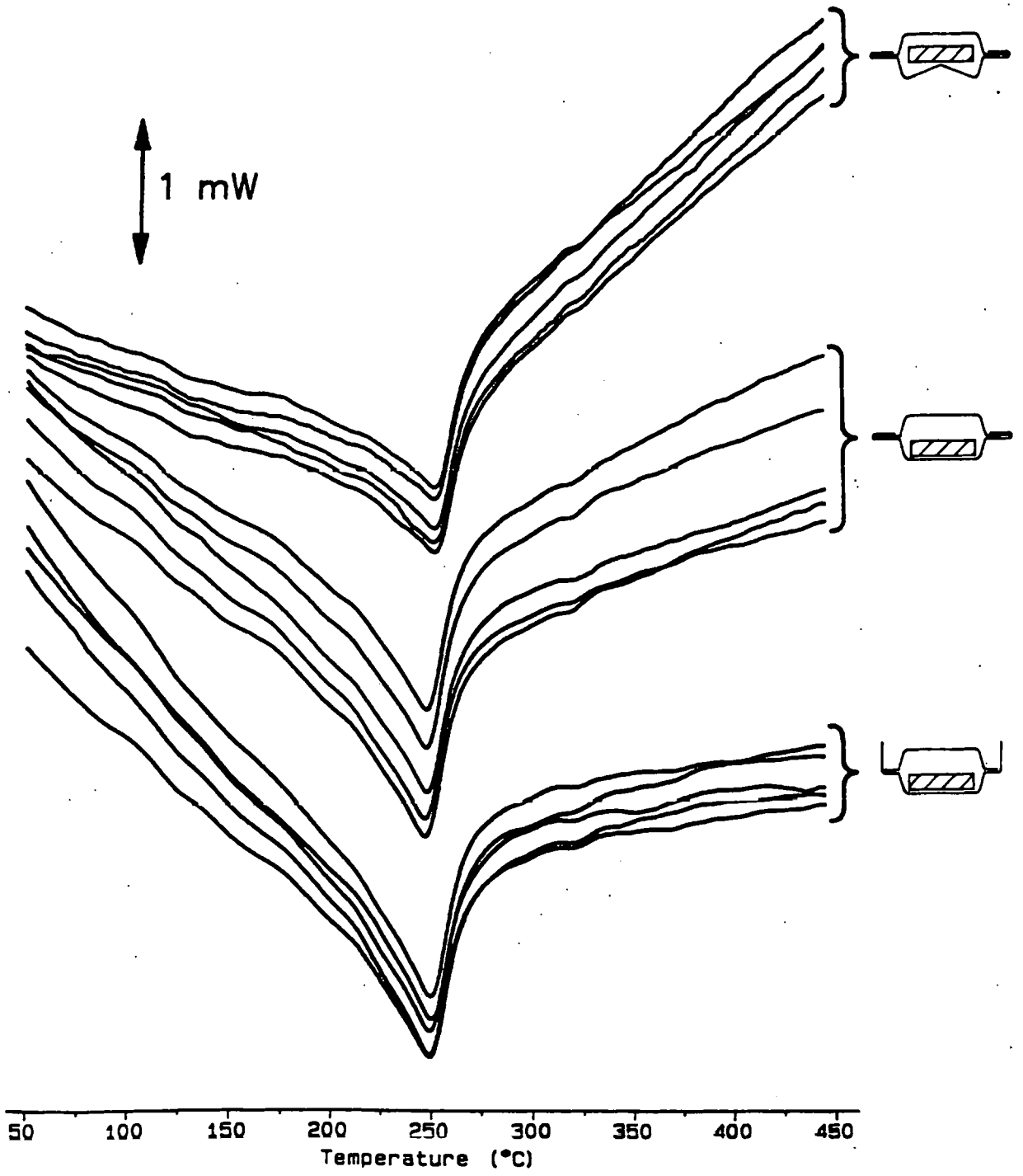

Figure 2.18 – Replicate DSC curves for a pellet of nickel(II) oxide in three pan configurations.

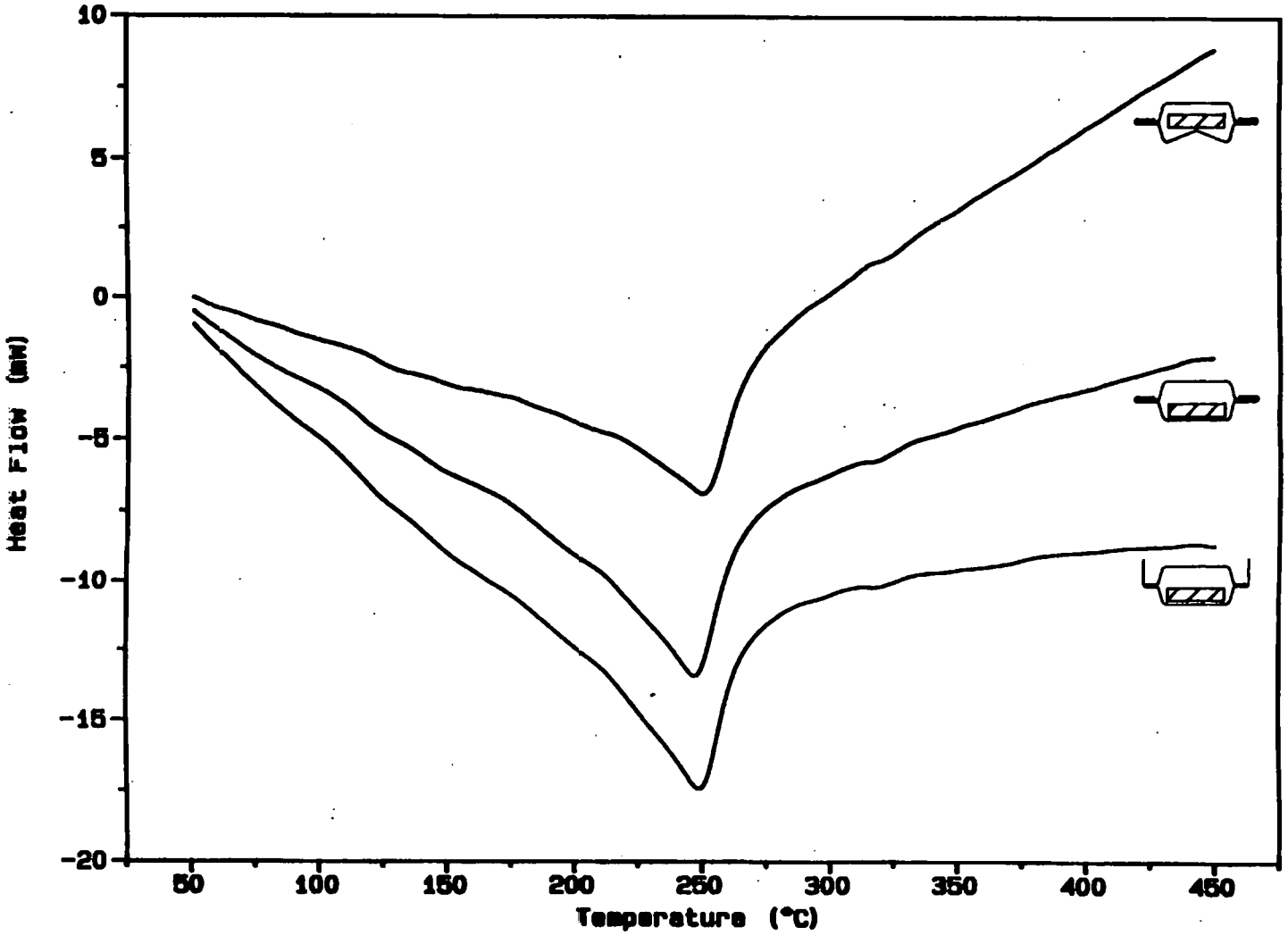

Figure 2.19 – Summation DSC curves for nickel(II) oxide in three pan configurations (cf. Figure 2.18).

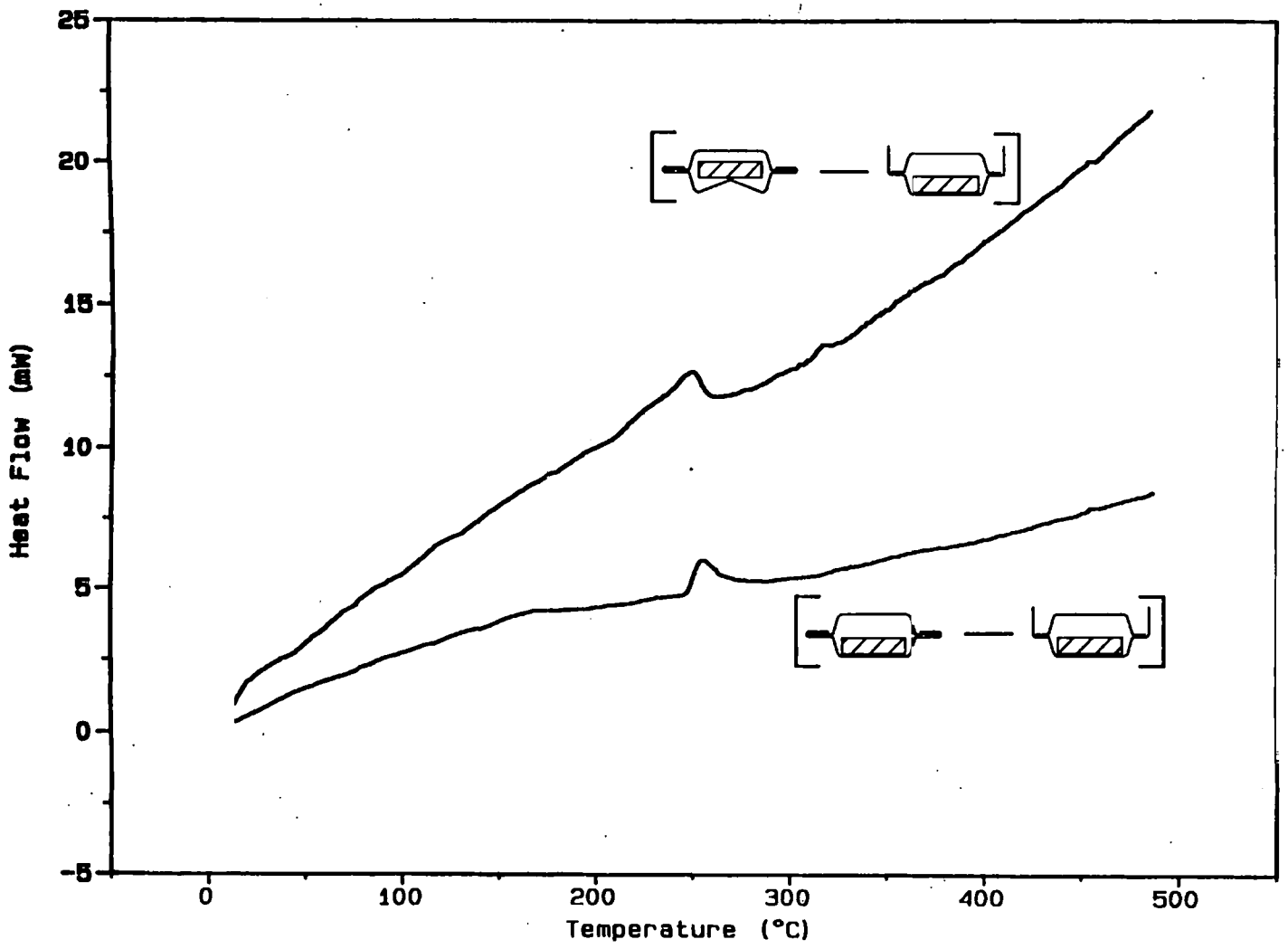

Figure 2.20 – Difference plots ([crimped]–[uncrimped]) of DSC curves for nickel(II) oxide (cf. Figure 2.19).

(a) Sample pan being loaded into the guide body.

(b) Plunger assembly located in the guide body.

(c) Tool being removed from the DSC cell.

PLATE 1 – Use of the DSC pan centring tool.

MATRIX EFFECTS IN DIFFERENTIAL SCANNING CALORIMETRY (VOLUME 2 OF 3)

by

M. THOMPSON M.Sc., C.Chem., MRSC.

Submitted to

THE OPEN UNIVERSITY

for the degree

DOCTOR OF PHILOSOPHY

FACULTY OF SCIENCE

1991

CHAPTER 3

INVESTIGATION OF MATRIX EFFECTS FOR ENDOTHERMIC EVENTS

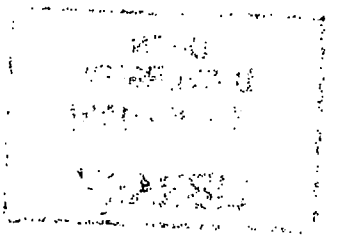

3.1 INTRODUCTION

In classical differential thermal analysis (DTA) a thermocouple buried in the sample was use to measured its temperature. This meant that the sample matrix acted as the heat conduction path between the furnace and thermocouple. Consequently, the thermal conductivity (λ) of the sample affected the shape of the DTA curve and changes of λ invariably led to curved and sloping baselines. These interferences were accepted as an intrinsic part of the technique, but they also served as a reminder that sample preparation was an important part of obtaining good results. The Boersma calorimeter was designed specifically to overcome these sample-matrix effects, by making the thermocouple part of the heat flow path to the sample rather than *vice versa*. Modern heat flux DSCs based on Boersma's design are capable of giving results which are at least cosmetically very good, even when little attention has been given to preparation of the sample. This tolerance has led to a widespread assumption that DSC response is independent of the sample matrix. Although sample-related problems are much less severe than in DTA, the measured rate of heat flow in DSC still depends on the total resistance between the thermocouple and the site of the thermal event within the sample. In most rising temperature DSC experiments a thermal event will be initiated at random points (nuclei) across the surface in contact with the sample container. As the event propagates through the bulk of the specimen, the interface will move away from its initiation site. The contribution by the internal resistance of the sample will increase with time and the heat flux for a given temperature difference will decrease. This 'matrix effect' will tend to distort the DSC peak and may invalidate comparison of results from samples whose physical properties are different. In the proposed study of solid-solid interactions by DSC, it was intended to use relatively large specimens as an aid to detecting small energy changes. An understanding of these matrix effects was therefore considered to be important in order to design valid experiments, which would not create artifacts, and to interpret the results correctly.

3.2 MODELLING OF HEAT FLOW IN A DSC SPECIMEN

3.2.1 Scope of the model

The effective thermal resistance of a solid specimen is influenced by the way it is prepared and how it is coupled to the DSC heat flow sensor via its container. A single model cannot represent all the possible permutations of sample morphology and container type, so this study was limited to a specimen in the form of a circular tablet with parallel planar faces. This shape was chosen to represent a powder compacted in a pellet press, as used for subsequent thermal conductivity and interaction studies. In the absence of gas evolution from the sample, or interactions with the atmosphere in the sample chamber, it is common practice to use a covered sample container. This is usually done for ease of handling and to prevent powdered samples being disturbed by the purge gas or by decrepitation. It was anticipated that heat flow via the wall and lid of the container would be important in determining the shape of the resistance gradient within the specimen. This is an important consideration because the change of effective resistance with time will alter the shape of the DSC peak. The contribution by conduction in the walls of the sample container was therefore given particular attention in the heat flow model described here.

The dimensions of the pelletised DSC specimens and the Du Pont sample pans resulted in a 0.25 mm air gap between the circumference of the pellet and the wall of the pan. The temperature difference across this insulating layer will be very small* and hence the heat flux will tend to zero. Temperature gradients across the two flat faces of the specimen will also be small because they are in contact with highly conductive aluminium plates (the pan lid and base). These radial temperature gradients will be much smaller than the axial gradient

---

*In this configuration, the behaviour of the polished pan wall is analogous to that of an adiabatic shield used in some larger scale calorimeters [50]. The temperature difference between the pan wall and the edge of the sample will be < 1°C during heating at $10°C \cdot min^{-1}$, based on the magnitude of thermal lag measured in section 3.6.1.

through the body of the more resistive specimen. In order to simplify the heat flow analysis, heat exchanges between the circumference of the specimen and the wall of the pan, and radial temperature gradients across the planar surfaces of the specimen were both considered to be negligible.

3.2.2 Analysis of the resistive matrix for a single interface

Consider a circular specimen with parallel planar faces, heated in an open DSC pan using a rising temperature programme. It was assumed that an endothermic phase transformation is initiated on the surface of the specimen which is in contact with the bottom of the pan. A planar interface will be formed which then advances up the vertical (z) axis of the specimen. Provided that the geometry of the transition interface is preserved as it travels through the specimen, it may be considered as occupying an infinitely thin horizontal plane within the specimen. If the specimen is covered by a close fitting lid, heat will be conducted along the wall of the pan to the upper surface of the specimen. The system then approximates to a cylinder in which heat flows from the bottom surface, via two parallel conduction paths, to the region where the transition is taking place (Figure 3.1). The corresponding heat flow paths within a DSC sample and its container are illustrated in Figure 3.2a. Heat is conducted from the DSC furnace to the sample platform (A) and across the contact area to the base of the pan (B). From here, part of the heat flows directly to the transition interface via the pan/specimen contact (BC) and lower portion of the specimen (CD). A significant fraction of the heat flow to the interface is assumed to pass via the pan wall, lid and upper fraction of the specimen (BFED).

Heat flow in this system was most easily analysed by considering its analogous electrical circuit (Figure 3.2b). The temperature-programmed furnace and heat flow sensing element (ΔT thermocouple) were represented by a variable voltage source and an ammeter respectively. Fixed value components were used for the resistance of the pan/lid conduction path (R_p) and contact resistances between thermocouple/pan (R_c) and pan/specimen (R_c'). The bulk resistance of the DSC specimen (R_s) was replaced by a variable resistor, in which

the position of the wiper contact represented the location of the transition interface. This position was given an axial coordinate (z) with values from 0 (bottom) to 1 (top). The fractional resistances representing the regions of the specimen below and above the interface then became $R_s \cdot z$ and $R_s \cdot (1-z)$ respectively. The total effective resistance (R_{tot}) between the sample thermocouple and transition interface (AD) was derived from the parallel resistance equation ($1/R_1 = 1/R_2 + 1/R_3$) as:

$$R_{tot} = R_c + \left[\frac{(R_c' + R_p + R_s \cdot \{1-z\}) \cdot (R_c' + R_s \cdot z)}{(2R_c' + R_p + R_s)} \right] \quad \ldots(3.1)$$

The main bracketed expression represents the resistance of the 'transportable' DSC specimen, i.e. the analytical specimen together with its container. This combination represents the resistive matrix over which the analyst has most control, in terms of sample preparation and coupling the specimen thermally to the calorimeter. In many cases therefore, it is appropriate to compare the effect of experimental changes by their influence on this local 'matrix resistance', where:

$$R_{matrix} = R_{tot} - R_c$$

In the case of a soft sample which deforms such that $R_c' \approx 0$, equation 3.1 simplifies to:

$$R_{tot} = R_c + R_s \cdot z - \left[\frac{(R_s \cdot z)^2}{(R_p + R_s)} \right] \quad \ldots(3.2)$$

This quadratic equation shows that the effective resistance reaches a maximum value within the body of the specimen rather than at the surface most physically remote from the heat source. It also indicates that the mean resistance over the range $z = 0$ to $z = 1$ will be lower than for a similar specimen in an open pan, which will have a linear resistance gradient.

3.2.3 Distortion of the peak shape by sample resistance

In the simple case of a DSC specimen heated in an open pan, the thermal resistance between the bottom of the specimen and the transition interface ($R_s \cdot z$) will increase as a linear function of the distance (z) travelled by the latter. This change of resistance will result in a curved leading edge to the DSC peak, with decreasing slope as temperature increases. The partial area of the peak up to a given point represents the transformed fraction of the sample (α). This is equivalent to the fraction of the total thickness of the sample along which the interface has travelled (i.e. $z = \alpha$). Analogy with the fusion onset slope method for measuring thermal conductivity (equation 1.12) shows that the tangent ($W \cdot K^{-1}$) at that point gives the instantaneous value of $1/R_{tot}$, where:

$$R_{tot} = (R_c + R_c' + (R_s \cdot \alpha)) \qquad \ldots(3.3)$$

A plot of R_{tot} vs. α should therefore be linear with slope equal to the total axial thermal resistance of the specimen (R_s) and Y-intercept = $R_c + R_c'$.

3.2.4 Double interface model for a covered specimen

If the specimen is covered by a lid which provides a significant conduction path between the heat source and the top of the specimen, nucleation will occur on both surfaces and two interfaces will be formed. The difference in resistance between the conduction paths (R_p) will result in a finite temperature difference between the specimen faces. Consequently, the second interface will begin to advance downwards shortly after the first leaves the bottom surface. When the two interfaces are fully established, the distance moved by each for a given increment of α will be half of that for a single interface and the change of resistance in the path to each interface will be correspondingly reduced. Furthermore, the presence of two parallel conduction paths means that the interfacial area is doubled. The combined effect is that, for a given value of α, the contribution of sample resistance to R_{tot} will be a quarter of that for the open configuration. The contact area between pan and specimen is also doubled and hence the contact resistance will be halved. The resistance measured from the onset slope will therefore be:

$$R_{tot} = (R_c + (R_c'/2) + (R_s \cdot \alpha/4)) \quad \ldots(3.4)$$

This shows that the slope of the resistance vs. α plot for a covered specimen will be a quarter of the specimen resistance. It is important to note that although the heat flow paths in the container are similar, those within the specimen are different for the single and double interface models. In the latter, two isothermal interfaces are present and hence there can be no heat flow in the layer of sample between them. The situation only approaches that of the single interface model when the two interfaces converge (i.e. as $\alpha \rightarrow 0.5$).

3.3 DESIGN OF A LAMINATE EXPERIMENT FOR STUDYING MATRIX RESISTANCES

Problems associated with studying matrix effects in a DSC specimen are similar to those encountered in the investigation of solid state mechanisms and kinetics. The position and geometry of the transition interface within the specimen must be identified at intervals of time and these related to the development of the DSC peak. The conductance of the specimen is most easily altered by changing its physical dimensions, but this also changes other bulk properties such as heat capacity and surface area. The latter properties of the specimen also influence the response of the DSC, which makes it difficult to correlate changes in the DSC curve with a single property of the system. In order to overcome these practical problems, a laminate structure was used to model the DSC specimen. The 'resistive' and 'active' components were represented by physically discrete layers, which constrained the transition interface to a planar conformation at a well defined location within the specimen. Consequently there was no requirement to measure the position of the interface during the DSC experiment.

3.3.1 Construction of indium/silica laminates

The resistive elements of the DSC sample were represented in this model by vitreous silica discs. Indium metal (T_{fus} = 156.6°C) was used for the active element because it is very malleable and gives a good physical contact when pressed against rough surfaces, thus minimising contact resistances. Laminates were constructed by interleaving two silica discs, of different thickness, with a disc of indium foil

(diameter = 4.0 mm). The indium disc was made smaller than the silica discs to prevent it coming into contact with the pan, because this would reduce the effective resistance of the system. Use of two dissimilar silica discs in each laminate allowed four axial locations of the 'interface' to be studied (Figure 3.3). The heat capacity and dimensions of the specimen will be the same in each configuration but the effective resistance between the sample thermocouple and indium will be different.

3.3.2 Topography of contacting surfaces

Contact resistance is strongly influenced by the conformity of the surfaces forming the contact, which in turn depends on their surface structure [51]. In order to rationalise the experimental resistance data, the topography of each contacting surface was investigated so as to assess their conformities. A visual investigation was carried out by scanning electron microscopy (SEM) to show the long-range profiles of the surfaces and the general form of asperities. The instrument used was a Jeol JXA-840 Scanning Microanalyser, although the elemental analysis facility was not used in this case. Quantitative measurements of surface texture were made using a Rank-Taylor-Hobson 'Form Talysurf' profilometer. This instrument mechanically scans a fine pointed stylus across the test surface and measures the displacement of the stylus by laser interferometry. The stylus used for these measurements had an included angle of 90° and a tip width of 2 μm.

Plate 2a shows a low magnification SEM photograph of the constantan disc in the DSC cell. The raised sample and reference platforms appeared from this view to have reasonably flat contact surfaces, each of which was in the form of a ring with a well at the centre. Low resolution profiles across one of these platforms (Plate 2, b & c) showed that the nominally flat surface was in fact concave, with the inner edge of the ring approximately 18 μm lower than the outer. The central well had a diameter of ~ 1.3 mm and a depth of ~ 0.2 mm. This profile resulted in a significant air gap between the pan and thermocouple. Consequently, the effective contact area was much smaller than it appeared from optical inspection. Plate 3 shows the constantan surface at magnifications of x200 and x1000. The random

grooves were caused by polishing with a glass fibre brush, which is the recommended procedure for cleaning the DSC sample chamber.

SEM photographs of an aluminium pan (Plate 4) showed the surface to be anisotropic, displaying a pattern of uni-directional grooves. The surface of the silica disc (Plate 5) appeared to be deeply pitted, with only minor evidence of linear scoring. This meant that the surface was virtually isotropic and hence that the aluminium/silica contact resistance would not be influenced by the orientation of the laminate relative to the pan surface.

Figure 3.4 shows short-range profiles of the three surfaces, plotted from the profilometer data, all of which displayed random features (irregular roughness). The ranking of peak-valley heights was in the order: Silica > Constantan ≥ Aluminium.
The overall curvature of the plot for the constantan surface resulted from the dished shape of the thermocouple contact area. It was difficult to assess the relative roughness of these surfaces solely by optical inspection. Comparison of the SEM photographs supported the profilometer data but unaided visual inspection was found to be misleading, since it suggested that the pan had the roughest surface. The profilometer plot also showed that surface features on the aluminium pan were less regular than they appeared from the SEM photograph.

3.4 DEVELOPMENT OF THE DSC PROCEDURE

3.4.1 DSC parameters used for the investigation

Three characteristic parameters of the DSC peak for fusion of indium were used to investigate heat flow in the laminates:

Onset slope ($W \cdot K^{-1}$) of the fusion endotherm is a measure of the thermal conductance (G) of the heat flow path between the sample thermocouple and the site of the transition within the sample. The instantaneous heat flux (Φ) from the sample platform to the melt interface depends on the total resistance (R_{tot}) of the conduction path between them:

$$\Phi = (T_i - T_{fus})/R_{tot} \quad \ldots(3.5)$$

Where T_i is the temperature indicated by the sample thermocouple and T_{fus} is the equilibrium temperature at the interface.

This is the basis of the 'fusion onset slope' technique for measuring thermal conductivity (section 1.6.2). Assignment of a negative value to an endothermic DSC signal is the convention used by most equipment manufacturers, in accordance with ICTA recommendations [31]. Thermal conductance cannot be negative and is therefore equivalent to the modulus of the fusion onset slope.

$$\text{Onset slope} = |\Delta\Phi/\Delta T_i| = 1/R_{tot} = G \quad \ldots(3.6)$$

Onset slope data in this work have therefore been tabulated and plotted as positive values, even though the axes on the DSC curves imply that they should be negative.

Extrapolated onset temperature is the accepted construction used to identify the beginning of an event (Figure 1.10), because the first deviation from the baseline tends to be subjective and has a large associated error. Although the extrapolation method does identify the true onset of the transition, a shift in this value can be used to detect differences in temperature lag between the heat source and transition interface, resulting from a change in thermal conductance.

Peak area indicates the total amount of heat conducted to the sample via the thermocouple. A change in the relative contributions of heat flux into the sample by this route and the undetected ('parasitic') flux through the sample chamber atmosphere will alter the calorimetric sensitivity of the cell. Changes of specific peak area ($J \cdot g^{-1}$) were therefore used to infer changes of the relative heat flux via these two paths.

3.4.2 Calibration of the DSC cell

The DSC cell used in these experiments was found to give a low calorimetric response, which will affect slope measurements as well as peak integration. Observations made using laminate configuration A(I) (Figure 3.3) were used for sensitivity calibration in the onset slope experiments. The standard enthalpy of fusion for indium was taken to be 28.57 $J \cdot g^{-1}$, from which the 95% confidence interval for the cell

calibration coefficient (k_{cell}) at each gain setting was calculated to be: 1.137 ± 0.002 for R = x10; 1.118 ± 0.004 for R = x1.

3.4.3 Test of indium contact resistance

The malleable nature of indium means that it deforms to give effective contact with most surfaces, resulting in a low contact resistance. In order to establish that the contact resistance in this particular system was negligible, the contact characteristics of indium powder were compared with those of indium foil. The contact area of a foil with the pan will be independent of sample mass provided that discs of constant diameter are used. Increasing the mass of a powdered sample will increase the contact area until the base of the pan is covered by a single layer of particles. The contact area will then remain constant as the bed depth increases, although the contact will be less efficient than for a flat disc. Thus if the pan/indium contact resistance is a significant factor compared with that for the thermocouple/pan, different relationships will be observed between fusion onset slope and sample mass for the two forms of indium.

Indium powder was used as supplied (Appendix I), while the wire was pressed between microscope slides to produce thin foils. The latter were cut into circles of 4.0 mm diameter by means of a circle punch. Indium specimens covering a range of mass up to ~ 6 mg were contained in covered pans, along with two silica discs (configuration A(I) in Figure 3.3). The silica discs were included so that the total heat capacity would be the same as for the other laminate configurations. Experimental conditions were as follows:

Heating rate: $10°C \cdot min^{-1}$
Purge gas: Dry nitrogen
Flow rate: $25\ cm^3 \cdot min^{-1}$
Amplifier range: x10 (gain ≈ 30,000)
Digitisation rate: 5 Hz

The onset slope data for both indium powder and foil displayed a very marked mass-dependence in the region below 3 mg, but tended to reach a plateau above this mass (Figure 3.5). Initial inspection showed no obvious differences in the slope vs. mass relationship between data

for the two physical forms. A statistical treatment (section 3.4.5) later confirmed that there were no significant differences.

These results confirmed that the pan/indium contact resistance was indeed small compared with that for the thermocouple/pan contact. Indium foil was used in all subsequent experiments because it was the easier form with which to construct laminates and the contact area could be measured directly.

3.4.4 Investigation of the mass dependence of the onset slope

Signal saturation of the differential (ΔT) amplifier was identified in Chapter 2 as a cause of non-linear calorimetric response, resulting in a sharp decrease in sensitivity for samples of mass > 5 mg. This suggested that the observed slope vs. mass relationship might also be an artifact resulting from non-linearity in this amplifier. In order to investigate this possibility, experiments were carried out on foil samples covering a higher mass range, but using a lower amplifier gain (Range xl; Gain $\approx$ 3,000). Because the gain was reduced by an order of magnitude, the ΔT amplifier was working in a different region of its response curve. If the form of the slope/mass curve was attributable to the characteristics of this amplifier, different relationships would be observed at different signal gains.

Slope values derived from observations on high mass samples were found to lie in the plateau region of the graph for low mass data obtained at the higher amplifier gain. These results indicated that the observed mass dependence of the onset slope was not related to electrical clipping or signal distortion. The reason for the low values of onset slope observed for small sample masses became apparent on comparing the shapes of peak leading edges (Figure 3.6). Normally the leading edge of a DSC fusion peak consists of three regions: (i) The initial deviation from the baseline is not sharp, because melting begins at random points where the contact resistance is least. As melting progresses, the contact area increases and the resistance to heat flow is correspondingly reduced. This means that the DSC response increases in a curve until a continuous melt interface of constant area has been established. (ii) The extended interface then

accelerates through the bulk of the specimen at a rate which depends on the rate of heating of the DSC cell. This acceleration corresponds to the linear region described by equation 3.6. (iii) Eventually, when a large amount of the available material has melted, the advancing interface becomes constrained by the physical boundaries of the specimen. The onset slope reduces in the curved region approaching the peak maximum.

All three regions were evident in the DSC curve for 2.5 mg of indium, but the smaller specimen did not show a linear region (Figure 3.6). Instead, the two curved regions impinged on one another to form an inflection point. Hence it appears that in small specimens the melt interface is not able to achieve a steady rate of acceleration before the curved region around the peak maximum is reached. In these cases the apparent onset slope is actually the gradient at the inflection point, where competition between nucleation/growth and interface decay occurs. The measured value of the slope at this point probably depends on the free path accessible to the advancing interface and is therefore limited by specimen geometry. Only in larger specimens is there sufficient bulk of material available for an extended solid-liquid interface to be established and propagate freely. The onset slope then becomes instrument limited, i.e. dependent only on the pan/thermocouple contact resistance.

3.4.5 Mathematical model for the onset slope/mass relationship

The relationship between onset slope and sample mass appeared from inspection to be of an exponential form. If the above 'restricted interface' interpretation of this mass dependence is correct, then the asymptotic slope, derived from an exponential equation which describes the relationship between onset slope and sample mass, will represent the 'true' thermal conductance of the system. Two exponential models were investigated by regression fitting to experimental data from both powder and foil samples. The first of these equations allowed for a detection threshold to be determined, while the second equation assumed that the regression line passes through the origin.

Model 1: $G = a - e^{(b - \{c \cdot mass\})}$ ...(3.7)

Model 2: $G = a \cdot (1 - e^{\{-c \cdot mass\}})$ ...(3.8)

Where G = thermal conductance. a,b and c are constants. Several non-linear regression procedures were tested [52], all of which gave similar values for the constants in both equations. The Marquardt method [53] gave faster convergence and smaller standard errors than other methods and was used for all subsequent work. Standard error values derived by this method are only approximate [54], but were adequate for significance testing in this application. The t-test was used to compare mean values of the constants derived from each equation, using data from both indium powder and foil. No significant differences (95% confidence) were found between values of the constants 'a' or 'c' derived from either equation or form of indium. The line described by equation 3.7 intersects the G-axis at $(a - e^{b})$, but both the powder and foil data gave confidence intervals for this term which included zero. This indicated that the onset slope response passes through the origin and that the simpler model (equation 3.8) adequately describes the exponential relationship. These results are summarised in Table 3.1. A typical scatter plot and regression line derived from equation 3.8 is shown in Figure 3.5

Fitting equation 3.8 to the data for masses > 20 mg (Table 3.2) gave a value for the asymptote (constant 'a') which was not significantly different from that derived by pooling the data for smaller masses. The difference between values of the exponent 'c' cannot be considered as significant because no data was obtained for small sample masses at the lower amplifier gain.

Equations containing higher order mass terms, including $(mass)^2$ $(mass)^3$ and $(mass)^4$, were also investigated. In each case, the associated constants were found to be small and had 95% confidence intervals spanning zero. Hence these terms were not considered to be significant and the simple model was used in regression fitting to data from all subsequent experiments.

3.5 MEASUREMENT AND ANALYSIS OF MATRIX RESISTANCES

3.5.1 Calculation of partial resistances from system dimensions

Dimensions of various parts of the pan and sample which were used in these calculations are listed in Appendix I. Literature values of thermal conductivity were used for aluminium (λ = 240 $W \cdot m^{-1} \cdot K^{-1}$ [55]) and silica (λ = 1.54 $W \cdot m^{-1} \cdot K^{-1}$ [56]).

Assumptions used to simplify the model

Estimates of the values of the pan/lid resistance (R_p) and bulk sample resistance (R_s) were derived from the physical dimensions of the conduction paths and the thermal conductivities of the materials forming them. An accurate solution would require complex calculations of radial temperature gradients across the pan base and lid, and of parasitic heat exchanges with the cell-walls. The accuracy and precision of the measured values in this work do not justify such a rigorous treatment, so several assumptions were made as follows:

(a) Contact resistances involving indium were assumed to be negligible compared with all other system resistances.

(b) The heat source (plate thermocouple) and heat sink (indium) were each treated as isothermal disks of 4.0 mm diameter.

(c) Parasitic heat exchanges (i.e. those through the atmosphere of the sample chamber) were considered to be negligible (see section 3.6.3).

The most difficult aspect of this treatment was in establishing confidence limits for the estimated resistance values. Consequently, these values are only approximate and may have relatively large associated errors.

Sample holder resistance (R_p)

Heat flow in the container walls is composed of three elements (Figure 3.7), two of which approximate to radial conduction in a hollow cylinder (pan base and lid), for which:

$$R = \frac{\ln(r_2/r_1)}{(2\pi \cdot \lambda \cdot h_1)} \qquad \ldots(3.9)$$

The vertical section of the pan is a hollow cylinder of different dimensions, for which:

$$R = h_2/(\lambda \cdot A) \qquad \ldots(3.10)$$

Where λ = thermal conductivity.

Dimensions h_1, h_2, r_1, r_2 and A are defined in Figure 3.7.

The radial elements R_1 and R_3 have the same physical dimensions and hence, from equation 3.9:

$$R_1 \approx R_3 = \frac{\ln(3.25/2.0)}{(2\pi \cdot 240 \cdot 8 \cdot 10^{-5})} = 4.02 \text{ K} \cdot \text{W}^{-1}$$

The height of the vertical section (h_2) is the total thickness of the laminate (silica and indium). A value of 0.25 mm was used for the thickness of the indium disc. This is equivalent to a sample mass of ~ 23 mg, which represents data in the asymptote region of the slope/mass plot.

From equation 3.10: $R_2 = 1/(240 \cdot \pi \cdot 6.5 \cdot 8 \cdot 10^{-5})$

$= 2.55 \text{ K} \cdot \text{W}^{-1}$

Since the geometry of the heat flow path is unambiguous (and assuming that the approximations made in this treatment are valid) the accuracy of this calculated resistance should be rather better than that of R_s (below). The physical dimensions of the pan and lid were measured with a precision of ± 10 μm (using a micrometer) and therefore make a negligible error contribution. On this basis, a nominal error limit of ± 10% was assigned, which is of the same order as the experimental error found for matrix resistances (section 3.5.2).

Thus the total pan/lid resistance is:

$$R_p = (R_1 + R_2 + R_3)$$

$$= 10.6 \pm 1.1 \text{ K} \cdot \text{W}^{-1}$$

Bulk sample resistances (R_s, R_s', R_s'')

Although the dimensions of the silica discs can be measured accurately, the exact geometry of the heat flow path through them is difficult to model. Consider the lower silica disc in configurations A(II) and A(III) (Figure 3.3). The heat source and heat sink were each considered to be isothermal discs of 4.0 mm diameter, connected by a

silica rod in series with the thermocouple/pan and pan/silica contact resistances. The highest estimate of the bulk silica resistance is obtained if conduction is assumed to take place along the axis of a 4.0 mm diameter cylinder, and edge-effects in the 1.0 mm thick silica sheath surrounding it are neglected:

$$R_s = h/(\lambda \cdot A) \qquad (cf.\ \text{equation } 3.10)$$

However, the bottom face of the disc is bridged by the highly conductive aluminium pan and consequently the effective heat source will have a larger surface area than the thermocouple. A radial temperature gradient will be present between the edge of the silica disc and the nominally isothermal region adjacent to the thermocouple, but an estimate of the minimum bulk sample resistance can be obtained by neglecting this. The conduction path then approximates to the axis of the frustum of a cone, with end face diameters of 6.0 mm and 4.0 mm. The effective cross-sectional area of this conduction body is given by:

$$A = \pi \cdot (r_1^2 + r_1 \cdot r_2 + r_2^2)/3 \qquad \ldots(3.11)$$
$$= 6.33\pi \ m^2 \cdot 10^{-6}$$

Thus for configuration A(IV) in Figure 3.3, where h = 0.75 mm, the bulk resistance has a possible range:

$$h/(6.33\pi \cdot \lambda \cdot 10^{-6}) \leq R_s \leq h/(4\pi \cdot \lambda \cdot 10^{-6})$$
$$24.5 \leq R_s \leq 38.8 \ K \cdot W^{-1}$$
$$R_s \approx 31.6 \pm 7.1 \ K \cdot W^{-1}$$

Note: This does not take into account the contact resistance between the silica discs (see following section).

Similarly, for the individual silica discs:

$R_s' \approx 11.0 \pm 2.5 \ K \cdot W^{-1}$ (for discs of mean thickness 0.26 mm)

$R_s'' \approx 20.6 \pm 4.6 \ K \cdot W^{-1}$ (for discs of mean thickness 0.49 mm)

The 'confidence intervals' for these estimated values of bulk sample resistance are very wide because of uncertainty as to the true geometry of the heat flow path.

3.5.2 Measurement of thermal resistances

(a) Contact resistances

In order to measure the various contact resistances, two further sets of experiments were carried out using a single silica disc (thickness = 0.51 mm) in configurations B(I)-(III), shown in Figure 3.8. The regression data calculated from these results (Table 3.3) were used in the following calculations. Contact resistances between constantan, aluminium and silica have been designated according to the materials forming the two surfaces in contact i.e. R_c(con/al) (= R_c used elsewhere), R_c(al/sil) (= R_c'), R_c(con/sil) and R_c(sil/sil).

Calculation of R_c(con/al)

This was the most precisely determined resistance because no other contact or bulk sample resistances were involved in its derivation. All data acquired with indium in direct contact with the base of the pan (configurations A(I) in Figure 3.3 and B(I) in Figure 3.8) were combined, giving over 100 observations covering a sample mass range 0.3-74.2 mg. This data, which included measurements at both amplifier gain settings, gave an asymptotic slope of 27.4 ± 0.7 $mW \cdot K^{-1}$ which was equivalent to:

$$R_{tot} \approx R_c(con/al) = 36.5 \pm 0.9\ K \cdot W^{-1}$$

Calculation of R_c(al/sil)

Assuming that the geometry of the conduction path through the silica disc in configuration B(II) lies between a cylinder and the frustum of a cone, then $R_s'' \approx 21.5 \pm 4.8\ K \cdot W^{-1}$. The asymptotic slope for this set of data was 15.8 ± 0.7 $mW \cdot K^{-1}$.

$$\therefore R_{tot}' = 63.4 \pm 2.8\ K \cdot W^{-1}$$

$$R_c(al/sil) = R_{tot}' - R_s'' - R_c(con/al)$$

$$= 5.4 \pm 5.6\ K \cdot W^{-1}$$

This showed that the cumulative error from the individual resistances used to calculate R_c(al/sil) was so large that a reliable value cannot be derived by this approach. The true value probably lies in the range between zero and 11 $K \cdot W^{-1}$, based on the calculated confidence interval.

Calculation of R_c (con/sil)

The asymptotic slope from configuration B(III) was 15.0 ± 0.8 $mW \cdot K^{-1}$.

$$\therefore R_{tot}'' = 66.8 \pm 3.7\ K \cdot W^{-1}$$

$$R_c(con/sil) = R_{tot}'' - R_s'' - R_c(al/sil)$$
$$= R_{tot}'' - R_{tot}' + R_c(con/al)$$
$$= 39.9 \pm 2.8\ K \cdot W^{-1}$$

(b) Matrix resistances

Calculation from measured resistance values

Regression fitting of Model 2 to onset slope data for the laminates involving two silica discs (Figure 3.3) gave constants as listed in Table 3.4. The matrix resistance for the pan/sample system in each of these configurations (see Table 3.5) was calculated from:

$$R_{matrix} = R_{tot} - R_c(con/al)$$

Estimation from calculated partial resistances

Of the laminate configurations in Figure 3.3, A(II) and A(III) are directly comparable to each other, differing only in the value of the axial coordinate (z). The other two configurations have the indium disc in direct contact with the aluminium pan or lid, and consequently lack one silica/aluminium contact. Configuration A(IV) also involves a direct contact between the silica discs which is not present in any of the other configurations. If it is assumed that the contribution of these additional resistances is small compared with the bulk sample resistance, then the simple relationship between axial coordinate and resistance (equation 3.2) can be applied. The equivalent R_{matrix} values, calculated from theoretical pan/lid and sample bulk resistances, were as follows:

Configuration A(II) (z = 0.35)

This is equivalent to:

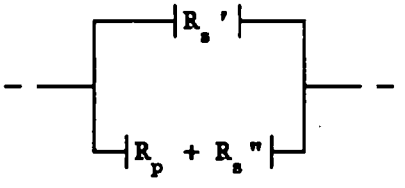

For which: $R_{matrix}(II) = 8.1 \pm 1.4\ K \cdot W^{-1}$

Configuration A(III) ($z = 0.65$)

This is equivalent to:

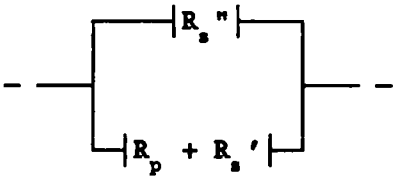

For which: $R_{matrix}(III) = 10.5 \pm 1.8\ K \cdot W^{-1}$

Configuration A(IV) ($z = 1.0$)

This is equivalent to:

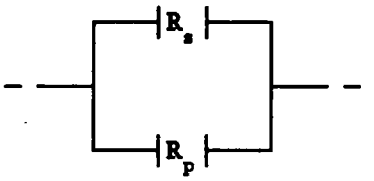

For which: $R_{matrix}(IV) = 7.9 \pm 1.0\ K \cdot W^{-1}$

The values of R_{matrix} calculated for configurations A(II) and A(IV) were not significantly different from the corresponding measured values. The difference between the measured and calculated values for A(III) was significant, provided that the errors in R_p and R_s were not under-estimated. However, the uncertainty was too great to allow these figures to be used in calculation of R_c(al/sil) and R_c(sil/sil). The calculated and measured resistance values (Table 3.5) were consistent in that both approaches gave a maximum value for R_{matrix} within the body of the specimen, rather than at the most physically remote surface from the thermocouple.

3.6 EFFECT OF MATRIX RESISTANCE ON OTHER PEAK PARAMETERS

3.6.1 Extrapolated onset temperature

Temperature lag across the thermocouple/pan contact is normally corrected for by carrying out calibration scans at the same heating rate as used for the sample experiments. However, as with peak shape, no account is usually taken of the possible influence of contact or bulk resistances associated with the sample itself. Heat flow through the laminate during a rising temperature experiment implies a

temperature gradient, even before a transition begins. In an attempt to quantify the temperature differences within the laminates, the mean extrapolated onset temperature for calibration ('reference') scans was compared with those for each of the other configurations. The individual onset temperatures did not show sample-mass dependence for any of the experiments, even in those cases where the peak was clipped due to amplifier saturation. However, it was not possible to simply compare the mean values of all onset temperatures measured for each configuration. It was found that the random error in measurement of onset temperature was of the same order of magnitude as the lags being measured. These experiments were carried out over a period of about two years, during which time the cell-base had been used for other work and periodically re-calibrated. This meant that any adjustment to the thermocouple reference junction, which was usually based on two or three calibration scans, effectively swamped the shift in onset temperature due to thermal lag. Only sets of 'reference' and 'sample' observations which had been acquired in the same period, between adjustments to the reference junction, were comparable. Consequently, only about 10% of the potential number of reference observations could be used. In spite of this limitation, the measurement precision was of the order ± 0.05 K for onset lag values in the range 0.4-0.8 K.

The onset temperature shifts observed for all laminate configurations are summarised in Table 3.6. Inspection of this data showed that:
(i) All of the laminate configurations in which the indium disc was isolated from the base of the pan gave a measurable lag of onset temperature relative to the calibration scans.
(ii) Configurations representing adjacent layers in the specimen gave significantly different onset lags i.e. A(II)/A(III), A(III)/A(IV).
(iii) The measured lags for configurations A(II) and A(IV) were not significantly different. This was consistent with the similarity in measured resistances for these configurations (Table 3.5).
(iv) The lag in configuration A(III) was <u>less</u> than in A(II) or A(IV), whereas A(III) would be expected to give a <u>larger</u> lag than the lower resistance configurations. The observed differences were significant, but this discrepancy could not be explained from the available information.

3.6.2 Calorimetric sensitivity

In the absence of amplifier saturation, the specific calorimetric response of the DSC is independent of sample mass. It might then be assumed that if parasitic heat exchanges are constant, specific peak areas should also be independent of matrix resistance even though the peak shape is affected. The results in Table 3.7 showed a low response for every configuration relative to the reference (A(I) or B(I)). The relationship between calorimetric response and measured resistance appeared to be of an exponential form, as shown in Figure 3.9. Configurations A(IV/black-lid) and B(III) gave particularly low response factors (off the scale of Figure 3.9) which were attributed to large contributions by parasitic radiation, as discussed in section 3.6.3.

Another consequence of changing the parasitic/measured heat flux ratio was noted by Baricco *et al* [90], although the cause was not identified. They compared calorimetric correction factors (k_{cell}), for the Du Pont DSC, which were derived from the heat capacities of copper, silver and sapphire (α-Al_2O_3). The measured values of k_{cell} were ranked in the order:

$$\alpha\text{-}Al_2O_3 \; > \; Ag \; \simeq \; Cu$$

This trend can be explained by different parasitic contributions as follows. The temperature difference between the walls of the DSC sample chamber and the exposed surface of the specimen (ΔT_{para}) is the driving force for parasitic heat exchange. Copper and silver have very high thermal conductivities, which means that the axial temperature gradient through the DSC specimen will be minimal. The resistance of the measured heat flow path to the top surface is therefore dominated by the constantan disc and the contact resistance R_c. Alumina has a much lower conductivity than copper or silver and makes a significant contribution to the total resistance of this flow path. This will have two effects: the measured heat flux will be reduced relative to Φ_{para} and there will also be a small increase of ΔT_{para}. These effects cooperate to reduce sensitivity and hence increase k_{cell}.

3.6.3 Investigation of errors due to radiative heat transfer

A significant amount of heat is transferred from the DSC furnace to the sample through the sample-chamber atmosphere. In the last chapter, the contribution by this 'parasitic' component was shown to be affected by changing the external configuration of the sample pan. If parasitic heat transfer involves a large component due to radiation, then detection of an event by DSC is likely to be affected by the overall emissivity of the pan and sample. A dark coloured specimen in an open pan will have a higher emissivity than one which is covered by a polished lid. This would be important for porphyrins, which are dark red or purple in colour, and for nickel oxide (particularly the black form). The effects of changing emissivity were investigated using laminates of configuration A(IV), whose lids had been anodised to a matt-black finish. This configuration, with the indium in contact with the pan-lid, should be the most susceptible to radiative heat flux.

The results (included in Table 3.7) showed a decrease in calorimetric response of (4.2 ± 0.3) % relative to the equivalent experiment carried out using a polished lid. The corresponding onset slope results (Table 3.4) were not significantly different, which showed that the oxide layer produced on the aluminium during anodisation had not appreciably increased the resistance of the pan/lid conduction path. It also indicated that any increase in parasitic heat transfer did not affect the temperature of the lid, since this would alter the temperature gradient along the pan/lid conduction path, and hence its apparent resistance. The latter observation is reasonable, since the lid temperature will remain constant during fusion of the indium in contact with it, irrespective of the magnitude and direction of the heat flow. Thus it appeared that the decrease in sensitivity, observed when the polished lid was replaced by one with a matt-black finish, was attributable to an increase in the radiative component of the parasitic heat flux.

The greatest loss of calorimetric sensitivity was observed for configuration B(III). This change cannot simply be attributed to an increase in thermal resistance, because the difference in geometry between B(II) and B(III) caused only a slight (and statistically

insignificant) increase in thermal resistance, whereas the relative calorimetric response decreased dramatically (from 97.0 to 91.2%). The major difference between these configurations was that the matt surface of the silica disc was shielded by the pan in B(II) but exposed in B(III). The ground silica surface will have a higher emissivity than that of polished aluminium. Consequently, this change of geometry would be expected to increase the parasitic heat flux between the region of the constantan disc surrounding the thermocouple and the exposed side and base of the pan/silica disc. This is consistent with the observed change in calorimetric sensitivity.

3.7 TEST OF THE LAMINAR INTERFACE MODEL FOR A HOMOGENEOUS SPECIMEN

The indium/silica laminates represent an idealised situation in which the transition interface is planar and occupies a fixed location within the specimen. In reality, a transition will occur in a finite volume whose geometry and location within the specimen will alter as the transformation proceeds. This transition region will not be physically isolated from the resistive matrix which constitutes the bulk specimen and will itself have a resistive component. The effects of distortion and 'smearing-out' of the interface on detection of a thermal event are difficult to predict, and they were most easily investigated by comparing practical results with the predictions of the simple laminar interface model.

3.7.1 Design of the experiment

An ideal medium in which to investigate interface dynamics would be a homogeneous solid which undergoes a sharply defined transition between two crystalline structures. Formation of a liquid phase is undesirable because this would radically alter the heat transport properties of the specimen and introduce a further deviation from the simple model. Most primary thermal standards are metals, which have high thermal conductivities and do not undergo phase transitions, other than fusion, in the temperature region which is of interest in this work (100-300°C). Du Pont have suggested a range of alternative materials as thermal standards [57], most of which are inorganic compounds which undergo well characterised polymorphic transitions. One of these is

potassium nitrate, which changes between two hexagonal crystal structures (γ-β) at 129.7°C.

3.7.2 Experimental procedure

Microcrystalline potassium nitrate was compacted in a 6.0 mm diameter pellet press at ~ 850 MPa to form circular tablets. These were heated through the transition region using a temperature programme 50-200°C @ $10°C \cdot min^{-1}$. Four pairs of experiments were carried out on specimens covering a range of thickness 0.2-0.9 mm. These tablets were contained in Du Pont aluminium pans, which were either open or covered with a close fitting lid. Additional experiments were carried out on very thick specimens (1.7 mm) which protruded beyond the walls of the Du Pont pans and hence prevented contact between the lid and pan. In this case flat Perkin-Elmer aluminium lids were used as specimen covers for those experiments in which the top surface of the specimen was to be protected from parasitic radiation. The effect of using Perkin-Elmer steel pans as sample containers was also investigated, in both the open configuration and with an isolated aluminium cover.

3.7.3 Peak shape analysis

The planar interface model predicts that the leading edge of an endothermic DSC peak will be curved, owing to the increase of thermal resistance with time. The degree of curvature will depend on the magnitude of the sample resistance and also whether one or two interfaces are present (determined by the pan/lid configuration). Comparison of the peak shapes for open and covered specimens (Figure 3.10) showed that this was at least qualitatively true, provided that the lid was actually in contact with the wall of the pan. Both peaks displayed marked curvature of their leading edge, but this was less severe for the covered specimen, which gave a much sharper overall peak shape.

The degree of curvature was analysed quantitatively by shape analysis of the leading edge region. Peak partial areas were calculated between the first deviation from the baseline and a series of points at temperature intervals of 0.25 K. The slope of the tangent to the DSC

curve was measured at each of these points to determine the corresponding thermal resistance (Figure 3.11). Plots of R_{tot} vs. α for data from pellets up to 0.9 mm thick, in both experimental configurations (Figure 3.12), were reasonably linear up to $\alpha \approx 0.4$, which corresponded to approximately 90% of maximum peak height. The least-squares linear regression slopes for data in this region were:

Open pan: 576 ± 21 K•W^{-1}

Covered pan: 116 ± 16 K•W^{-1}

The ratio of these slopes was 4.97 ± 0.72 compared to a theoretical value of 4.0 predicted by the planar interface model (equations 3.3 and 3.4). The effective resistance between the sample thermocouple and specimen surface(s) was also calculated from the Y-intercept ($\alpha = 0$) of these equations:

Open pan: 53.9 ± 8.2 K•W^{-1} $(= R_c + R_c')$

Covered pan: 50.0 ± 5.9 K•W^{-1} $(= R_c + (R_c'/2))$

The covered pan was expected to have a lower pan/specimen contact resistance than the open pan because the contact area was doubled and was also under pressure from the tightly fitted lid. The measured difference between the two configurations was not significant and the major component of each was attributable to the pan/thermocouple contact ($R_{tot} \sim 36.5$ K•W^{-1}). The remainder (~ 15 K•W^{-1}) was attributable to the pan/specimen contact (*cf.* calculation of R_c' in section 3.5.2).

Specimens having the same height as the sample pan (~ 1.7 mm) prevented contact between the pan and lid. In this case there was no significant difference in peak shape between DSC curves for covered and open specimens. This indicated that breaking the heat flow path to the top surface of the specimen prevented the formation of a second transition interface. The R/α plots for these experiments showed marked deviations from linearity and therefore shape analysis was not attempted.

3.7.4 Calorimetric effects

Calorimetric results for the polymorphic transition (Table 3.8) showed more scatter than for fusion of a metal. Consequently, no significant relationship between sample thickness and calorimetric sensitivity

could be identified from this limited data set. Inspection of the data suggested that the measured values of $\Delta H_{p.t.}$ were lower for the 1.7 mm specimens than for the rest. Use of steel pans will increase the resistance between the thermocouple and sample and, as expected, this appeared to reduce the sensitivity still further. However, in both cases the data set was too small to support these observations statistically. Covering the top surface of the specimen increased the calorimetric sensitivity by ~ 2-4%, as shown by the relative $\Delta H_{p.t.}$ values. These relative peak areas showed no apparent variation with sample thickness or pan type.

3.8 DISCUSSION

Broadening of endothermic DSC peaks due to the presence of contact resistances is not a novel concept - it is inherent in the theory of DSC instruments and forms the basis of several experiments for measuring thermal conductivity (λ) (see references in section 1.6.1). However, this investigation showed that sample resistance has a very significant effect on DSC response in other applications, apart from measurement of λ. The most important consequences of having a high sample resistance are distortion of the peak shape and loss of calorimetric sensitivity. Shift of the overall DSC peak, due to the steady-state temperature lag during heating, did not appear to be a major effect. In the laminate experiments, a maximum lag of about 4 seconds (i.e. 0.7 K @ $10°C \cdot min^{-1}$) was detected for a matrix resistance of 8 $K \cdot W^{-1}$. It is unlikely that effects of this magnitude would be significant since peak broadening under non-steady state conditions (during the transition) may be one or two orders of magnitude greater.

3.8.1 The effect of contact resistance

Most of the problems associated with temperature lag in this type of calorimeter are a consequence of the large contact resistance between the sample thermocouple and pan. Investigation of the cell construction showed that the high resistance in Du Pont cells is largely due to the dished shape of the platform thermocouples. The surface topography measurements showed that contact resistances in the laminates should be ranked:

$$R_c(\text{con/sil}) > R_c(\text{con/al}) \gg R_c(\text{al/sil})$$

This ranking was confirmed by the experimental measurements of thermal resistance. The first two values were found to be similar (but significantly different) which confirms that the contact resistance is dominated by the effect of the dished sample platform but that the contribution by the second contacting surface can also be detected. However, there is a considerable discrepancy between the value of the contact resistance R_c(con/al) found in this work (36.5 ± 0.9 $K \cdot W^{-1}$) and that reported by Du Pont [13] (ca. 90 $K \cdot W^{-1}$). There are several possible reasons for this difference:

(i) The onset slope for fusion of indium was used to calculate R_c in both studies, but Du Pont do not appear to have recognised any mass dependence. The mass used was not reported in their work, but a small mass would give a relatively low onset slope and hence an erroneously high value for R_c.

(ii) The pan type was not specified in [13] and may have been hermetic. A contact resistance of 75 $K \cdot W^{-1}$ was measured for Du Pont hermetic aluminium pans (Chapter 2) in the same DSC cell as used for the rest of this work.

(iii) The surface of the sample and reference platforms in some (especially older) DSC cells is very irregular, owing to distortion during spot-welding of the chromel discs onto their under-sides. This would cause particularly poor contact between the pan and thermocouple, resulting in a very high contact resistance.

3.8.2 The role of the sample container

Analysis of heat flow in the sample and its container showed that the conduction path along the wall of the pan and the lid makes a significant contribution to the way a DSC event is detected, leading to:

- change of the resistance profile along the axis of the specimen from a linear to a quadratic form.
- formation of two transition interfaces, converging from opposite ends of the specimen.
- an increase in sharpness of the DSC peak, with less curvature of the leading edge.

The exact form of the resistance profile could not be proved from the results of this work because of the magnitude of the experimental errors. However, the data were sufficiently precise to prove (with 95% confidence) that a maximum resistance occurs within the body of a specimen in a covered container. This is consistent with the predicted quadratic profile and confirms that heat flow in the wall of the specimen container is not negligible.

Reducing the effective resistance of the specimen gave a small increase in calorimetric sensitivity, but direct effects by radiative heat flux were greater. Sensitivity was increased by covering the specimen with an aluminium plate (of low emissivity), even when this was not in direct thermal contact with the wall of the pan. Exposure of any high emissivity surface on the sample or pan reduced the sensitivity.

3.8.3 Interface propagation in the DSC specimen

The model for propagation of a transition was based on planar interface geometry and the peak shape analysis assumed that the tangential slope at a point on the leading edge of a DSC peak is equal to the effective thermal conductance ($G \equiv 1/R_{tot}$). However, these conditions are not essential to confirm the formation of a second interface at the top surface of the specimen. A relative curvature of the DSC peak onset regions for the open and covered configurations of 4:1 is sufficient to support formation of two interfaces in the latter, provided that:

- both interfaces in the covered specimen, and the single interface in the open specimen, all have the same geometry (but not necessarily planar)
- the resistance of each heat flow path increases by the same amount ($R_s \cdot \Delta z$) for a given increment of interface advance (Δz).

Within experimental error, the relative shapes of the experimental DSC curves were sufficiently close to confirm formation of two interfaces of similar geometry. The second criterion also appeared to be met up to $\alpha \approx 0.4$, but non-linearity of the R/α plots above this point implies a change of interface geometry. It is feasible that planar geometry can only be maintained over a short distance of travel, which

was calculated to be ~ 0.35 mm at α = 0.4 (for a single interface in a tablet 0.87 mm thick).

The planar model is almost certainly overly simplistic, but the shape of the R/α plot and the 4:1 ratio of slopes for one and two interfaces are also compatible with a more complex interface geometry. Specimens formed by compaction of a crystalline powder are not microscopically homogeneous, but consist of well-ordered crystallites separated by regions of plastic deformation. These grain boundaries contain a high density of dislocations, which recrystallise exothermically [58]. At the transition temperature, ordered crystals of the β and γ forms are in equilibrium, and the mobility of the crystal lattice will tend to initiate crystallisation of the amorphous regions. This exothermic recrystallisation to the high temperature (β) form will then propagate along the grain boundaries as a dendritic structure. At some point during this process, and certainly when the boundary regions have been consumed, the transition will expand into the residual grains of un-transformed material. This point, at which the geometry of the advancing interface changes, may correspond to the end of the linear region in the R/α plot. In the case of two interfaces, non-linearity could also be caused by the opposing dendrites impeding each other's growth.

3.8.4 Measurement of thermal conductivity by shape analysis

A consequence of the planar interface model is that the absolute slope of the R_{tot} vs. α plot can be related directly to the thermal resistance of the DSC specimen. Shape analysis of DSC peaks which are distorted by the internal resistance of the specimen itself might therefore be way of measuring thermal conductivity without resorting to fusion of another material. The potassium nitrate specimens used in the open and covered configurations had thicknesses 0.866 and 0.872 mm respectively. The cross sectional areas were both 2.827×10^{-5} m^2. These dimensions were used to calculate values of thermal conductivity from the apparent axial thermal resistances:

$$\lambda_{open} = 0.053 \pm 0.002 \ W \cdot m^{-1} \cdot K^{-1}$$

$$\lambda_{covered} = 0.066 \pm 0.009 \ W \cdot m^{-1} \cdot K^{-1}$$

Reliable literature values of λ for inorganic compounds are rare and none could be found for KNO_3. The most relevant data relating to pressed microcrystalline powders were:

KNO_2 2.1 $W \cdot m^{-1} \cdot K^{-1}$ $Ba(NO_3)_2$ 1.3 $W \cdot m^{-1} \cdot K^{-1}$ (both at 273 K).

Assuming that the behaviour of potassium nitrate is not anomalous, the calculated value of λ value appears to be 1-2 orders of magnitude too low. A potential problem in preparing specimens by compaction of a powder is the inclusion of voids, which would lead to a decrease in thermal conductivity. The pressed pellets had measured densities of 2.071 ± 0.029 $g \cdot cm^{-3}$, compared with a literature value of 2.110 $g \cdot cm^{-3}$ for γ-KNO_3 @ 91°C (calculated from unit cell dimensions). This corresponds to a volume fraction of voids < 3%, which does not account for the observed discrepancy in λ. A more likely explanation is that the interface geometry is complex. The change in resistance for a given increment of α would be much greater for a dendritic structure than for a continuous plane covering an uninterrupted cross section of the specimen. If the slope of the shape analysis plot has any physical significance it is likely to be a geometrical factor related to the path followed by the interface. A high value of slope, which corresponds to a severely curved leading edge on the DSC peak, would then indicate that the advancing interface follows a tortuous path along narrow grain-boundaries. This could be tested by cutting a DSC specimen from a single crystal of potassium nitrate, to give the same geometry as that for the compacted powder. The interface geometry should be much simpler in the mono-crystalline specimen and give a much sharper DSC peak for the γ-β transition.

3.8.5 The effect of anisotropy in the DSC specimen

A subject of long-standing interest in the author's laboratory is the glass transition (T_g) event in thermoset polymers. Many of these are reinforced using glass fibres which are aligned parallel to each other and which lie along a single axis of the composite (to make its mechanical properties anisotropic). The thermal conductivity of these composites is also anisotropic (see section 5.5.1) and experiments were carried out to establish whether the orientation of these fibres within the DSC pan would affect detection of T_g. It was anticipated that axial temperature gradients in the DSC specimen would be reduced

when the relatively conductive fibres were aligned vertically in the pan, rather than lying horizontally. This should reduce the apparent temperature interval over which the glass transition takes place and so increase sensitivity.

This investigation was not successful because, although the step at T_g was detectable for pure polymers, the dilution effect of the glass-fibres reduced the energy change to below the baseline noise level. The change of heat capacity at T_g is very small for thermoset polymers, because only a very limited number of regions in the cross-linked structure have rotational freedom. The proposed DSC experiments are more likely to succeed for reinforced rubbers, which give a much larger T_g step. However, rubber composites are generally reinforced with fabric fibres (for example in tyres) rather than glass. The conductivity of the inclusions is similar to that of the continuous phase, which would make anisotropic effects difficult to detect by DSC.

Table 3.1

Constants derived by fitting of two exponential equations to onset slope data for fusion of indium

Physical form of indium	Number of observations	Mass range of samples /mg	Model*	Constant		
				a	b	c
Powder	28	0.25 - 6.4	1	26.0 ± 1.8	3.54 ± 0.32	1.32 ± 0.58
			2	25.9 ± 1.6	-	1.35 ± 0.31
Foil	44	0.46 - 5.1	1	25.9 ± 1.4	3.84 ± 0.40	1.44 ± 0.50
			2	26.4 ± 1.4	-	1.16 ± 0.23

*Model 1 : Slope = $a - e^{(b-\{c \cdot mass\})}$
*Model 2 : Slope = $a \cdot (1 - e^{\{-c \cdot mass\}})$

Table 3.2

Constants derived by fitting Model 2 to onset slope data obtained using different ΔT amplifier gains

Cell-base amplifier range	Number of observations	Mass range of samples /mg	Constant	
			a	c
x10	88#	0.3 - 16.6	27.8 ± 0.9	1.05 ± 0.12
x1	14	21.2 - 74.2	26.9 ± 1.0	0.17 ± 0.13

#All data in Table 3.1, with additional observations

Table 3.3

Data which were used in the calculation of contact resistances

Configuration of laminates	Number of observations	Mass range of samples /mg	Constant	
			a	c
A(I)/B(I)	102*	0.3 - 74.2	27.4 ± 0.7	1.06 ± 0.11
B(II)	12	16.6 - 65.1	15.8 ± 0.7	0.25 ± 0.40
B(III)	15	21.9 - 70.1	15.0 ± 0.8	0.17 ± 0.17

*All data in Table 3.2, with additional observations

Table 3.4

Data which were used in the calculation of matrix resistances

Configuration of laminates	Number of observations	Mass range of samples /mg	Constant	
			a	c
A(II)	27	1.0 - 16.6	23.9 ± 1.5	0.41 ± 0.09
A(III)	49	0.8 - 16.9	20.5 ± 0.6	0.42 ± 0.05
A(IV) (polished lid)	22	1.4 - 17.6	22.1 ± 0.9	0.76 ± 0.22
A(IV) (black lid)	28	3.4 - 19.4	21.7 ± 0.7	0.26 ± 0.02

Table 3.5

Measured and calculated matrix resistances for indium/silica laminates

Laminate configuration	R_{matrix} /K·W^{-1}	
	Measured resistances*	Calculated resistances#
A(II)	6.0 ± 2.7	8.1 ± 1.4
A(III)	13.0 ± 0.9	10.5 ± 1.8
A(IV) (polished lid)	9.4 ± 1.1	7.9 ± 1.0
A(IV) (black lid)	10.1 ± 0.9	7.9 ± 1.0

*Calculated from $R_{matrix} = R_{tot} - R_c$(con/al)

#Calculated from system dimensions

Table 3.6

Lag of extrapolated onset temperature for fusion of indium in laminates

(component attributable to R_{matrix})

Configuration of laminates	Number of observations	Confidence interval of onset lag /K
A(II)	27*	0.75 ± 0.06
A(III)	47*	0.50 ± 0.05
A(IV) (polished lid)	22*	0.72 ± 0.06
A(IV) (black lid)	23*	0.67 ± 0.07
B(II)	12#	0.44 ± 0.05
B(III)	14#	0.49 ± 0.04

*18 reference observations: Amp. range = x10

#10 reference observations: Amp. range = x1

Table 3.7

Calorimetric results for fusion of indium in all laminate configurations

(raw data, with no correction for instrumental sensitivity)

Configuration of laminates	Number of observations	Mean specific area /J·g^{-1}	Relative calorimetric sensitivity /%
A(I)	78*	25.12 ± 0.05	(Reference = 100%)
A(II)	16*	24.64 ± 0.08	98.1 ± 0.2
A(III)	38*	24.41 ± 0.09	97.2 ± 0.2
A(IV) (polished lid)	11*	24.48 ± 0.11	97.5 ± 0.2
A(IV) (black lid)	17*	23.45 ± 0.11	93.4 ± 0.2
B(I)	14#	25.56 ± 0.10	(Reference = 100%)
B(II)	12#	24.78 ± 0.11	97.0 ± 0.4
B(III)	14#	23.32 ± 0.12	91.2 ± 0.4

*Data below amplifier saturation limit: Amp. range = x10

#Mass range 20-70 mg: Amp. range = x1

Table 3.8

Calorimetric results for the phase transition (γ–β) in potassium nitrate

Specimen thickness /mm	$\Delta H_{p.t.}$ /J•g^{-1}		Relative $\Delta H_{p.t.}$
	Open	Covered	[covered/open]
0.20	49.5	50.9	1.028
0.44	47.1	48.5	1.030
0.62	48.5	49.5	1.021
0.87	48.4	50.5	1.043
1.72	46.8	48.4#	1.034
1.68	44.1*	45.5*#	1.032

All measured in Du Pont aluminium pan/lid except:

*Perkin-Elmer steel pan

#Perkin-Elmer aluminium lid

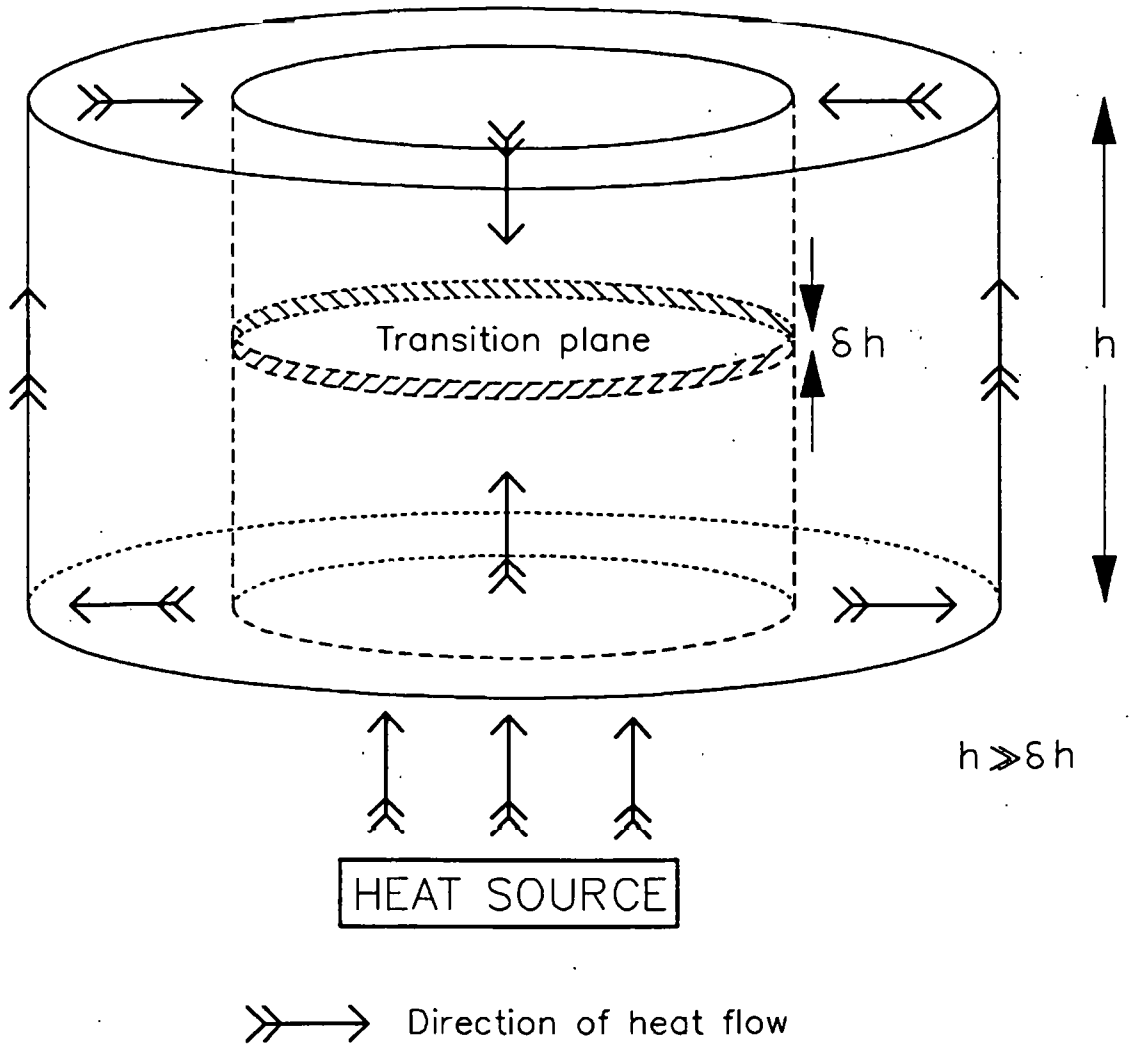

Figure 3.1 – Heat flow paths in the model for a localised endothermic transition in a resistive matrix.

(a) Heat flow paths in the DSC

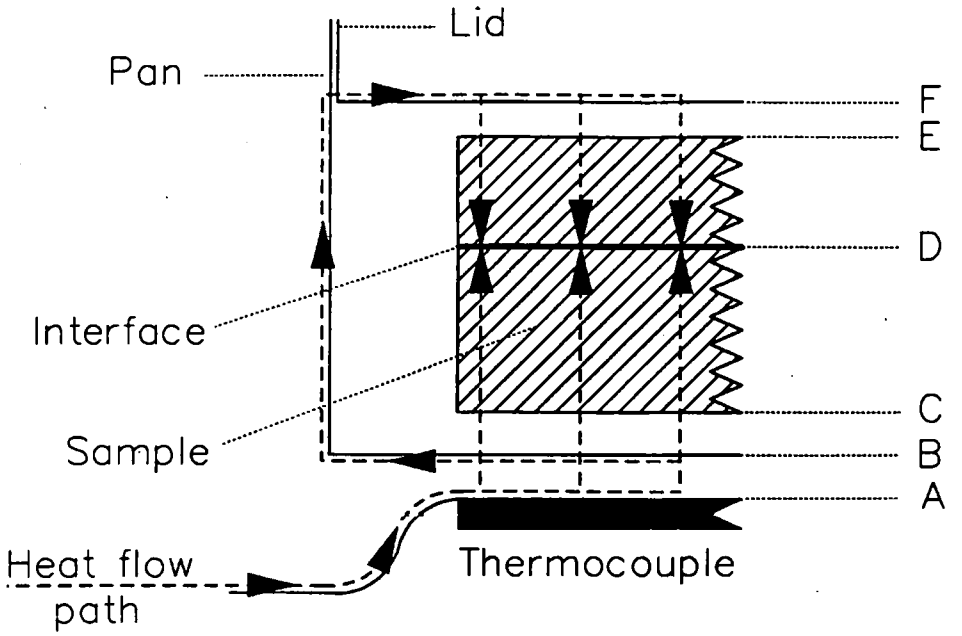

(b) Analogous electrical circuit

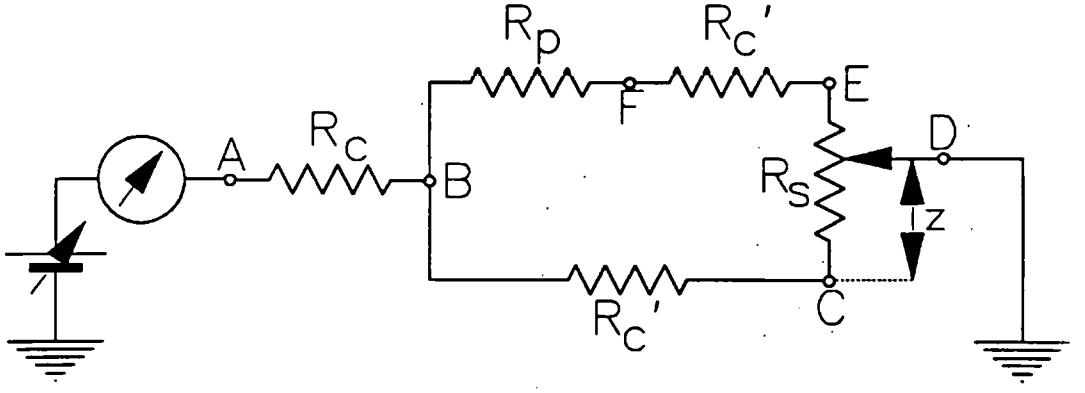

Figure 3.2 – Laminate model for a single interface.
(resistances refer to equations in the text)

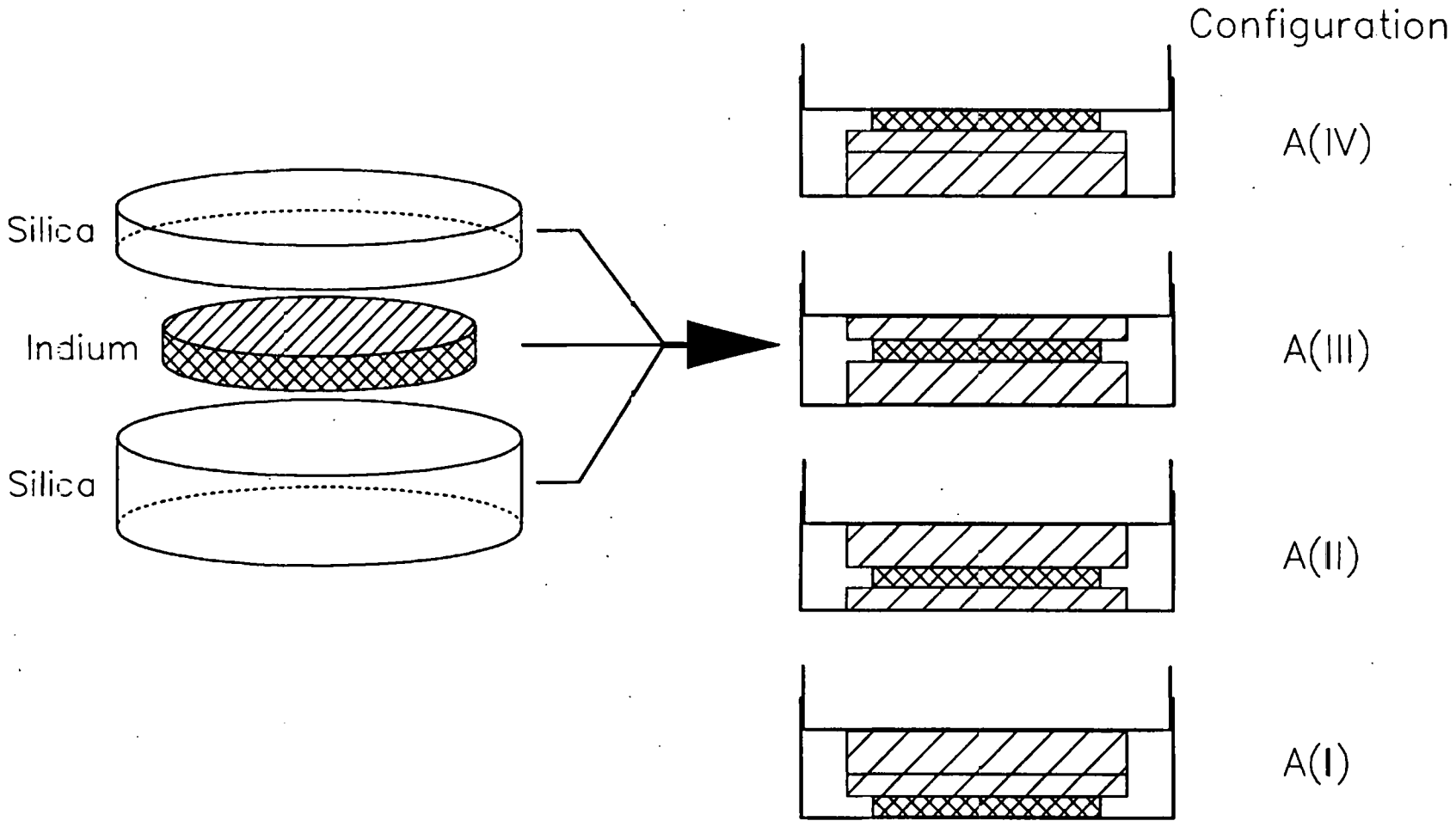

Figure 3.3 – Construction of the indium/silica laminates.

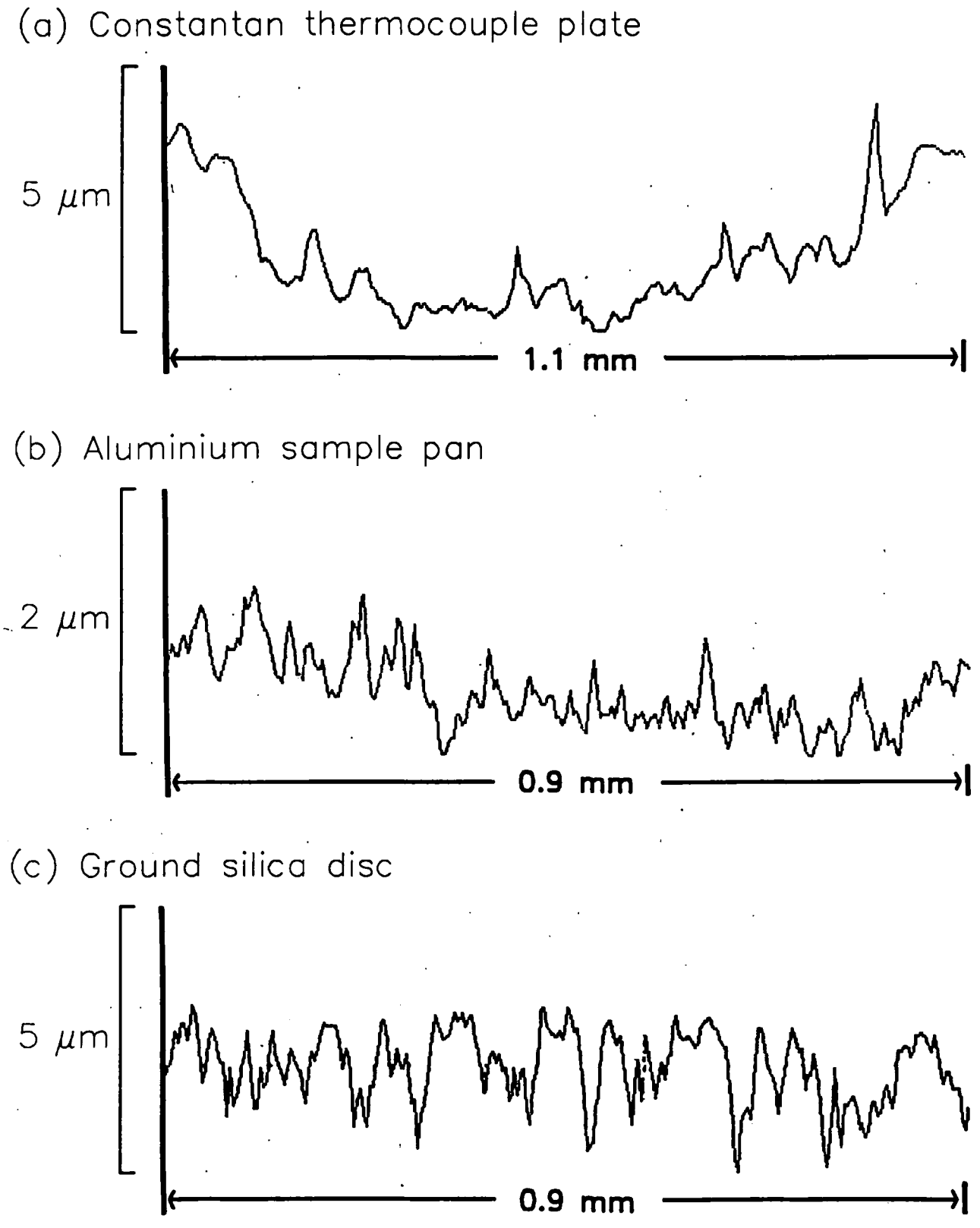

Figure 3.4 – Short range profiles of contacting surfaces in the laminates.
(plotted from 'Form–Talysurf' data)

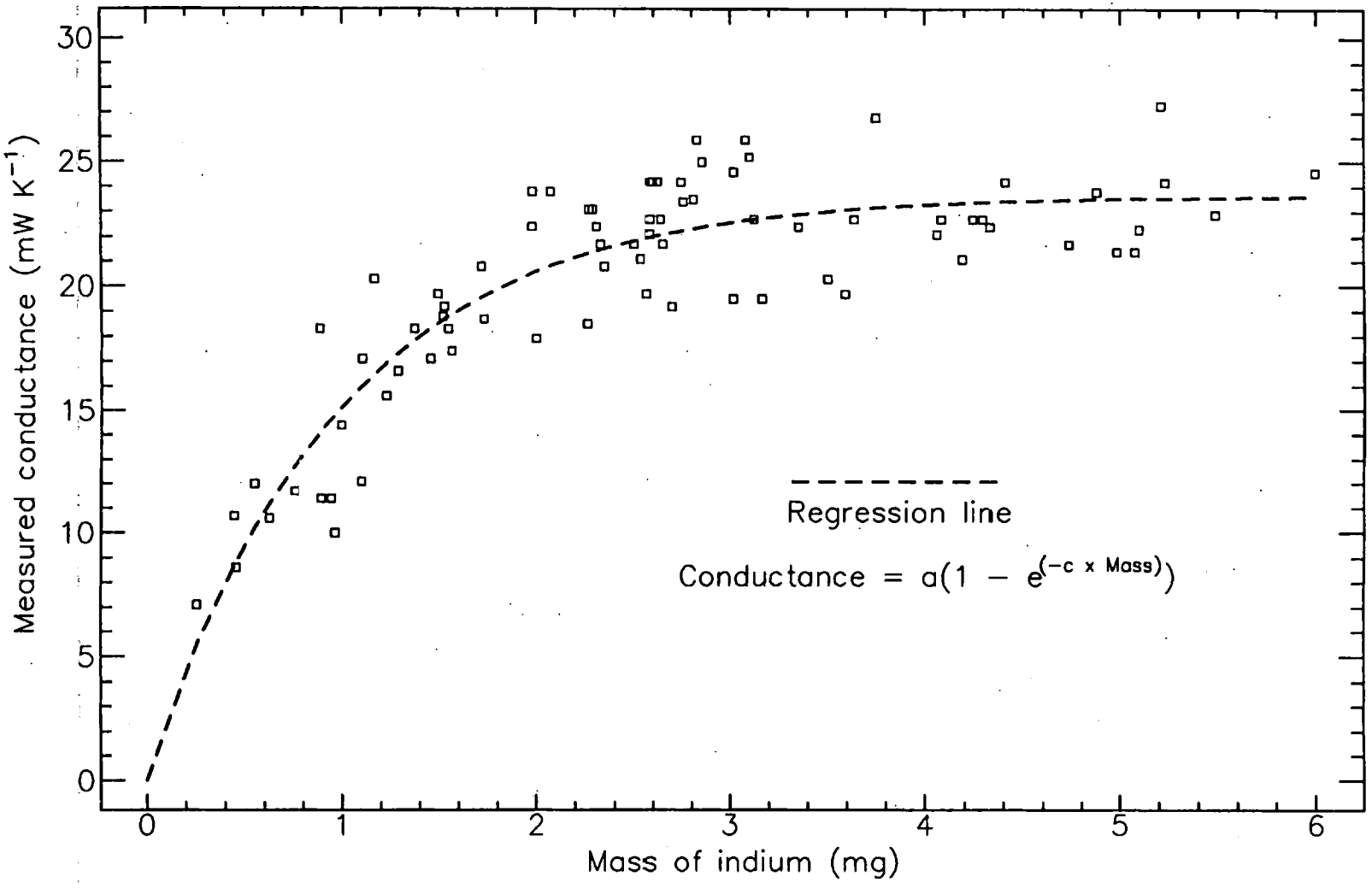

Figure 3.5 – Relationship between sample mass and DSC onset slope (thermal conductance) for fusion of indium.

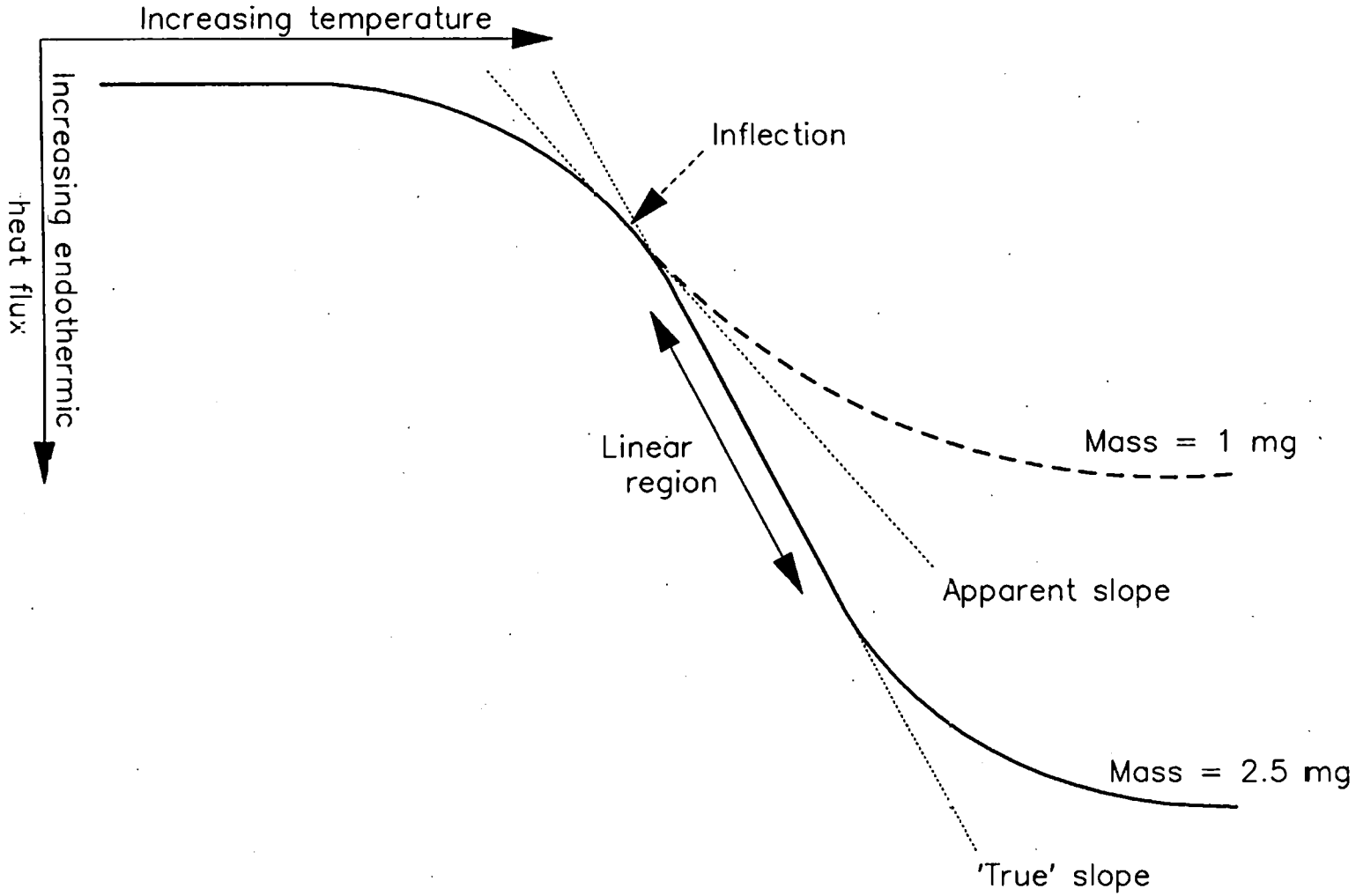

Figure 3.6 – Effect of sample mass on the shape of the DSC peak onset. (fusion endotherm for indium)

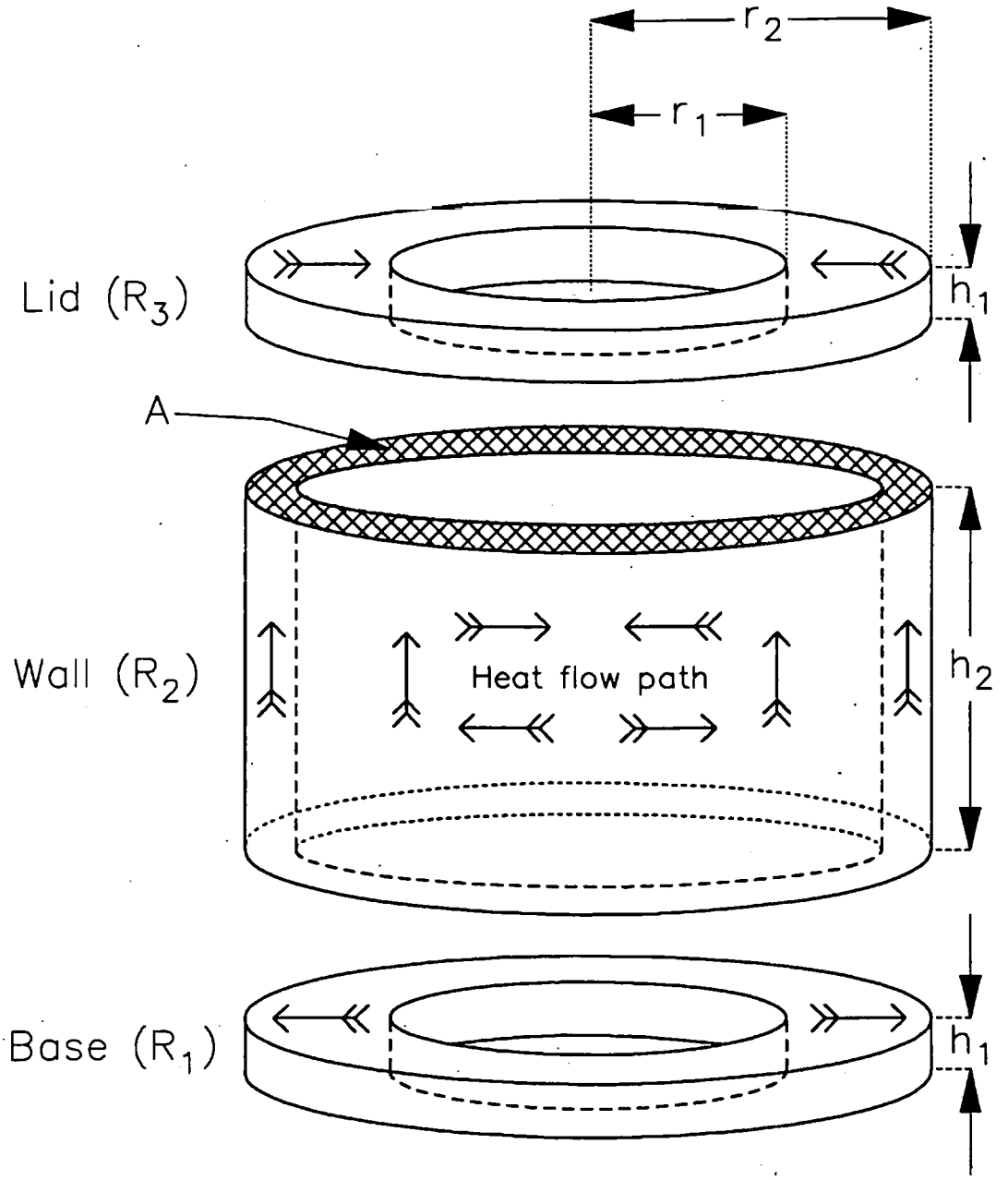

$$R_p = R_1 + R_2 + R_3$$

Figure 3.7 – Resistive elements and dimensions of the pan/lid conduction path.

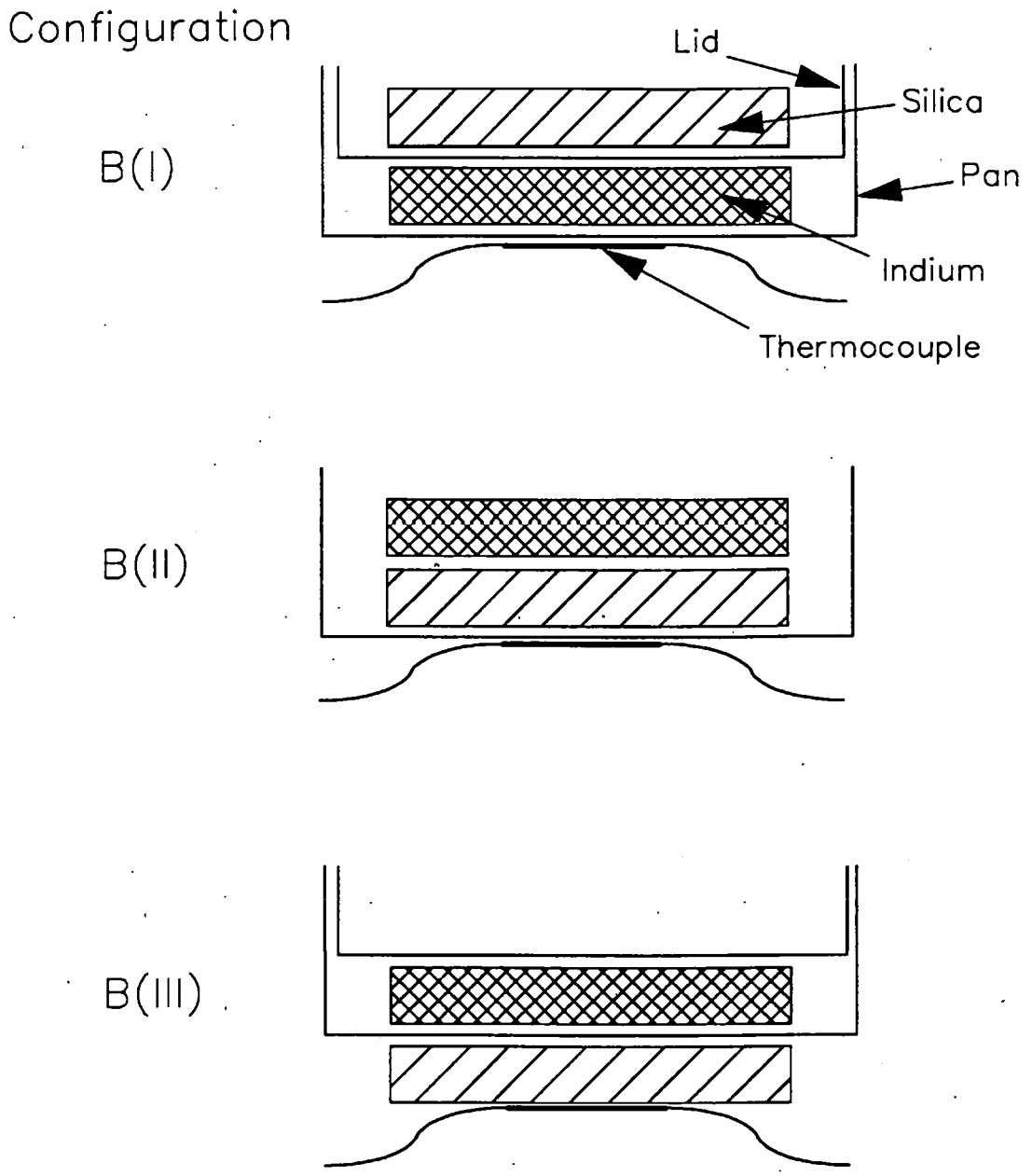

Figure 3.8 – Experimental configurations used for measurement of contact resistances.

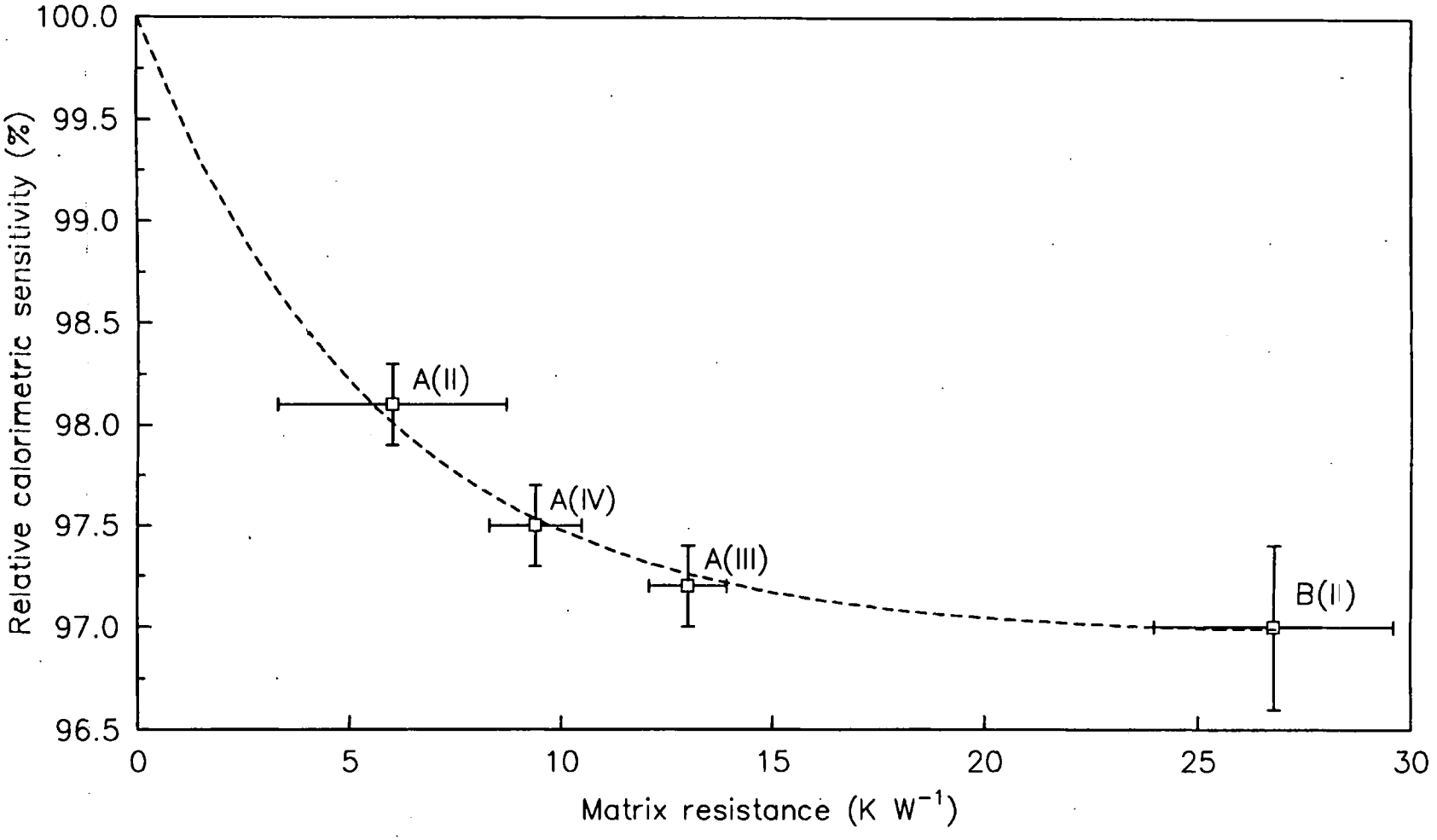

Figure 3.9 – Effect of matrix resistance on calorimetric sensitivity for fusion of indium in laminates with silica.

(error bars are 95% confidence intervals for differences relative to A(I)/B(I) as reference)

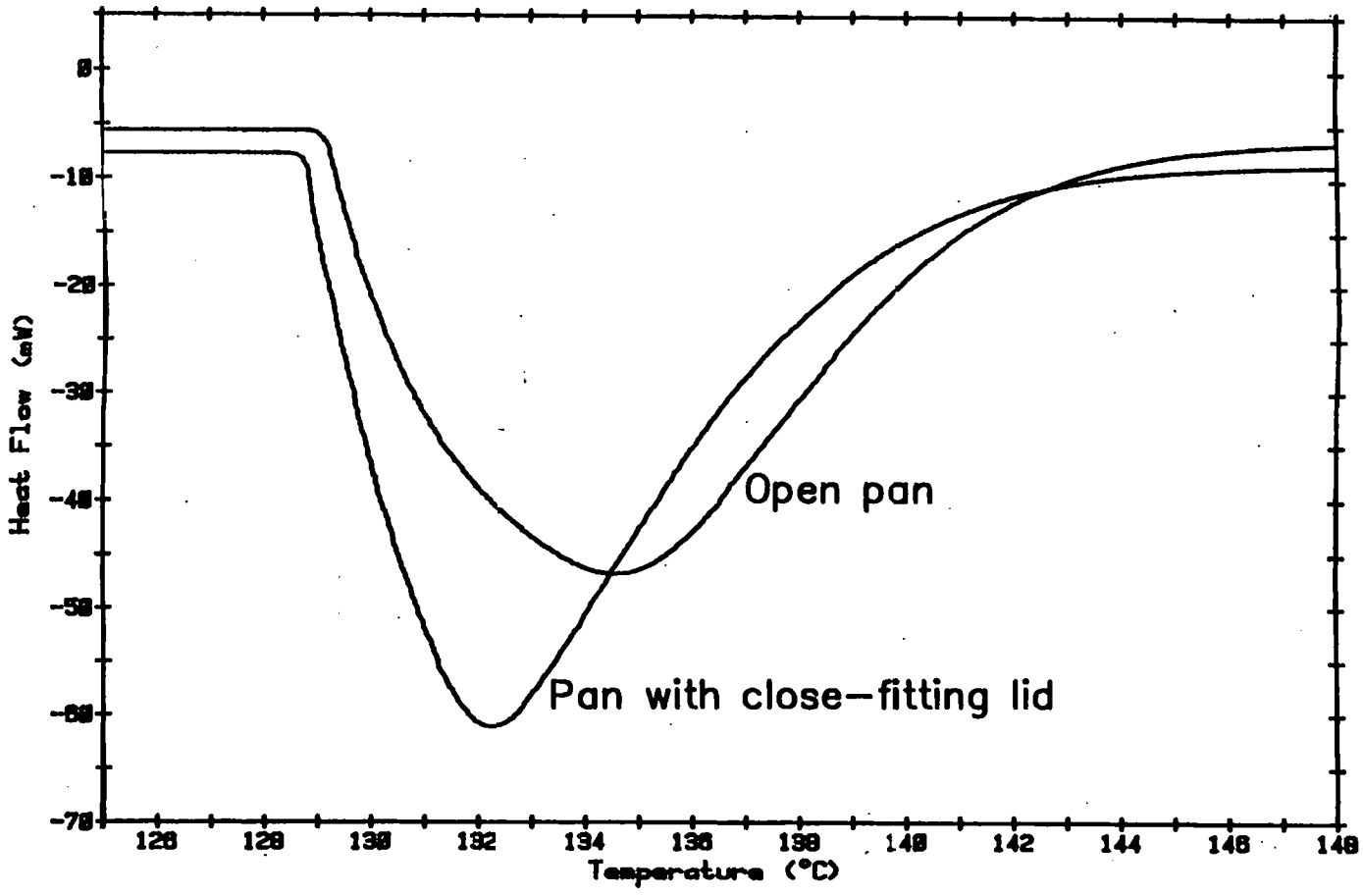

Figure 3.10 – DSC peaks for the polymorphic transition in potassium nitrate showing the effect of sample pan configuration.

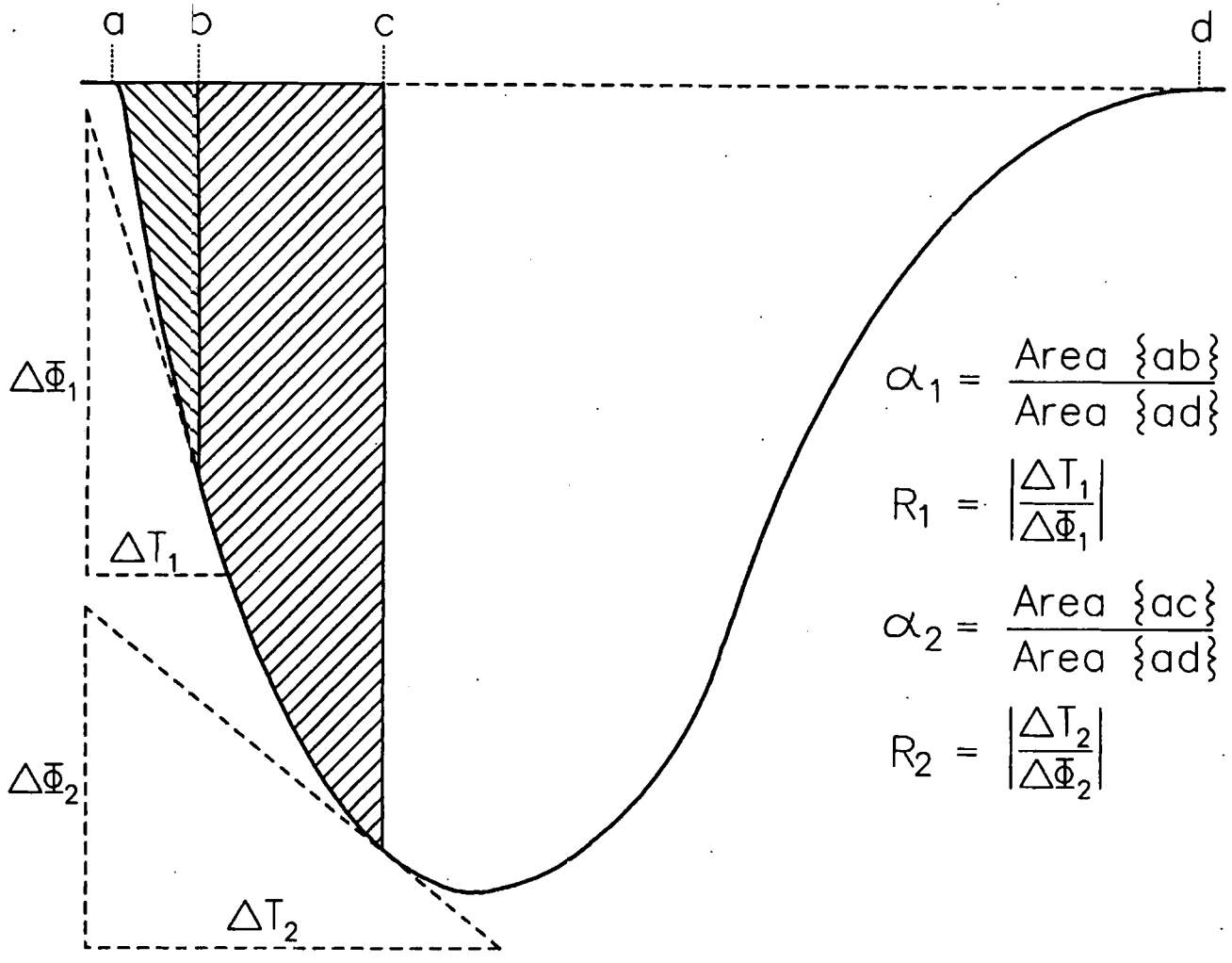

Figure 3.11 – Construction used for shape analysis of the leading edge of a distorted DSC peak.

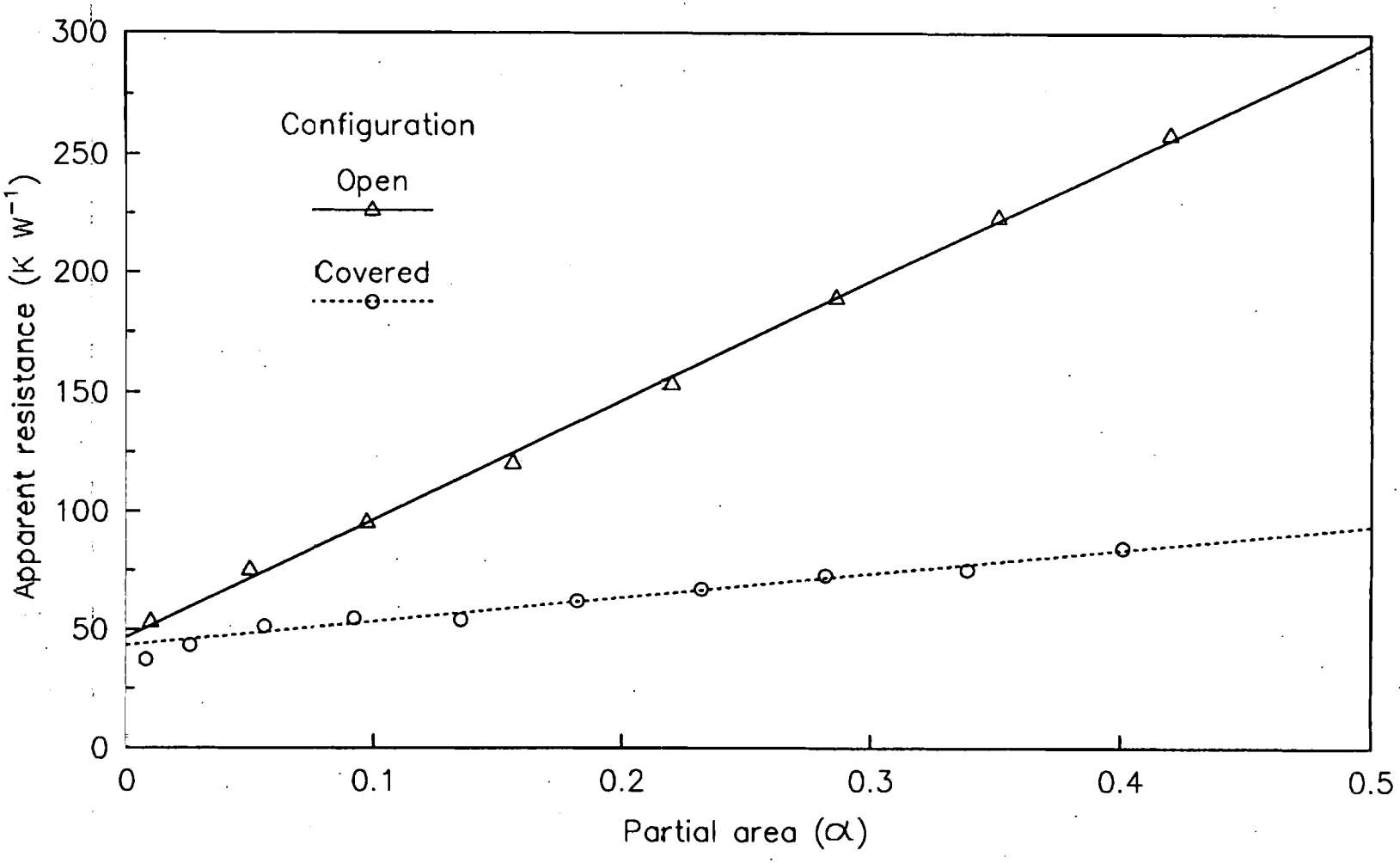

Figure 3.12 – Shape analysis plots for the polymorphic transition in a 50 mg pellet of potassium nitrate.

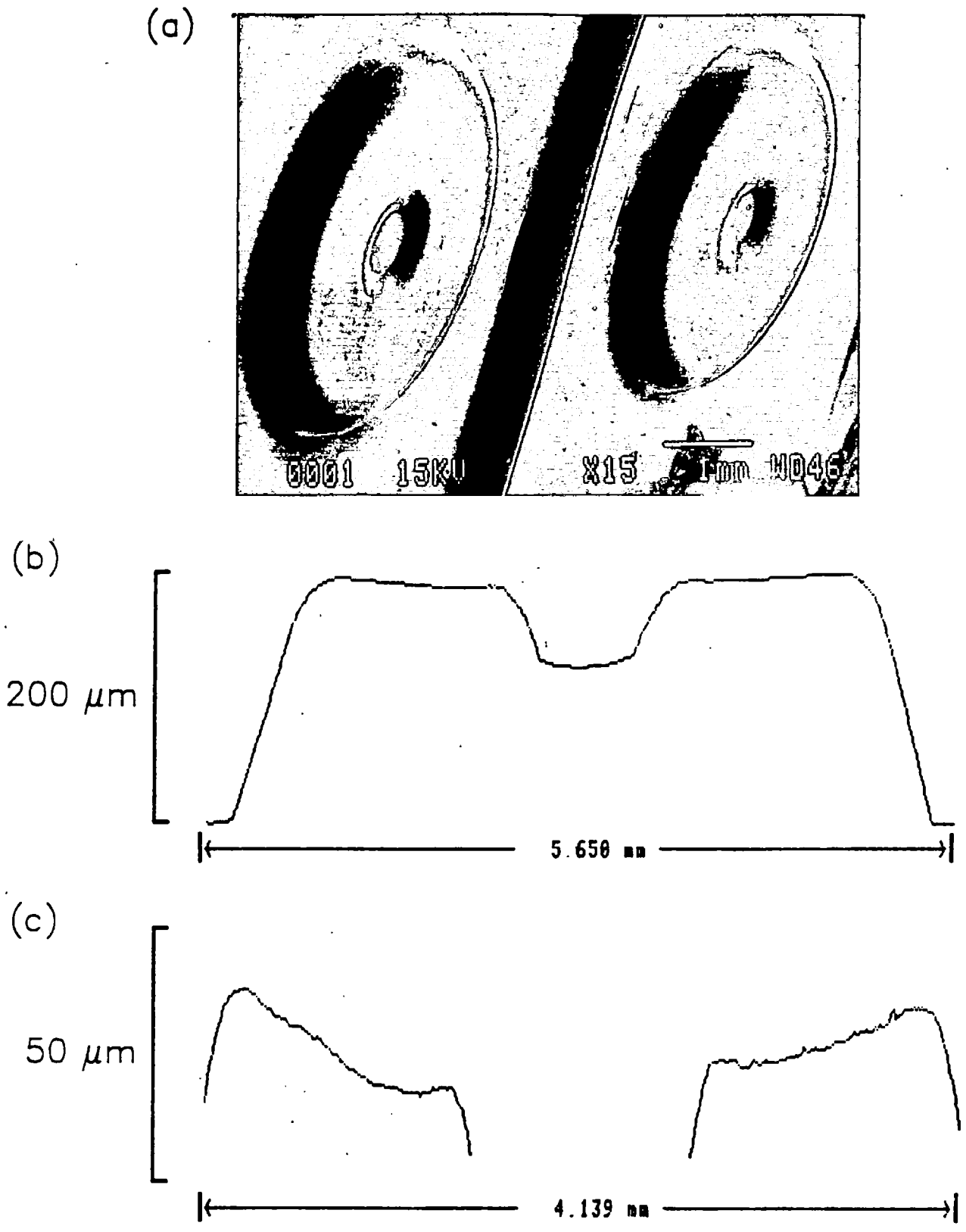

PLATE 2 – Du Pont 910 DSC thermocouple plate

(a) Scanning electron micrograph showing the sample and reference platforms.
(b) Profile across the sample platform.
(c) Profile across the contact area of the sample platform.

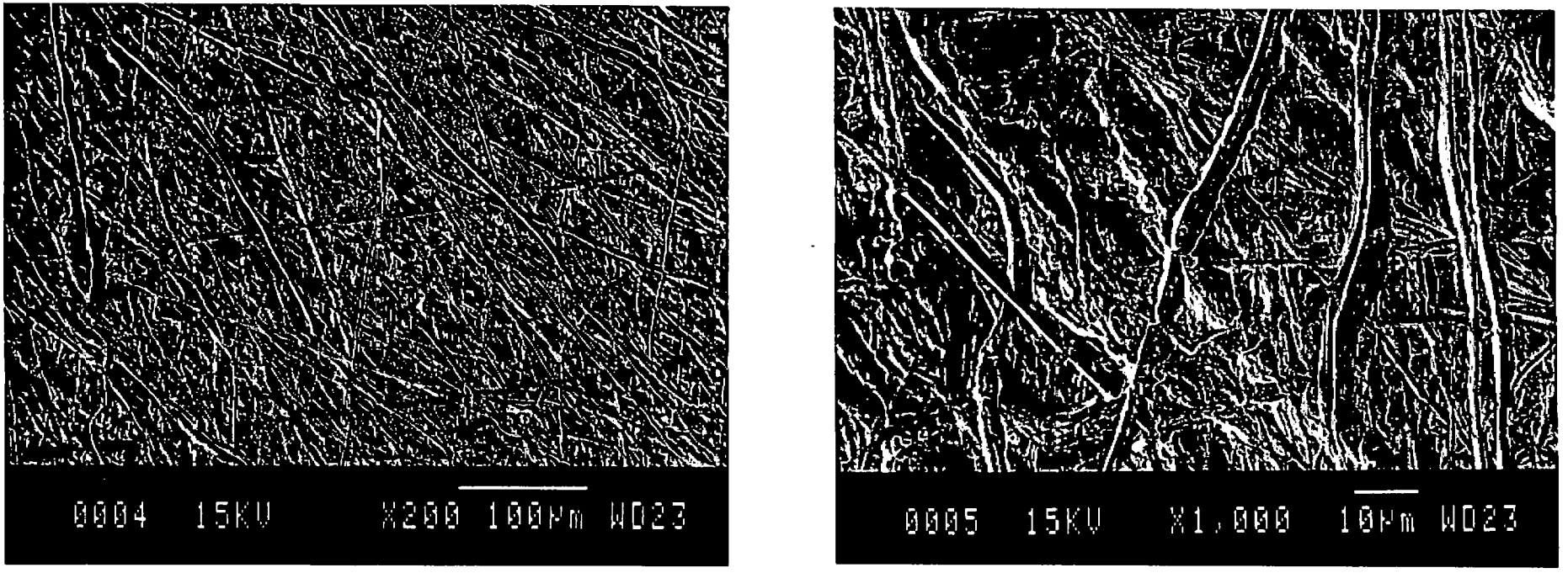

PLATE 3 — Scanning electron micrographs showing scoring on the surface of the constantan thermocouple plate.

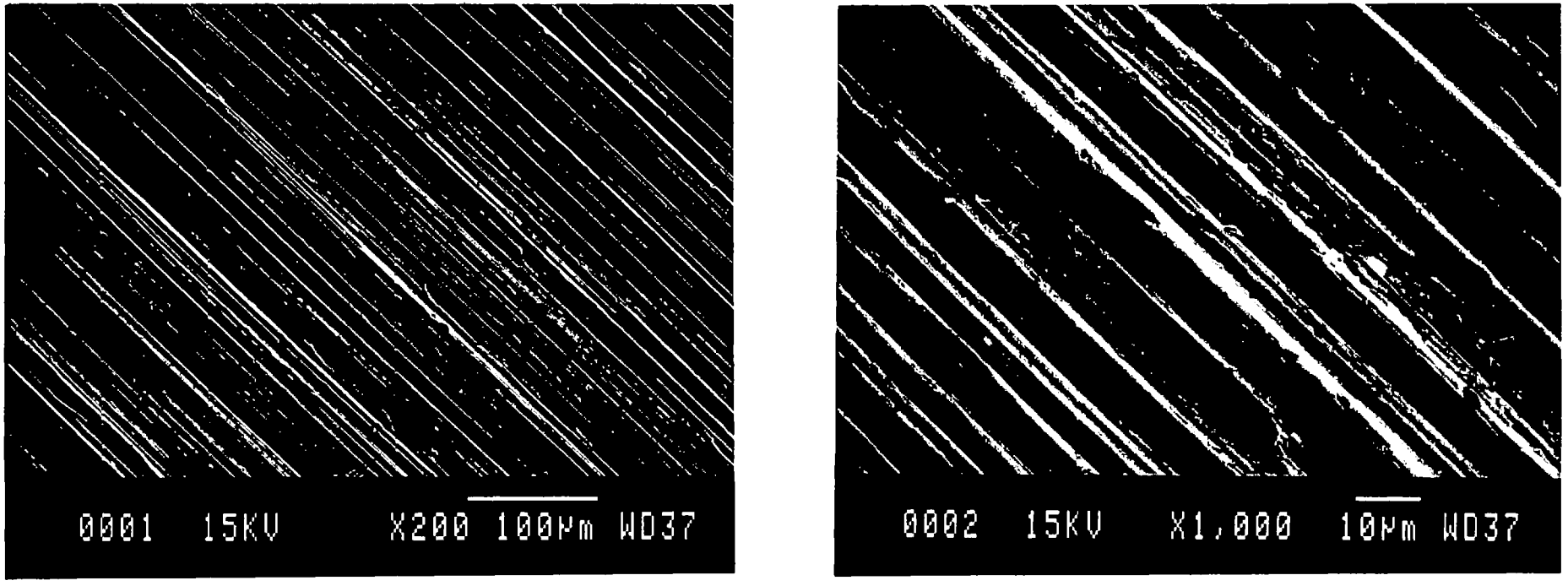

PLATE 4 — Scanning electron micrographs of an aluminium DSC pan, showing the anisotropic surface finish.

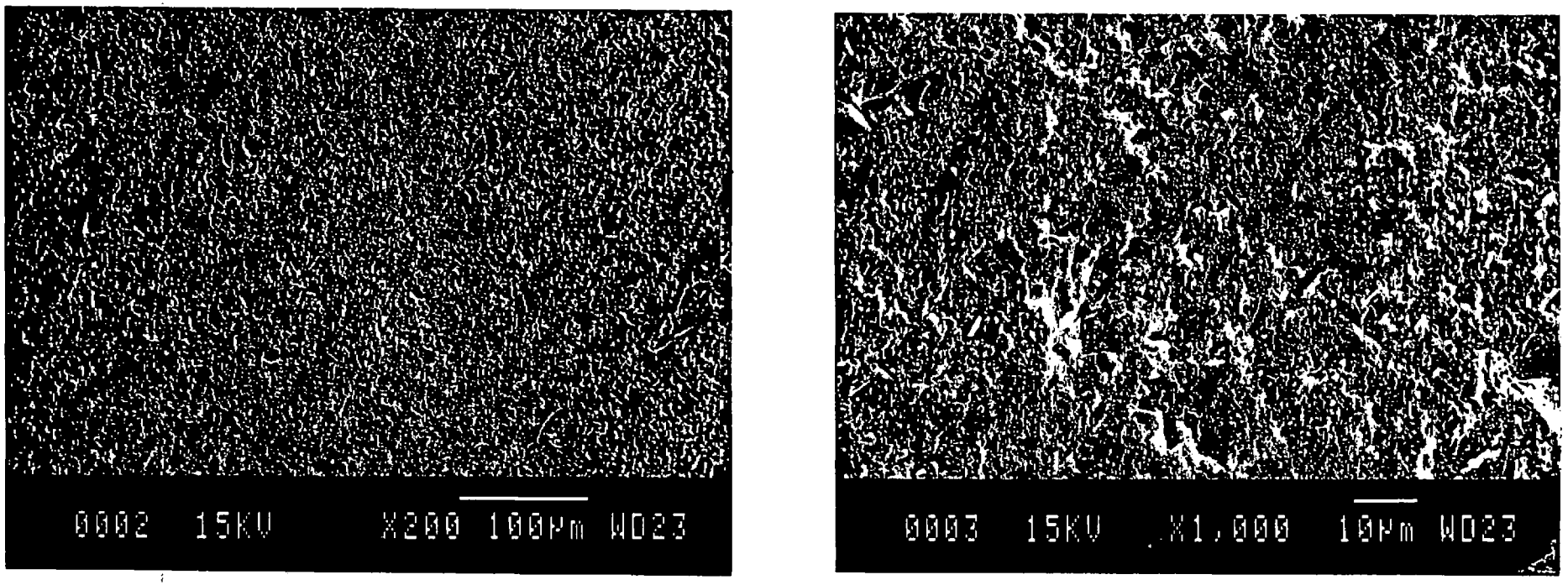

PLATE 5 — Scanning electron micrographs of a ground silica disc, showing the randomly pitted surface.

CHAPTER 4

INVESTIGATION OF MATRIX EFFECTS FOR AN EXOTHERMIC EVENT

4.1 INTRODUCTION

The work described in the previous chapter showed that detection of endothermic events was influenced by the internal thermal resistance of the specimen. This in turn was shown to depend on coupling between the specimen and its container, i.e. the 'matrix resistance' of the transportable DSC specimen. The following study was intended to give a complementary picture of how detection of an exothermic process is affected by changes of sample resistance and containment in the DSC. O'Neill carried out an experimental study using a Perkin-Elmer power compensation DSC [59], which showed that calorimetric sensitivity to endothermic and exothermic processes was identical. It was also demonstrated that varying the coupling resistance (= R_c) did not affect sensitivity. The event studied was crystallisation of a molten metal on cooling, which O'Neill claimed was sufficient to demonstrate the accuracy of this DSC for all exothermic processes. Dötsch and Fink [60] used a Du Pont DSC to study reactions occurring in large (~ 4 mm high) catalyst pellets. They found that increasing sample resistance caused a reduction of sensitivity to an exothermic reaction, which was attributed to the parasitic component of heat flux. This observation was consistent with the work described in Chapter 3 and suggested that matrix effects will be important when the Du Pont system is used to study exothermic interactions. Two factors precluded use of the previous results to infer a relationship between matrix resistance and DSC response for exothermic events:

(i) During a rising temperature programme the temperature of the DSC sample lags behind that of its associated thermocouple. This lag will increase during an endothermic event but the direction of all heat flows in the calorimeter remains the same. Conversely, as the rate of an exothermic reaction increases, the temperature lag will diminish and eventually become an increasing lead of the sample temperature over that of its thermocouple. Some heat flows in the system will then be reversed, including the measured flux across the ΔT thermocouple-pair and the inferred flux via other conduction paths in the constantan plate surrounding the sample thermocouple. If the temperature rise in the sample is sufficiently large, the parasitic flux through the atmosphere in the sample chamber may also be

reversed. The sensitivity of the DSC cell is determined by the ratio between the measured flux and all other routes of heat transport to or from the specimen. Thus a strongly exothermic event may change this sensitivity during the peak interval and hence distort the DSC curve.

(ii) Endothermic events are often reversible and, for a physical equilibrium process such as fusion, the rate of transformation is proportional to the heat flux into the sample. Exothermic events in the heating mode tend to be spontaneous and irreversible. Although the rate of reaction will be affected by the external temperature (i.e. that of the calorimeter) the critical factors are the instantaneous sample temperature and the proportion of the sample which has already reacted. The effect of altering resistance on the shapes of endothermic and exothermic peaks would therefore be expected to be different.

It is relatively easy to predict the effect of thermal resistance on an equilibrium process using simple heat flow theory, but the response of a complex self-propagating reaction is far more difficult to assess. A general model describing all types of exothermic event would be speculative and therefore difficult to validate using a single set of exothermic data in isolation. Hence an experimental approach was adopted in which the DSC response to endothermic and to exothermic events was compared over a range of thermal resistance in order to identify differences from the previously established endothermic model.

The choice of sample materials for this investigation was limited because, by definition, any material undergoing an exothermic reaction is thermodynamically unstable and consequently there are no well-characterised 'standards'. Chemical reactions such as oxidation or decomposition generally involve absorption or evolution of gas. This would complicate the experiment because a facile route for gas-exchange would have to be provided. Furthermore, mass transport into or out of the specimen would affect both the rate of reaction and the contact resistances. Amorphous metallic alloys are metastable and crystallise exothermically on heating. Many are stable at room temperature and hence their properties do not change over the duration

of a series of DSC experiments. The amorphous alloy used in this study was the same as that used to investigate the effects of amplifier saturation as described in Chapter 2.

4.2 PROPERTIES OF GLASSY SOLIDS

It would have been possible to utilise crystallisation of an amorphous alloy as a model exothermic event without discussing the structure of these novel materials, or their mechanism of crystallisation. This was felt to be undesirable because conclusions based on a single material may not be applicable to a different type of exothermic process. Some background information was therefore required so as to keep the observations in context and to help in assessing their broader applicability. This topic proved difficult to summarise briefly and hence this section has been included as a somewhat lengthy aside, even though it is not essential to the rest of the thesis.

4.2.1 Preparation and structure of amorphous alloys

Amorphous metallic alloys are most commonly prepared by directing a jet of molten alloy at the periphery of a rotating metal wheel. The melt solidifies on contact with the cold metal surface and the motion of the wheel then causes the solid to spin off as a continuous ribbon - a process known as 'melt-spinning' [61]. The cooling rate during solidification is $> 10^6$ $K \cdot s^{-1}$, which is so rapid that crystallisation nuclei do not have time to form. The structure which is frozen into the solid phase is similar but not identical to that of the liquid metal, hence the term 'metallic glass'.

The most common alloys which have been used to prepare glasses consist of a transition metal with about 15-25 atomic % of a metalloid such as B, C, P or Sb (commonly called T-m glasses). Many glass-forming combinations of late transition metals (Fe, Co, Ni, Pd, Cu) with early transition metals (Ti, Zr, Nb, Ta, Hf) also exist. Commercial interest is encouraging research into lightweight amorphous alloys based on the group IIa metals (Mg, Ca and Sr).

Strictly speaking, the term 'amorphous' is misleading because even liquids have some structural order, even though it may only extend over a distance of a few atomic diameters. The distinction between amorphous and crystalline character in solids frequently depends on the spatial resolution of the analytical technique being used. X-ray diffraction (XRD) is the most commonly used technique for detecting and identifying crystalline structure. Diffraction peaks produced by a powder become broader as the size of the crystallites decreases, making the image progressively more diffuse. A similar effect is found as the degree of disorder in larger crystals increases, as a result of heating or irradiation. The XRD patterns produced by the two cases become indistinguishable when the dimensions of the regular domains are ~ 5 nm [62]. Non-crystalline metallic alloys produced by melt-spinning contain short range atomic order which extends over ~ 1 nm and therefore appear to be amorphous by XRD.

The structure of metallic glasses has been investigated by various techniques [61,63] including: diffraction of monochromatic X-rays, electrons and neutrons; Mössbauer and nuclear quadrupole resonance spectroscopies; extended X-ray absorption fine structure (EXAFS) and transmission electron microscopy. Agreement has not yet been reached on a single model to describe the overall structure, but various short range features have been identified:
(i) Metalloid atoms in T-m glasses very rarely occur as nearest neighbours, but predominantly as second nearest neighbours. This is termed 'compositional (or chemical) short range order' (CSRO).
(ii) Metal-metal glasses rarely display CSRO - the two types of atom tend to be randomly distributed.
(iii) T-m glasses all show a coordination number ~ 8.9 for the metalloid. Coordination around the metalloid atoms is not totally random.

The first widely accepted description of the structure of metallic glasses [64] was based on Bernal's model for liquid metals [65]. This assumed that the metal atoms are arrayed in a manner which is essentially random and homogeneous, as predicted by dense random packing of hard spheres (DRPHS). The array of metal atoms will contain interstitial vacancies ('Bernal voids', Figure 4.1a) which have a

greater range of size and more diverse geometries than those in a regular crystalline lattice. Metalloid atoms were assumed to fit in whichever voids had the correct dimensions to accommodate them. The DRPHS model fails for alloys with a high metalloid content because it predicts too few Bernal voids of sufficient size to accommodate all of the guest atoms. Coordination number of the metalloid should also vary in the range 7.5-9, depending on the radius ratio of the elements, rather than being virtually constant at ~ 8.9. Both of these limitations were attributed to the assumption of a fixed radius ratio for a given pair of elements. Relaxation of the hard-sphere model to allow the radius ratio to vary according to the local coordination geometry gave better agreement with experimental data. This formed the basis of the 'DRPSS' (soft-sphere) model [66,67].

An alternative approach considered that the coordination around each metalloid atom was not random but adopted the preferred configuration for that pair of elements as found in the crystalline state. This model was initially developed for Pd-Si glass [68] but was later shown to provide a more widely applicable description of the structures of T-m glasses than did DRP [69]. Data for a series of Ni-B glasses [70] supported a geometry consisting of a trigonal prism, with the three rectangular faces capped by metal atoms (Figure 4.1b). This gives the required 9-fold coordination and may well be the local structure in other T-m glasses. The arrangement of these 'unit cells' would be random in the glass (Figure 4.1c) and any relationship between them would depend on the stoichiometry of the mixture.

4.2.2 Thermal de-vitrification of glasses

Phase reactions

An important consequence of glasses having structure, rather than being truly amorphous, is that a given atomic composition may give rise to various metastable configurations. This allows the possibility of relaxation from a stressed state (similar to that induced by cold working of metals) into a glass, or between discrete glassy states. Evidence for the existence of various forms of ordering in the supposedly random glass came from Egami's measurements of the bulk density [71] and Curie temperature [72] of ferrous alloys. It was

found that both of these properties could be reversibly cycled between fixed values by annealing under a cyclic temperature programme. Egami ascribed this behaviour to transition between metastable structures which differed in their enclosed free-volume (i.e. the void space). These results further supported the idea that the metal atoms are not packed in a random manner but have local order - a feature summarised by Egami as 'topological short range order' (TSRO).

Phase separation can result in coexistence of crystalline and glassy phases before bulk crystallisation occurs. Thus a series of phase reactions may occur, for example:

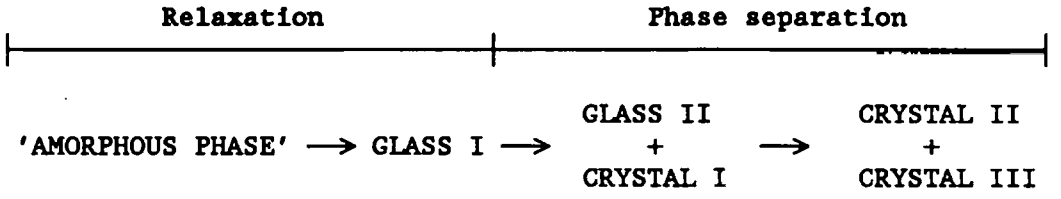

One of the most extensively studied metallic glasses is $Fe_{80}B_{20}$ which, in spite of its simple composition, undergoes several transformations during annealing and crystallisation. Initial phases formed are a metastable tetragonal form of Fe_3B along with a supersaturated solid solution of boron in α-Fe. The tetragonal boride then transforms to the more stable orthorhombic form before crystallisation of the final equilibrium phases (α-Fe + Fe_2B) takes place. The mechanism proposed by Duhaj and Hanic [73] for this series of events illustrates the close relationship between amorphous and crystalline structures. Their results indicated that a common structural unit is present in all the phases, consisting of two boron atoms bridged by a pair of iron atoms. This means that nucleation and crystallisation do not require diffusion of boron over long ranges. Only small displacements of the existing structural units are required. A general description of the type of localised atomic motion required to convert the glassy state into a crystal was proposed much earlier, by Cohen and Turnbull [74] (Figure 4.2). They proposed that the central (interstitial) atom is surrounded by a 'free volume' resulting from the difference between its atomic volume and the internal volume of the cage formed by its nearest neighbours. Oscillation of this cage may cause the free volume to exceed a critical value, allowing the central atom to shift. When

the cage re-collapses into a regular (crystalline) array, a different set of neighbours surround the central atom. This means that short range diffusion has occurred. Köster and Herold [75] rationalised the various modes of crystallisation and the role of diffusion in each. For alloys in the Fe-B system they described local reordering with short-range diffusion as 'polymorphous crystallisation'. This occurs when the atomic compositions of the glass and crystalline product are identical as in the exothermic transformation:

$$Fe_{75}B_{25}\{glass\} \rightarrow Fe_3B\{crystal\}$$

Medium-range diffusion was proposed for the initial 'eutectic crystallisation' of glassy $Fe_{80}B_{20}$ into crystalline α-Fe + Fe_3B. Long-range diffusion is required for the 'primary crystallisation' of α-Fe from an iron-rich glass such as $Fe_{86}B_{14}$.

Kinetics

The early stages of crystallisation of a glass are usually controlled by the rate at which nuclei are formed. In a heterogeneous solid, only a limited number of sites have the potential for nucleus formation and these will decrease with time as they are either converted into true nuclei or consumed by the advancing interface. Various local structures will have different tendencies to react and therefore the 'activation energy' for nucleation will vary. The glassy state is considered to be essentially homogeneous and hence nucleation in a particular alloy may be expected to have a single activation energy (or at least a limited range). Nucleation kinetics have been studied by optical methods [76] and found to have activation energies of the order 740 $kJ \cdot mol^{-1}$ (for a commercial ferrous alloy - Metglas 2826). Not all nuclei which are formed are actually viable and some may revert back to their glassy state. This occurs when crystallisation is accompanied by a change of surface free energy, which leads to strain at the interface between the nucleus and surrounding glass. Depending on the magnitude of this free energy change, the nucleus will have a critical size below which it can revert to its initial state [77].

When a stable nucleus has been formed, the phase transformation propagates out into the bulk of the specimen. These processes may be concerted or separated by an induction period during which some form of pre-crystallisation reordering takes place. Both nucleation and

growth in metallic glasses have been described [78] by the Johnson-Mehl-Avrami equation:

$$\alpha(t) = 1 - \exp[-k(T) \cdot t^n] \qquad \ldots(4.1)$$

where: $\alpha(t)$ = fraction converted at *reduced* time t
(t is corrected for the induction period).
$k(T)$ = specific rate constant (s^{-1}) at temperature T.

The exponent 'n' is related to the product crystal morphology and is sometimes identified as the 'geometric factor'. It is important to note that the 'order of reaction' (also denoted by an exponent 'n'), as used in homogeneous kinetics, has no significance in solid state reactions. The 'molecularity' expression in the overall rate equation is replaced by one related to a change of nucleation rate or to the geometry of the reaction interface.

i.e. n = 1; uni-directional growth (needles), nucleation not rate determining.
n = 2; two-dimensional growth (plates), or constant rate of nucleation followed by one-dimensional growth.
n = 3; three-dimensional growth, or constant rate of nucleation followed by two-dimensional growth.

In calculating the activation energy for nucleation or crystallisation the rate is generally assumed to have an exponential temperature dependence (see next section). This approach gives typical values - 200-250 $kJ \cdot mol^{-1}$ for the activation energy of crystallisation in ferrous glasses such as $Fe_{80}B_{20}$ [76].

4.3 KINETIC ANALYSIS OF DSC DATA

4.3.1 Borchardt and Daniels' treatment

One of the most widely used treatments for the kinetic analysis of DSC data is that due to Borchardt and Daniels [79]. This was developed for a special type of differential thermal analysis (DTA) experiment which was used to study reactions occurring in solution. It was based on the Arrhenius equation, which describes the temperature dependence of reaction rate in terms of an exponential relationship of the form:

$$k(T) = Z \cdot \exp(-E/R \cdot T) \qquad \ldots(4.2)$$

where: $k(T)$ = specific rate constant (s^{-1}) at temperature T

Z = Arrhenius frequency factor (s^{-1})

E = activation energy ($J \cdot mol^{-1}$)

R = gas constant (8.314 $J \cdot mol^{-1} \cdot K^{-1}$)

The reaction kinetics were also assumed to be influenced by the concentration (or activity) of reactants involved in the rate determining step. The rate equation was therefore given the familiar form of a power law:

$$d\alpha/dt = k(T) \cdot (1 - \alpha)^n \qquad \ldots(4.3)$$

where: α = fraction reacted at time t

n = order of reaction

Combining equations 4.2 and 4.3 gives:

$$d\alpha/dt = (1 - \alpha)^n \cdot Z \cdot \exp(-E/R \cdot T) \qquad \ldots(4.4)$$

The temperature difference (ΔT) in Borchardt and Daniels' DTA experiment was a measure of the rate of reaction, while the area under the reaction exotherm was related to the enthalpy change. The significance ascribed to the peak parameters in their experiment is similar to that for the output from a modern DSC apparatus. The height of the DSC curve from the signal baseline is the heat flux ($\Phi = dH/dt$) at that point, which gives the instantaneous rate of reaction:

$$d\alpha/dt = \Phi/\Delta H_0 \qquad \ldots(4.5)$$

where ΔH_0 is the peak area (or specific enthalpy change if Φ is also normalised with respect to sample mass). If ΔH_T is the partial area of the peak up to temperature T, then $\alpha = \Delta H_T/\Delta H_0$. Substituting for the α terms in equation 4.4, taking logs and rearranging then gives:

$$\ln\left[\frac{dH}{dt} \cdot \frac{1}{\Delta H_0}\right] = \ln Z - \frac{E}{R \cdot T} + n \cdot \ln\left[1 - \frac{\Delta H_T}{\Delta H_0}\right] \qquad \ldots(4.6)$$

A series of equivalent values of t, T, α and Φ may be obtained from the DSC curve. Equation 4.6 can be solved by multiple linear regression analysis, which means that values for Z, E and n can be obtained using the data from a single rising temperature DSC scan.

This principle of 'maximum information from least effort' is one of the most attractive aspects of the method and has led to virtually all the manufacturers of DSC equipment offering software packages based on Borchardt and Daniels' treatment. The ready availability of kinetic data 'at the push of a button' has resulted in a flood of published papers in which a wide variety of systems have been 'analysed' with little thought and no theoretical justification for applying this treatment.

4.3.2 Temperature dependence of solid-state reactions

The problems which arise in using Borchardt and Daniels' approach for analysing DSC data are related to the nature of the sample rather than the equipment itself. The Arrhenius equation assumes a homogeneous system in which the component molecules have a Maxwell-Bolzmann distribution of energies. This was valid for the solution state DTA experiment on which Borchardt and Daniels based their work, but not for a solid DSC specimen (even one which is nominally homogeneous). Garn [80] has discussed some of the fundamental errors in this approach and points out that in a solid, a perfect crystal represents the minimum energy state. A heterogeneous solid will display local energy fluctuations which depend on the physical coupling between individual oscillators. Even though the energy distribution in a solid represents a marked deviation from the behaviour assumed by the Arrhenius equation, it is found that the rates of many solid state reactions do show exponential temperature dependence. This arises because many of the true rate determining factors display Arrhenius-like behaviour. For example the rate of diffusion in a solid lattice [58] is given by:

$$D = D_{\infty} \exp(-Q/R \cdot T) \qquad \ldots(4.7)$$

where: D - diffusion coefficient at temperature T (K)

D_{∞} - limiting diffusion coefficient (at ∞ temperature)

Q - energy of activation of diffusion (related to opening up the lattice).

There has been extensive discussion as to whether the constants in the Arrhenius equation can have the same significance in a solid as in a fluid, or indeed have any physical significance at all. One of the

problems lies in the use of the gas-constant (R), whose applicability in a condensed system is debatable. The molar dimension of R also creates uncertainty in the magnitude of quantities derived from it, because molarity is largely irrelevant in a solid system. It is worth noting that the pre-exponential term in equation 4.7 is a real quantity but that it is not identical to the classical 'frequency factor'.

In homogeneous kinetics, the 'Arrhenius constant' (Z) is generally identified with a particular vibration in the molecular array which represents the activated complex of transition state theory. Cordes [81] has proposed that, in solid state reactions, a low value of Z indicates either surface area dependence or a tightly bound activated complex. Higher values indicate looser binding and freer rotation of the complex. Very high values were equated with free translation on the solid surface. These interpretations are consistent with the values of entropy of activation on formation of the activated complex and their effect on the value of z.

The concept of a mobile activated complex is easy to visualise for some solid state reactions, particularly those which involve a gas-solid interface as in:

$$\text{Solid(1)} \rightarrow \text{Solid(2)} + \text{Gas}\uparrow$$

These reactions include decomposition of metal carbonates for which an intermediate has been suggested [82] consisting of a O—C—O rotor connected to the solid surface via a third C---O bond which was part of the precursor carbonate ion. Correspondingly, the 'activation energy' (E) has been identified with the energy required to break this bond and release the CO_2 as a free gas. It is less easy to identify an intermediate structure for glass de-vitrification. However, a physical barrier to diffusion is perfectly feasible and both nucleation and crystal growth display exponential temperature dependence. The overall rate equations for many materials are similar to equation 4.4.

Although the applicability of kinetic models derived for homogeneous systems to reactions in solids is debatable, this approach has been used in the current work as a simple means of shape analysis for DSC peaks. The data derived from Borchardt and Daniels' treatment is

therefore intended for comparison within this study, rather than being formal kinetic parameters.

4.3.3 The kinetic compensation effect

When the 'activation energy' for a solid-state reaction is measured under various experimental conditions, it is often found that a range of values are obtained rather than a unique figure. In many such cases the Arrhenius pre-exponential factor varies sympathetically with activation energy, and a linear relationship exists between lnZ and E.

i.e. $$\ln Z = a \cdot E + b \qquad \ldots(4.8)$$

This is the so called 'kinetic compensation effect' (KCE), which has been a subject of debate in the thermal analysis literature for many years. Garn [80,83] has dismissed KCE as an artifact resulting from mis-application of the Arrhenius equation. Zsakó [84] holds the alternative view that KCE is a genuine effect which may give insight into the behaviour of a reacting system. Apart from the decomposition reactions mentioned above, many catalytic systems show kinetic compensation behaviour. Galwey [85] has reviewed some of these and discussed several possible reasons for KCE.

Compensation behaviour has been observed in a wide variety of systems and these have been discussed widely. In spite of this, consensus has not been reached on the significance of the KCE. Curtis-Connor [86] proposed a general explanation, but this simply resulted in further debate [87,88]. It seems probable that, if indeed compensation behaviour is a genuine property of reacting systems, more than one factor is responsible. KCE-like artifacts undoubtedly exist, which further complicate the search for an explanation. In any case, the debate will continue for many years and is unlikely to be fully resolved.

4.4 EXPERIMENTAL

4.4.1 Thermal behaviour of $Fe_{72}Al_{11}P_9C_8$ metallic glass

This alloy was prepared in 1981 by melt-spinning and was in the form of a ribbon ~ 1 mm x 0.03 mm, with a nominal atomic composition $Fe_{72}Al_{11}P_9C_8$. Analysis of the freshly prepared melt-spun ribbon by DSC showed the following behaviour (Figure 4.3): Initial heating at 20°C min^{-1} gave a broad shallow exotherm in the region 255-465°C, which included at least two poorly resolved peaks. Continued heating resulted in a strong exotherm, beginning at approximately 465°C, which was attributed to crystallisation of the amorphous material (see section 4.5.1). Re-heating of a specimen which had been heated to the end of the major exothermic event gave a featureless baseline over the entire region. A fresh specimen was heated in the DSC and quenched in liquid nitrogen when its temperature reached 465°C. Subsequent re-heating showed that the broad exotherm in the region 255-465°C had been removed and two underlying features revealed: (i) A gradual increase of heat capacity up to ~ 267°C, at which point a very sharp decrease occurred; (ii) A larger step increase of heat capacity, beginning at ~ 440°C and continuing up to the onset of the major exothermic event at 465°C. Several cycles of quenching and re-heating a single specimen showed that both of these second order (change of heat capacity) events were repeatable provided that the specimen was quenched at $\leq$ 465°C.

When the study of matrix effects described here was carried out, the alloy sample had been stored at ambient temperature for more than five years. Comparison of the DSC curves obtained for the freshly prepared and aged ribbons showed that the broad event < 465°C had disappeared during storage. Only the major exotherm remained and this had a smooth, gradual onset from a flat baseline with no preceding glass transition. This event was eliminated by a single scan to 480°C, with subsequent scans giving only a smooth baseline. It is likely that ΔH for this peak had also decreased during storage, but the analyser used in 1981 lacked data storage and analysis facilities and hence the two sets of results could not be compared retrospectively.

4.4.2 Mass dependence of the exothermic onset slope

It was shown in section 3.4.4 that small specimens of indium give anomalously low values of onset slope for the fusion endotherm. The possibility of a similar mass dependence for crystallisation was therefore investigated prior to designing the variable resistance experiment. The amorphous alloy ribbon was cut into short (~ 4 mm) lengths, which were contained in covered aluminium pans. The onset slope of the crystallisation exotherm was measured over a range of sample mass 0.6-13.5 mg using a rising temperature programme of 400-500°C @ $10°C \cdot min^{-1}$. Mass dependence of a similar form to that for fusion of indium was observed (Figure 4.4). A simple mathematical relationship, based on a first order exponential expression, did not fit the onset slope / mass data for crystallisation as closely as it had fitted the data derived from fusion of indium. However, the inference was the same in each case - that only in the plateau region does the data reflect the response of the measuring system rather than the constraints of the sample geometry.

4.4.3 Design of a new laminate experiment

The requirements of this experiment were similar to those in the last chapter - the resistance between the sample thermocouple and specimen should be variable while the other thermal properties of the system were kept constant. However, triple-layer laminates of the type used previously were not compatible with the physical form of the metallic ribbon. Randomly stacked alloy strips located between the silica discs gave poor repeatability of the contact and uneven support resulted in frequent breakages of the fragile 0.25 mm thick discs. The sample mass was also limited to < 2 mg by the difficulty of retaining alloy strips between the discs, while avoiding contact with the surrounding walls of the pan. In order to overcome these problems, an experiment was designed which was based on one of the laminates used previously (configuration B(III) in Figure 3.8). The main advantage of this configuration over the triple-layer laminates was that the specimen made effective and repeatable thermal contact with its container, via both the base of the pan and the lid. However, it was noted in the last chapter that a significant reduction of calorimetric sensitivity

occurred in experiments where the silica disc was located underneath the pan. This was attributed to parasitic heat exchange between the constantan disc and the dull surface of the exposed silica. In order to achieve a large thermal resistance, comparable to that of an organic material, the present study required even more silica discs to be employed in a stack below the pan. Consequently the design was modified so as to minimise the effects of stray radiation.

The modified experiment employed four laminate configurations (Figure 4.5), each of which included two dissimilar silica discs and two polished aluminium plates (Perkin-Elmer DSC pan lids: 6.5 mm diameter, 0.1 mm thick). The aluminium discs were included in the external resistive stack of configurations C(II)-C(IV) to act as radiation shields. The additional aluminium/silica contacts also contributed to the overall stack resistance and gave a maximum resistance of ~ 75 $K \cdot W^{-1}$ without having to employ more than two silica discs. The aluminium discs were wider than the silica discs and only left a small aspect of the latter exposed to stray radiation. The most efficient shielding was in the direction of the nearby constantan surface. Any silica and aluminium discs not used in the resistive stack were contained in the well of the sample container lid. This served to maintain the total heat capacity of the system constant and also ensured that none of the configurations resulted in a matt silica surface being exposed on the top of the specimen. Although precautions were taken to minimise the effects of stray radiation in the cell, some parasitic exchange with the external resistive stack was bound to persist. This was difficult to quantify, particularly since the effects were likely to be different for each configuration and probably not in proportion to the dimensions of the stack or its resistance. This uncertainty was corrected for by carrying out a back-to-back comparison between the crystallisation behaviour of the metallic glass and fusion of zinc in each of the laminate configurations. Any spurious effects which persisted would therefore affect both the exothermic and endothermic parts of the experiment. This should make comparison of <u>relative</u> effects between the two types of event equally valid for all the laminate configurations. Zinc (T_{fus} = 419.4°C) melts at a slightly lower temperature than the range in which the alloy crystallised when heated at 10°C·min^{-1} (~ 465-480°C).

This was the closest match among the available calorimetric standards and the difference of ~ 50°C was not considered to be critical.

It was evident from the preliminary investigation that a simple first order exponential equation would not be adequate to describe the slope / mass relationship for the crystallisation process. Only a limited amount of the alloy was available, which precluded carrying out sufficient measurements to identify a valid model and then to carry out a large number of measurements in each laminate configuration. At a heating rate of $10°C \cdot min^{-1}$ the onset slope was virtually independent of mass in the region > 8 mg. A nominal sample mass of 10 mg was therefore chosen as being representative of the instrument-limited region of the response curve. This allowed five replicate experiments to be carried out for each laminate configuration. The same number of reference experiments were carried out using zinc as the specimen.

4.4.4 Sample preparation

The hard, brittle metallic glass ribbon was very difficult to cut accurately, which made preparation of repeatable sample masses virtually impossible. Randomly aligned ribbons also tended to distort the base of the pan, making repeatable contact between the pan and thermocouple (or silica disc) difficult to achieve. Both of these problems were overcome by powdering the alloy prior to the experiment. Amorphous metals tend to be brittle and can be milled or ground, but mechanical working tends to initiate crystallisation which, being exothermic, then goes to completion. The ribbon was ground to a fine powder in a 'Spex' vibratory freezer mill, with the sample immersed in liquid nitrogen. It was found that grinding under these conditions reduced the area of the DSC crystallisation peak by ~ 18% (from ΔH ~ 140 $J \cdot g^{-1}$ for the cut ribbon). Subsequent analysis by X-ray diffraction (XRD) showed that crystallisation had not been induced by this treatment, even though part of the potential energy of crystallisation had been lost.

Specimens for reference (endothermic) experiments were stamped from a 0.5 mm thick sheet of high purity zinc, using a 5 mm diameter disc-punch, and pressed to give discs with optically flat faces,

diameter ~ 6.4 mm and masses 70 ± 2 mg. Scans carried out in configuration C(I) were used to calibrate the temperature scale and calorimetric sensitivity of the DSC cell. All experiments on the powdered alloy were carried out with a sample mass of 10.0 ± 0.4 mg.

4.5 RESULTS

4.5.1 Investigation of the crystallisation event

Samples of the powdered alloy were analysed by (XRD) to assess the effects of grinding and subsequent heating in the DSC on its crystallinity. The diffraction plot for the unheated powder (Figure 4.6a) displayed a single broad peak centred at $2\theta \approx 43.1°$, which corresponded to a d-spacing of ~ 0.21 nm. The shape of this feature was characteristic of regions of short range ordering with no long range crystallinity (i.e. a glassy structure) and showed that milling at liquid nitrogen temperatures had not induced crystallisation of the alloy. Conversely, the XRD plot for a specimen which had been heated to 480°C (Figure 4.6b) showed a high degree of crystallinity, with the strongest reflection at $2\theta = 44.4575°$ (d = 0.2036 nm) indicating the presence of crystalline α-iron. Most of the other peaks were assigned to aluminium-iron carbides of approximate formula $AlFeC_{0.5-0.7}$. Small amounts of iron-rich phosphides, such as Fe_2P, may also have been present. Other phases which were sought but not detected/identified were: FeC FeP_2 FeP_4 Fe_3Al AlP AlC.

4.5.2 Effects of matrix resistance

Varying the configuration of the external stack of silica and aluminium discs gave a range of thermal resistance ~ 28-76 $K \cdot W^{-1}$ (Table 4.1). It was evident from visual comparison of the DSC curves (Figure 4.7) that changing the matrix resistance had a much more dramatic effect on the fusion peak than on that for crystallisation. This was confirmed by the fact that the exothermic peak temperatures were indistinguishable between the various stack configurations (Table 4.2) whereas the fusion peak was shifted by more than 5°C on going from C(I) to C(IV). It would be expected that the standard deviation of each measured parameter would increase with an increasing number of

contacts in the external stack (C(I)→C(IV)). The data in Tables 4.1-3 showed that onset slope was the only parameter for which the width of the confidence interval varied with stack configuration. The form of variation was opposite to that which was expected, i.e. the C.I. became narrower with increasing stack height. The coefficient of variation was virtually constant and equal to ~ 3% of the onset slope. Consequently, the onset slope data were treated in isolation but the four sets of data were pooled to obtain best estimates of true standard deviation ($s_{(pooled)}$) for the other parameters. The C.I.s shown within the tables are for individual sets of data, while pooled values for s, and 95% C.I.s based on them, appear under each column.

Temperature lag

The temperature lag through the largest resistive stack was 0.8 ± 0.3 K for a resistance of 48.2 ± 3.9 $K \cdot W^{-1}$ (i.e. the difference between configurations C(IV) and C(I)). This value was in good agreement with data obtained for uni-directional heat flow using indium where a lag of 0.44 K was measured across a resistance of 26.8 $K \cdot W^{-1}$ (i.e. the difference between configurations B(II) and B(I) in Figure 3.8). The shift of extrapolated onset temperature for the exothermic event (Table 4.2) may be of a similar order but, because the experimental error in this data was rather worse than that for zinc, the difference between configurations C(IV) and C(I) of 0.5 ± 0.4 K was barely significant (at 95% confidence, based on $s_{(pooled)}$).

Calorimetric sensitivity

The data in Tables 4.1 and 4.2 showed that calorimetric sensitivity for both endo- and exothermic events decreased with increasing thermal resistance. Figure 4.8 shows that the form of the response was similar for the two types of event, although the curves were offset due to the difference in specific enthalpy change.

Peak shape analysis

The structural mechanism of crystallisation and the rate determining process(es) were not identified for the complex $Fe_{72}Al_{11}P_9C_8$ glass, which meant that an appropriate kinetic model could not be identified. Since many rate-determining processes in de-vitrification have been reported to show exponential temperature dependence, the applicability

of Borchardt & Daniels' treatment was investigated. A Du Pont software package (PN 994377-912) was used, which analyses a section of the DSC curve between 10% of maximum peak height and 50% area. Twenty data points are taken at regular temperature intervals in this region and fitted to equation 4.6 by multiple linear regression.

This model gave a good fit to all the experimental DSC crystallisation data, as illustrated by the Arrhenius plot in Figure 4.9. Although the actual values of the factors derived from this equation are unlikely to have any real physical significance the phase reaction was the same in each experiment. It was therefore considered valid to use this treatment for comparative shape analysis of the DSC curves derived from different laminate configurations. The values of the three parameters for data from each laminate configuration are given in Table 4.3.

4.6 DISCUSSION

4.6.1 The nature of the crystallisation event

The XRD analysis showed that the un-heated $Fe_{72}Al_{11}P_9C_8$ powder had a glassy structure characterised by regions of short-range atomic order. The position of the broad peak in the diffraction pattern suggested that these ordered regions were most probably arrays of iron atoms. The crystalline products which were identified in the heated specimen were iron-rich, and likely to consist of a pure iron phase together with separate domains containing iron and aluminium with a regular interstitial distribution of carbon and phosphorus. Alternatively, a single crystalline phase may have been formed, consisting predominantly of an iron lattice with random substitution by aluminium and random inclusion of the metalloids. In either case, it appears that the phase-reaction detected as a DSC peak in the 470-480°C region did not involve pre-existing crystalline nuclei. It is more likely that initial crystallisation occurs around the more ordered regions within the glassy iron, which are too small to be considered as 'formal' nuclei. As these regions grow into microscopic crystals, phase separation will take place in the disordered glassy phase surrounding them. The resulting concentration gradient, between the

continuous phase and the surface of the expanding crystalline region, will then cause the process to become diffusion controlled. The continuous form of the DSC crystallisation peak indicated that nucleation and growth are concerted, rather than being discrete and resolvable events.

The behaviour displayed by amorphous $Fe_{72}Al_{11}P_9C_8$ on heating was typical of that reported for other iron-based metallic glasses. The broad pre-crystallisation event observed for the freshly prepared ribbon has been ascribed to stress-relaxation, separation into discrete glassy phases and crystallisation of dendritic α-Fe [89,90]. Analysis by XRD showed that crystallisation of the alloy had not occurred to any detectable degree on storage. Stress-relaxation and phase separation are likely to have taken place, but these would not be detected by XRD. The shape of the DSC event at ~ 270°C closely resembled that for the Néel transition in nickel(II) oxide (see Chapters 2 & 6) and has been identified in ferrous glasses as the Curie point (ferromagnetic→paramagnetic transition) [61]. The other second order event had the same form as glass transition events in a wide variety of other metallic and polymeric materials. It represents an increase in structural mobility which allows reordering to take place as part of the crystallisation process. Formation of α-Fe and iron-containing compounds as discrete phases is a common route for crystallisation of glassy ferrous alloys.

3.6.2 Calorimetric effects

The ratios between the specific areas of the DSC peaks for crystallisation and fusion were not significantly different between the various configurations:

Configuration	$(\Delta H_{exo}/\Delta H_{endo})$
C(I)	1.05 ± 0.01
C(II)	1.03 ± 0.02
C(III)	1.03 ± 0.01
C(IV)	1.04 ± 0.03

These results showed that the change of calorimetric sensitivity associated with a change of matrix resistance was independent of the direction of heat flow. The baseline interval for both types of event

remained virtually unchanged when resistance was altered (Figure 4.7). The observed change of sensitivity cannot therefore be due to the parasitic heat flow acting over a longer time interval. Endothermic peak height was affected much more than the exothermic peak, but the calorimetric effect was the same for each. This showed that maximum heat flux was not a critical factor. Only the matrix resistance, and hence its ratio to the parasitic resistance (R_s), was the same for both directions of heat flow. This suggests that a simple parallel resistance model is adequate to describe the change of sensitivity with R_{matrix}.

4.6.3 Peak shape and kinetics

Subjectively, the effect of resistance on peak shape was much more severe for fusion than for crystallisation of an amorphous material. This difference is attributable to the nature of the transition rather than the response of the calorimeter. Armand *et al* [91] studied heat transfer and temperature gradients in an epoxy resin undergoing cure in a DSC. They analysed the process in terms of heat flow from the calorimeter superimposed on heat generated within the sample by the curing reaction. It was shown that temperature gradients within the sample were proportional to the enthalpy change, which meant that the reaction was effectively self-propagating and not quenched by contact with the calorimeter. The effect of matrix resistance was not discussed explicitly in Armand's work but there are similarities between the curing process and the crystallisation studied here. Both are evidently less strongly influenced by the heat transport properties of their surroundings than is a simple reversible process which relies on external heating to shift an equilibrium. The significance of the change of peak shape for crystallisation of the amorphous alloy became apparent when 'kinetic' analysis was carried out. Equations derived from the Borchardt and Daniels treatment gave a very good fit to the experimental data and might therefore be assumed to describe the crystallisation kinetics. The mechanism of crystallisation should not be affected by a change of matrix resistance, and this was supported by the common value of exponent 'n'. However, the data in Tables 4.1 and 4.3 showed that the apparent 'activation energy' was actually proportional to the resistance of the

heat flow path. It was evident from Figure 4.10 that 'E' and 'lnZ' were strongly correlated, with a linear relationship (*cf.* equation 4.8) indicating classical kinetic compensation behaviour. For the results presented here, KCE must be considered as an artifact related to heat transport rather than being an intrinsic property of the de-vitrification process. A resistance term should therefore be included in the rate equation if any physical reality were being sought for the constants.

Table 4.1

Peak parameters for fusion of zinc

Configuration	Onset Temperature /°C	Specific Area /$J \cdot g^{-1}$	Onset Slope /$mW \cdot K^{-1}$	'Stack' Resistance /$K \cdot W^{-1}$
C(I)	419.4 ± 0.1	108.4 ± 0.7	35.5 ± 1.2	28.1 ± 0.9
C(II)	419.8 ± 0.2	101.4 ± 0.7	22.9 ± 0.8	43.6 ± 1.6
C(III)	419.9 ± 0.1	97.0 ± 0.5	19.3 ± 0.8	51.9 ± 2.3
C(IV)	420.2 ± 0.2	88.5 ± 1.1	13.1 ± 0.5	76.3 ± 2.6
$s_{(pooled)}$	0.12	0.56		
95% C.I.	± 0.2	± 0.8		

Table 4.2

Peak parameters for crystallisation of the metallic glass

Configuration	Onset Temperature /°C	Peak Temperature /°C	Specific Area /J·g^{-1}	Onset Slope /mW·K^{-1}
C(I)	476.2 ± 0.4	480.4 ± 0.3	113.7 ± 0.9	12.6 ± 0.3
C(II)	476.5 ± 0.3	480.6 ± 0.1	103.9 ± 1.5	12.4 ± 0.2
C(III)	476.6 ± 0.3	480.7 ± 0.2	99.7 ± 0.3	12.4 ± 0.2
C(IV)	476.7 ± 0.1	480.6 ± 0.2	91.9 ± 2.0	12.4 ± 0.2
$s_{(pooled)}$	0.22	0.14	0.98	0.17
95% C.I.	± 0.3	± 0.2	± 1.4	± 0.2

Table 4.3

Pseudo-kinetic parameters for crystallisation of the metallic glass

Configuration	Geometric factor (n)	Apparent activation energy (E) /kJ·mol^{-1}	Pre-exponential factor (lnZ)
C(I)	1.16 ± 0.04	2588 ± 22	181.2 ± 1.5
C(II)	1.20 ± 0.06	2689 ± 38	188.4 ± 2.7
C(III)	1.16 ± 0.02	2727 ± 36	191.0 ± 2.8
C(IV)	1.19 ± 0.03	2832 ± 37	198.4 ± 2.3
$s_{(pooled)}$	0.029	24.2	1.72
95% C.I.	± 0.04	± 34	± 2.4

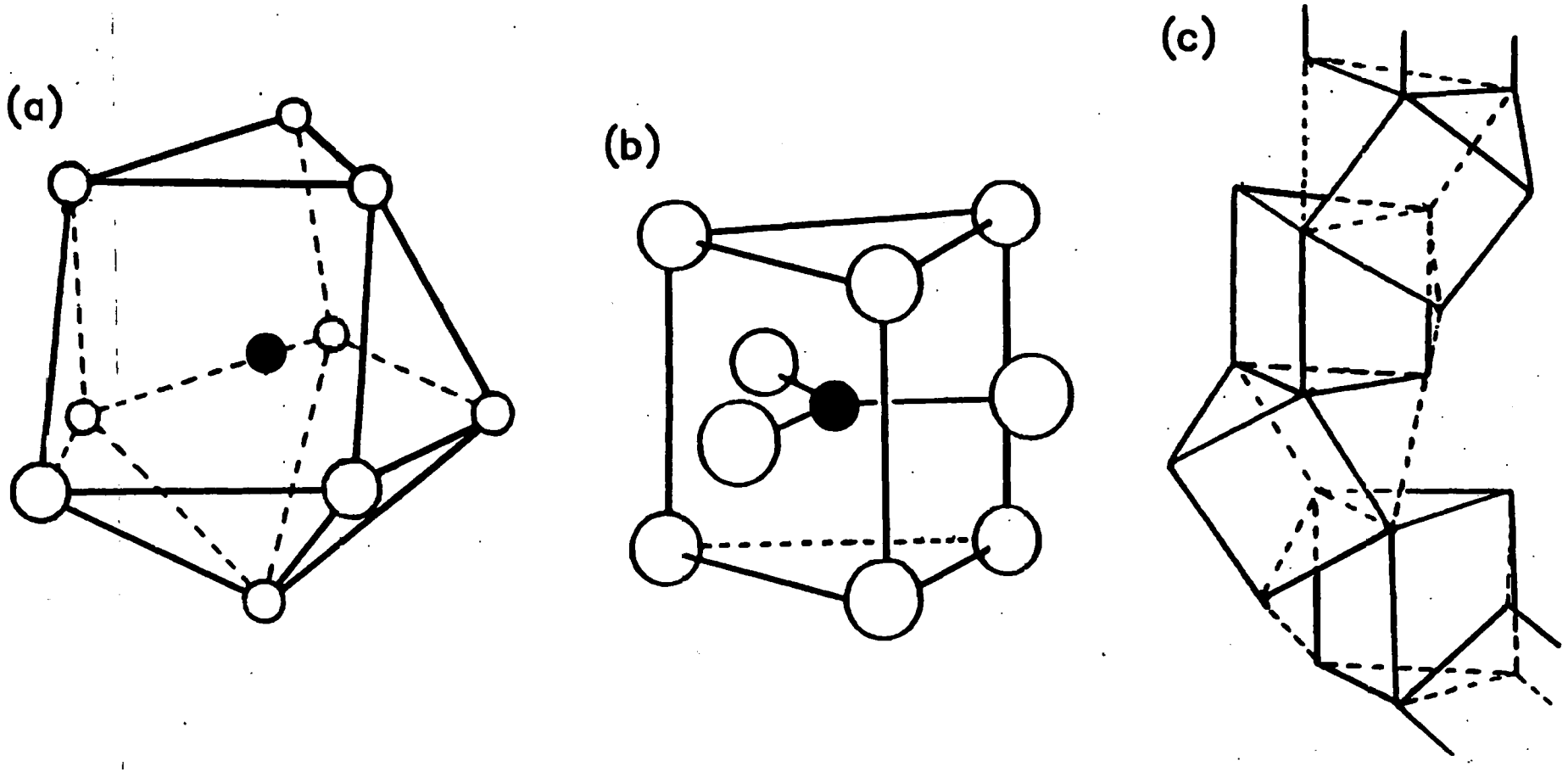

Figure 4.1 – Hypothetical structural elements in a metallic glass.
(a) 9–coordinate Bernal void. (b) Tri–capped prism (TCP).
(c) Medium range structure formed by random sharing of edges by TCPs.

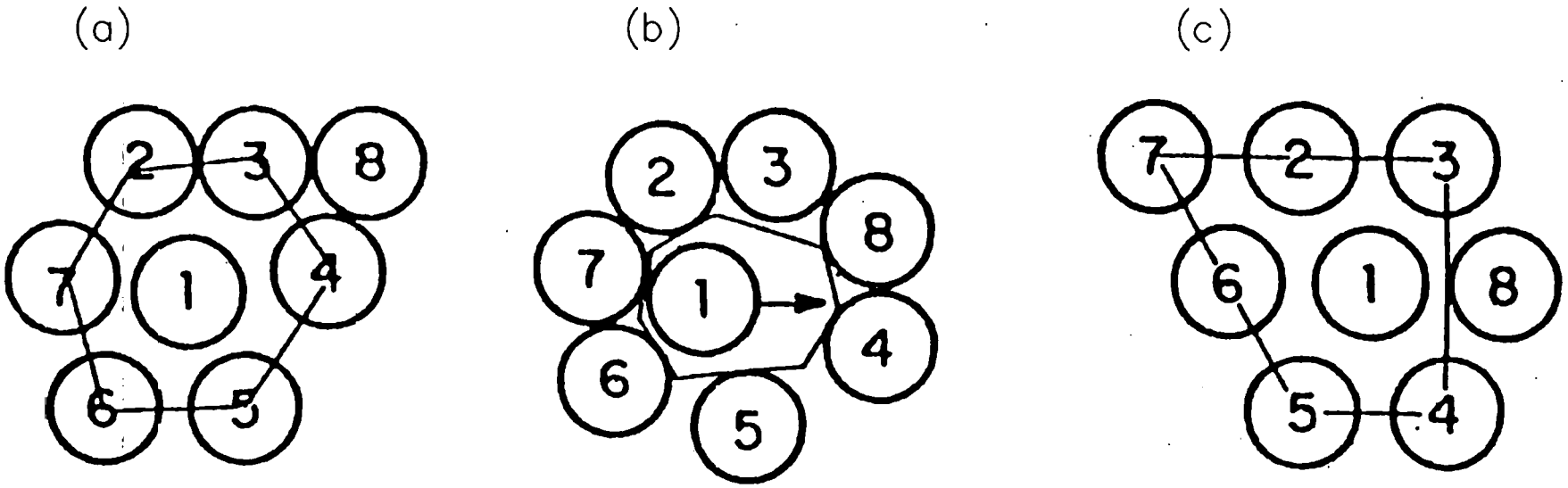

Figure 4.2 – Free–volume model for crystallisation of a glass.

(a) Initial configuration: central atom is surrounded by an asymmetrical cage of nearest neighbours.

(b) Cage expands until the critical free–volume is reached, allowing the central atom to undergo translation.

(c) Cage collapses into a regular array, leaving the central atom surrounded by a different set of nearest neighbours.

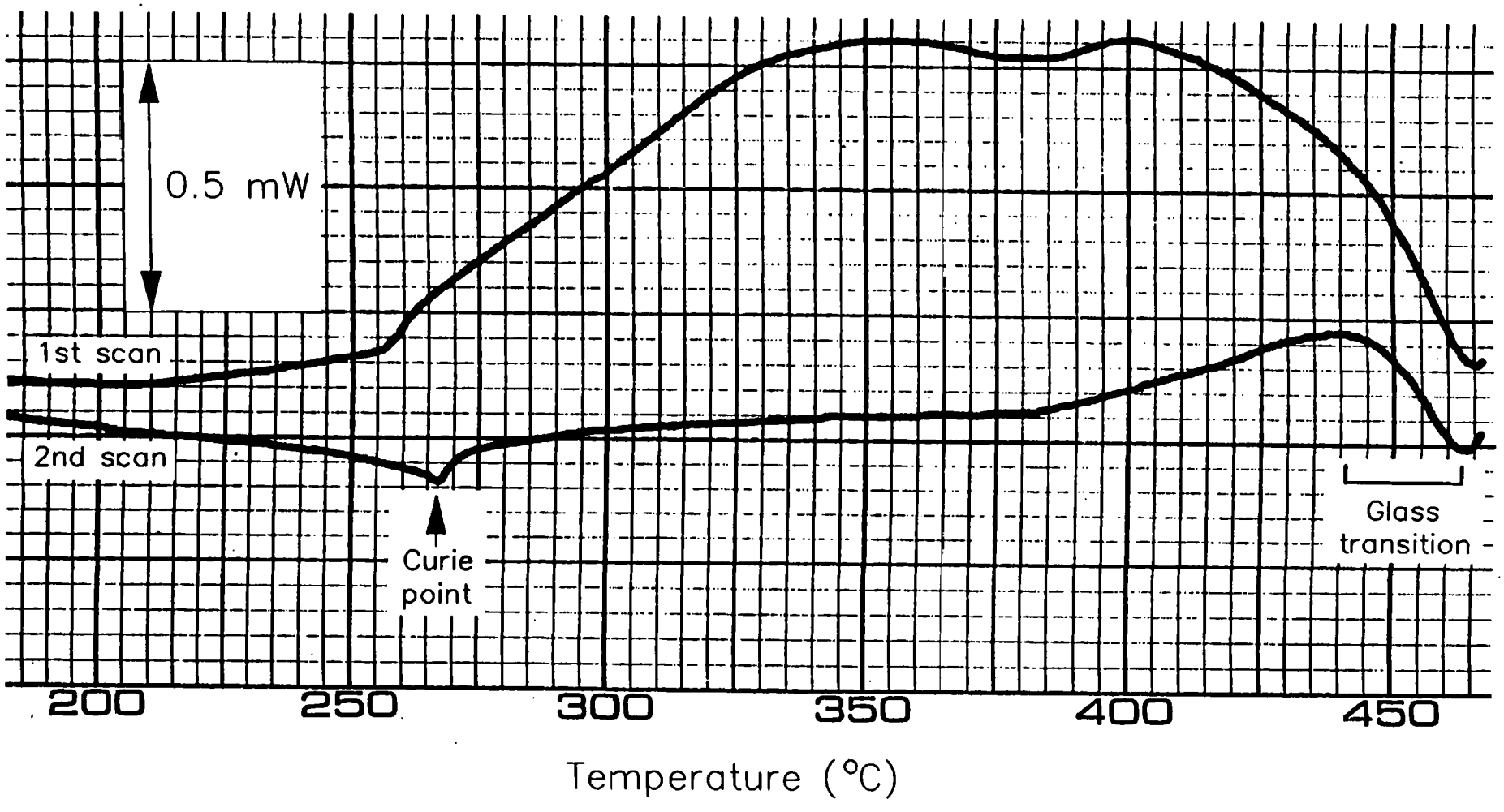

Figure 4.3 – Pre–crystallisation events in the DSC curve of a freshly prepared ferrous glass [$Fe_{72}Al_{11}P_9C_8$].

(Data ex. Du Pont 990 analyser, recorded in 1981)

(Sample mass: 16.4 mg. Heating rate: 20°C min^{-1})

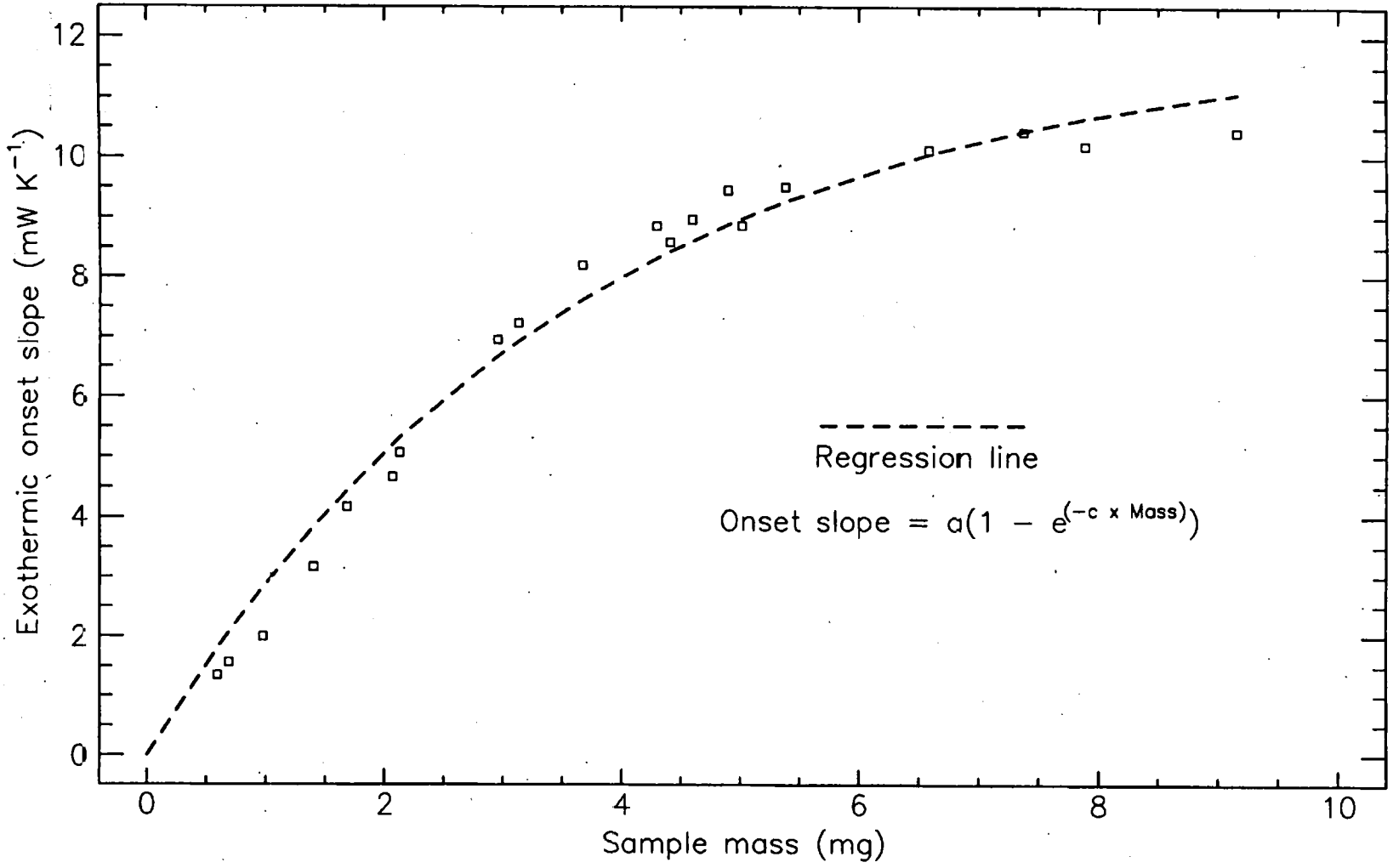

Figure 4.4 – Relationship between sample mass and onset slope for crystallisation of the metallic glass in the DSC.

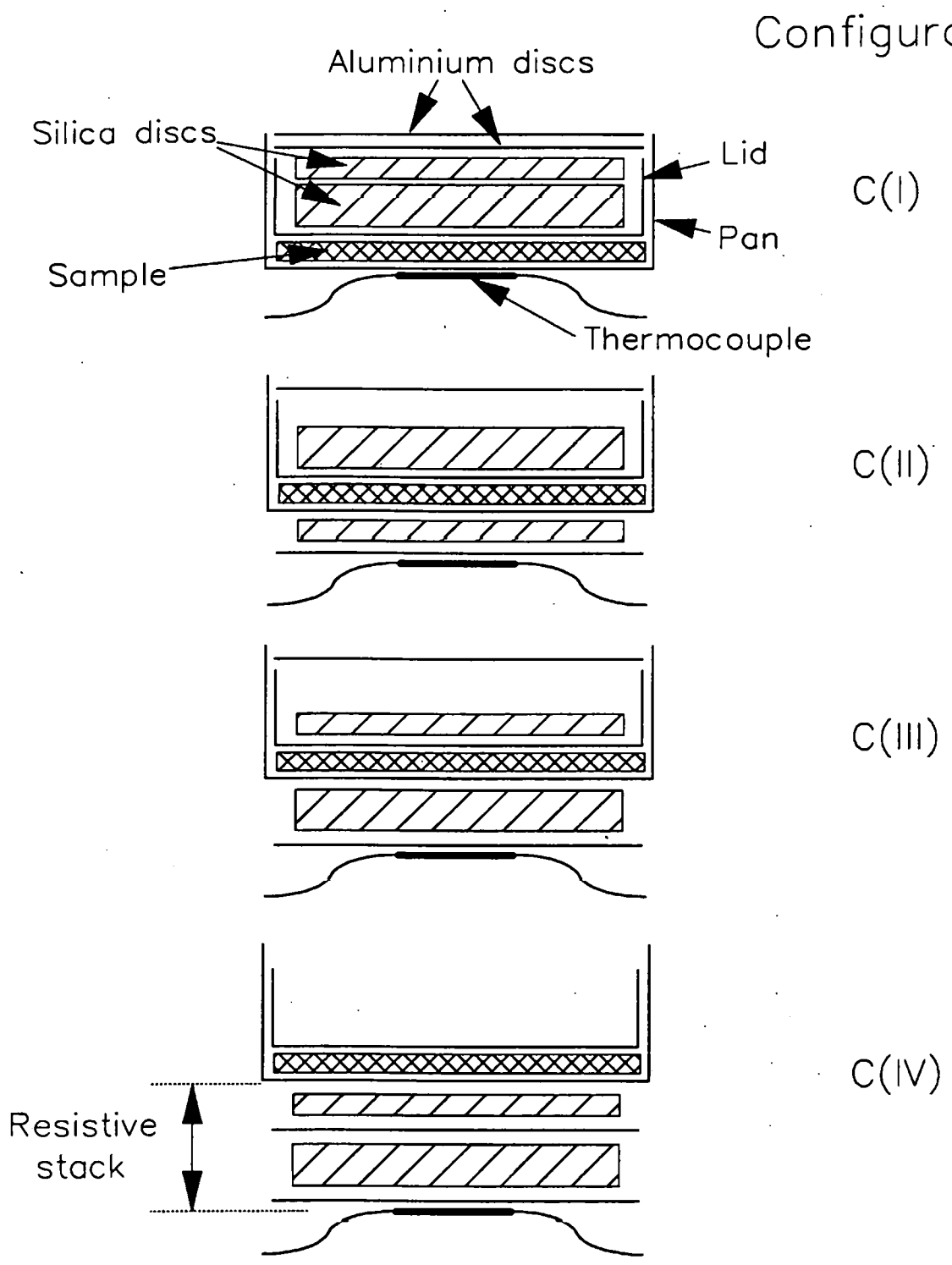

Figure 4.5 – Configurations of the laminates which were used to study matrix effects for an exothermic process.

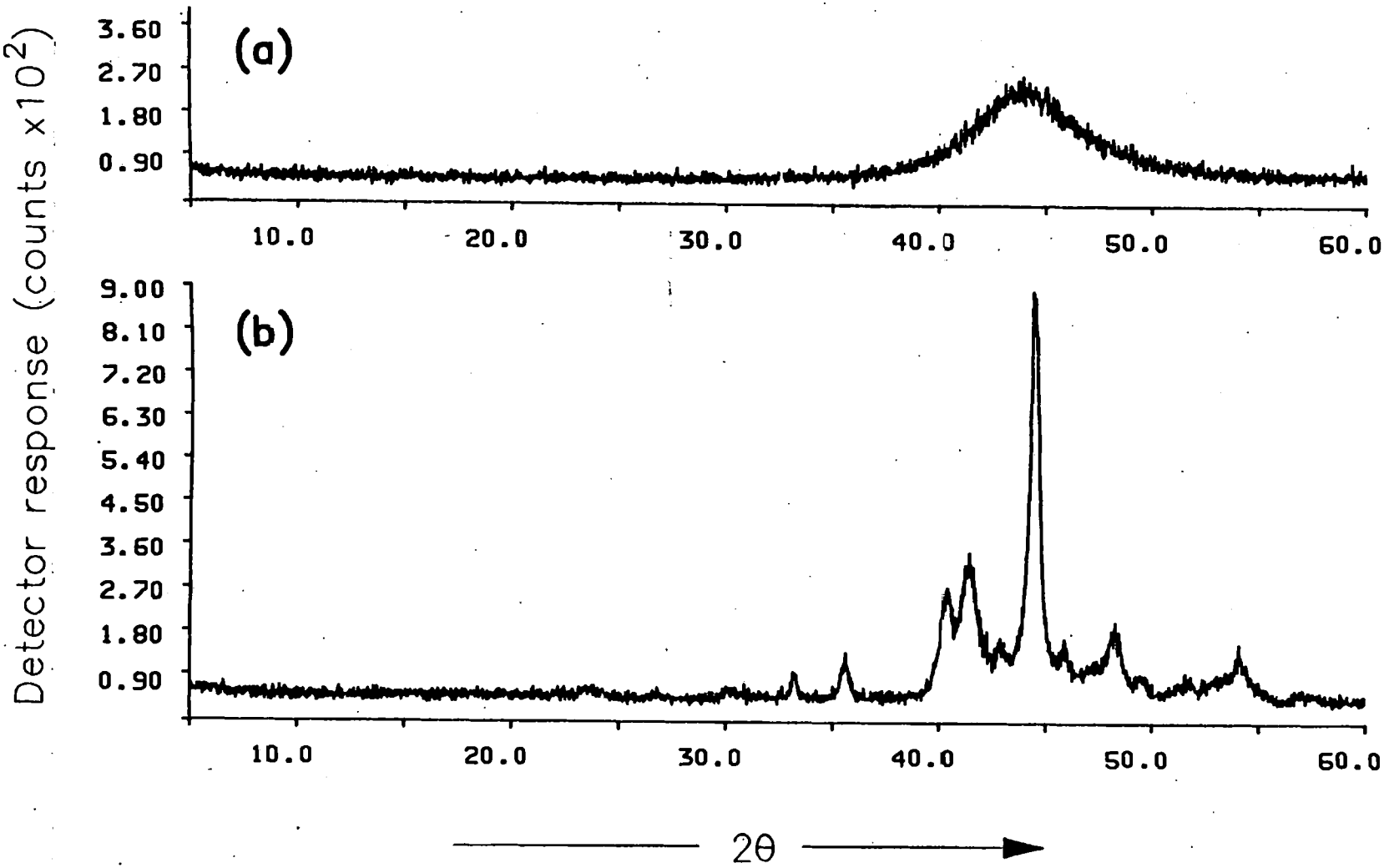

Figure 4.6 – X-ray diffraction plots for the powdered $[Fe_{72}Al_{11}P_9C_8]$ alloy.
(a) Un-heated (glassy form). (b) Crystallised by heating to 480°C.

(a) Exothermic

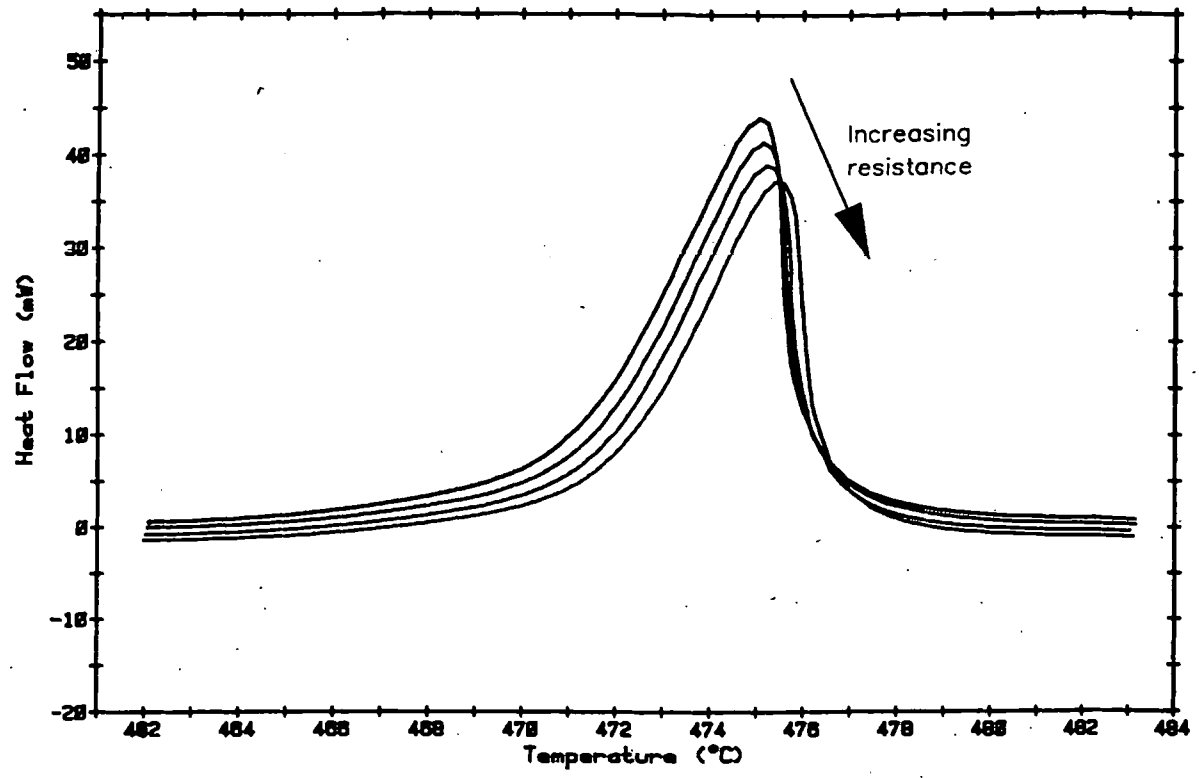

(b) Endothermic

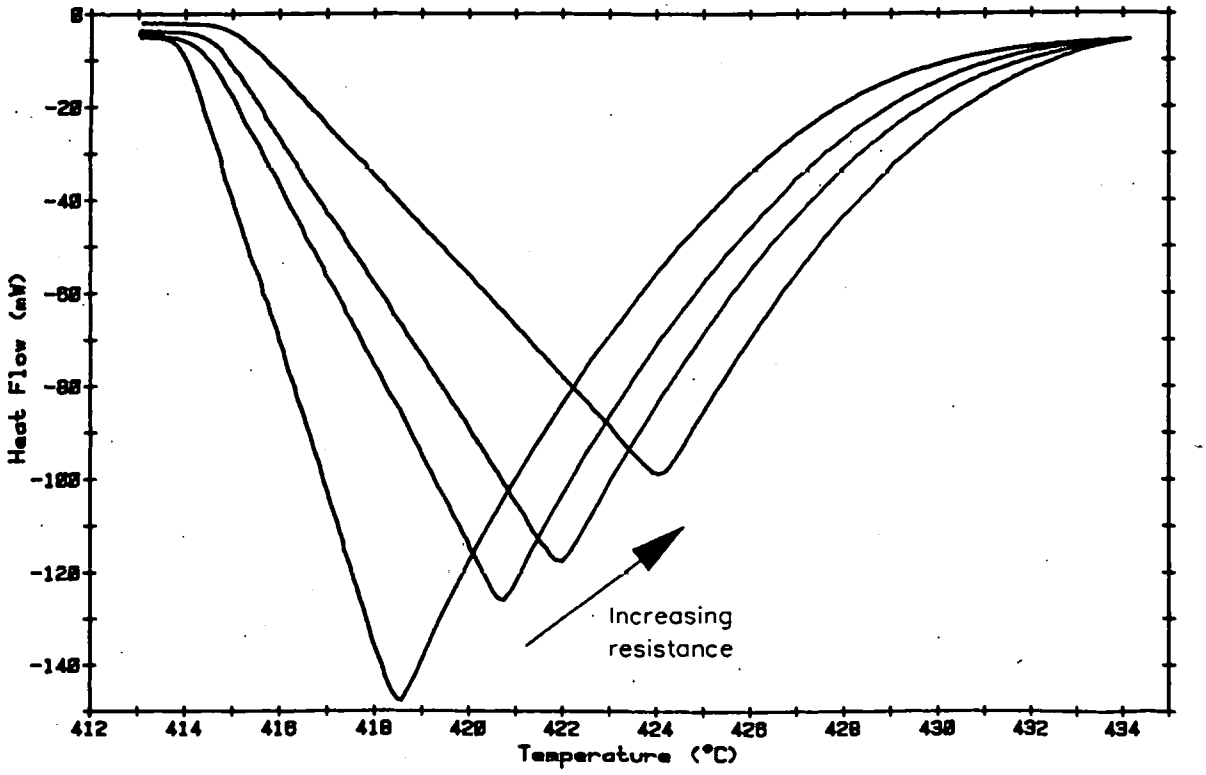

Figure 4.7 – Effect of 'stack' thermal resistance on DSC peak shape for:
(a) Crystallisation of a ferrous glass.
(b) Fusion of zinc.
(Range of resistance: 28–76 K W^{-1})

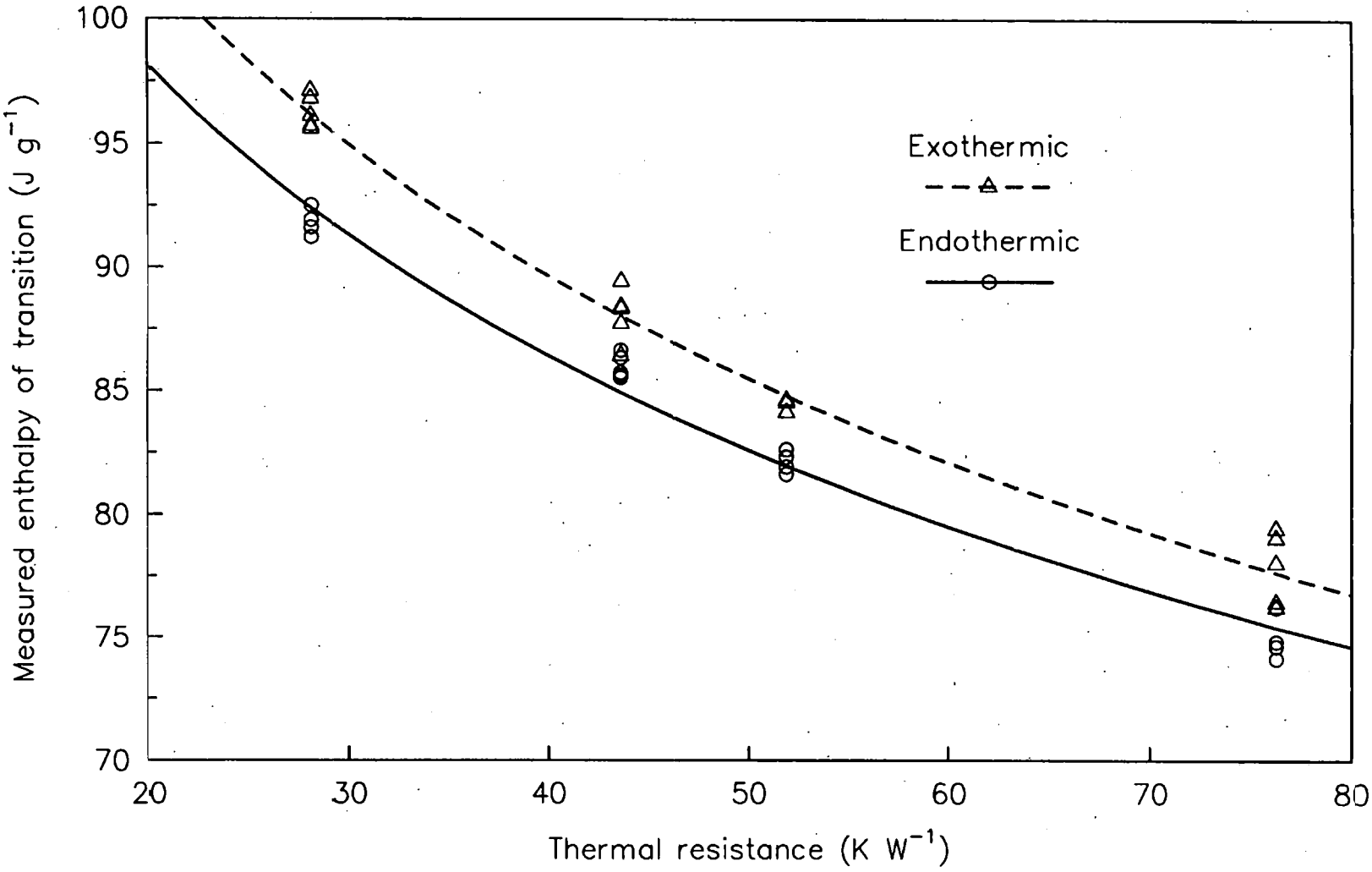

Figure 4.8 – Effect of thermal resistance on calorimetric sensitivity.

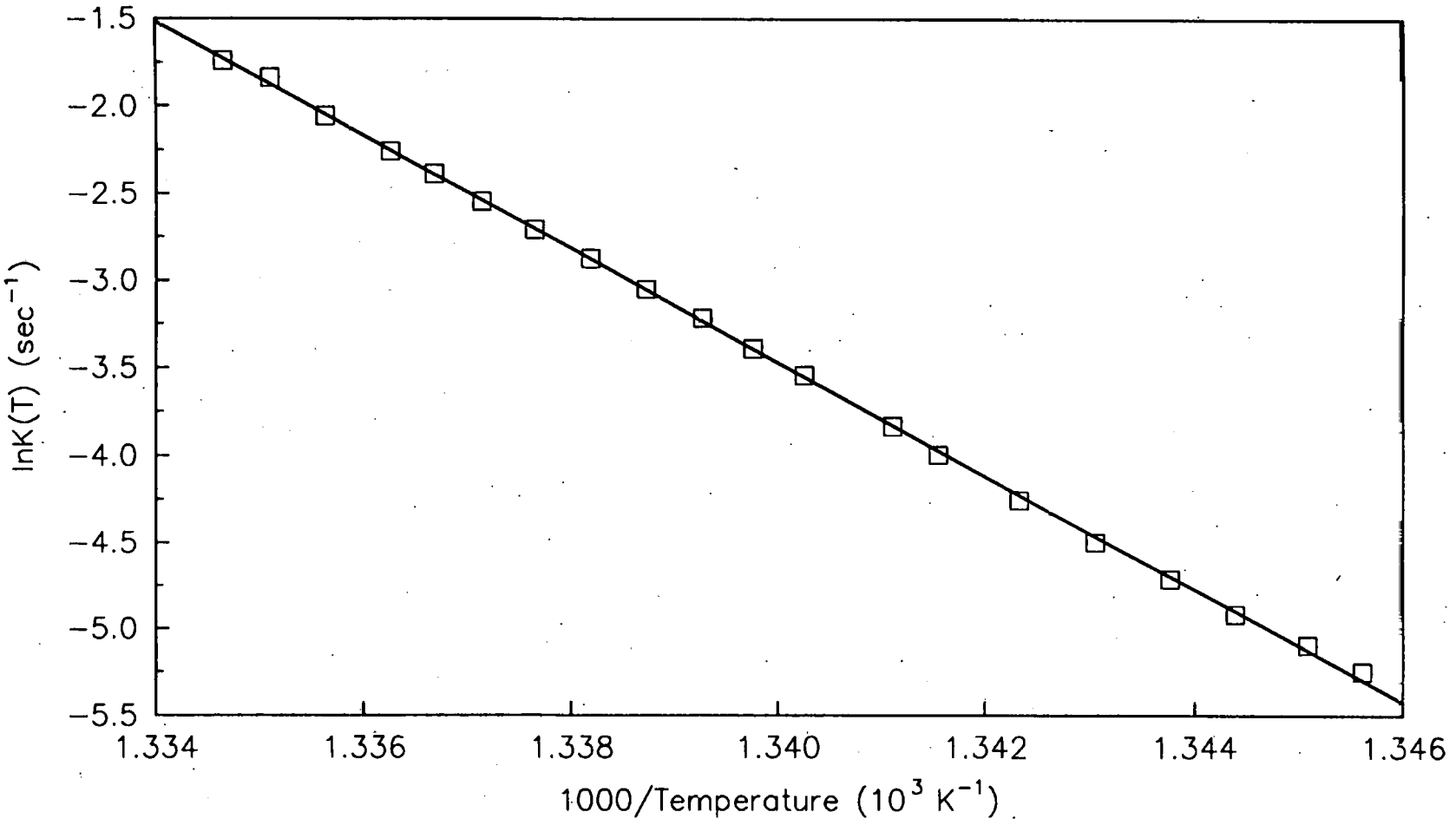

Figure 4.9 – Arrhenius plot for crystallisation of the metallic glass.

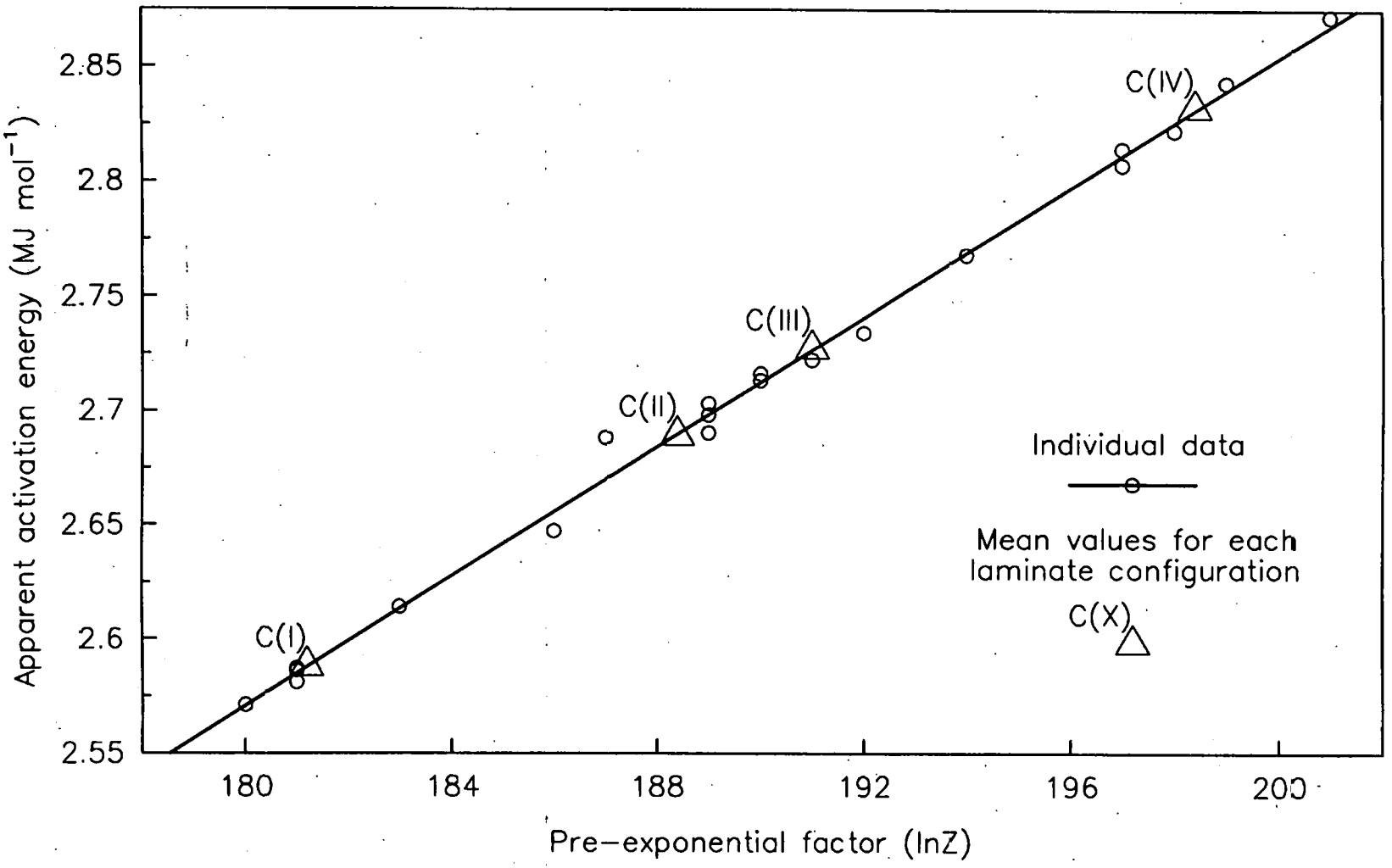

Figure 4.10 – Kinetic compensation plot for crystallisation of the metallic glass.

MATRIX EFFECTS IN DIFFERENTIAL SCANNING CALORIMETRY (VOLUME 3 OF 3)

by

M. THOMPSON M.Sc., C.Chem., MRSC.

Submitted to

THE OPEN UNIVERSITY

for the degree

DOCTOR OF PHILOSOPHY

FACULTY OF SCIENCE

1991

CHAPTER 5

THERMAL CONDUCTIVITY OF PORPHYRINS AND BINARY MIXTURES

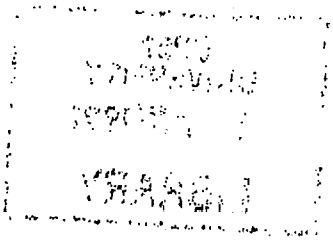

5.1 INTRODUCTION

In the exothermic matrix experiments, the variable resistive stack formed part of the external heat flow path connecting the sample to the calorimeter. This was intended to simulate the more realistic experimental situation in which the conductivity of the sample matrix itself varies. A situation may be envisaged in which several related materials are examined by DSC in a fixed experimental configuration. An identical reaction mechanism might operate in each case, but if the thermal resistances of the specimens were different the shape of the DSC curves would be affected. The magnitude of this change for an exothermic reaction would be small compared with that for an endothermic process, but still detectable. One of the most important consequences would be a change in the apparent kinetics of the reaction. This might easily be attributed to mechanistic rather than physical differences between the samples. Interactions between porphyrins and nickel oxide involve relatively small enthalpy changes and occur in a matrix of high thermal resistance. This leads to uncertainty as to whether differences observed in the DSC curves for various mixtures really reflect differences in reactivity, or whether they are simply artifacts resulting from variations in the heat transport properties of the matrix. In order to compare results for different porphyrins, as described in the next chapter, it was necessary to measure the thermal conductivity (λ) of several materials. This allowed results from the two studies of matrix effects to be related to the behaviour of the composites in order to identify potential errors in analysing results from the latter. The specific information required was:

(i) λ for each porphyrin.

(ii) How the conductivity of the matrix is affected by inclusion of nickel oxide and by subsequent interaction between this and the porphyrin.

(iii) Whether λ changes when the free-base is converted to its nickel complex.

In order to investigate various mathematical models for analysing λ, additional data was required on binary mixtures in which interaction between the separate phases should not occur. Crystalline metallic silver was used as the included phase for this study.

Only relatively small amounts of the pure porphyrins were available, so it was not possible to carry out thermal conductivity measurements by classical macro-techniques. Small scale methods based on DSC were therefore investigated. Specimens used in the porphyrin/oxide interaction studies were in the form of discs, which were ideal for conductivity measurements using the fusion onset slope method. The physical basis of this method (detection of a thermal event via a resistive medium) is analogous to the broader study of reactions occurring in a resistive matrix. These two factors made DSC the preferred method for measuring λ in this application.

5.2 MEASUREMENT OF THERMAL CONDUCTIVITIES

5.2.1 Preparation of test specimens

Thermal conductivity measurements were carried out on six porphyrins:

- β-Octaethylporphyrin (OEP);
- *meso*-Tetraphenylporphyrin (TPP);
- *meso*-Tetrakis(pentafluorophenyl)porphyrin (T(PFP)P);
- *meso*-Tetrakis(*p*-methoxyphenyl)porphyrin (T(*p*-MP)P);
- Phthalocyanine (PTC);
- Nickel(II)phthalocyanine (NiPTC).

Four binary mixtures were also examined:

- Phthalocyanine + silver (at two different volume fractions);
- Phthalocyanine + nickel(II) oxide;
- Nickel(II)phthalocyanine + nickel(II) oxide.

Mixtures were prepared by vibratory mixing of the dry powders. This was a relatively mild treatment which should not cause significant fragmentation of the nickel oxide particles. Samples were compacted into discs by means of a hydraulic press, using a 6.0 mm diameter circular die. The materials varied greatly in their cohesiveness and consequent ease of pelletisation - PTC formed good specimens after 10 minutes at 300 MPa using clean die-faces, whereas T(PFP)P needed more than 60 minutes at ~ 850 MPa and tended to fragment unless the die-faces were coated with a mould-release agent. In order to reduce the number of variables between experiments, the highest available compaction pressure (850 MPa) and a mould-release agent was used for all the samples, irrespective of their cohesiveness.

The density of each tablet was calculated from its mass and external dimensions. A micrometer was used to measure the thickness of the discs and this also proved to be a convenient way of checking that the faces of the specimen were parallel. Some discs, usually among those < 0.6 mm thick, were found to be wedge shaped and were rejected. This was attributed to uneven distribution of the powder in the die. The number of rejects was reduced by tapping the die on a hard surface before compression in the hydraulic press. Density measurement provided a useful check that the compacted specimen did not contain voids.

Thermal conductivity standards were prepared from vitreous silica, whose thermal properties are well documented. Silica standards were in the form of 6.0 mm diameter discs, as used for the laminate experiments, with a range of thickness 0.25-1.75 mm.

5.2.2 Calibration of the DSC cell

The calorimetric sensitivity and temperature measurement of the DSC cell used in these experiments were both calibrated using the same test metal and pan combination as for the corresponding resistance measurements (described later), i.e. either lead foil/aluminium pan (k_{cell} = 1.190) or tin foil/steel pan (k_{cell} = 1.298). The calorimetric cell constant derived from the appropriate combination, heated at $10°C \cdot min^{-1}$, was used to correct the measured fusion onset slope in the resistance measurements, i.e. $R = |\Delta T/(\Delta \Phi . k_{cell})|$. These corrected values were used to derive all of the axial thermal resistance and conductivity values in Tables 5.1, 5.2 and 5.4.

5.2.3 Preliminary experiments

Initially, lead foil (T_{fus} = 327.5°C) was chosen as the fusible standard because its melting point is in the middle of the temperature range where reactions between porphyrins and nickel(II) oxide have been detected. Thermal conductivity data at this temperature should therefore be the most applicable to the reacting system. Furthermore, the heat capacity curve for NiO is reasonably flat above 250°C and did not interfere with the conductivity measurements.

In order to reduce the contact resistance between the metal foil and specimen, several attempts were made to press them into intimate contact by means of the pellet press. Although very low pressures were used, this approach was not successful and resulted in either fracture or flow of the organic material. Consequently the foil was cut into discs and the faces pressed to optical flatness in the pellet press. Physical conformity was then assumed to give a fairly repeatable, if relatively high, contact resistance. The clearance between the wall of a Du Pont aluminium pan and the 6 mm diameter test specimens is only 0.25 mm. The lead discs were therefore cut to 5.0 mm diameter (mass ~ 58 mg) so that they would be protected from accidental contact with the pan-wall, which would result in a thermal short-circuit and consequent reduction in the apparent resistance of the specimen. Heat leakage through the sample chamber atmosphere was also considered as a possible source of interference. The specimen and lead foil were protected by covering the pan with an inverted aluminium lid (Figure 5.1a). This has a disadvantage in that it limits the maximum height of the specimen to ~ 1 mm. DSC experiments with lead as the fusible material were carried out using a temperature programme 250-350°C @ $10°C \cdot min^{-1}$.

Data was obtained for two of the porphyrins (TPP and PTC, Figure 5.2) but the broad scatter and limited range of the data resulted in unacceptably large errors for the specific resistances:

i.e. TPP: $104.9 \pm 25.1\ K \cdot W^{-1} \cdot mm^{-1}$

PTC: $84.6 \pm 27.7\ K \cdot W^{-1} \cdot mm^{-1}$.

It was anticipated from the molecular structure of these porphyrins that PTC would have a higher conductivity than TPP. Although the mean values were in the expected order, their poor precision meant that the results were not significantly different. Lead proved to be unsuitable for measuring the thermal conductivity of OEP because its fusion endotherm is only partially resolved from that of the porphyrin.

Another problem with this experimental configuration is that, for thick specimens, the close proximity of the lid to the fusible metal disc may allow a significant amount of heat to be conducted through the narrow air gap, which would act as a parallel flow path to that through the sample. In some experiments, a sudden increase in the rate

of heat flux was detected during the fusion event. This corresponded to contact between the lid of the pan and the molten metal as it contracted into a spherical droplet.

5.2.4 Improved DSC procedure

Several changes to the experimental procedure were made in order to overcome the limitations identified in the previous experiments:
(i) The lid from a Perkin-Elmer (PE) stainless steel hermetic DSC pan was used as the container. This gave more clearance at the circumference and could accommodate thicker pellets than the Du Pont aluminium pans (Figure 5.1b). The pan base was flattened between the faces of a micrometer in order to minimise its contact resistances with the thermocouple and test specimen. These pans have a relatively smooth surface finish, which should also help to reduce the associated contact resistances. Because the steel pans are very robust, the same pan was used for all the experiments - thus eliminating one variable which might give rise to differences in thermal contact.
(ii) The relatively large diameter of the PE steel pans resulted in a very small gap between sample and reference positions if two pans of the same type were used. Consequently a Du Pont non-hermetic covered aluminium pan, containing five PE aluminium pan-lids to increase its heat capacity, was used as a reference. This eliminated most of the baseline offset due to the heavy steel sample pan, while maintaining an acceptable clearance between the two pans.
(iii) Tin (T_{fus} = 232.0°C), pressed into 6.0 mm diameter discs (mass ~ 40 mg), was used as the test metal. This was found to be much easier to handle than lead because its greater rigidity helped to maintain its flatness and conformity with the face of the test specimen. The polished tin disc, covering the entire top face of the specimen, was felt to offer sufficient protection from radiation without the need for a separate lid.
(iv) The lower temperature of the tin experiments caused much less damage to the porphyrin discs than was observed with lead. This meant that, in most cases, duplicate experiments could be performed on each specimen - giving greater confidence in the results for each individual pellet. The repeatability of these measurements was better

than ± 5% with no consistent bias between first and second determinations, except for the NiO/NiPTC mixture (see section 5.3.3).

This method was readily applicable to all the materials examined, although some problems were encountered with T(PFP)P (see section 5.3.2). The heat capacity of nickel(II) oxide increases fairly rapidly with increasing temperature up to 250°C. This results in an endothermic baseline slope and consequent overestimate of λ for the mixtures containing NiO. The magnitude of this error for NiO at the concentrations in these mixtures was ~ 0.3 $mW \cdot m^{-1} \cdot K^{-1}$, which was < 0.1% of the measured values. No correction was made for this minor bias.

The easily pelletised materials were held under pressure for a range of times between 10 minutes and 2 hours, but no difference in measured density or conductivity was found which could be attributed to compaction time.

5.2.5 Treatment of data

Common intercept treatment for resistance plots

The limited range of specimen thickness over which data can be obtained using the fusion onset method results in wide confidence limits for the slope and intercept of the resistance vs. thickness plot. The 95% confidence intervals for the Y-intercepts were of the order 63 ± 18 $K \cdot W^{-1}$ for the porphyrins and binary mixtures. All of the specimens which were prepared by compaction in the pellet press had a good surface finish. Provided that the dissimilar pellets do not distort by different amounts when heated to the measurement temperature, they should all have the same contact resistance (within experimental error) and hence the same Y-intercept. The data sets are therefore complementary and the 'true' value for the total contact resistance will be measured much more accurately from a model which assumes a common intercept for all the materials. This also gives a more precise estimate of the true thermal conductivities than would separate linear regression fitting.

Calculation of thermal conductivity from resistance data

The thermal conductivity of the sample material can be calculated from the slope of the measured resistance vs. thickness plot (R/h) and the geometry of the specimen, using the one-dimensional form of the Fourier heat-flow law, which gives:

$$\lambda = \frac{1}{A \cdot (R/h)} \qquad \ldots(5.1)$$

Where A is the cross sectional area of the pellet (2.827×10^{-5} m^2). This formula was used to calculate the 'Fourier' thermal conductivity values from resistances which had been corrected for the sensitivity of the DSC cell. This treatment makes many assumptions about heat flow in the sample, in particular that heat exchanges through the atmosphere and radial temperature gradients in the pellet are neglected. These errors can be corrected for by carrying out an identical procedure to measure λ for a well characterised reference material of the same geometry. The ratio

$$\frac{\lambda_{sample}}{\lambda_{reference}} = \frac{(R/h)_{reference}}{(R/h)_{sample}} \qquad \ldots(5.2)$$

then gives a more accurate measure of λ_{sample} which does not require assumptions to be made about heat flow geometry.

5.3 RESULTS

5.3.1 Vitreous silica

Analysis of vitreous silica discs (Figure 5.3) gave a slope R/h = 27.8 ± 2.8 $K \cdot W^{-1} \cdot mm^{-1}$, which corresponded to λ = 1.27 ± 0.13 $W \cdot m^{-1} \cdot K^{-1}$ (literature value = 1.63 $W \cdot m^{-1} \cdot K^{-1}$ @ 232°C [56]). This result showed that the treatment based on Fourier's equation underestimated λ by approximately 22%, which represents good agreement considering the liberal assumptions which are involved. A correction factor of 1.283 was subsequently used to convert the 'Fourier' conductivities to more accurate relative values.

5.3.2 Porphyrins (single phase)

Difficulties were encountered in making good quality pellets of T(PFP)P because they tended to split across the cylindrical axis both when removing them from the die and after heating in the DSC. In spite of this, the precision of measured densities for T(PFP)P was no worse than for the other porphyrins (Table 5.1). Initial DSC results on this material suggested that the linear resistance/thickness relationship failed for specimens > 2 mm thick, with the measured resistance increasing rapidly above this value. When more data had been acquired, it became evident that the scatter increased markedly for thick specimens (> 2 mm) with a strong bias to the high resistance side of a linear regression line based on data < 2 mm. This porphyrin had the lowest thermal conductivity and poorest cohesiveness of any of the materials examined. It is reasonable to suppose that mechanically weak pellets would suffer distortion and/or internal fracture when subjected to a high temperature gradient. This would result in anomalously high resistance values. Several obviously erroneous data points were omitted from the analysis (i.e. those within the dashed boundary in Figure 5.4) but others, although widely scattered, could not justifiably be rejected. The increase in the error resulting from inclusion of these points in the regression analysis was minimised by assuming a common intercept with the regression lines from all the other materials.

Specimen thickness for the other porphyrins was kept < 2 mm and no problems of thermal fracture or excessive scatter in the data were encountered. Duplicate determinations were carried out on all those pellets which maintained a good surface finish. Linear regression plots for data from four of the single-phase porphyrins are shown in Figure 5.5. This graph also illustrates the increased scatter for thick specimens of T(PFP)P.

5.3.3 Phthalocyanine/inorganic mixtures

Silver was used as an included phase to test the applicability of various models for calculation of effective thermal conductivity (section 5.5). It should not undergo reaction with free-base

porphyrins at these temperatures and therefore the interface should have a simple binary structure with low contact resistance. Phthalocyanine was the most cohesive of the materials examined, even when 50% v/v of silver was included. This allowed the thickness of PTC/Ag pellets examined to be extended to 2.75 mm. No problems of fracture or erroneously high resistance values were encountered with these specimens. This supported the conclusions drawn from the T(PFP)P results concerning the effect of high temperature gradients on specimen integrity.

The mixtures containing nickel oxide showed different behaviour between the free-base phthalocyanine and the nickel complex. Duplicate measurements on each disc of the PTC/NiO composite showed no significant bias between first and second values of resistance (ΔR = 0.3 ± 13.9 $K \cdot W^{-1} \cdot mm^{-1}$). The NiPTC/NiO composite showed a small but consistent decrease of resistance on repeated scans to 250°C, reaching a minimum resistance after four measurements (total ΔR = − 4.9 ± 2.2 $K \cdot W^{-1} \cdot mm^{-1}$). Heating for 1 hour at 350°C caused no further reduction of resistance and results from replicate measurements on these stabilised pellets showed the same degree of random variation as for all the other materials examined. Although a directional change of resistance was noted, the total change over the first four scans was within the experimental repeatability of the method. All of the resistance data for the NiPTC/NiO composite were therefore used to calculate λ, irrespective of the thermal history of the specimen. The conclusions drawn from these data would not have been altered by taking only values from the first or last scans on each pellet. Plots for phthalocyanine and related materials are shown in Figure 5.6, which illustrates the similar heat transport properties of four of the samples. Resistance was found to decrease significantly on inclusion of a large volume fraction of silver in phthalocyanine or nickel oxide in nickel phthalocyanine. Other mixtures did not show significant changes of resistance due to the inclusions. Composition and density data for these mixtures are given in Table 5.3.

5.3.4 Use of the common intercept treatment

The Y-intercept for silica (37.2 ± 7.3 $K \cdot W^{-1}$) was significantly lower than for the samples and hence this data set had to be treated as independent from those for the pressed organic materials. The intercept values for all of the porphyrins and binary mixtures were found to be equivalent, within experimental error, but inclusion of T(PFP)P data in the common intercept treatment resulted in a loss of precision and a corresponding increase in the width of the confidence intervals for the slopes and intercepts of the individual lines. The common intercept derived from all the data was 61.9 ± 4.2 $K \cdot W^{-1}$ while the analysis without T(PFP)P data gave 62.4 ± 2.7 $K \cdot W^{-1}$. Inspection of the data for this porphyrin showed that the broadly scattered data for thick specimens was responsible for the loss of precision. Because of this a separate analysis excluding T(PFP)P was carried out for the other materials.

The discrete and common intercept treatments did not give significantly different values of λ for any one porphyrin (Table 5.2), but the common intercept model gave 95% confidence intervals which were less than half of those derived by treating the data sets as independent. Common intercept results for the binary mixtures are given in Table 5.4.

5.4 SCANNING ELECTRON MICROSCOPY

Sieved nickel(II) oxide and several composites were examined by scanning electron microscopy (SEM). This was done to measure the pore size in the oxide and in an attempt to provide visual evidence of surface interactions between the oxide and porphyrins.

5.4.1 Techniques used

SEM was carried out using a Jeol JXA-840 Microanalyser, as mentioned previously, all specimens having been carbon-coated prior to analysis. Composite pellets were fractured along the central axial plane and the exposed surface examined. All of the composites were photographed using both secondary and backscattered electrons, which give

complementary images. Secondary electrons (SE) have low energies (~ 50 eV) and are emitted from the surface near to the point of impact of the electron beam. These are the usual source of SEM images, which often have a 3-dimensional appearance owing to the formation of shadows and bright edges. Bright artifacts can occur at edges, and also at non-conducting sites, due to electrical charging. Backscattered electrons (BS) are emitted from the surface with very little loss of energy. The intensity of these high energy electrons is directly related to the mean atomic number of the impact site. The BS images therefore show contrast due to compositional differences across a specimen - areas of highest mean atomic number (nickel oxide in this case) being the brightest.

5.4.2 Observations

The sieved nickel(II) oxide consisted of randomly shaped agglomerates of cubic crystals which showed evidence of sintering (Plate 6). Composites of nickel(II) oxide with both PTC and NiPTC were examined immediately after compaction and after heating to 350°C. The latter were heated in the DSC from 25°C at $10°C \cdot min^{-1}$ and held isothermally at 350°C for 1 hour. The BS images helped to distinguish between the NiO (bright) and PTC/NiPTC (darker) regions. These were not always distinct in the SE images, because charging of some organic regions caused bright artifacts. The following observations were made from the images shown in Plates 7-11:

(i) The microscopic structures of the two composites were quite different. NiPTC/NiO appeared to consist of a continuous organic phase with particles of NiO dispersed randomly throughout. Conversely, the oxide appeared to be the continuous phase in PTC/NiO, with dispersed regions of PTC. Some of the latter appeared to be needle-shaped, but they were fractured randomly and hence covered a wide range of size and morphology.

(ii) Heating the NiPTC/NiO composite did not cause any significant change in the appearance of the fracture surface (Plates 7 and 8).

(iii) Heating the PTC/NiO composite caused it to fracture preferentially along the interfaces, rather than randomly through the PTC crystals (Plates 9 and 10). The heated composite displayed monolithic needles of PTC protruding from the fracture plane.

(iv) In spite of observation (iii), close inspection of the PTC←→NiO interface region (Plate 11) showed no apparent difference between heated and unheated specimens.

It was not possible to detect diffusion of nickel into the PTC by X-ray mapping for two reasons. A high background level was present throughout the organic phase owing to transmission of X-rays from underlying NiO. The interface was not distinct on the X-ray image because of penetration of the electron beam into the NiO and random emission of X-rays through the adjacent organic phase.

5.5 MODELS FOR THERMAL CONDUCTIVITY OF MULTIPHASE SYSTEMS

The thermal conductivity of a heterogeneous material depends on the volume fraction and conductivity of each phase and also on the spatial relationship between the various components. Calculation of the macroscopic physical properties of a heterogeneous system from the properties of its microscopic constituents is not trivial, and no single treatment is applicable to all systems. Batchelor [92] has discussed some of the relationships for transport properties such as thermal and electrical conductivity, dielectric constant, magnetic permeability, shear viscosity, elastic properties and mobility of particles in a fluid or fluid in a porous solid. Niklasson *et al* have also discussed similar approaches for the calculation of bulk optical properties [93].

The system under investigation in this work was nominally composed of two phases - relatively conductive particles (nickel oxide) embedded in a less conductive matrix (porphyrin) - but two structural features make it more complex than a binary system. The oxide particles are porous, which reduces their conductivity and also makes the porphyrin/oxide interface discontinuous. If a chemical reaction, rather than physical interaction, takes place, the products will alter the structure of the interface and possibly its transport properties. These factors make the microscopic structure fairly complicated and consequently its behaviour was expected to deviate from that predicted by simple two-phase models.

5.5.1 Boundary conditions

The rule of mixtures can be used to calculate boundary values for the bulk thermal conductivity, by considering extreme cases (Figure 5.7) where the resistive components are in series and in parallel [94]. The series model assumes identical heat flow through each layer but a much larger temperature gradient across the relatively insulating layer. In this case:

$$\lambda_c = \frac{\lambda_i \cdot \lambda_m}{f \cdot \lambda_m + (1 - f) \cdot \lambda_i} \qquad \ldots(5.3)$$

Where λ_c = thermal conductivity of the composite (effective medium)
λ_m = " " " continuous (matrix) phase
λ_i = " " " inclusions (dispersed phase)
f = volume fraction of the inclusions

The parallel model assumes identical temperature gradients and different rates of heat flow, which gives the relationship:

$$\lambda_c = \lambda_i \cdot f + \lambda_m \cdot (1 - f) \qquad \ldots(5.4)$$

These boundary values converge as the difference between the conductivities of the two phases decreases, but a wide span results for component phases which differ appreciably in their conductivities. For example, consider a 50% v/v binary mixture in which the components have conductivities of 1 and 100 $W \cdot m^{-1} \cdot K^{-1}$. The calculated boundary values of λ_c for this system would then be 1.98 (series) and 50.5 (parallel) $W \cdot m^{-1} \cdot K^{-1}$. Anisotropic systems may show marked directional dependence of the thermal conductivity. An extreme case is illustrated by uni-axially fibre-reinforced composites, in which the conductivity along the fibres will be virtually that predicted by the parallel model, while that perpendicular to the fibres will be much lower - tending towards the series model. The experimentally determined conductivity of an isotropic composite should lie between the extremes predicted by the method of mixtures. Various models have been proposed for calculation of these intermediate properties, the simplest of which is the geometric mean of the component conductivities:

$$\lambda_c = \lambda_i^{(f)} \cdot \lambda_m^{(1-f)} \qquad \ldots(5.5)$$

This equation gives a value of $\lambda_c = 11.0\ W \cdot m^{-1} \cdot K^{-1}$ for the above example, but experimental studies [94] have shown that the geometric mean overestimates λ_c when the ratio of the component conductivities exceeds 20.

5.5.2 Porous solids

A porous solid can be considered as a heterogeneous binary mixture in which the dispersed phase is a fluid. In a micro-porous solid containing a medium of relatively low conductivity, such as air, heat transport across small pores is mainly by radiation (assuming that the dispersed medium is reasonably transparent to infra-red radiation). Loeb [95] has discussed the effect of pore geometry on heat flow in porous materials and derived a relationship which covers laminar, spherical and oriented cylindrical pores. For a solid containing spherical pores [96], Loeb's relationship becomes:

$$\lambda_c = \lambda_m \cdot \left[(1 - v_p) + \frac{v_p}{\left[1 - v_p + \frac{3 \cdot \lambda_m \cdot v_p}{8 \cdot \epsilon \cdot \sigma \cdot d \cdot T^3} \right]} \right] \qquad \ldots(5.6)$$

Where v_p = volume fraction of pores (= f)
d = mean pore diameter
ϵ = emissivity
σ = Stefan-Boltzmann constant ($5.67 \times 10^{-8}\ W \cdot m^{-2} \cdot K^{-4}$)

The complex second term describes the component due to radiation across the pores. Francl and Kingery [97] showed that the radiation term is not significant at temperatures < 500°C and for pores with $d < 100\ \mu m$. Equation 5.6 then reduces to:

$$\lambda_c = \lambda_m \cdot (1 - v_p) \qquad \ldots(5.7)$$

(Equation 5.4 also approximates to this form when $\lambda_m \gg \lambda_i$)

Kingery *et al* [98] have applied this treatment to a wide range of porous refractory materials including nickel oxide.

NOTE: Equation 5.6 is printed incorrectly in [96]. The correct general form, for various pore geometries, may be found in [97].

5.5.3 Effective medium model for two-phase systems

The situation becomes complicated when the dispersed phase has a significant thermal conductivity but different from that of the continuous phase. In this case the rule of mixtures gives widely different boundary values, as shown above. A rigorous mathematical treatment was developed by Bruggeman [99] for calculation of electrical and thermal conductivities and dielectric constant. This was based on the assumption that each inclusion behaves as an isolated sphere surrounded by an 'effective medium' whose properties are those of the mixture (Figure 5.8). It is a realistic model because it does not assume an even distribution of the inclusions. The relationship for bulk conductivity of a two-phase system (λ_c) is given by:

$$\frac{\lambda_i - \lambda_c}{\lambda_i + 2\lambda_c} \cdot f + \frac{\lambda_m - \lambda_c}{\lambda_m + 2\lambda_c} \cdot (1 - f) = 0 \qquad \ldots(5.8)$$

Lyle and Collins [100] have demonstrated that this treatment gives a good prediction of the thermal conductivity of syntactic foams, consisting of hollow glass microspheres ($\lambda_i \sim 0.05\text{-}0.12$ $W \cdot m^{-1} \cdot K^{-1}$) embedded in poly-vinyl chloride ($\lambda_m \approx 0.2$ $W \cdot m^{-1} \cdot K^{-1}$).

A slightly different model was used by Hashin and Shtrikman (H&S) [101], for calculation of magnetic permeability, which was based on a spherical inclusion surrounded by a concentric sphere of the matrix phase. This body was then considered to be surrounded by the 'effective medium' as in Bruggeman's model. The relationship derived from this treatment was:

$$\lambda_c = \lambda_m \cdot \left[1 + \frac{f}{[(1 - f)/3] + [\lambda_m/(\lambda_i - \lambda_m)]} \right] \qquad \ldots(5.9)$$

It was shown that this value of λ_c represents a lower bound when

$\lambda_i > \lambda_m$ and an upper bound when $\lambda_i < \lambda_m$. Although the treatment was derived for calculation of magnetic permeability it should be equally applicable to other transport properties. Considering the example in section 5.5.1 (λ_m = 1 and λ_i = 100 $W \cdot m^{-1} \cdot K^{-1}$) the two effective medium models give λ_c = 27.1 (Bruggeman) and 3.83 (H&S) $W \cdot m^{-1} \cdot K^{-1}$. These values are consistent with the conditions in [99] and [101]: both values lie within the bounds derived from the method of mixtures; the value given by equation 5.9 is lower than that from 5.8, since $\lambda_i > \lambda_m$. It is interesting to note that the geometric mean, which should overestimate λ_c for this mixture, actually gives a lower value than the Bruggeman model.

5.5.4 Coated sphere model for a three-phase system

An extension of the binary model in Hashin and Shtrikman's work was for a specific three-phase system in which particles of the dispersed phase are each coated with a layer of another material. This is a good representation of the situation when two initial phases (such as PTC and NiO) have reacted to form an interface or barrier layer, with a different thermal conductivity (λ_b) from that of either reactant. In this treatment, Hashin and Shtrikman considered the inclusion and its barrier layer as a two-phase system in order to derive the effective conductivity of a 'composite sphere' (λ_{ib}). Although the inclusion and barrier phases are not discrete or randomly distributed with respect to each other, the solution for λ_{ib} was found to be similar to Bruggeman's model:

$$\frac{\lambda_{ib} - \lambda_b}{\lambda_{ib} + 2\lambda_b} = \frac{\lambda_i - \lambda_b}{\lambda_i + 2\lambda_b} \cdot \left[\frac{r_i}{r_b} \right]^3 \qquad \ldots(5.10)$$

Where r_i and r_b are the radii of the inclusion and barrier layer.

The derived property of the 'composite sphere' can then be substituted for that of the simple inclusion in the two-phase H&S model.

5.5.5 Calculations for the porphyrin/nickel oxide system

Porous nickel(II) oxide

The validity of the simplification to equation 5.7 was tested for the nickel oxide used in this work by means of calculated or published values as follows:

Electron microscopy (Plate 6) showed the oxide to be composed of sintered cubic crystals, with irregular pores of diameter:

$$d \leq 1\ \mu m$$

The measured densities of PTC and the NiO/PTC composite (Tables 5.1 and 5.3) were used to calculate the porosity of the oxide:

$$v_p = 0.284 \pm 0.005$$

Thermal conductivity of non-porous nickel(II) oxide at 232°C was calculated by interpolation between values in published data [98] as:

$$\lambda_m = 9.25\ W \cdot m^{-1} \cdot K^{-1}$$

Emissivity of nickel oxide depends on its method of preparation and covers a range 0.59-0.86 [102]. The radiation term in equation 5.6 increases with increasing emissivity, so the highest contribution was calculated by taking: $\epsilon = 0.86$

The contributions due to conduction through the bulk oxide and radiation across the pores were calculated to be:

λ_c = {6.623 (conduction)} + {1.67 x 10^{-5} (radiation)} $W \cdot m^{-1} \cdot K^{-1}$

This confirmed that the radiative contribution is negligible and hence that the simplification to equation 5.7 is justified. The calculated value of 6.623 $W \cdot m^{-1} \cdot K^{-1}$ was in good agreement with the value of 7.03 measured by Kingery for pressed nickel oxide powder of porosity 0.257.

Binary mixtures

Theoretical values of bulk thermal conductivity were derived for the four mixtures using the geometric mean, Bruggeman and H&S models. The thermal conductivities of PTC and NiPTC (λ_m) were taken from the common intercept/silica reference treatment in this work (Table 5.2). Other values were taken to be:

Silver; λ_i = 413 $W \cdot m^{-1} \cdot K^{-1}$. Porous NiO; λ_i = 6.623 $W \cdot m^{-1} \cdot K^{-1}$.

These results are listed in Table 5.4.

5.6 DISCUSSION

5.6.1 Scope and limitations of the fusion onset slope method

Previously published methods [42-44] for measuring λ from fusion onset slope data all appear to overlook one or more factors which can bias the results. Resistances at the thermocouple/pan/specimen contacts are either neglected or attempts made to minimise them by the use of 'heat sink compound'. The latter approach is not universally applicable because the volatility of the conductive paste (usually containing silicone grease) limits the accessible temperature range. Deviation from the Fourier heat flow model can only be compensated for by running a reference material under the same conditions. Even in this case, contact resistances will bias the results unless the resistance of the reference specimen is identical to that of the sample. It has been suggested that minimisation of the contact resistance between the sample and fusible standard is important and can be achieved by pre-melting the standard before the analysis is carried out. It was found in this work that the geometry of the re-solidified disc was unpredictable. In many cases the melt had contracted into a bead, which would lead to an increased contact resistance. All of these interferences were minimised in the procedure developed in this work.

(i) Measurements were made over a range of sample thickness and the specific resistance determined by linear regression - this eliminated the effect of contact resistance for each individual sample.

(ii) Although the actual contact resistance is not important it must be repeatable in order to give good precision for individual resistance measurements and also to allow the common intercept analysis to be used. This was achieved by optimising the conformity of each contact by using a polished, flattened, robust sample pan and preparing the test specimen and fusible disc in a die with optically flat faces.

(iii) Errors in the calibration factor derived from measurements on silica were reflected in the relative λ values for the samples. These had 95% confidence intervals of about ± 10%, which were similar to those for the discrete linear regression fits. It would be advantageous to extend the range of thickness for silica specimens, but much of the error arises because the silica data cannot be

analysed in a common intercept set with data from pressed organic samples.

(iv) Ideally, several materials covering a range of λ should be analysed together to give the best confidence intervals from the common intercept treatment. Improved accuracy would be achieved by using well characterised reference materials with conductivities closer to those of the samples and preferably bounding the λ range of interest. These should be prepared in the same way as the test specimens and analysed in the same common intercept set. Thermally stable organic polymers such as PTFE ($\lambda \approx 0.25$ $W \cdot m^{-1} \cdot K^{-1}$) are potentially suitable but the literature values of conductivity are very variable. A good surface finish is difficult to obtain by machining PTFE and thin specimens tend to distort on heating. Hot pressing may be an appropriate way of preparing reference specimens so that their contact resistance is the same as for the samples, but the pressing temperature would have to be higher than the maximum reached in the analysis because of the 'shape-memory' properties of PTFE. In view of the increasing interest in this technique, it is desirable to have certified conductivity standards available for DSC.

(v) An upper limit for sample thickness in this method was not identified but very thick specimens, having high resistances, may be anticipated as leading to a significant increase of the relative heat leakage through the sample chamber atmosphere (*cf.* Chapter 2). This was the reason initially assigned to the anomalous T(PFP)P data. Although the method appeared to be applicable to fairly thick specimens the main advantage of the technique is its ability to use small amounts of sample. It is probably best to restrict measurements to specimens < 3 mm thick and rely on good reference materials and careful data analysis to give accurate results.

(vi) The mechanical stress imposed by high temperature gradients does appear to be a limiting factor in the analysis of materials having poor cohesive properties. It was evident from the studies of binary mixtures that analysing such materials as a composite and calculating the component properties would introduce large errors. The only option in these cases would be to use thinner specimens and/or a slower heating rate.

5.6.2 Structure-dependence of the thermal conductivity of porphyrins

Thermal conductivity in non-metallic solids is generally considered to occur by transmission of 'thermoelastic waves' or 'phonons' through a system of coupled oscillators. The Debye equation for thermal conductivity of crystals is:

$$\lambda = (\rho \cdot c \cdot \bar{v} \cdot \bar{L})/4 \qquad \ldots(5.11)$$

Where ρ = density

c = heat capacity

$\bar{v}$ = mean phonon velocity

$\bar{L}$ = mean phonon free-path

In an ideal lattice, where all the lattice interactions are perfectly harmonic, the phonon free-path will be infinite, or at least bounded by the dimensions of the crystal. However, coupling of different modes in the lattice will lead to anharmonic vibrations and a reduction in the free path. Any factor, such as change from a crystalline to glassy state or the presence of defects, which reduces $\bar{L}$ will also tend to reduce λ. These considerations are complicated for a well ordered inorganic lattice, but are even more so for large organic molecules with many degrees of freedom. The thermal conductivity of crystalline porphyrins will depend on several factors including the spatial relationship and packing of adjacent molecules, accessible modes of vibration and coupling between vibrations of adjacent molecules. A full analysis, which would be very complex and would require accurate structural data for all the porphyrins, was outside the scope of this work. Furthermore, such a rigorous treatment is probably not justified for a compacted powder in which the concentration of defects will be extremely high and $\bar{L}$ is probably limited by the size of the crystallites. In spite of these limitations, qualitative correlation was found between thermal conductivity of the porphyrins and their closeness of molecular packing.

Published values of density were only found for the three most common porphyrins and nickel phthalocyanine. In each case, the measured density of the tablets (Table 5.1) was slightly lower than the value derived from floatation or X-ray measurement of unit cell volume. This is to be expected because it is not possible to achieve the close

packing found in a uniform crystal by compaction of a micro-crystalline powder. In spite of this bias, the agreement was sufficiently close to show that the tablets did not contain a high void concentration and that the method can achieve efficient and repeatable compaction of organic materials of this type.

Since a consistent set of density data for well-formed crystals was not available, the measured density values from this work were used to calculate the effective 'molecular volume' (V_{mol}) for each pure porphyrin. The relationship is:

$$V_{mol} = \frac{M \times 10^{-6}}{N_a \cdot \rho} \quad m^3 \qquad \ldots(5.12)$$

Where M = Molar mass (grams)

N_a = Avogadro's constant (6.022045×10^{23} mol^{-1})

ρ = measured density ($g \cdot cm^{-3}$)

These values (Table 5.2) indicate the mean closeness of packing of the porphyrin molecules in the compacted micro-crystalline state. The trend of calculated molecular volumes for the free-base porphyrins i.e.

$$PTC < OEP < TPP < T(p\text{-}MP)P < T(PFP)P$$

was consistent with their molecular conformations. PTC is virtually planar and the molecules pack closely owing to π–π stacking interactions [103]. The spacing between the molecular planes is 0.337-0.340 nm [104] compared with the inter-laminar spacing of 0.340 nm in graphite. The central porphyrin skeleton in the other materials may be almost planar or slightly ruffled, depending on the crystalline form, but the major factor which affects their packing is the size and flexibility of substituent groups. The ethyl chains in OEP are fairly flexible and adopt a 'chair-conformation' [105] to allow reasonably close packing, but not as close as for PTC. In the *meso*-arylated porphyrins, non-bonded interactions between the pyrrole β-hydrogens and *ortho*-hydrogen (or fluorine) atoms on the aryl groups prevent the substituents from lying in the plane of the porphyrin skeleton. This causes the aryl groups to adopt a propeller-like

conformation [105] which results in an increased separation between the porphyrin planes of adjacent molecules. The consequences of this were particularly apparent in comparing TPP and T(PFP)P, where the only structural difference is replacement of the twenty phenyl-hydrogen atoms by fluorine. Fluorine has a slightly larger van der Waal's radius than hydrogen (0.135 vs. 0.12 nm) but the fluorinated porphyrin showed a disproportionate increase of molecular volume. The excess difference is presumably due to intermolecular dipole-dipole repulsion. T(*p*-MP)P is not strictly analogous to the other two aryl porphyrins, which lack bulky *para*-substituents. Interactions perpendicular to the porphyrin plane should be similar to those for TPP, but in-plane steric and dipolar interactions will be greater than for TPP and possibly greater than for T(PFP)P. The intermediate value of V_{mol} for T(*p*-MP)P was consistent with these aspects of its conformation, but any closer correlation would require accurate crystal structure determinations.

The decrease of molecular volume (2.8%) which results from replacing the pyrrolic hydrogens in PTC by Ni^{2+} was less easy to explain than the trends for the metal-free porphyrins. It did not appear to be an artifact resulting from errors in the density measurements - the difference in V_{mol} (Table 5.2) was statistically significant and a similar difference (1.3%) has been measured by X-ray diffraction and floatation methods [103]. The electronic structure of square-planar nickel complexes suggests that closer molecular packing might be attributable to interaction between the vacant *d*-orbital on the nickel ion and π-orbitals of an adjacent porphyrin. However, this is not consistent with the complexation behaviour of nickel porphyrins in solution. These only accept neutral donor ligands when the porphyrin carries strongly electronegative substituents, such as sulphonic acid or *N*-methyl pyridyl-cation groups [106]. This type of specific intermolecular interaction would not therefore be expected in the solid. The corresponding complexation of Ni^{2+} by OEP resulted in an increase of molecular volume of 4.5% for the triclinic forms [107,108]. A reliable value for the interplanar spacing between porphyrin cores in OEP does not appear to have been measured, but the separation in the nickel complex is 0.344 nm [108], which indicates some steric interaction due to the alkyl chains. It has been suggested

that the ruffled porphyrin skeleton, found in the tetragonal polymorphs, is the lower energy state because the increase in σ-bond strength of the N-Ni bonds is greater than the loss of resonance energy in the porphyrin π-orbitals [108]. This factor is not likely to be significant in the above cases as the porphyrin core is virtually planar in triclinic NiOEP and monoclinic NiPTC. It seems most likely that complexation reduces the π-electron density in the porphyrin system and polarises the orbitals of the pyrrole rings towards the central metal ion, thus inducing a localised dipole. The offset stacking of porphyrin molecules in the crystal would then result in anti-parallel alignment of some of these local induced-dipoles, leading to increased attraction between adjacent molecules.

5.6.3 Application of thermal conductivity measurements to the study of solid state interactions

According to the two effective medium models, inclusion of 3.2% v/v silver should have caused a measurable increase in the conductivity of PTC (based on 95% confidence intervals). In fact no detectable difference was found, which suggests that both models overestimate λ_c. The results for the mixture containing 50% v/v silver confirmed this and showed that the bias of the various models changes over a wide range of conductivity. The magnitude of the error from the Bruggeman equation increased dramatically for this sample, but its conductivity was not typical of those for the porphyrin/oxide mixtures. The calculated λ_c values from the Bruggeman and H&S models were in reasonable agreement for the other three mixtures. In all cases the H&S treatment gave the lower value, which is consistent with its representing a lower bound for the Bruggeman model when $\lambda_i > \lambda_m$. Geometric mean values were all much higher than the experimental results, which is consistent with Woodside and Messmer's findings as discussed by Pratt [94]: the ratio of conductivities for nickel oxide and the phthalocyanines is ~ 20, while that for the mixtures containing silver is ~ 1200.

The H&S model gave the best agreement with experimental values for all of the composites, but the derived values were actually higher than those measured for all except that containing 50% silver. Assuming

that the measured values are accurate, this shows that the H&S model gives a reasonable estimate of λ_c for mixtures of the type in this work, but that it cannot be taken as defining the lower bound.

The ratio of predicted conductivity, from the H&S model, to the experimental value for the three lower conductivity composites showed that PTC/NiO behaved differently from the other two mixtures:

Mixture	$\lambda_{H\&S}/\lambda_{expt.}$
PTC/NiO	1.69
PTC/Ag (3%)	1.10
NiPTC/NiO	1.11

The most important difference between PTC/NiO and the other two mixtures is that only the former should undergo chemical reaction. If the acidic hydrogen atoms in a free-base porphyrin are represented as being discrete from the ligand, the expected reaction is:

$$PORPH{\cdot}H_2 + NiO \rightarrow PORPH{\cdot}Ni + H_2O\uparrow$$

The data in Table 5.2 showed that the conductivity of the nickel complex was not significantly different from that of the free-base. Formation of a surface layer of NiPTC should not therefore affect the conductivity of the included particles. The other product, being a gas in the temperature range where reaction occurs, is likely to affect the integrity of the interface. Disruption of the contact between the two phases will lead to a significant increase of the contact resistance and hence the <u>effective</u> conductivity of the inclusions will be reduced. This hypothesis is consistent with the observed change of morphology of the fracture surface in the PTC/NiO composite. SEM showed that heating caused the PTC crystals to become detached from the oxide, probably due to formation of water vapour by the complexation reaction. If the structure of the reaction product is represented by the H&S 'coated-sphere' model for a ternary composite, the experimental data may be used to calculate the properties of the barrier layer.

(a) Considering the data for the PTC/NiO mixture, the measured conductivity of the composite was identical to that of pure PTC. This means that the composite sphere (NiO + barrier layer) has the same effective conductivity as the matrix

$$\therefore \lambda_{ib} = \lambda_m = 0.35\ W{\cdot}m^{-1}{\cdot}K^{-1}$$

If we assume that the barrier layer consists predominantly of water vapour at 15 psi, then $\lambda_b \approx 0.034$ $W \cdot m^{-1} \cdot K^{-1}$ (@ 500 K).
Taking $\lambda_i = 6.623$ $W \cdot m^{-1} \cdot K^{-1}$, the ratio between the radii of the barrier and inclusion layers was calculated from equation 5.10 to be:

$$r_b/r_i = 1.092$$

If the mean radius of the NiO particles is taken to be 30 μm, then the thickness of the barrier layer is ≈ 3 μm.
(b) Alternatively, it may be considered that the effective conductivity of the porous NiO particles is < 6.623 $W \cdot m^{-1} \cdot K^{-1}$ because their surface structure makes the interface discontinuous. Considering the data for the NiPTC/NiO composite:
Substituting $\lambda_c = 0.654$ $W \cdot m^{-1} \cdot K^{-1}$, $\lambda_m = 0.348$ $W \cdot m^{-1} \cdot K^{-1}$ and $f = 0.305$ into equation 5.9 gives $\lambda_i = 3.370$ $W \cdot m^{-1} \cdot K^{-1}$. Taking this effective value for λ_i in equation 5.10 then gives:

$$r_b/r_i = 1.087$$

and therefore the same approximate value for the thickness of the barrier layer as that found previously. Examination of the interface region by SEM (Plate 11) showed that no visible disruption had taken place. Fissures wider than ~ 0.5 μm would be readily distinguished by inspection.

The experimental results showed that the conductivity of these composites is insensitive to the presence of small volume fractions of very high conductivity material (e.g. 3% silver). Even a large fraction of highly conductive material dispersed in the low conductivity continuous phase had a surprisingly small effect. These effects were reflected in the λ values calculated from the H&S binary model, which appeared to be the most applicable to the porphyrin/oxide system. The ternary (coated-sphere) model, and the barrier layer properties calculated from it, were found to be insensitive to the effective conductivity of NiO, and would not therefore be a suitable for predicting it. This model did not give a realistic prediction of the thickness of the PTC$\leftrightarrow$NiO barrier layer, but uncertainty as to the composition and pressure of the interfacial gas meant that the calculated thickness was unlikely to be accurate to better than an order of magnitude. Although no suitable model was identified for predicting the contribution of the interface layer to λ, the modified fusion onset slope method was able to detect very significant changes

in this region. The ΔR data also provided useful information. This showed that disruption of the PTC/NiO interface was complete by 250°C, whereas the improved NiPTC/NiO contact which resulted from heating was not optimised after a single scan to this temperature.

Table 5.1

Physical properties of compacted porphyrin tablets (ø = 6.0 mm)

Sample	Number of observations	Density /g·cm^{-3}		Axial Thermal Resistance /K·W^{-1}·mm^{-1}	
		This work	Literature*	Discrete intercept	Common intercept
OEP	15	1.172 ± 0.005	$1.19_{(tri)}$ [107]	141.4 ± 14.7	137.6 ± 4.2
TPP	15	1.220 ± 0.012	$1.27^{(tet)\ [109]}_{(tri)\ [110]}$	159.3 ± 11.0	171.6 ± 4.5
T(*p*-MP)P	13	1.250 ± 0.002	n.a.	139.1 ± 13.3	143.2 ± 4.2
PTC	17	1.391 ± 0.006	$1.45^{\#\ [103]}_{(mono)\ [104]}$	131.4 ± 8.7	130.6 ± 4.1
NiPTC	14	1.589 ± 0.005	$1.63_{(mono)}$ [103]	129.1 ± 9.1	128.2 ± 2.4
T(PFP)P	30	1.628 ± 0.009	n.a.	200.4 ± 14.3	199.0 ± 3.5

* From XRD and/or flotation.
Crystal form: $_{(tri)}$ = triclinic, $_{(tet)}$ = tetragonal, $_{(mono)}$ = monoclinic

\# Another source [111] gives the density of monoclinic PTC as 1.67, but the lower value [103,104] is more consistent with the current work and the existence of another monoclinic structure, which is stable at high pressure [112], with a density of only 1.50.

Table 5.2

Calculated physical properties of single-phase porphyrins

Sample	Thermal conductivity /$W \cdot m^{-1} \cdot K^{-1}$			Molecular volume /$m^3 \times 10^{-28}$
	Fourier (one-dimensional)		Relative to silica	
	Discrete intercept	Common intercept		
OEP	0.250 ± 0.026	0.257 ± 0.008	0.330 ± 0.034	7.58 ± 0.03
TPP	0.222 ± 0.015	0.206 ± 0.005	0.264 ± 0.026	8.37 ± 0.08
T(*p*-MP)P	0.254 ± 0.024	0.247 ± 0.007	0.317 ± 0.032	9.76 ± 0.02
PTC	0.269 ± 0.018	0.271 ± 0.009	0.348 ± 0.035	6.14 ± 0.03
NiPTC	0.274 ± 0.019	0.276 ± 0.005	0.354 ± 0.036	5.97 ± 0.02
T(PFP)P	0.177 ± 0.013	0.178 ± 0.003	0.228 ± 0.022	9.94 ± 0.05

Table 5.3

Composition of binary mixtures

Mixture	Matrix phase	Included phase	Mass fraction of inclusions	Volume fraction of inclusions	Measured density of composite /g·cm^{-3}
1	PTC	Ag(< 152 μm)	0.200	0.032	1.66 ± 0.08
2	PTC	Ag(< 251 μm)	0.883	0.500	5.99 ± 0.15
3	PTC	NiO*	0.500	0.222	2.163 ± 0.012
4	NiPTC	NiO#	0.574	0.305	2.700 ± 0.052

* sieved (38-75 μm), no thermal treatment
\# sieved, annealed in argon (24 hours @ 300°C)

Table 5.4

Thermal conductivity data for binary mixtures

Mixture (Composition) {Number of obs.}	Thermal conductivity /W·m^{-1}·K^{-1}				
	Measured*		Calculated		
	Fourier	Rel. silica	Geom. mean	Bruggeman	Hashin-Shtrikman
1 (PTC/0.032Ag) {8}	0.274 ± 0.009	0.349 ± 0.036	1.57	0.385	0.382
2 (PTC/0.500Ag) {16}	1.342 ± 0.102	1.722 ± 0.212	20.9	104.0	1.387
3 (PTC/0.222NiO) {28}	0.273 ± 0.006	0.350 ± 0.035	1.96	0.722	0.593
4 (NiPTC/0.305NiO) {25}	0.510 ± 0.022	0.654 ± 0.069	2.27	1.039	0.729

* ex. common intercept with all data in Table 5.2 except T(PFP)P

(a) Du Pont aluminium pan.

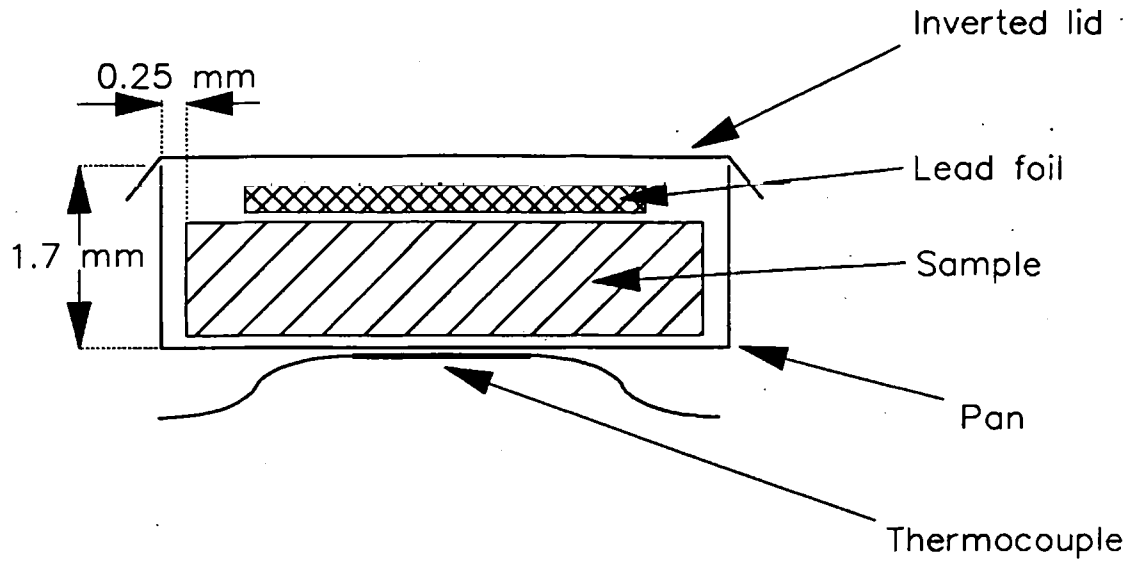

(b) Perkin–Elmer steel pan.

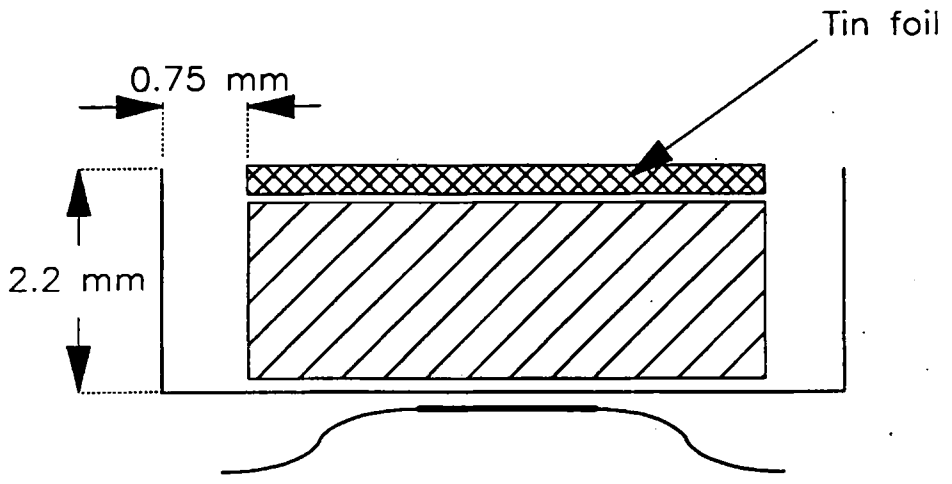

Figure 5.1 – Critical dimensions in the thermal conductivity experiments.

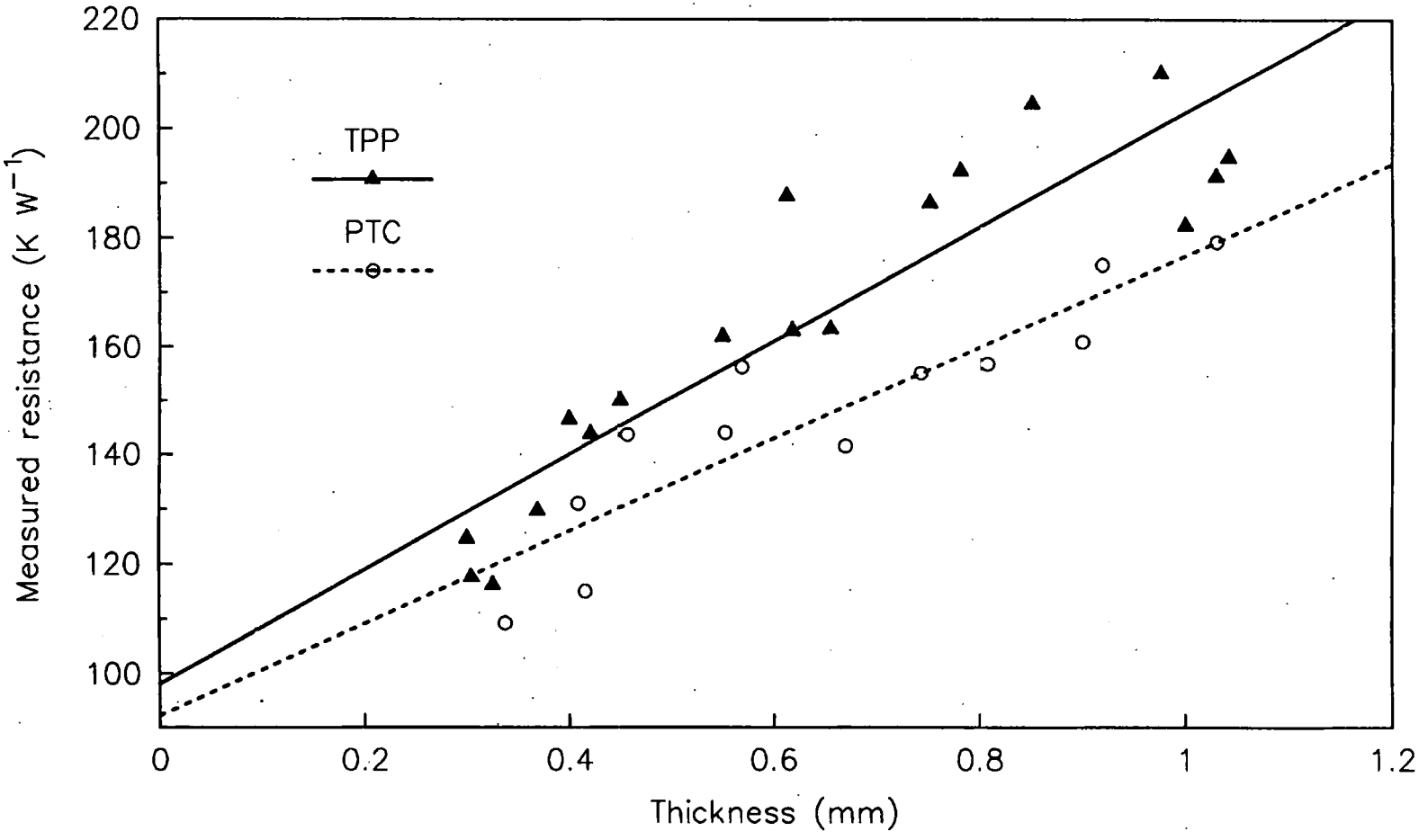

Figure 5.2 – Linear regression plots for preliminary data.
(~ 328–332 °C ex. fusion of lead)

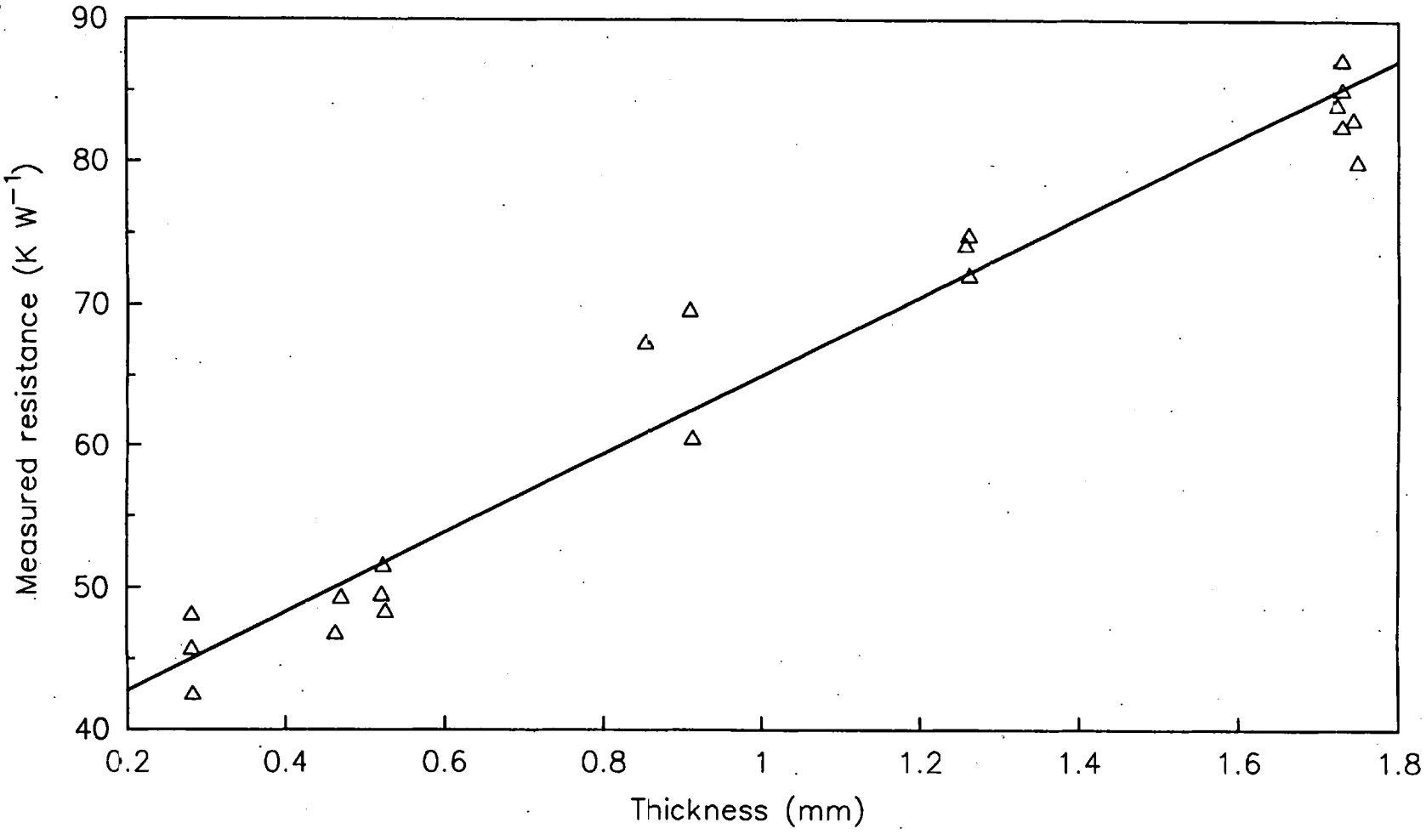

Figure 5.3 – Calibration plot using data for vitreous silica.
(~ 233–238°C ex. fusion of tin)

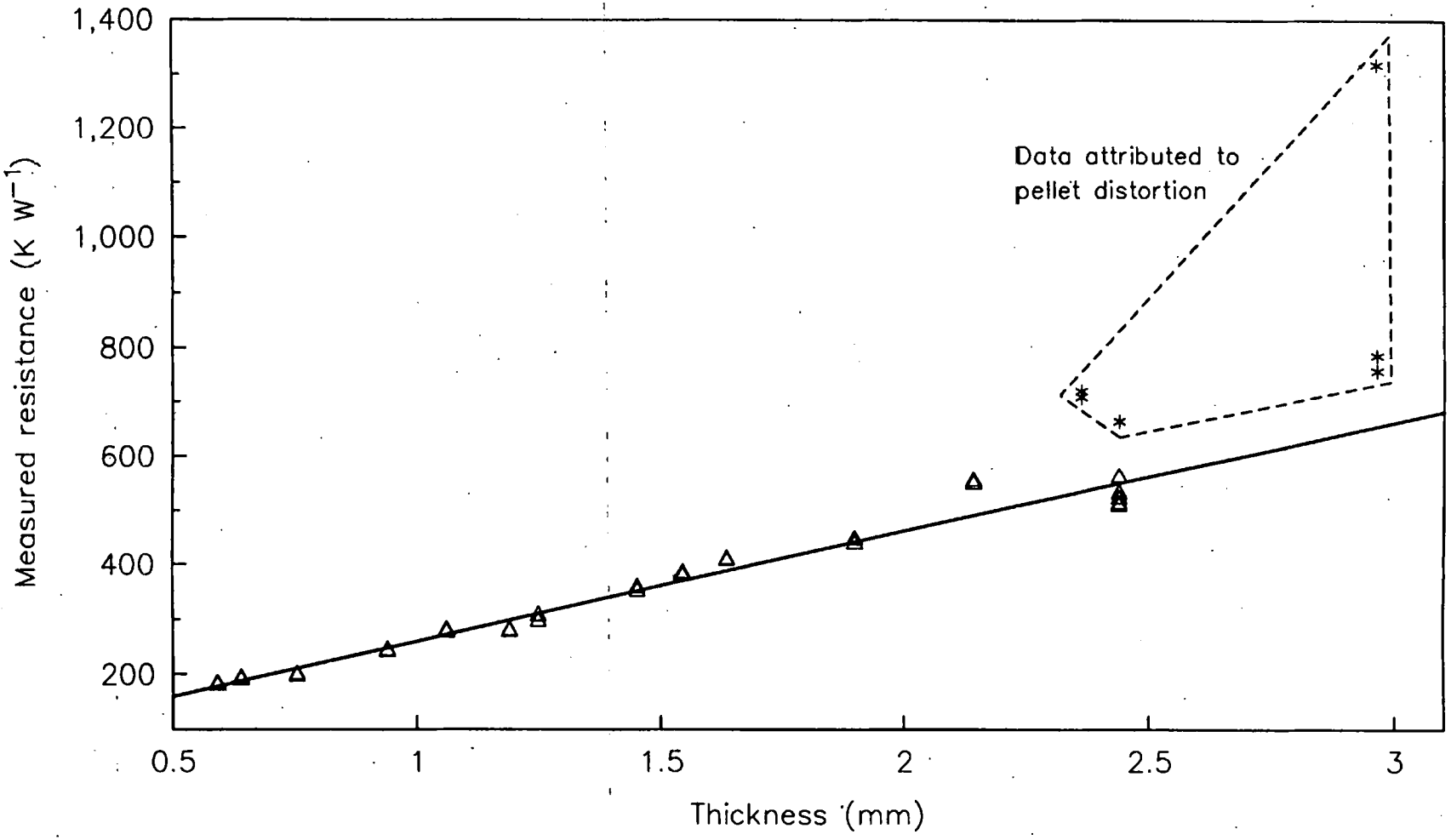

Figure 5.4 – Linear regression plot for T(PFP)P data.
(~ 233–238°C ex. fusion of tin)

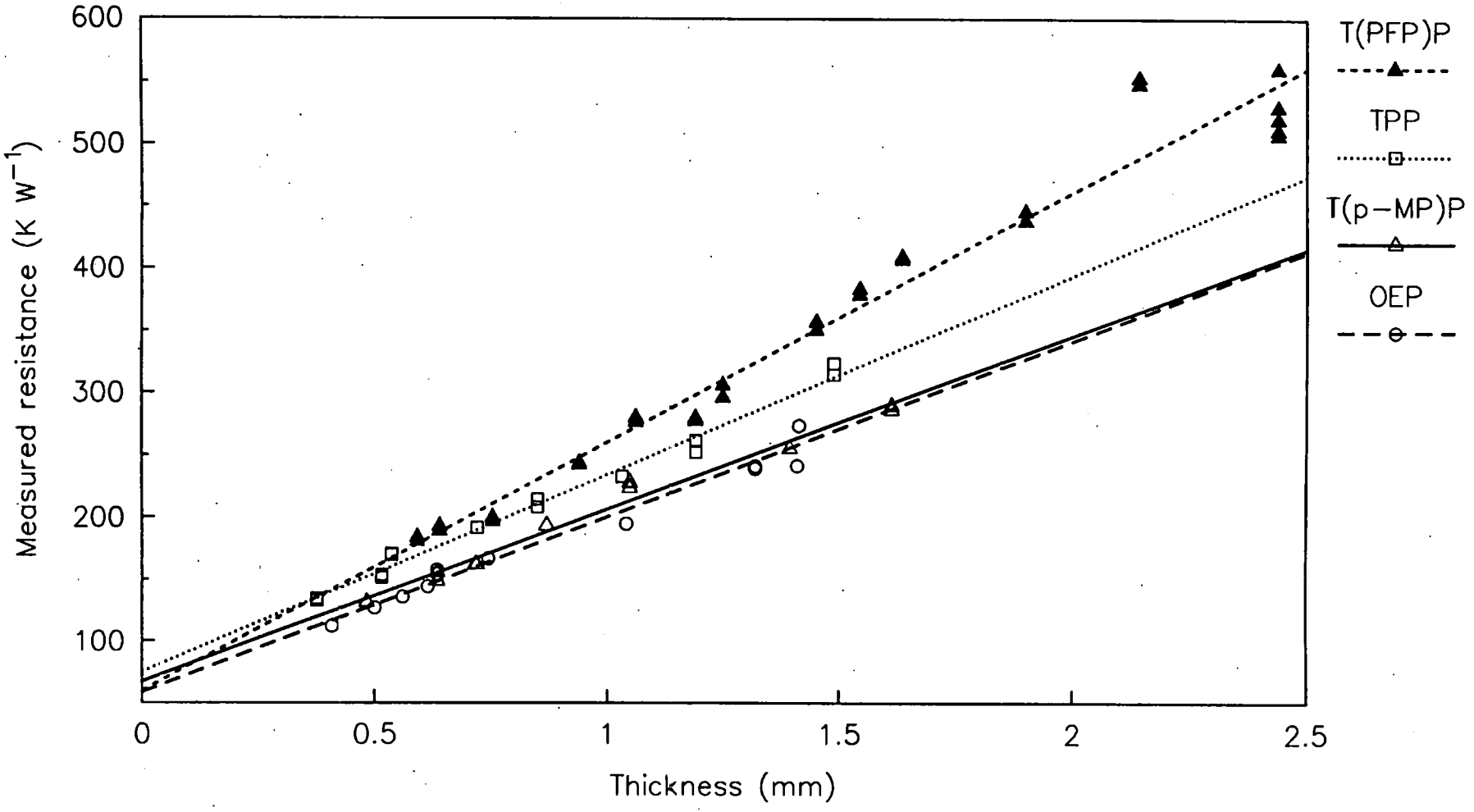

Figure 5.5 – Linear regression plots for porphyrin data.
(~ 233–238°C ex. fusion of tin)

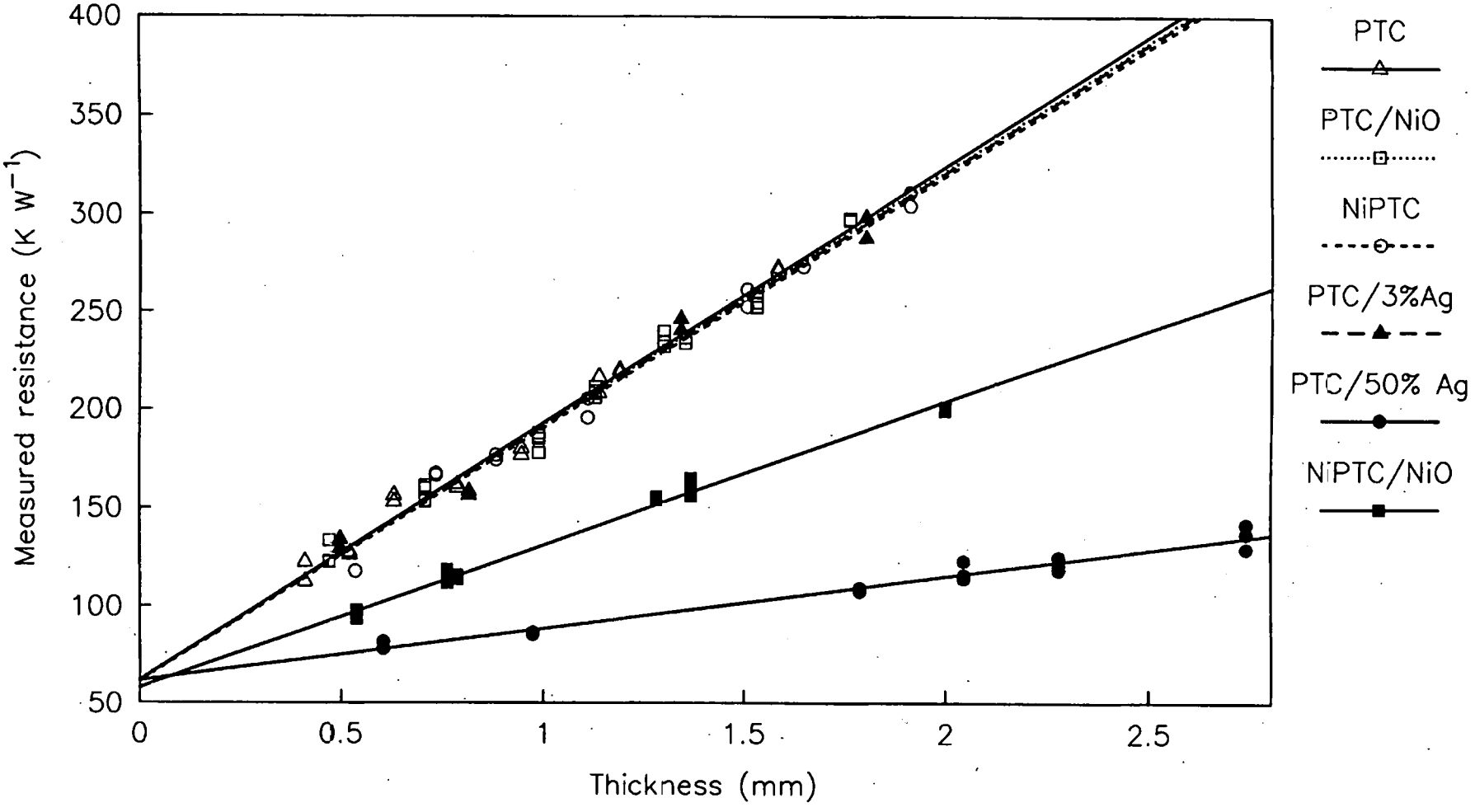

Figure 5.6 – Linear regression plots for phthalocyanine and binary mixture data. (~ 233–238°C ex. fusion of tin)

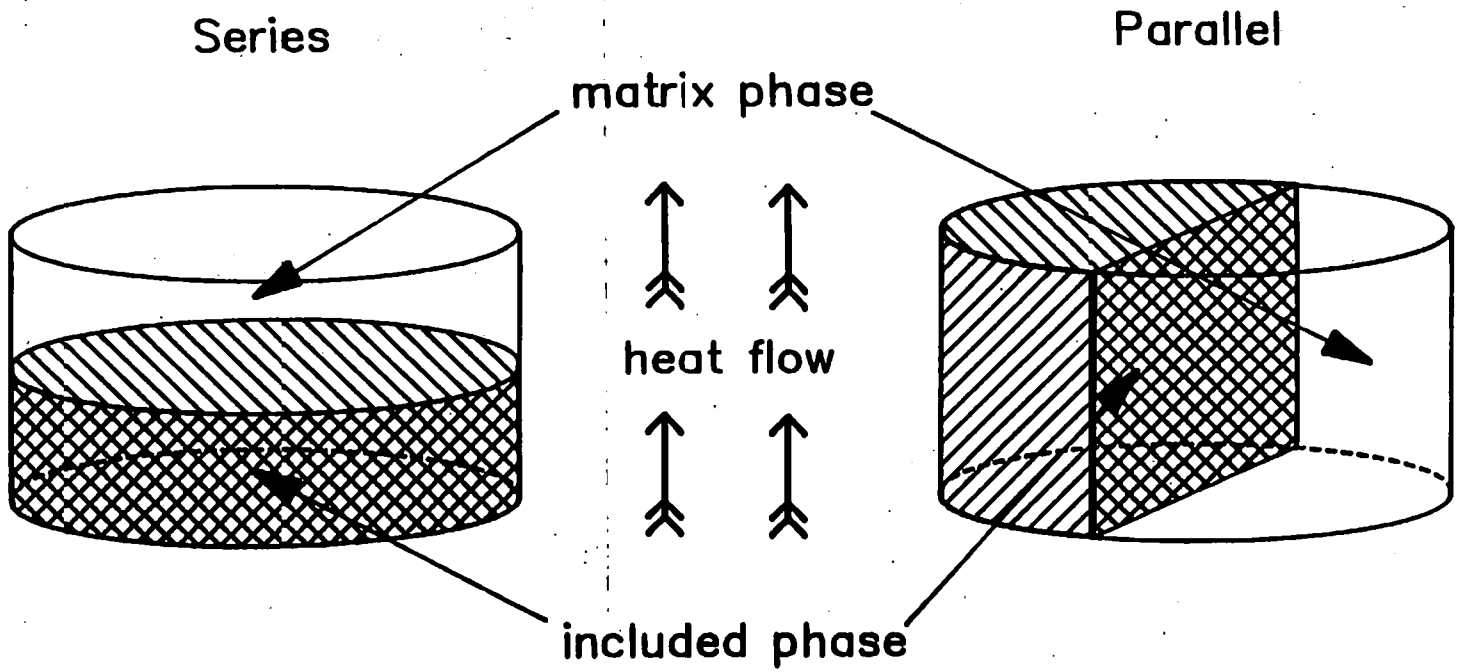

Figure 5.7 – Boundary models for calculation of bulk transport properties.

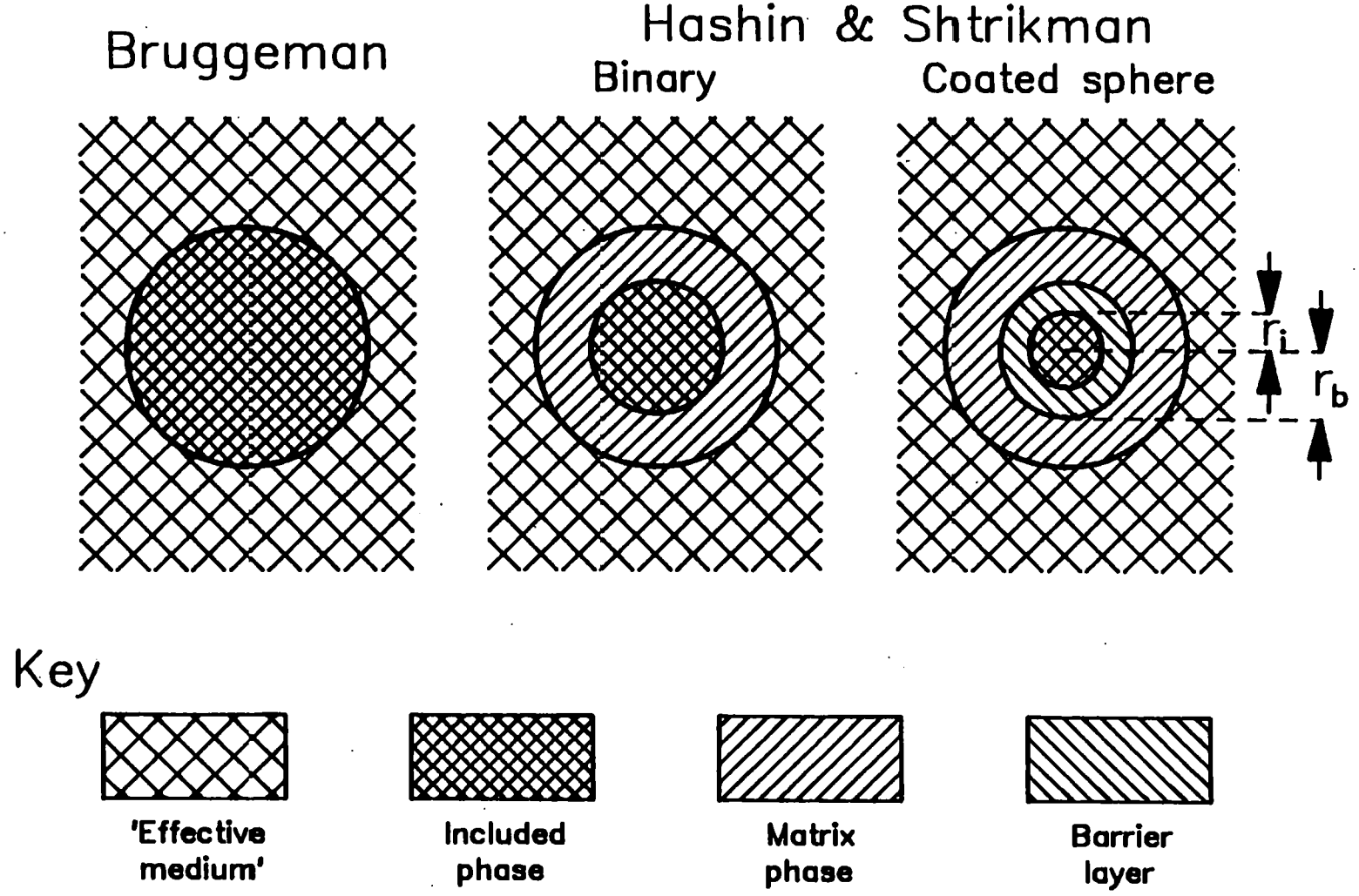

Figure 5.8 – Effective medium models for calculation of bulk transport properties.

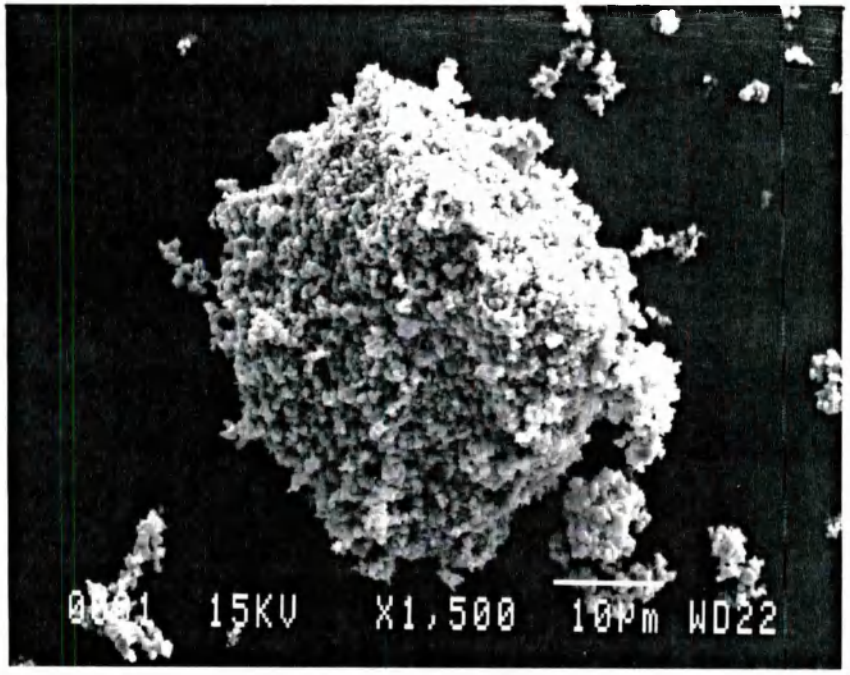

(a) Magnification x1,500, showing general grain morphology.

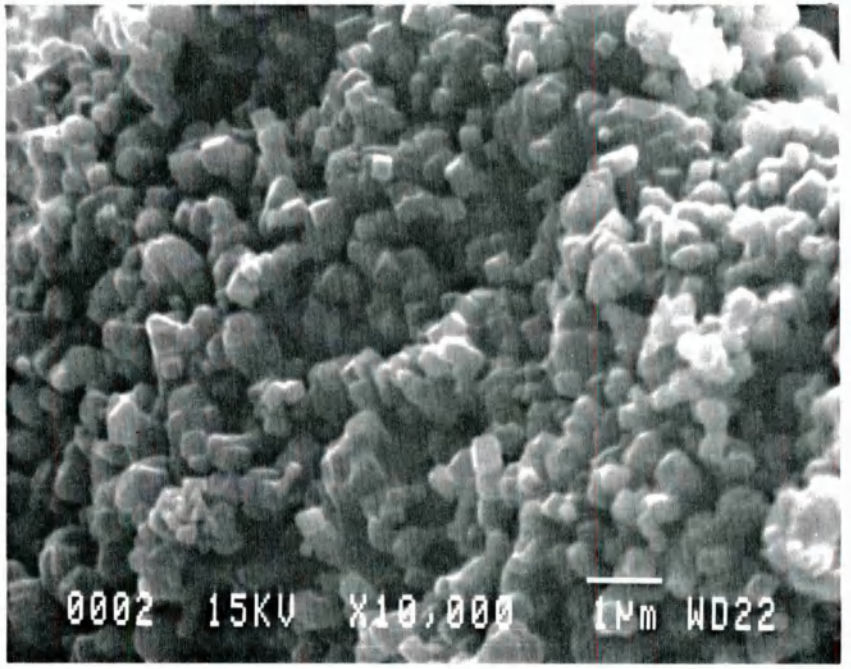

(b) Magnification x10,000, showing microstructure.

PLATE 6 – Scanning electron micrographs of sieved (38–75 μm) nickel(II) oxide.

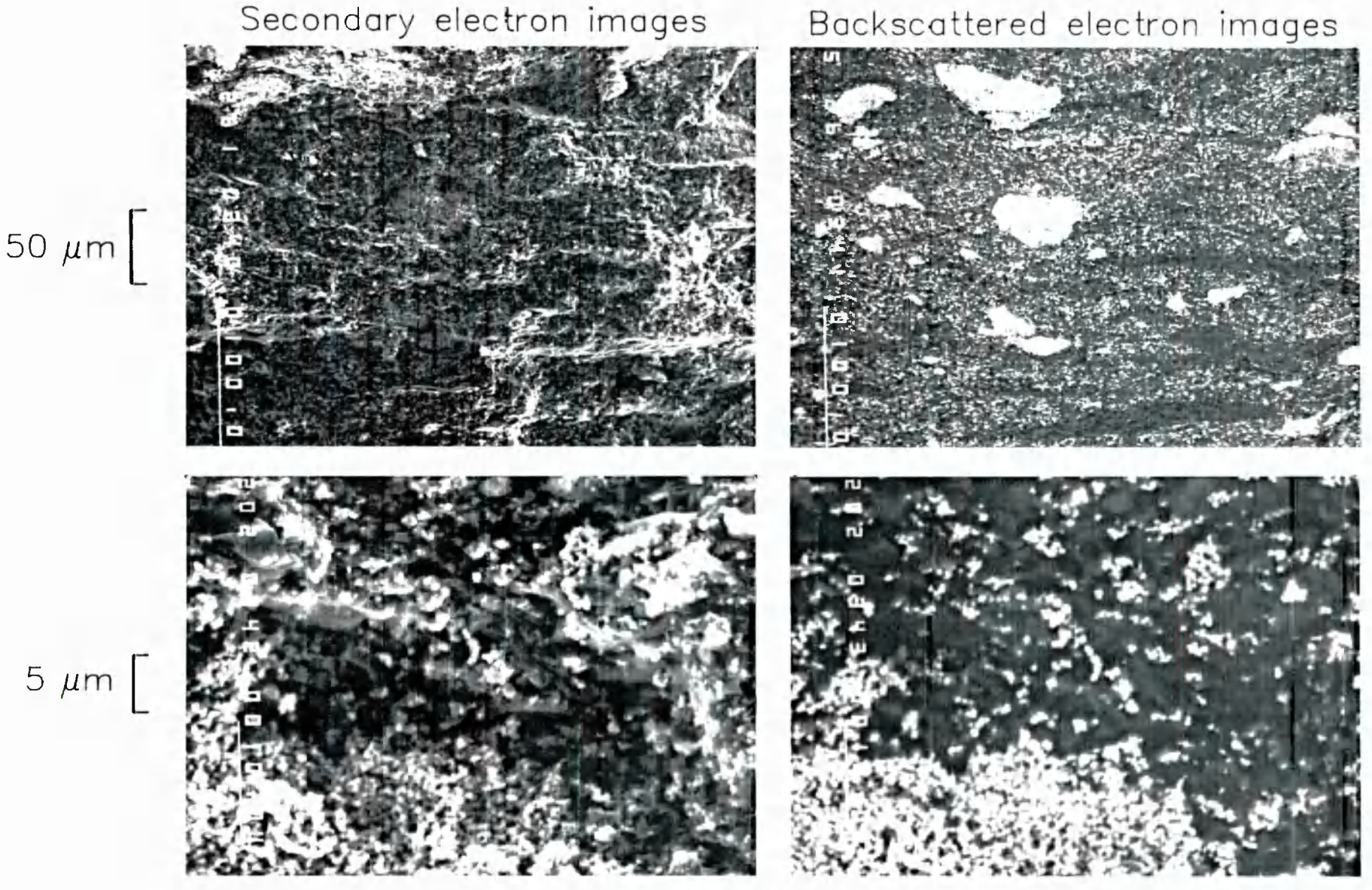

PLATE 7 – Scanning electron micrographs of a composite containing nickel(II)phthalocyanine + nickel(II) oxide: before heating.

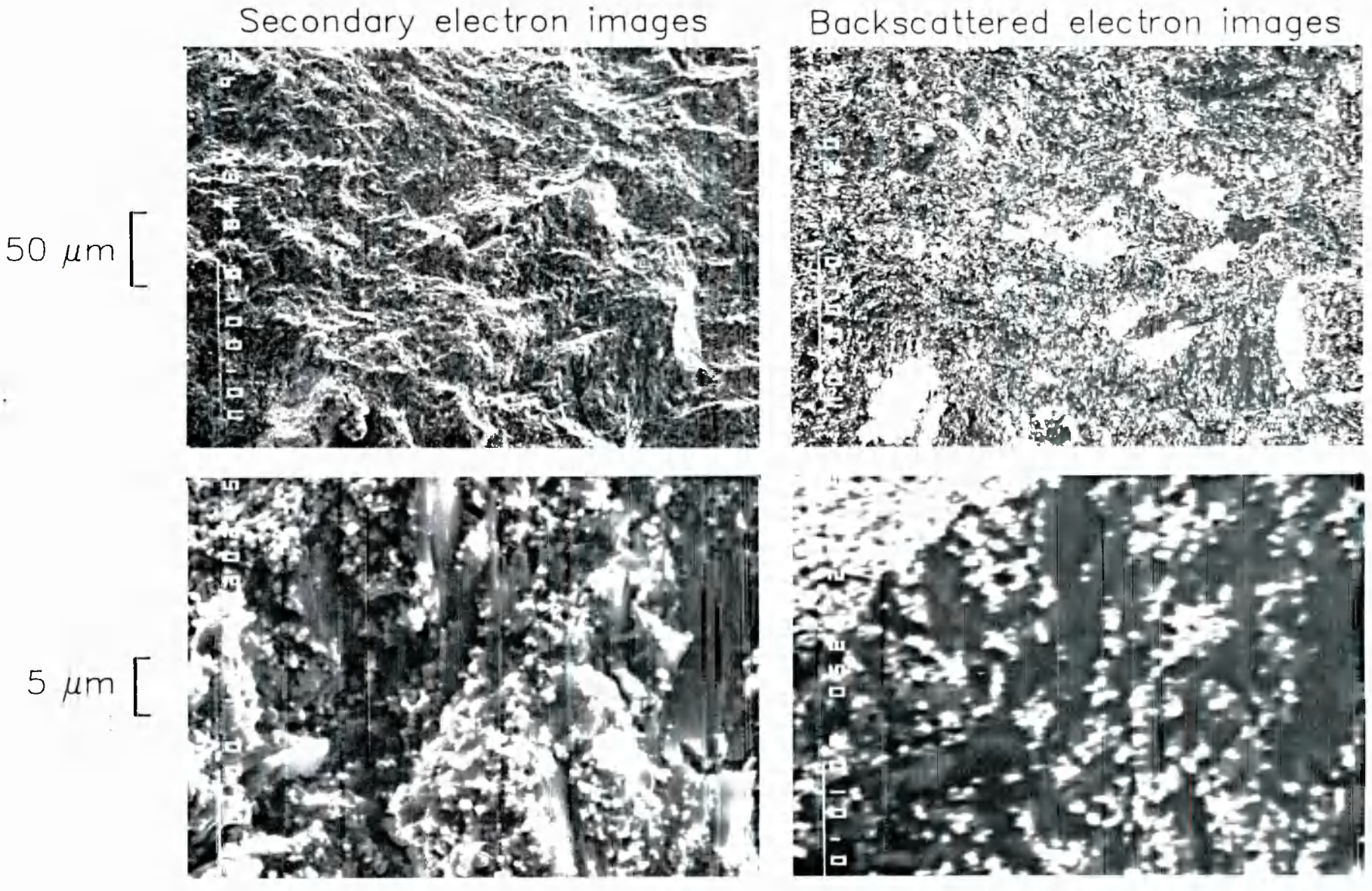

PLATE 8 – Scanning electron micrographs of a composite containing nickel(II)phthalocyanine + nickel(II) oxide: after heating to 350°C.

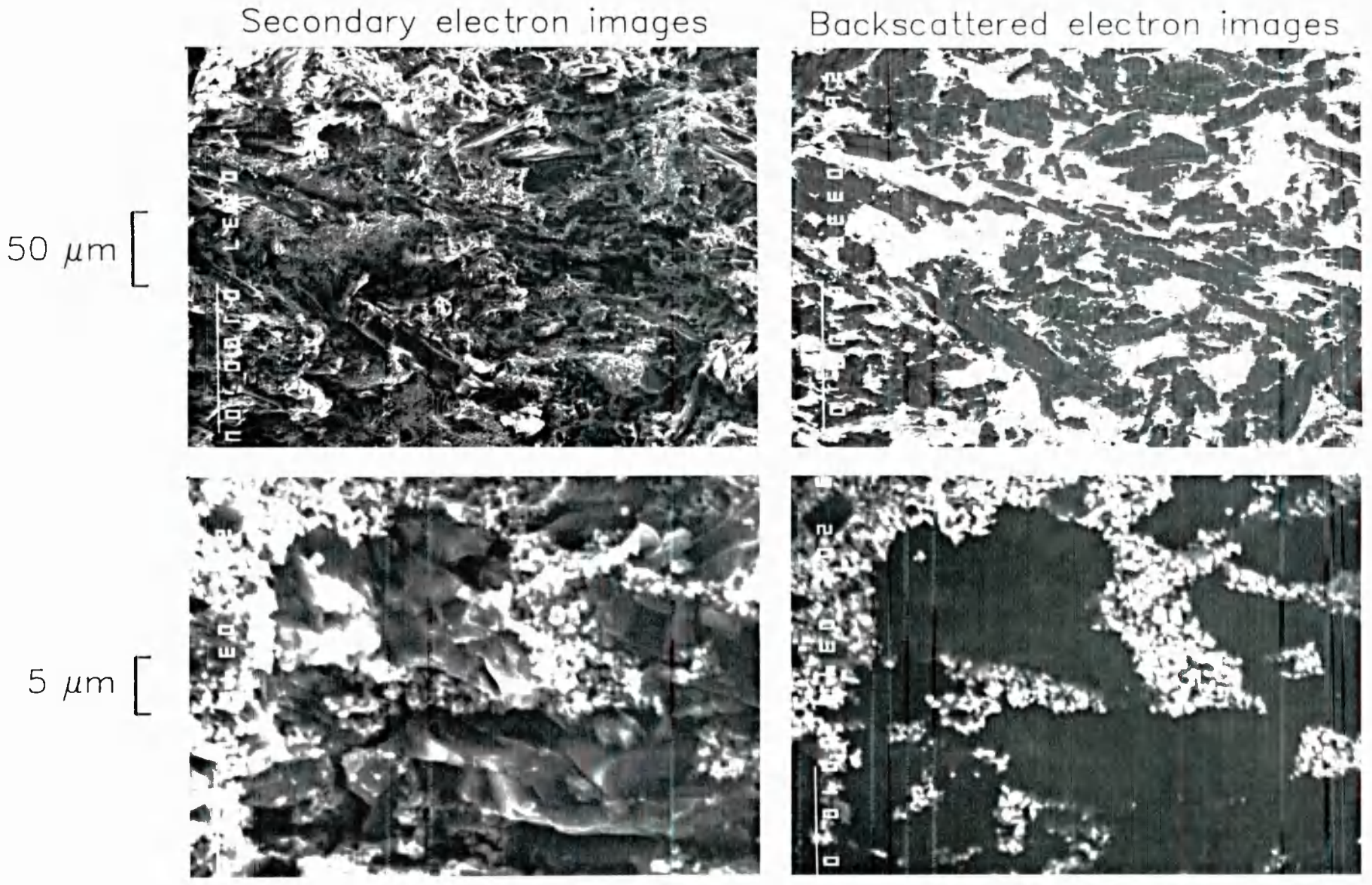

PLATE 9 – Scanning electron micrographs of a composite containing phthalocyanine + nickel(II) oxide: before heating.

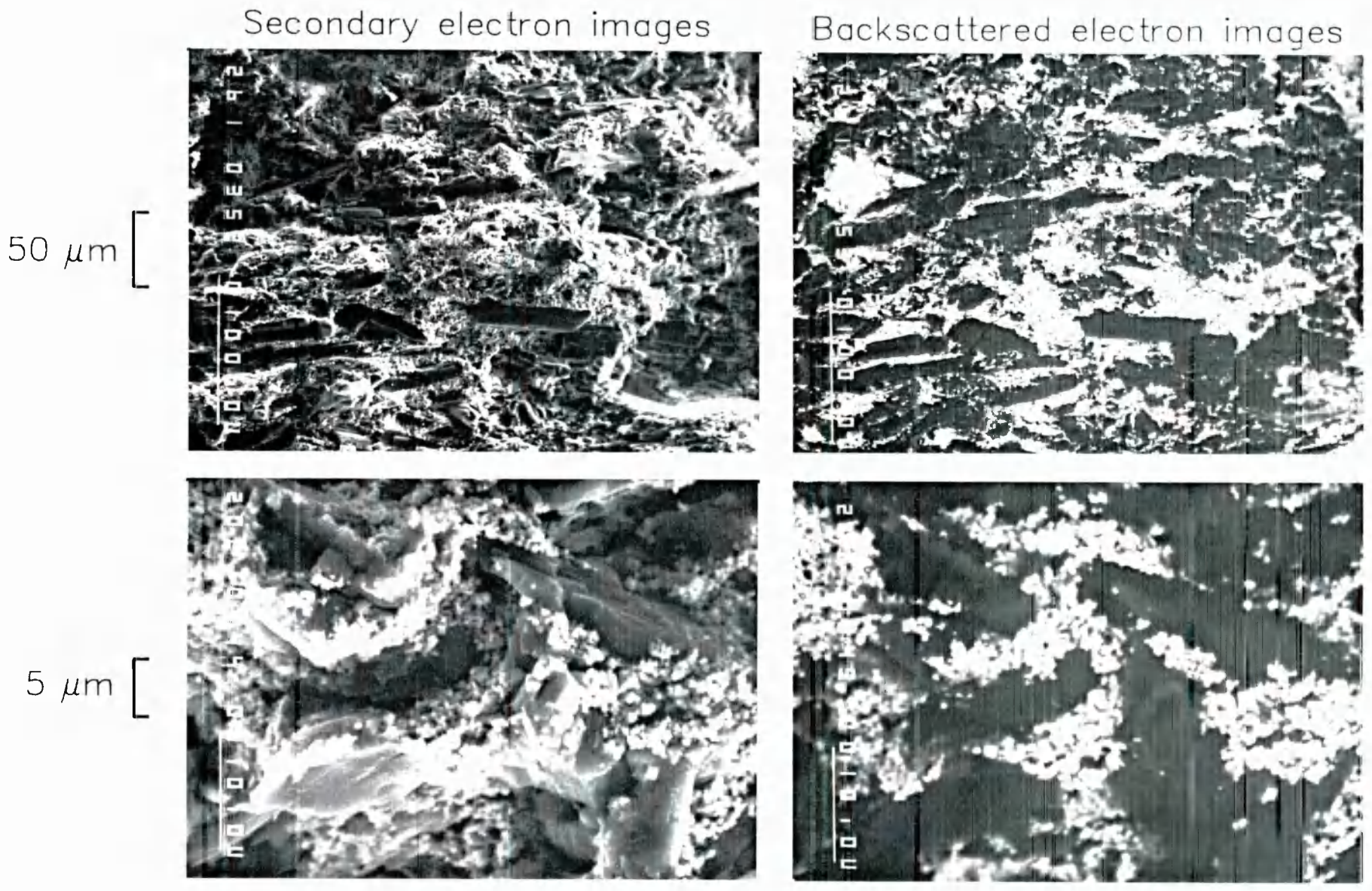

PLATE 10 — Scanning electron micrographs of a composite containing phthalocyanine + nickel(II) oxide: after heating to 350°C.

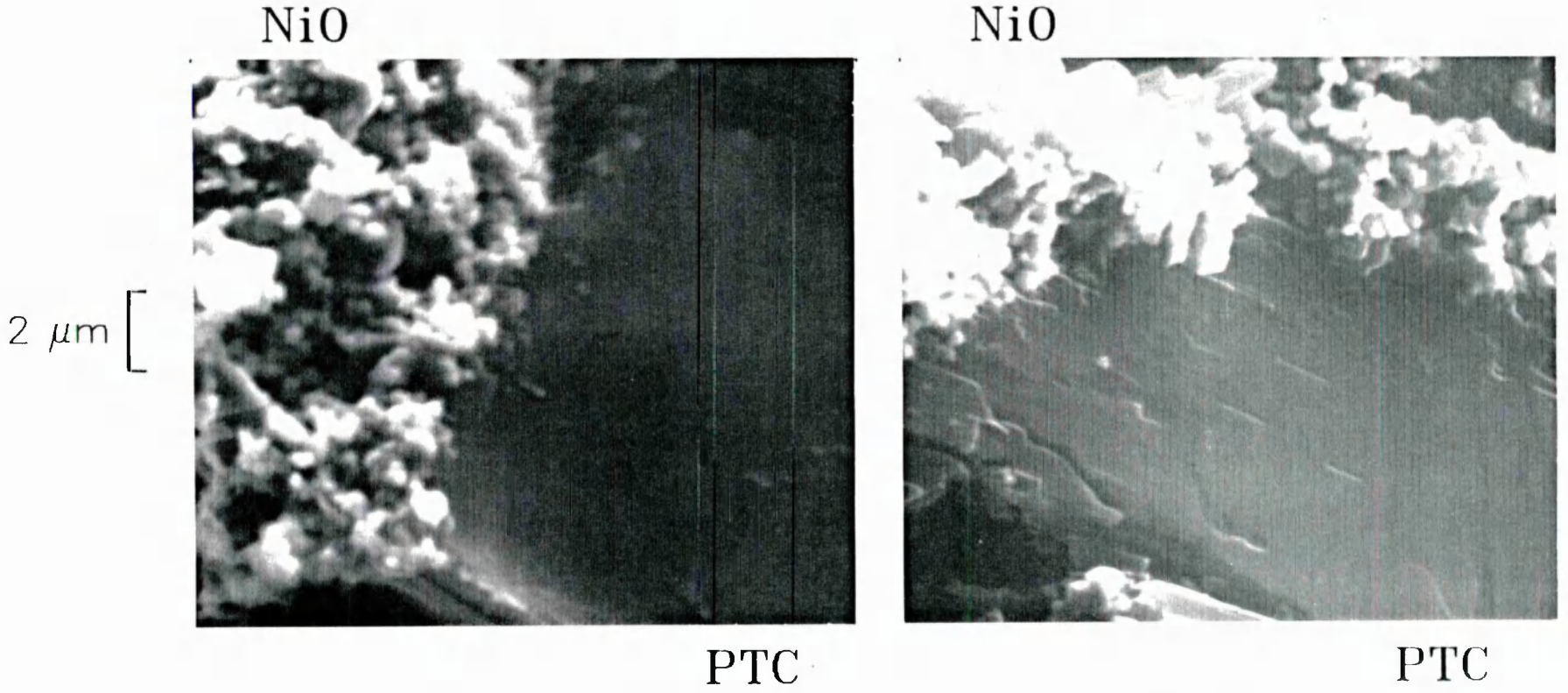

(a) Before heating

(b) After heating to 350°C

PLATE 11 – Scanning electron micrographs of the interface region in a phthalocyanine/nickel(II) oxide composite.

CHAPTER 6

THE USE OF DSC TO DETECT INTERACTIONS BETWEEN PORPHYRINS AND NICKEL(II) OXIDE

6.1 INTRODUCTION

The effects of temperature gradients in large DSC samples have been analysed in detail [113,114] for Setaram's model DSC-111 (Tian-Calvet) calorimeter. These studies focused on its application to detecting the curing reactions in rubbers and thermosetting resins. Very large samples (~ 150 mg) were used because the materials tended not to be homogeneous. This led to poor DSC repeatability when smaller sample sizes were used. Both rising temperature and isothermal experiments were considered and the latter were found to give the greater practical difficulties. Problems arose because the initial part of an isothermal DSC experiment involves rapid heating of the cell from ambient conditions to the required steady temperature. The offset of the DSC baseline during this period is much larger than the height of the exothermic peak due to curing. Furthermore, the curing reaction often begins during the initial temperature stabilisation period. The reaction exotherm was successfully deconvoluted from the overlaid offset by carrying out two identical temperature-jump/isotherm experiments on each sample. The sample was fully cured after the first heating and hence the second DSC curve showed the $\Delta\Phi$ offset and subsequent steady baseline in the absence of reaction. Provided that the starting temperature was the same for each experiment, subtraction of the two time-based plots then gave a simple DSC peak for the curing reaction which had a virtually flat baseline.

Although file subtraction can be very useful in correcting for interfering background events, it is not widely used in thermal analysis. Because of the wide variety of experimental variables, there are no standard techniques or even guidelines. The most important factor is that <u>everything</u> apart from the reaction event under investigation must be closely matched between the initial DSC scan and the reference scan which is subtracted from it. If this is not done, artifacts are likely to be created and the situation will be worse than if the raw data were used. Figure 2.20 illustrated formation of a peak at the Néel point for nickel(II) oxide simply by altering the external geometry of the sample container. Similar effects are to expected if the effective resistance or resistance profile within the specimen are altered. One of the main objectives in carrying out data

subtraction in the work described in this chapter was to correct for the complex background curve due to nickel(II) oxide. In theory, a reference file could be created by combining DSC curves for separate scans on the porphyrin and nickel oxide. However, the difficulty of matching the resistance for each of these specimens with that of the composite made this approach unattractive. Peaks are likely to be produced at the Néel point by differences between the thermal conductivity of the sample and the materials used as references. If events were observed in the Néel point region of the subtracted curve, they could not be assigned with any confidence to interactions within the composite. An alternative approach was that used by Vergnaud [113] and Liu *et al* [114] for quasi-isothermal experiments, i.e. to use the fully reacted specimen as the reference. This was felt to be the better approach for rising temperature experiments, being both simpler and offering a better match of sample resistance than scanning the components separately.

6.2 SIGNIFICANCE OF THE Néel TRANSITION IN SOLID-STATE REACTIONS

Ferromagnetic materials become paramagnetic at a characteristic temperature known as the Curie point. It has been found that the kinetics of various surface reactions change at this point: several ferrous metals and alloys show a maximum rate of nitriding [115] or cycloalkane dehydrogenation [116] during the transition; reduction of NiO shows a discontinuity of its temperature dependence at 350°C [117], which corresponds to the Curie point of metallic nickel. Kirilyus [116] attributed anomalous reactivity at the Curie point to the 'Hedvall Effect', which assumes that the mobility of a crystalline lattice, and hence diffusion through it, increases during a phase transition. If the rate controlling process for a solid state reaction is diffusion in one of the reactants (or a product which forms a barrier layer) then the reaction rate should increase during a transition in that phase. The existence of the Hedvall Effect is subject to debate [118], but in many cases a change of reactivity may also be explained by interfacial stress caused by dimensional changes during the transition. Stress tends to increase the rate of nucleation and can also disrupt an existing product layer which acts as a barrier.

The Néel transition (antiferromagnetic→paramagnetic) has a different low temperature phase from that in the Curie transition, but both events involve changes of heat capacity and unit cell dimensions. Heating nickel(II) oxide through the Néel transition (at 250°C) changes its unit cell from rhombohedral to cubic symmetry, with dimensional changes of +0.1% and −0.05% occurring along perpendicular axes of the crystal lattice [119]. Anomalous reactivity at the Néel point does not appear to have been reported, but there is circumstantial evidence connecting decomposition of nickel(II) hydroxide at ~ 230°C [120] with the transition in nickel oxide.

The $Ni(OH)_2$ lattice has a 1:2:1 planar structure (CdI_2 type) in which layers of OH^- ions are adjacent to each other and alternate with single layers of Ni^{2+} ions. Cubic nickel(II) oxide has the NaCl structure, in which the Ni^{2+} ions are hexagonally packed in the (111) plane. This corresponds to the basal hexagonal plane (0001) in the hydroxide:

i.e. $$(0001)Ni(OH)_2 \,||\, (111)NiO.$$

Other correlations have been identified between crystal planes in the two structures [121,122], which are the reactant and solid product in the dehydroxylation reaction:

$$Ni(OH)_2 \rightarrow NiO + H_2O\uparrow$$

These structural relationships define the reaction mechanism as being topotactic*. The rhombohedral form of nickel(II) oxide (< 250°C) is slightly distorted relative to the cubic structure and will have a different lattice energy. The structure of the product is particularly important in topotactic reactions and one of the NiO crystal structures will be thermodynamically preferred as a product. This means that, if the reaction is already under way at 250°C, the rate of reaction is expected to change at this point. Alternatively, the energetic changes at the Néel point may be such that reaction is actually initiated during the transition.

---

*Transformations in which there is 3-dimensional accord between the lattice structures of initial and product phases are known as topotactic. Epitactic processes involve a 2-dimensional relationship.

When the adjacent layers of OH^- ions in $Ni(OH)_2$ decompose, the crystal cleaves along the basal planes into hexagonal plates (Figure 6.1) and water vapour escapes via the interlamellar spaces. The stack then collapses perpendicular to this plane ($d_{0001} \rightarrow d_{111}$), with a dimensional change of −48%, while the radius of the plates decreases by 5.6% [122]. The overall decrease in volume of the solid is 53%, which is the difference between the molar volumes of nickel hydroxide and oxide. Chemisorption of atmospheric water and carbon dioxide will create a surface layer on the oxide, whose structure is likely to resemble a complex nickel hydroxide/carbonate. This is the reverse of the mechanism described by Shannon [82] for decomposition of carbonates. Heating the oxide will decompose the surface compounds and, although they are in the form of a relatively thin layer, the dimensional changes per unit volume during decomposition are much larger than those due to the Néel transition in the underlying oxide. In a porphyrin/nickel oxide composite, all of the following processes are therefore likely to contribute to a build up of stress at the interfacial contact:

(a) Dimensional changes in the NiO lattice during the Néel transition.

(b) Dimensional changes in the $Ni(OH)_x(CO_3)_y$ lattice of the surface layer during decomposition.

(c) Build up of pressure by water vapour, which is contained at the interface by the surrounding porphyrin matrix.

The last two will be concurrent: expansion due to (c) will tend to oppose shrinkage, but it is unlikely that the net effect will be zero. The dimensional changes in (a) and (b) are anisotropic and hence, even at constant volume, shearing stress will be generated preferentially in some directions. Whichever mechanism predominates, stress will be induced somewhere in the interfacial region and is likely to affect the reaction.

6.3 PRELIMINARY INVESTIGATIONS

Differential scanning calorimetry (DSC) is an obvious technique for investigating relationships between the transition in nickel(II) oxide and interfacial processes. The enthalpy change accompanying an interaction will be detected simultaneously with the heat capacity

change at the Néel point, making concurrence of the two events easy to identify. However, the complex form of the DSC curve for nickel(II) oxide in this temperature region makes it difficult to detect superimposed thermal events. Furthermore, the limited area of the solid-solid contact means that the extent of interaction is limited and associated energy changes are small. These factors make the study of interactions in the porphyrin/NiO system a particularly rigorous test of the capabilities of DSC.

An initial set of experiments was carried out to establish that reaction can occur between a solid porphyrin and nickel(II) oxide and be detected by DSC. Commercially available nickel oxide and *meso*-tetraphenylporphyrin (TPP) were used 'as supplied' in this study, without any pre-treatment or purification.

6.3.1 Reaction under DSC conditions

The dry reactants were mixed together and compressed into circular tablets using a 6 mm diameter die and a compaction pressure of ~ 850 MPa (as for the λ measurements in the last chapter). Mould release agent was not used because it might undergo detectable interaction with the composite. In spite of this, none of the composites gave problems of adhesion onto the die faces. The effect of pellet composition on the DSC curve was not investigated but 40% m/m of TPP was found to produce cohesive pellets which did not fracture on heating. Pellets weighing ~ 40 mg were contained in covered aluminium pans and analysed under the following conditions:

Temperature programme; 25-420°C @ 20°C•min^{-1}
Atmosphere; dry nitrogen, flowing at 25 cm^3•min^{-1}.
Amplifier range; x10
Digitisation rate; 1 Hz.

The DSC curve (Figure 6.2) showed several events in the temperature region 120-400°C. These events were relatively small and superimposed on a steeply sloping background, which made it difficult to identify their onset and termination points. Temperatures of 100, 180, 240, 300 and 400°C were selected by inspection as nominal boundaries for the regions of apparent thermal activity.

6.3.2 Development of an HPLC procedure

Normal and reversed-phase high performance liquid chromatography (HPLC) have both been applied to the separation and analysis of porphyrins [151]. Most work has been done on porphyrins derived from petroleum ('petroporphyrins') in which the nucleus is most often β-alkylated rather than carrying aryl groups at the *meso* positions. In order to detect the formation of tetraphenylporphyrinato-nickel(II) (NiTPP) in the composites, and to quantify it in mixtures containing excess free-base, both chromatographic techniques were investigated.

The apparatus consisted of a Waters model 6000A pump with a Cecil 2112 variable wavelength UV detector. Porphyrins have a very strong $\pi \rightarrow \pi^*$ absorption (the Søret band) in the 380-420 nm region of the ultraviolet which is commonly used for detection in HPLC. A preliminary UV scan of NiTPP dissolved in toluene showed that the absorption maximum was at ~ 410 nm. This wavelength was used for detection while chromatographic conditions were being developed. Initial investigations using silica (5 μm Spherisorb) as a stationary phase, with toluene or toluene/methanol mixtures as eluent, were not successful. The peak for the complex tailed badly, probably due to decomposition on the active silica surface, and resolution was poor. Separation by reversed-phase chromatography, with tetrahydrofuran (THF) in acetonitrile as the eluent, was found to be more efficient. In both cases, the solvent mixture was stabilised by ultrasonic agitation for 20 minutes, left to stand for 24 hours and finally degassed with helium before use.

The detection wavelength was optimised using a standard solution containing 10^{-4} mol$\cdot$l^{-1} of both TPP and NiTPP in THF. Repeated injections of 2 μl were made at 2 nm increments of the detector (Figure 6.3). This showed that the peak response for NiTPP in THF/acetonitrile lay in the 412-414 nm region, while that for TPP was at longer wavelength. Consequently, 412 nm was chosen to give the best discrimination in favour of the complex.

The analytical conditions finally selected were:

Column: 250 x 4.6 mm Spherisorb ODS-2 (5 μm)
Mobile phase: 15% v/v THF in acetonitrile
Flow rate: 2 $cm^3 \cdot min^{-1}$
Detector: Absorbance range = 0.2; λ = 412 nm.

6.3.3 Analysis of reaction products from DSC

Pellets of the NiO/TPP composite were heated in the DSC to each of the boundary temperatures identified above. On reaching the required temperature, the sample was removed from the cell and quenched in liquid nitrogen to prevent further reaction. The pellets were then crushed and extracted by ultrasonic agitation in THF. Each solution was filtered through a glass-fibre filter and diluted to 50 cm^3 with THF. These solutions contained a large excess of unreacted TPP, which meant that baseline separation between the free-base and complex was not achieved (Figure 6.4). In order to make the calibration representative of the analytical samples, standards covering a range of NiTPP concentrations 5-100 $mg \cdot l^{-1}$ were made up in a solution containing 300 $mg \cdot l^{-1}$ TPP in THF. These gave a linear response up to ~ 50 $mg \cdot l^{-1}$ of NiTPP for 5 μl injections.

Analysis of the heated pellets showed that nickel complex was formed predominantly in the intervals 180-240°C and 300-400°C. Integrating the corresponding DSC peaks as shown in Figure 6.2 gave approximate values for the enthalpy of reaction in these two temperature regions of −81 and −42 $kJ \cdot mol^{-1}$ of NiTPP respectively. The total yield of nickel complex up to 400°C corresponded to ~ 18% of the initial porphyrin having undergone reaction. No complex was detected in pellets which had been heated up to 100°C, which indicated that < 0.05% of the free-base porphyrin had reacted (based on the estimated detection limit at a signal:noise ratio of 5:1). This result also showed that neither compaction in the pellet press nor ultrasonic agitation in the presence of solvent caused any detectable reaction.

A further experiment was carried out using black, non-stoichiometric nickel oxide ($NiO_{x>1}$) in place of the green, stoichiometric form. The specified nickel content of the black oxide used in this experiment

was equivalent to a composition $NiO_{1.13}$. Pellets of the same nominal composition as before (40% TPP) were heated to 400°C in the DSC. These DSC curves did not show any thermal events which might represent reactions taking place, but analysis of the heated pellets showed that NiTPP had been formed. The total yield at 400°C was equivalent to ~ 19% of the starting porphyrin, which was almost identical to that produced from green nickel oxide. No minor reaction products were evident in the HPLC chromatograms of products from heating TPP with either of the two forms of nickel oxide.

Having established that detectable reactions did occur under these experimental conditions, the reactants were treated and/or purified as described in Appendix II.

6.4 COMPLEMENTARY DATA

The following measurements were carried out to assist in planning the DSC experiments and interpreting the results.

6.4.1 Thermogravimetry (TG) of model nickel compounds

Nickel hydroxide and carbonate were considered as possible surface compounds on the nickel(II) oxide which could influence its reaction with porphyrins. It was of particular interest to investigate the temperature region in which these compounds begin to decompose under the conditions of the DSC experiment and whether the onset of reaction coincided with the Néel transition in nickel(II) oxide. However, these decomposition reactions are reversible and the rate of reaction depends on the ease with which gaseous products can escape. This means that the apparent 'onset temperature' measured by TG is not a formal parameter for the reaction and is therefore difficult to correlate with the Néel transition in nickel oxide. Comparison of DSC and TG data from separate experiments is further complicated by the relatively large temperature gradients in TG. Temperature measurement accuracy is degraded by thermal lag in the TG balance, while temperature gradients within the specimen tend to broaden the measured event. The TG experiment was designed to minimise these instrumental

effects and to create a sample environment which simulated that at the interface in a composite.

Dehydroxylation of a particle embedded in a solid matrix (of porphyrin) will take place in the water atmosphere generated by the initial dehydration step. The sample container used for these TG measurements allowed the decomposing sample to create its own local atmosphere, with minimal internal flushing by the purge gas passing through the TG furnace tube. Powdered samples were packed tightly into Du Pont hermetic aluminium pans, each of which had an effusion hole (0.1 mm diameter) in the crimped lid. This container was placed in the platinum pan of a Du Pont 951 TG balance, in close proximity to the sample thermocouple, as shown in Figure 6.5. A temperature programme of 50-450°C @ 10°C•min^{-1} was used, with a nitrogen atmosphere flowing at 50 cm^3•min^{-1}. The sample thermocouple was calibrated by the melt-drop procedure [123], using indium, tin and lead as temperature standards. Indicated temperature values are believed to be accurate to ± 2°C.

Thermogravimetric analysis was carried out on two commercially available 'compounds' whose compositions were specified as $Ni(OH)_2.xH_2O$ and $Ni_5(CO_3)_2(OH)_6.4H_2O$. Both displayed a gradual loss of mass, beginning almost at the onset of heating, which reached ~ 3% for the hydroxide and ~ 18% for the basic carbonate at 250°C. The form of these events was typical of loss of adsorbed and lattice (crystalline) water. The observed mass losses represent approximately $0.2H_2O$ and $6.3H_2O$ respectively in the nominal formulae of the two compounds. The major event for each sample was a well defined step (Figures 6.6 & 6.7), whose onset (as detected using the derivative (dTG) curve) appeared to be in the 230-250°C region. The corrected step height (normalised to the mass after the initial dehydration up to 250°C) for this event was:

	MASS LOSS (%)	
	(observed)	(calculated*)
$Ni(OH)_2$	~ 16	19.4
$Ni_5(CO_3)_2(OH)_6$	~ 24	10.5

(*based on complete dehydroxylation according to the equations:

$Ni(OH)_2 \rightarrow NiO + H_2O\uparrow$; $Ni_5(CO_3)_2(OH)_6 \rightarrow Ni_5O_3(CO_3)_2 + 3H_2O\uparrow$)

Hazel and Irving [124] found that only about 80% of the theoretical amount of water was lost from $Ni(OH)_2$ on heating, even though X-ray powder diffraction indicated complete reaction. This was attributed to physical retention of water in the porous oxide. The mass loss found here for the simple hydroxide was in good agreement with their findings. The very high mass loss for the basic carbonate indicated that decomposition of the carbonate function had taken place in the same TG step as dehydroxylation. Complete conversion of all carbonate and hydroxide groups to oxide would give a 27.6% mass loss for a basic carbonate of the above formula.

6.4.2 Anion analysis of nickel(II) oxide

The nickel(II) oxide used in this work had a specified purity of > 99.999% (ex. Aldrich) and was supplied with a batch analysis for metallic impurities. No analytical data was provided for extraneous anions. Aldrich indicated that this product is prepared by a two step thermal decomposition of nickel(II) nitrate in air - initially at 400°C, followed by a period at 750-800°C. The product is currently controlled to < 20 ppm NO_3^-, but older batches (including that used in the work described in this thesis) were not analysed for anions.

Sieved samples of nickel(II) oxide, both 'as supplied' and after annealing at 300°C, were analysed for anionic impurities as follows. A weighed sample of oxide (0.5 g) was mixed with 7.5 cm^3 of purified water (ion exchanged and ultrafiltered using the Millipore 'Milli-Q' system) in a sealed vial. The vial was immersed in a water bath at 40°C and subjected to ultrasonic agitation for 1 hour. The oxide dispersion was then filtered < 0.45 μm and the filtrate analysed for anions by means of a Dionex model 12/SP dual column ion-chromatograph. The analytical conditions were as follows:

Separator column: AS4A

Eluent: 1.8 $mmol \cdot l^{-1}$ Na_2CO_3 + 1.7 $mmol \cdot l^{-1}$ $NaHCO_3$ (aqueous)

Cation suppression: AMMS (anion micro membrane suppressor) column, with counterflow of 2.5 $mmol \cdot l^{-1}$ H_2SO_4(aq) at 3 $cm^3 \cdot min^{-1}$.

Detection: conductivity cell.

The results of this analysis (Table 6.1) allowed minimum values for the anion contents of the oxide samples to be calculated, because extraction under these conditions cannot be quantitative. Hence the oxide as supplied was found to contain a trace of nitrate (~ 1 ppm m/m), most of which was lost on heating at 300°C. Sulphate was not detected and the oxide actually removed traces of these ions from the water used for extraction. The difference between the chloride ion contents of each oxide and the water blank indicated that the oxide contained ≥ 60 ppm m/m Cl^-, which was not expelled on heating at 300°C.

6.4.3 DSC of nickel(II) oxide

Reference DSC scans of the sieved and heated nickel(II) oxide showed the heat capacity change at 250°C as the only detectable event (Figure 6.8). The shape of the DSC curve was consistent with the heat capacity data published by Kelley [125]: the heat capacity increased fairly rapidly with increasing temperature up to the Néel point (antiferromagnetic form [126]) after which it increased only slightly (paramagnetic form [119]). The transition corresponds to a decrease in C_p of ~ 27%. It is important to note that this change of heat capacity is not accompanied by an enthalpy change - there was no evidence of an exothermic peak on the DSC curve around the transition point. This indicates that all the excess energy is employed in the magnetic disordering process, which involves uncoupling the d-electron spins of Ni^{2+} ions which are coupled antiferromagnetically by 'superexchange' through oxide ions [127].

6.4.4 DSC of porphyrins

The phase behaviour of purified free-base and nickel porphyrins was investigated primarily to establish their fusion temperatures. This was particularly important so that experiments could be carried out in the solid region. Phase transitions other than fusion were also of interest, since these might affect reactivity. Measurements were carried out using two types of sample container. One of these was the normal Du Pont aluminium non-hermetic type as used for the subsequent interaction studies. Although these pans were the most suitable for

identifying the onset of fusion, sublimation or decomposition of the porphyrins caused them to leak. In order to establish the form of the DSC curves when sample loss could not occur, experiments were also carried out in hermetically sealed DSC crucibles (marketed by Setaram). These are constructed from 316L stainless steel, have a working capacity of 50 μl and can withstand an excess internal pressure of 1500 psi at 300°C. They are also much taller than the Du Pont pans (5.5 mm vs. 1.7 mm). To accommodate these crucibles in the 910 DSC cell, the sample chamber lid was raised by fitting a silver ring of 3 mm square cross-section inside the top rim of the cell. The DSC temperature scale and calorimetric sensitivity were calibrated for each type of pan, using both tin and lead as standards in each case.

Scans carried out in hermetically sealed pans showed varying degrees of stability among the melted porphyrins, as indicated by the resolution between the fusion endotherm and the onset of (exothermic) decomposition. The greatest separation between these events (~ 30°C) was found for OEP, which melted at the lowest temperature, but this index of stability did not correlate with fusion temperature. The only other sample which showed complete resolution of the two events was NiPTC, which had the highest melting point of all. Exothermic decomposition began within the temperature span of the fusion endotherm for all the other materials apart from T(PFP)P, which gave a very sharp exothermic onset with no preceding endothermic shift. Varying degrees of overlap between the fusion and decomposition peaks are illustrated by the DSC curves in Figure 6.9. These indicate that, for the *meso*-arylated porphyrins, increasing electronegativity of the substituent decreases the stability of the fused porphyrin. The overall ranking of endo/exo resolution, based on the interval between the corresponding onset points, was:

OEP >> NiPTC > TPP > PTC > NiTPP > T(*p*-MP)P > T(PFP)P.

Scans carried out in non-hermetic pans gave what appeared to be well defined fusion endotherms for the first three members of this series. However, only the first two gave the same enthalpy of fusion in both types of container. All the other samples for which a well-defined baseline allowed the peaks to be integrated showed a higher

endothermic ΔH and lower exothermic ΔH in non-hermetic pans. This is attributable to leakage from the pan, because sublimation of the porphyrin and/or evaporation of its decomposition products will increase the endothermic component of the curve, as illustrated in Figure 6.10. Extrapolated onset temperatures for fusion are summarised in Table 6.2. Enthalpy data for fusion and decomposition are given in Table 6.3.

6.5 INTERACTION STUDIES

The thermal and atmospheric history of a material are very important in determining its surface properties, but only limited information was available regarding the nickel(II) oxide. It was considered important that the oxide be pre-treated under controlled conditions (see Appendix II) so that the results of this work could be reproduced using independent batches of reactants. Heating above the Néel transition temperature, in a high flow rate of inert gas, was intended to decompose residual nitrate (and any unidentified impurities) and also to relax mechanical stress. Following this treatment, exposure to the atmosphere will lead to rapid formation of a surface layer on the oxide due to chemisorption. Because it was not practicable to carry out the entire sample preparation and DSC experiment in an enclosed system, precautions beyond storing the treated oxide in a sealed vial were considered to be pointless.

In view of the high temperature at which the oxide was prepared (~ 800°C), it was initially assumed that subsequent heating at 300°C would not cause any dramatic change in its properties. This supposition was supported by the anion analysis described previously, which indicated only a minor loss of nitrate ions during heating. However, a subsequent literature survey (discussed with references in section 6.6.4) revealed that annealing at moderate temperatures has a dramatic effect on the surface properties of nickel oxide, particularly with respect to the state of adsorbed oxygen. Comparison of the behaviour of annealed and un-heated oxide in composites with TPP showed dramatic differences between the DSC curves. This observation effectively doubled the number of possible interaction experiments. A further complication arose because the relatively

strong TPP/NiO interactions detected in the initial study were virtually eliminated by purifying the porphyrin. The remaining events were of much lower energy and could only be detected by using a more rigorous DSC procedure, which involved several replicate scans. These factors precluded carrying out a full set of experiments using both annealed and un-heated oxide with every porphyrin, or continuing investigations with the black form of nickel oxide. Consequently, the composites which were tested for interactions do not represent a consistent or structured combination of the possible reactants. Combinations which were investigated are denoted ***:

PORPHYRIN	Treatment of 38-75 μm NiO	
	300°C/24 hrs	None
NiTPP	***	
TPP	***	***
PTC	***	***
OEP		(***)#
T(*p*-MP)P		***
T(PFP)P		***

Incomplete data; no second scans

6.5.1 Sample preparation

The use of small samples in DSC means that if one of the reactants covers a wide range of particle sizes the distribution in the analytical sample may vary considerably. This alters the apparent reactivity because small particles, having a larger specific surface area, tend to react to a greater extent than coarse aggregates. Nickel(II) oxide was sieved to 38-75 μm in order to remove both extremes and to give a repeatable size distribution. The recrystallised porphyrins were in the form of very fine feathery crystals and were given no further mechanical treatment. All of the purified porphyrins were found to be less effective than un-purified TPP at binding the nickel oxide particles. It was therefore necessary to increase the porphyrin content of the composites in order give the

pellets sufficient strength to survive heating in the DSC without fragmenting. A 1:1 mass ratio of the reactants was used for all subsequent experiments, irrespective of the molecular mass or density of the porphyrin.

The powdered reactants were mixed by slow tumbling on a sample roller, to avoid generating fines from the oxide. Approximately 40 mg of the mixture was compacted in an evacuated pellet press at ~ 850 MPa to give circular tablets of 6.0 mm diameter and ~ 0.7 mm thickness. Sample pellets were contained in Du Pont aluminium pans and covered with close fitting lids. The contacting surfaces of the pan and lid were carefully flattened to ensure good contact with the top and bottom surfaces of the pellet and hence minimise the thermal resistance gradient through the specimen.

6.5.2 DSC procedure

The following procedure for detecting weak interactions was based on previous studies of factors which affect DSC sensitivity and baseline repeatability.

(1) The DSC cell was maintained isothermally at 450°C for about 1 hour (to allow the thermocouple connectors to reach a stable temperature and hence minimise drift).

(2) The DSC was cooled rapidly to 25°C, using liquid nitrogen in a quenching can, and sample and reference pans loaded by means of a centring tool (to minimise random variations in slope and offset due to asymmetry). The sample chamber lid, radiation shields and bell jar were replaced very carefully to avoid displacing the pans from their central locations.

(3) The cell was cooled to −25°C by passing 10 $l \cdot min^{-1}$ of dry nitrogen gas through a coil of tubing immersed in liquid nitrogen and then to the 'cool' port on the cell base (to avoid contamination by atmospheric moisture). The cell chamber was purged with 25 $cm^3 \cdot min^{-1}$ of dry nitrogen, supplied at room temperature.

(4) When the cell was stable and under control (about 5 minutes) the cooling gas stream was switched off. The cell was then heated at $10°C \cdot min^{-1}$ to ~ 20°C below the onset of fusion for the porphyrin. The

higher ΔT amplifier gain (R x10) was used (to minimise digitisation noise) and data was acquired at 5 Hz.
(5) At the end of the run, the cell was cooled to 25°C, by means of the quenching can, and steps (3) and (4) repeated using the same specimen. This created a reference DSC curve representing the sample background in the absence of reaction. Subtraction of this from the initial DSC curve then gave a plot of events occurring in the first scan but not in the repeat.

6.5.3 Data manipulation

First and second DSC scans for a single PTC/NiO pellet are shown in Figure 6.11. Differences are evident above 250°C but the onset region is masked by the Néel transition. Curve (a) in Figure 6.12 is a difference plot ($1^{st}-2^{nd}$ scan) derived from these two curves. This shows that the step at the Néel point was matched in the two scans to within the baseline noise level and hence gave no residual in the difference curve. In spite of careful centring of the pans and temperature stabilisation of the DSC cell, a significant level of variation of the baseline slope and curvature persisted. This made it difficult to identify the initial deviation from the baseline, even in the difference plots. It was found that by carrying out the double-scan procedure on three separate composite pellets and combining the difference curves, random variations could be reduced to an acceptable level. Curve (b) in Figure 6.12 shows a greatly improved peak-peak signal:noise ratio compared with that obtained from one double-scan experiment (curve a). This gave a much higher level of confidence in identifying the onset of interaction by inspection.

This procedure of carrying out three replicate double-scan experiments was used for each of the composites. The resulting 'interaction DSC curves' are therefore equivalent to heating 120 mg of each porphyrin/NiO mixture. It would be useful to relate the measured enthalpy changes to a unit area of the interface, but the latter is almost impossible to quantify. The best alternative, given that all the composites contain a 1:1 mass ratio of the reactants, is to relate the DSC peak area to half the mass of the sample. This gives a specific enthalpy change relative to either component (without any assumption

as to which is definitive) and hence quoted ΔH values are in units: 'Joules per gram *of one component*'.

6.5.4 Observations

Phthalocyanine (PTC)

A potential source of error in these experiments arises from the method used to prepare the composite pellets. Compaction under high pressure may induce stress in the specimen which could relax on heating, in a similar way to that observed for cold-worked metals. Furthermore, Collins and Mohammed [128] have observed that micro-crystallites of phthalocyanines can grow to form larger crystals on heating in the DSC. Either of these exothermic processes could contribute to the energy release detected on heating the PTC/NiO composite pellets. To test this, pure PTC was compacted to form two 30 mg pellets, each of which was scanned twice in the DSC. The combined difference plot obtained from these (Figure 6.13a) represents an amount of PTC equivalent to the total in the three composite pellets which gave the interaction curve (Figure 6.13b). The difference in peak area between these curves showed that only ~ 25% of the enthalpy change in the PTC/un-heated NiO composite could be attributed to relaxation of PTC. Another important observation was that the exothermic onset temperature for the composite (~ 150°C) was much lower than that for PTC alone (~ 270°C), which showed that the interaction was not initiated by relaxation in the organic phase.

The interaction DSC curve obtained for pellets of PTC/annealed NiO (Figure 6.14b) was very similar to that for PTC alone, with no significant difference between the enthalpy changes for the exothermic peaks:

$$\Delta H_{PTC/NiO} = -5.3\ J \cdot g^{-1} \qquad \Delta H_{PTC} = -5.4\ J \cdot g^{-1}$$

This showed that annealing at 300°C caused some change in the nickel oxide which prevented detectable interaction with PTC. The remaining energy change was entirely attributable to physical re-ordering in the organic phase and independent of the included NiO particles.

meso-Tetraphenylporphyrin (TPP)

This was the only porphyrin, other than PTC, for which a full set of 3x2 scans was obtained using both annealed and un-heated nickel oxide. The DSC curve for pure TPP showed a broad and poorly defined endotherm in the 418-428°C region ($\Delta H \sim 8\ J \cdot g^{-1}$). This was replaced by two much sharper endotherms at 360°C and 410°C in the first scan for the composites. These peaks were virtually absent from the second scans for the TPP/annealed NiO composite, being replaced by: a complex event of poor repeatability in the 0-50°C region, a small but repeatable endotherm at 146°C ($\Delta H = 0.6\ J \cdot g^{-1}$) and an exothermic drift beginning at ~ 360°C. The first of these events appeared to be an endotherm with a smaller exotherm superimposed on it. The shape of this complex event was variable but the average, shown inverted in the interaction curve (Figure 6.15), is a fair representation. This curve also shows the onset of a weak exothermic interaction at ~ 230°C, but the endotherm at 360°C in the first scan interferes with the latter part of this. A minimum value for the exothermic component* was measured up to the leading edge of the endotherm at 360°C: $\Delta H \geq -5\ J \cdot g^{-1}$.

The behaviour of the TPP/un-heated NiO composite was different from that with annealed NiO, apart from the two high temperature (360/410°C) events in the first scan. A small but well defined exotherm was evident at about the Néel point in the first scan. The difference plot (Figure 6.16) revealed an additional peak, which appeared as a broad exotherm in the 100-190°C region of the first scan. Correction for the background step in NiO showed that the first deviation for the sharp exotherm lay in the region 230-240°C and allowed the peak to be integrated, giving $\Delta H = -1.6\ J \cdot g^{-1}$. The extrapolated onset temperature was measured to be 251.5°C, which was not significantly different from the Néel point. The superimposed

---

*In those interaction DSC curves where an endothermic shift obscured the end of the broad exotherm, the baseline immediately before the event was extrapolated to its intersection with the DSC curve. (This construction is illustrated most clearly in Figure 6.18). The bounded area then represented the minimum possible exothermic energy change. $\Delta H \geq -X\ J \cdot g^{-1}$ means that the 'true' value will be more negative than '−X'.

curve (dashed line) in Figure 6.16 is the region around 250°C for the second (reference) scan, which shows the close correlation between the Néel transition and the TPP/NiO interaction peak.

meso-Tetraphenylporphyrinato-nickel(II) (NiTPP)

The first scans showed a sudden endothermic shift ~ 430°C, shortly after which heating was stopped. The interaction plot (Figure 6.17) showed that the exotherm beginning at ~ 150°C changed abruptly at ~ 275°C to an endotherm which curved gradually in the temperature region up to 410°C and then much more steeply. As before, extrapolation of the preceding baseline was used to measure the approximate energy change for the exothermic component, which gave: $\Delta H \geq -9.2\ J \cdot g^{-1}$.

meso-Tetrakis(pentafluorophenyl)porphyrin (T(PFP)P)

In each replicate experiment, the second scan displayed a rather variable exothermic drift beginning at ~ 400°C. This may be due to mechanical breakdown of the specimen because T(PFP)P was the most difficult porphyrin to pelletise and the composites tended to fracture on heating. The interaction plot (Figure 6.18) showed a smooth exothermic onset at ~ 180°C but the end of the event could not be distinguished because of interference by the inverted exotherm from the second scans. An approximate enthalpy change of $\Delta H \geq -12.4\ J \cdot g^{-1}$ up to 420°C was calculated as before.

meso-Tetrakis(*p*-methoxyphenyl)porphyrin (T(*p*-MP)P)

The first scan for this composite (Figure 6.19) showed a small endotherm, in the region of the Néel point, which was also present in the DSC curve of the porphyrin alone. This peak was absent from the second scan but a slightly narrower endotherm had appeared at lower temperature. The interfering step due to NiO had been eliminated in the interaction DSC curve (Figure 6.20), which allowed the endotherm in the initial scan to be integrated and also showed that its onset was quite distinct from the Néel point. Despite the shift of position between the two scans, the two peaks were not significantly different in energy ($\Delta H \sim 5.5\ J \cdot g^{-1}$). The location of these two peaks, combined with what appeared to be a broad shallow endotherm in the same region,

meant that weak exothermic interactions of the form observed for some of the other porphyrins could not be distinguished.

β-Octaethylporphyrin (OEP)

The DSC curve for OEP alone showed a minor endotherm which was resolved from the onset of fusion. The OEP/NiO composite was heated to 310°C, which was ~ 25°C below the onset of fusion but just above this minor event. The behaviour of the pellets after heating was peculiar. If the DSC cell was cooled to room temperature and then opened, it was found that the lid of the pan had been displaced and the sample converted to a large volume of fine powder which covered the base of the sample chamber. If the cell was opened immediately on reaching 310°C and the sample transferred to a cold metal plate to quench it, the lid remained in place for about 30 seconds, after which the contents erupted as a stream of fine powder. Destruction of the specimen meant that it was not possible to carry out a reference scan for subtraction.

6.5.5 Investigation of solvent effects

Endothermic events appeared in the second scans for two reaction mixtures: T(*p*-MP)P/un-heated NiO and TPP/annealed NiO. The similarity between the enthalpy change in the first and second scans for the T(*p*-MP)P composite suggested that these events might be related. A phase transition with a change of environment between first and second scans was a possible explanation. The temperature of the peaks for the TPP composite suggested that they might be due to phase transitions in water in an environment such as a filled capillary.

Porphyrins are known to form crystalline solvates [129,130] with various solvents, including those used in this work for chromatography and recrystallisation. The possibility that the irreversible effects noted above were due to migration of solvent molecules from the porphyrin into the porous oxide were investigated by doping nickel oxide with a mixture of solvents and compacting with PTC to 'cap' the pores in the oxide particles. The amount of each solvent used corresponded to a 1:1 molar ratio with the PTC in the composite.

A mixture consisting of 100 mg un-heated NiO, 16 μl toluene, 6 μl methanol and 3 μl water was sealed in a vial and stored at 50°C for 24 hours. The vial was then cooled to 15°C and the contents mixed with 100 mg PTC. Three 40 mg pellets were prepared and analysed using the double-scan procedure as before. None of the DSC curves for this mixture showed evidence of solvent transitions. The interaction plot (Figure 6.14a) showed that ΔH had been reduced from $-21.3\ J \cdot g^{-1}$ to $-6.6\ J \cdot g^{-1}$, which was close to the values measured for PTC/annealed NiO and for PTC compacted alone.

6.6 DISCUSSION OF POSSIBLE INTERACTION MECHANISMS

6.6.1 Participation of liquid phases

Most common synthetic methods for preparing metallo-porphyrin complexes utilise a solvent which is able to dissolve both the free-base porphyrin and a salt or complex containing the metal ion [131]. The solvent is usually chosen to have a high boiling point and the reaction is carried out under reflux. In the case of transition metals, which form very stable complexes, various protogenic and protophilic solvents have been used, including acetic acid, phenol, pyridine and *NN*-dimethylformamide. More labile complexes, such as those of Group IIa metals, can only form in protophilic media. Some work has been carried out on heterogeneous reactions [132] in which the source of metal ions was the parent metal or metal oxide, while the porphyrin was dissolved in water or an organic solvent. The experiments described here did not employ a solvent for either reactant. This means that for a chemical reaction to propagate beyond the initial surface contact, solid diffusion is needed to transport the complex away from the surface and replace it with free-base.

Commercially available porphyrins are mostly specified to be ~ 97% pure, based on elemental analysis (particularly nitrogen content). However, purification of the porphyrins used here revealed the presence of much larger amounts of impurities than expected. About 30% m/m of a sweet-smelling reddish brown oil was isolated from TPP by preparative column chromatography on alumina. This was a highly polar fraction which was eluted by methanol. The synthetic route used to

prepare porphyrins (discussed in section 6.7.1) suggests that these impurities are most probably open-chain pyrrylmethene oligomers. These have virtually the same elemental composition as the corresponding porphyrins and would not be detected by elemental analysis. Because the impurity fraction was a polar liquid, it must be considered as a solvent, even though a 'formal' solvent was not added intentionally. Interactions in composites prepared from crude porphyrins cannot therefore be considered as true solid-state processes. Rigorous purification of the porphyrins allowed increased confidence that the events detected subsequently did not involve participation of liquid organic impurities. Although it is possible that minor amounts of impurities remained in the porphyrins after purification, the following evidence suggests that these were not responsible for the broad exothermic peaks beginning in the 150-200°C region. Un-heated nickel oxide showed very similar interactions with PTC and T(PFP)P, even though the precursors and method of purification were totally different for these two materials:

PTC is derived from either phthalic anhydride and urea, or 1,2-dicyanobenzene (phthalonitrile) and a metal alkoxide or halide. It was purified by extractive crystallisation from a bed of alumina, using boiling chlorobenzene.

T(PFP)P is prepared by the conventional route to symmetrical porphyrins, using pyrrole and pentafluorobenzaldehyde. It was purified by chromatography on alumina followed by crystallisation from a mixture of toluene and methanol.

Impurities derived from such disparate starting materials would be expected to have very different chemical and physical properties. The use of dissimilar procedures for purifying the porphyrins also helped to ensure that the properties of any persistent residues were different between the two materials as used in the composites.

Heating the porphyrin/NiO composites will displace adsorbed water from the oxide and form more by reaction. Water cannot escape from the specimen and will remain at the interface, or within the porous oxide, unless cracks develop in the composite. Aqueous phases play an important role in propagating nominally solid-state reactions which liberate water, and where at least one of the reactants is water-soluble [133-5]. Pure water will not be effective in solubilising

either the free-base porphyrin or complex, but nickel ions may be mobilised if ionic impurities are present. When hydrated nickel salts are heated, water liberated by partial dehydration tends to dissolve the remaining lower hydrate. This dissolution occurs at 56.7°C for pure $Ni(NO_3)_2.6H_2O$ and at 36.4°C for $NiCl_2.6H_2O$. Traces of anionic impurities in the oxide, coupled with adsorbed water, may behave in a similar manner and form an interfacial aqueous phase containing Ni^{2+}, although the transition temperatures will be different from those of the pure salts. Nitrogen(IV) oxide, formed above 136°C by decomposition of nickel(II) nitrate, will dissolve in water and attack the oxide. However, the small amount of nitrate ions (~ 1 ppm) in the oxide means that they should only make a minor contribution to the reaction. Chloride ions were present at much higher level (≥ 60 ppm) and have the potential to make a more significant contribution. Nickel(II) chloride is thermally stable (it sublimes at ~ 970°C) but a reaction of the form

$$PORPH.H_2 + NiCl_2 \rightarrow PORPH.Ni + 2HCl\uparrow$$

would create a strongly acidic aqueous phase. This would not prevent formation of the very stable nickel complex, but would be effective in dissolving the oxide and transporting nickel ions to the reaction site.

6.6.2 Adsorption mechanisms

In the absence of intervening fluids, there are several possible modes of solid-solid interaction between porphyrins and nickel oxide. The simplest of these is a polar interaction between surface dipoles on the oxide and the aromatic π-orbitals. Castro [136] has reviewed the routes of electron transfer in porphyrins, several of which are relevant to adsorption mechanisms. The highly polarisable nature of the extended π-system on the porphyrin means that charge separation can take place, leading to very strong electrostatic interactions with the surface of the oxide. More specific localised interactions could take place by:

Electrostatic interaction at Lewis sites:

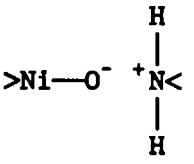

Hydrogen bonding:

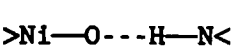

σ-coordination:

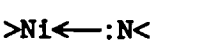

π-coordination:

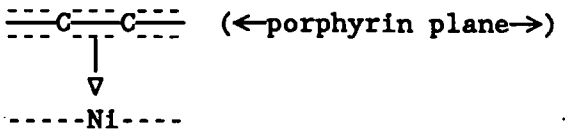

Morales and Galiasso found that Lewis acid centres were the predominant sites for adsorption of oxovanadium porphyrins on a Co-Mo-alumina catalyst [137]. Adsorption also occurred on areas of the surface which were doped with cobalt and molybdenum ions, and hydrodemetallation occurred selectively on these sites. Amphoteric oxides such as alumina are rich in Lewis sites but nickel oxide will contain relatively few. Adsorption by hydrogen bonding or coordination onto nickel ions is therefore more likely on this substrate. Both hydrogen-bonding and σ-coordination will tend to cause distortion of the porphyrin from planarity to a dished shape, owing to the change of geometry at the nitrogen atoms.

6.6.3 Molecular distortion of porphyrins

Distortion of the porphyrin skeleton is opposed by the accompanying loss of resonance energy but deviations from planarity are favoured in certain cases. For example, the porphyrin nucleus of TPP is virtually planar in triclinic crystals [110] but puckered in the tetragonal form [109]. Distortion is an important part of the reaction mechanism for metallation of porphyrins in solution. Comparison of the rates of complexation for various metal perchlorates by TPP and *N*-methylTPP showed that the latter, which is non-planar, reacted much faster [138]. The reaction mechanism was found to involve distortion of the porphyrin and stepwise displacement of the solvation layer from the metal ion. Large ions such as Hg^{2+} and Cd^{2+} have been shown to catalyse formation of metalloporphyrins from Mn^{2+}, Co^{2+} and Ni^{2+} [139]. The larger metal ion is believed to form a weakly bound complex in which the porphyrin nucleus is deformed. The smaller ion then

approaches from the opposite side of the porphyrin, forming a heterodinuclear activated complex which dissociates by loss of the larger ion, i.e. a transmetallation reaction (Figure 6.21). *N*-methyl porphryins reacted faster than their un-substituted analogues but the kinetics of complexation were unaffected by the addition of large cations. This confirmed that deformation of the porphyrin (in this case by the methyl substituent) enhanced reactivity even though the intermediate was mononuclear. ^{15}N solid state NMR spectroscopy [140] has shown that at room-temperature the central (acidic) protons in planar triclinic TPP are much less mobile than those in the distorted *meso*-tetra-*p*-tolylporphyrin. Distortion of the porphyrin skeleton may therefore increase rates of reaction in the solid state as well as in solution.

6.6.4 Oxidation reactions

In the preceding discussions it was assumed that the inorganic phase consisted of a bulk lattice containing Ni^{2+} and O^{2-} ions, with a surface layer of OH^-, CO_3^{2-} and H_2O. Although the green form of nickel oxide is widely assumed to be stoichiometric, with the black form being oxygen-rich, the former invariably contains excess oxygen. Bulk and surface oxygen contents contribute to this excess and these are affected by the annealing temperature of the oxide [141]. Degassing at 400°C effectively removes the surface excess of oxygen but does not affect the bulk level. Higher temperatures (approaching 1000°C) reduce the bulk oxygen content, giving the closest approach to stoichiometry and the lowest overall levels of Ni^{3+}. The fractional surface coverage (θ) which occurs on re-exposure to O_2 depends on the annealing temperature and reaches a maximum in the 700-900°C region. The coverage fraction varies substantially with temperature. Typical values measured by Deren and Stoch were:

$$\theta_{400°C} \approx 0.05 \qquad \theta_{800°C} \approx 0.3$$

The nickel(II) oxide obtained from Aldrich had been annealed at a temperature which gives the maximum propensity for adsorption of oxygen. Subsequent re-annealing at 300°C in argon will almost certainly have reduced θ, probably to the minimum value.

Analysis of bulk nickel oxide may indicate that it is virtually stoichiometric, but defect ions are not evenly distributed throughout the solid. Finster *et al* [142] identified a substantial surface concentration of Ni^{3+} on NiO specimens which had been annealed at ~ 1000°C. Their studies, using X-ray photoelectron spectroscopy, led them to the conclusion that the excess oxygen was in the form of O^{2-} ions associated with Ni^{3+}. However, other workers, using reflectance infrared spectroscopy, identified O_2^- as an adsorbed species [143]. More importantly, the latter showed that the adsorbed oxygen was very reactive, and readily oxidised carbon monoxide even at temperatures as low as 77K. Adsorbed oxygen can completely alter the mechanism of reactions occurring on NiO. Decomposition of formic acid on a chemically clean NiO surface was found to take place via an anhydride intermediate, but even at low oxygen coverage the intermediate species changed to formate ion [144]. Analogy with these observations suggests that under normal conditions, when chemisorbed oxygen is adsorbed on the oxide surface, the preferred state of adsorption for porphyrins will be the mono- or di-anion. This will be independent of the degree of coverage, provided that some excess oxygen is present.

The oxidising properties of nickel oxide are likely to affect the chemistry of its interactions with porphyrins. Bonnett and Ridge [145] discovered that octaethylporphyrin can be oxidised by hypofluorous or peroxyacetic acid to give a porphyrin-*N*-oxide. Balch *et al* prepared the nickel(II) complex from this, identified its crystal structure and showed that the porphyrin skeleton is distorted [146] (Figure 6.22). Although the crystal structure of the free-base *N*-oxide was not determined, analogy with its nickel complex and also the *N*-methyl porphyrins shows that it is also likely to contain a distorted porphyrin nucleus. This will make it more reactive than the simple porphyrin. The presence of strongly oxidising species (Ni^{3+}/O_2^-) in the surface layer of nickel(II) oxide means that porphyrin-*N*-oxides and their nickel complexes are viable reaction products in these composites. If oxidation of the free-base is the first step, analogy with the mechanism in solution suggests that the intermediate porphyrin-*N*-oxide must flip, as shown in Figure 6.22, before metallation can occur. Provided that oxidation is rapid, the overall

rate of complex formation may well be increased by going via the distorted *N*-oxide intermediate.

6.7 CONCLUSIONS REGARDING THE ASSIGNMENT OF DSC EVENTS

Several different types of thermal event occurred in porphyrin/NiO composites on heating and were detected by DSC. These have been classified into four groups as follows:

(1) Relatively strong exothermic events in the first scan for crude TPP, corresponding to formation of NiTPP.

(2) Sharp endothermic peaks appearing in the second scans for TPP and T(*p*-MP)P.

(3) A sharp exothermic peak in the first scan for TPP at about the Néel transition point.

(4) Broad shallow exothermic peaks, beginning above 150°C, which appeared in the first scans for composites of several porphyrins

These categories do not include the exceptional behaviour of OEP/NiO, for which the rate of reaction at 310°C was sufficient for it to become self-propagating. Continued reaction will be assisted by the low thermal conductivity of the matrix, which insulates the reaction sites from external quenching. The time interval between quenching the DSC specimen and the contents of the pan erupting is probably not due to an induction period for the reaction. It is more likely to represent build up of sufficient pressure to force the lid off the DSC pan. Destruction of the pellet appeared to be caused by evolution of gas, but decomposition of the porphyrin is unlikely to be the cause. A rapid complexation reaction, liberating large volumes of water vapour, is a more likely explanation. This reaction may be initiated by a phase transition corresponding to the minor DSC peak, but confirmation of this would require reference scans for subtraction.

6.7.1 Formation of NiTPP from crude TPP

During the preliminary studies, using a TPP/NiO composite based on crude TPP, two temperature regions were identified in which exothermic DSC peaks corresponded to formation of NiTPP. Composites containing TPP which had been purified, by chromatography and recrystallisation,

showed much smaller exothermic peaks which occurred at different temperatures than before. This showed that the impurities were participating in the reaction and that the mechanism was not a true solid-solid interaction between NiO and TPP. The fact that both the black and green forms of nickel oxide gave the same total yield of nickel-complex makes the absence of distinct peaks in the DSC curve for the black oxide surprising. The particle size of this was not investigated, but the powder appeared much finer than the sieved green oxide. A larger particle surface area and excess oxygen is likely to make black NiO the more chemically reactive form. Reaction to form the porphyrin complex may therefore begin at a lower temperature and progress steadily over a wide temperature range, giving no discrete regions of reactivity. In spite of this important difference, both forms gave the same product yield, which suggests that some component of the porphyrin was the limiting factor.

Porphyrins are usually synthesised by condensation of a pyrrole with an aldehyde: TPP is prepared from pyrrole itself and benzaldehyde. Reaction occurs stepwise via an oligo-pyrrylmethene chain which increases in length until it can cyclise to form the macrocyclic porphyrin skeleton. The rate of reaction can be increased by adding metal ions which are chelated by the intermediate linear oligopyrrole. As this wraps around the metal ion, the ends of the chain are brought together in the correct orientation for cyclisation to take place. This is known as template synthesis. Zn^{2+} is generally used as the template ion because the resulting zinc complex is readily dissociated by addition of acid, liberating the free-base porphyrin. Intermediate synthesis and isolation of open-chain pyrrylmethenes has also been used as a route to unsymmetrically substituted porphyrins [147].

The oily impurity fraction from TPP was not analysed chemically, but its chromatographic behaviour was consistent with that expected for open-chain pyrrylmethenes, which probably comprise the bulk of the polar material. These may be envisaged as participating in the reaction with nickel oxide several ways:

(a) The impurity fraction was a mobile polar liquid which would be an excellent solvent for both free-base TPP and the nickel complex. It could therefore act as a flux to increase mobility of these

compounds in the interface region and hence maintain the reaction.

(b) The impurities (assuming that they are pyrrylmethene oligomers) may form non-macrocyclic chelate complexes with nickel ions.

(c) Chelates formed via (b) may be cyclised to the nickel-porphyrin i.e. template synthesis.

Although there was some uncertainty as to the location of the DSC baseline in the two regions of reaction, there did appear to be a significant difference between the corresponding ΔH values. This, along with the large temperature interval (~ 100°C) separating them, suggests that different mechanisms operate in the two regions. If all of these processes occur within the same experiment, the solvent mechanism (a) must correspond to the lower temperature interval because cyclisation will cause the fluid phase to solidify. However, the reaction need not involve TPP itself because the fraction of the initial crude material (~ 18%) needed to account for the total amount of NiTPP produced is less than the polar impurity content (~ 30%). The template mechanism has been demonstrated in at least one other solid matrix. Balkus and Ferraris found that 1,2-dicyanobenzene in a Co^{2+}-exchanged NaY zeolite was cyclised to cobalt(II)phthalocyanine via template synthesis. Reaction was detected as an exothermic DSC peak, which occurred at a higher temperature than for cobalt ions which were not constrained in a zeolite cage [148]. The reactions detected in the crude-TPP/NiO composite most probably involve solvent and template mechanisms, but whatever their precise nature, they are clearly not true solid state processes.

6.7.2 Second-scan endothermic peaks

The form and temperature of the endothermic events detected in the second scans for TPP/heated NiO and T(*p*-MP)P/un-heated NiO suggested that phase transitions due to entrained solvent might be responsible. Porphyrins are known to form 1:1 solvates with water and methanol [129] in which the solvent molecule is hydrogen-bonded to one or more of the pyrrolic N–H groups. Simple stoichiometric solvates with aromatics do not appear to have been reported, but very highly

solvated derivatives of tetraphenylporphyrinato-zinc(II) have been identified [130] with tetrachloromethane, pyridine and benzene:

$$ZnTPP \cdot 16CCl_4 \qquad ZnTPP \cdot 18C_5H_5N \qquad ZnTPP \cdot 26C_6H_6$$

Smaller numbers of aromatic molecules should be easily accommodated by the porphyrin lattice, where they will be strongly bound by $\pi-\pi$ stacking interactions. One explanation for the thermal behaviour of these two composites is that small, mobile molecules formed by decomposition of a porphyrin-solvate in the first scan migrate into pores in the nickel oxide. These would adsorb on the internal surfaces of the oxide and, if the resulting multi-layer became sufficiently thick, could eventually fill the smaller pores. In the second scan the clustered solvent molecules would undergo phase transitions whose temperature and form depended on their physical state and on any dissolved impurities.

Attempts to reproduce this type of phase transition by doping the oxide with a mixture of solvents were unsuccessful, but this does not disprove the solvent migration hypothesis. The design of this experiment was very simple and ignored possible interactions between the solvents. These interactions may have suppressed sharp phase transitions, but it was not practicable to investigate each of the single solvents and binary mixtures. PTC was chosen to cap the oxide pores because it did not show any interfering DSC events, but it may have a particular affinity for these solvents and not release them on heating at the temperatures used for this study.

6.7.3 Exothermic event at the Néel point

The TPP/un-heated NiO composite was the only one which showed evidence of a specific event occurring in the region of the Néel point. This appeared as a very sharp exothermic peak in the first scan. The interaction plot showed that the first deviation for the peak was somewhat below 250°C and appeared to coincide with the onset of decomposition for nickel hydroxide. A much stronger correlation existed between the extrapolated onset temperature and the Néel point. The steep leading edge of the peak above this temperature suggested transformation from a metastable state, with the process accelerating rapidly once initiated. The termination was also very rapid,

indicating a limited and localised supply of reactant rather than propagation through the bulk of either solid phase. The peak was eliminated by annealing the oxide at 300°C, which showed that some characteristic of the surface had been affected. This treatment will alter both the degree of oxygen coverage and the composition and structure of the OH^-/CO_3^{2-} surface layer. All of these observations were consistent with an interfacial process whose mechanism is linked to decomposition of surface compounds on the oxide and to the bulk transition in NiO.

6.7.4 Broad exothermic peaks (first scan)

A broad exothermic peak, beginning in the 150-200°C region, was observed for composites of PTC, T(PFP)P, NiTPP and TPP, with the energy of interaction apparently decreasing in that order (Figure 6.23). Quantitative comparisons of ΔH could not be made because of interfering events in the DSC curves for the last three materials, and the indeterminate contribution by relaxation of these organic phases. The effect of matrix thermal conductivity must also be considered. The conductivity of PTC is ~ 50% higher than that of T(PFP)P, which will make DSC peaks slightly sharper and increase the apparent ΔH for composites containing PTC. The peak height for the TPP/heated NiO composite was ~ 0.5 mW, which was the same as that attributed to relaxation in PTC. Annealing the oxide eliminated detectable interactions with PTC and hence the small exothermic baseline shift given by TPP/NiO cannot be taken to imply a significant degree of interaction.

All of the mechanisms of interaction discussed previously require facial orientation of the porphyrin relative to the adsorption site. Although porphyrin molecules will be ordered within each crystallite, their orientation at the interface will be random. This means that for optimum interaction to occur, sections of the porphyrin lattice must rotate, leading to an 'activation energy' for the process. Tammann noted that blocks of a crystalline lattice develop translational freedom at a value of T/K of about half the melting temperature [149,150]. This point ($T_{Tammann}$) corresponds to the onset of bulk diffusion, sintering and various solid-state reactions [58,133]. The

actual value of the ratio $T_{Tammann}/T_{fus}$ depends on the type of material (e.g. organic, metal, glass). Within a series of materials, such as porphyrins, increasing steric hindrance will tend to increase the value of the Tammann ratio at which reaction begins. Three of the porphyrins gave broad exothermic peaks which appeared to be at least partly due to interaction with nickel oxide, rather than relaxation. The onset temperatures for these peaks, relative to the melting point of the porphyrin, were:

$$PTC = 0.53 \cdot T_{fus} \quad NiTPP = 0.56 \cdot T_{fus} \quad T(PFP)P = 0.62 \cdot T_{fus}$$

These are in the correct relative temperature region to be 'Tammann temperatures', which supports initiation of this event by mobilisation of the porphyrin lattice. The temperature region corresponding to $0.5 \cdot T_{fus}$-$0.6 \cdot T_{fus}$ for OEP is ~ 30-90°C, which means that the corresponding interaction would have been initiated long before 310°C - the maximum temperature reached in the DSC.

It is not certain that the free-base porphyrins interact with NiO by the same mechanism as do their nickel-complexes. The results of this investigation do not allow the mechanism of interaction to be identified conclusively among the following possibilities: non-specific dipole-π type adsorption; coordination at Ni^{2+}; hydrogen-bonding; oxidation by Ni^{3+}/O_2^-. The results for PTC, T(PFP)P and NiTPP allowed the following observations to be made:

(a) Annealing at 300°C or treatment with a mixture of polar solvents deactivated the surface towards PTC, but apparently not towards NiTPP. The latter is unconfirmed because the form of interaction with the un-heated oxide, and the contribution by relaxation, are unknown.

(b) NiTPP has no available >N: or >N–H groups and cannot adsorb by coordination or hydrogen-bonding. The shape of the exothermic peak for NiTPP/NiO was somewhat different from those for the other two composites, with an abrupt change of curvature at ~ 275°C indicating the onset of a competing endothermic process.

(c) The 'propeller-blade' conformation of the pentafluorophenyl groups in T(PFP)P results in strong steric hindrance perpendicular to the plane of the porphyrin skeleton. The order of steric hindrance

$$PTC < NiTPP < T(PFP)P$$

is the same as for the Tammann temperatures, which suggests that steric effects are important in this mechanism.

(d) There was no apparent change of heat flow corresponding to decomposition of OH^-/CO_3^{2-} or to the Néel transition.

Table 6.1

Analysis of aqueous extracts from nickel(II) oxide

SAMPLE	Anion content (ppm m/v)		
	Cl^-	NO_3^-	SO_4^{2-}
Water blank	1	0.07	0.2
Extract from un-heated NiO	5	0.15	< 0.1
Extract from annealed NiO	5	0.03	< 0.1

Table 6.2

'Melting points' of porphyrins measured by DSC

(ranked by T_{fus}/°C)

PORPHYRIN	Extrapolated onset of fusion* /°C	
	Du Pont aluminium pan (non-hermetic)	Setaram 316L-SS pan (hermetic)
OEP	336.9	334.7
T(*p*-MP)P	445.4	432.8
TPP	452.0	449.6
T(PFP)P	461.5	458.1#
NiTPP	486.6	486.8
PTC	536.4	528.7
NiPTC	564.5	573.4

* Average of two measurements, approximate 95% C.I. ± 1°C.

\# Exothermic decomposition, with no evidence of fusion.

Table 6.3

Approximate enthalpy changes for fusion/decomposition of porphyrins

(ranked by endo↔exo resolution)

	Specific peak area* /J·g^{-1}			
	Du Pont aluminium pan (non-hermetic)		Setaram 316L-SS pan (hermetic)	
PORPHYRIN	ΔH_{endo}	ΔH_{exo}	ΔH_{endo}	ΔH_{exo}
OEP	84.0	None	78.1	###
NiPTC	55.2	###	50.8	###
TPP	77.0	None	64.0	303
PTC	662	None	162	380
NiTPP	92.4	20.7	46.6	270
T(*p*-MP)P	43.4	123	16.5	565
T(PFP)P	24.4	54.9	None	901

* Average of two measurements, approximate 95% C.I.:
± 5% for fully resolved peaks; ± 10% for partly resolved peaks.

No distinct baseline for integration

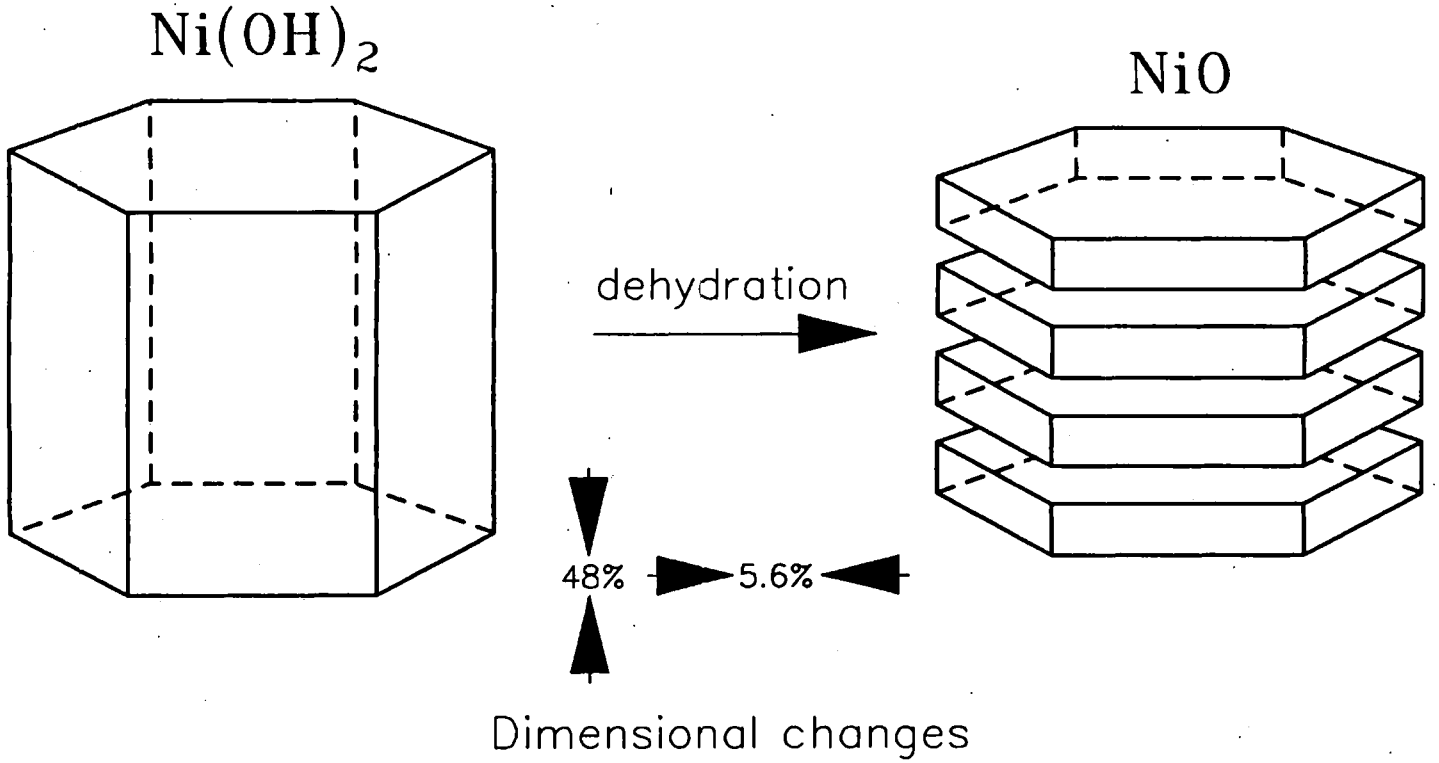

Figure 6.1 – Splitting of a nickel(II) hydroxide crystal into plates during dehydration to nickel(II) oxide.

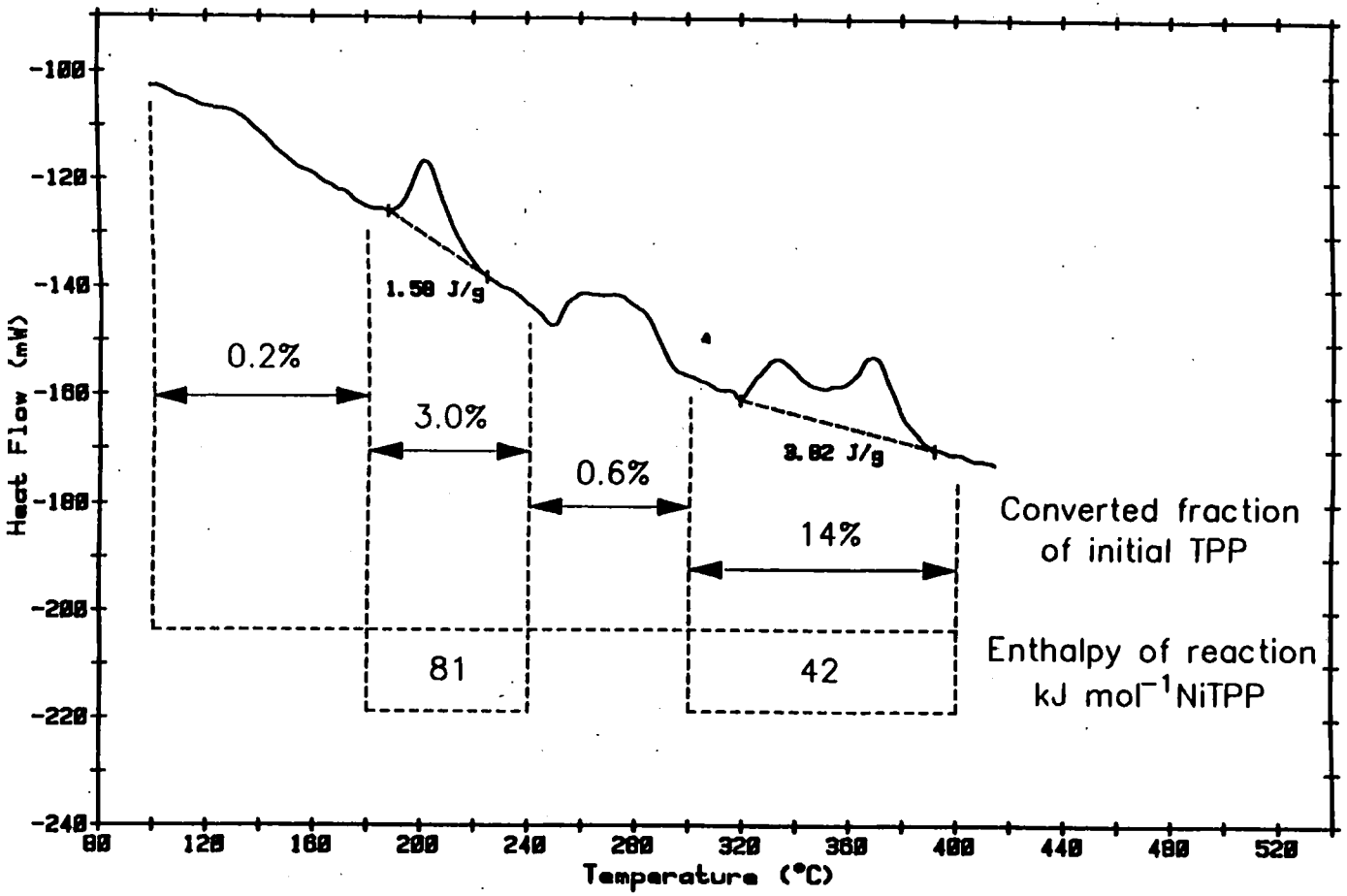

Figure 6.2 – DSC curve for a composite of nickel(II) oxide and crude meso–tetraphenylporphyrin.
(sum of scans for 2x40 mg pellets: Amp. range x10)

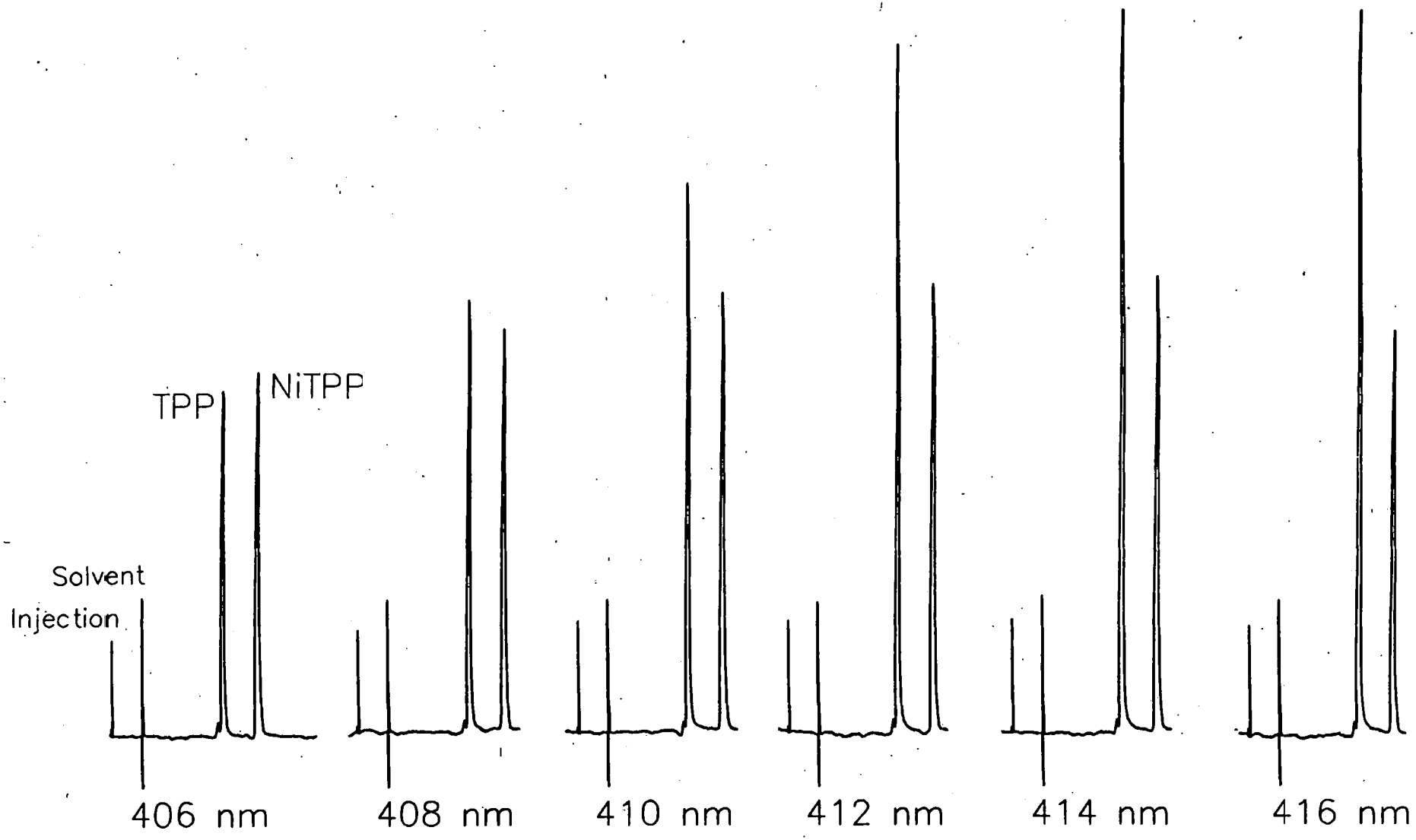

Figure 6.3 – Optimisation of detection wavelength for analysis of reaction products from TPP/NiO by HPLC.
(Equimolar mixture of TPP and NiTPP in acetonitrile/THF)

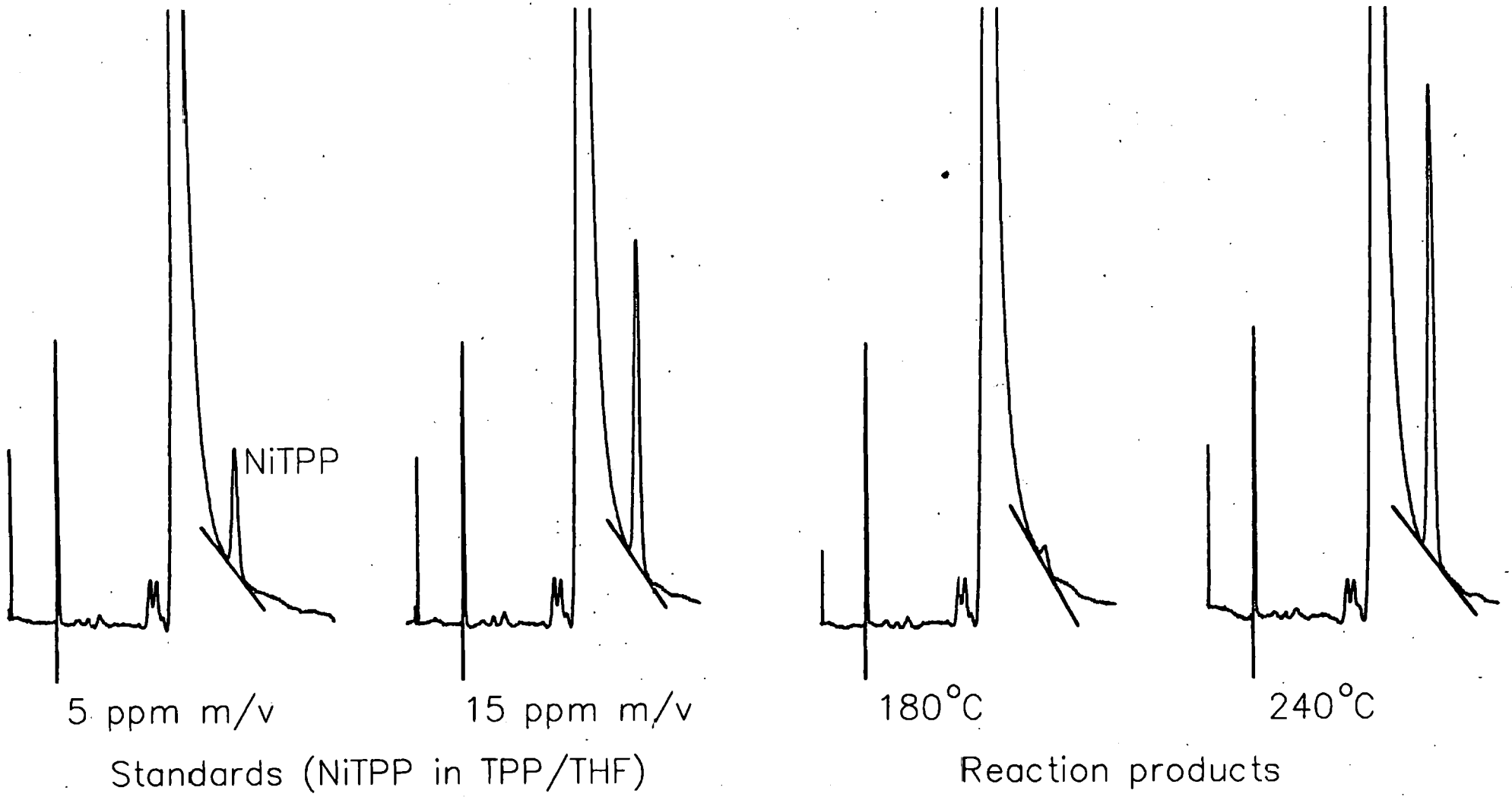

Figure 6.4 – Separation of NiTPP from excess TPP using reversed-phase HPLC (UV detection @ 412 nm).

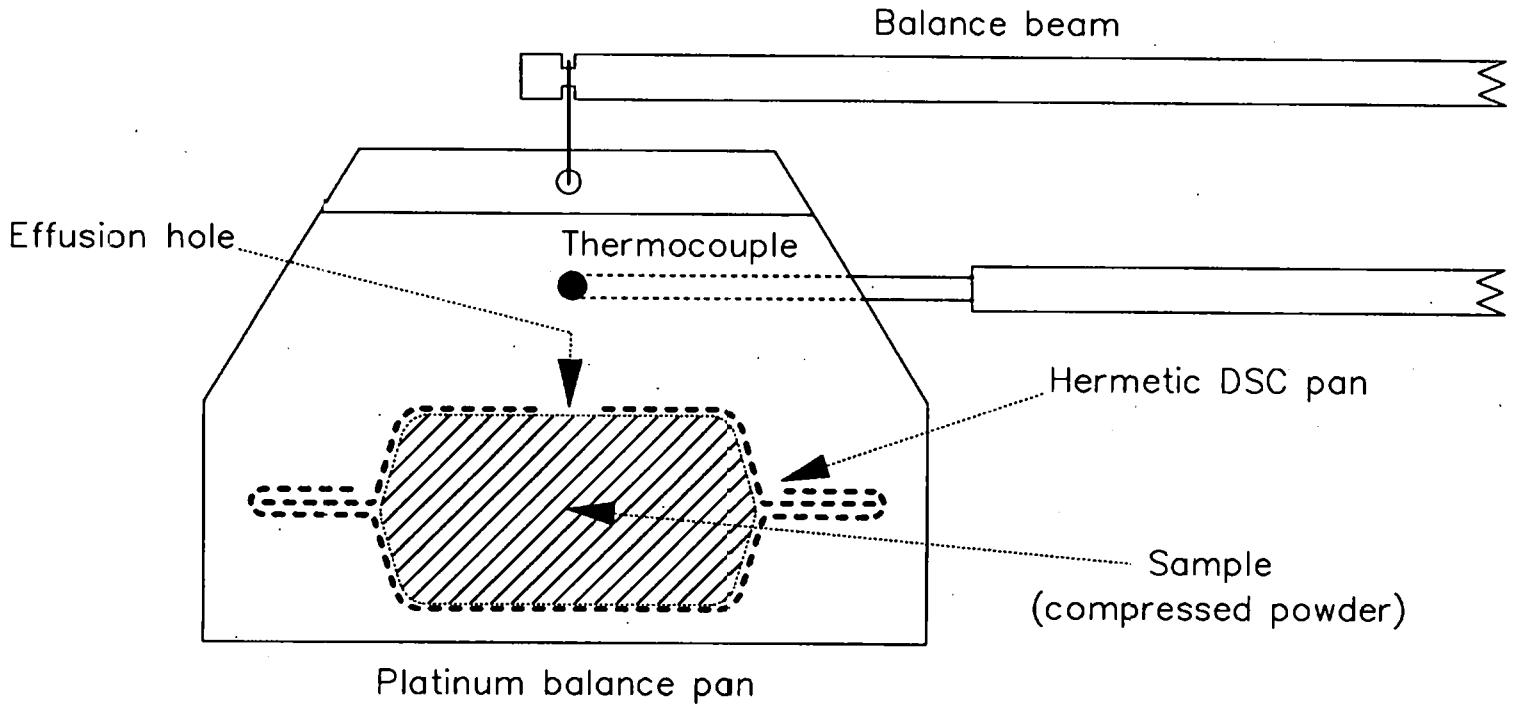

Figure 6.5 – Experimental configuration used for TG measurements.

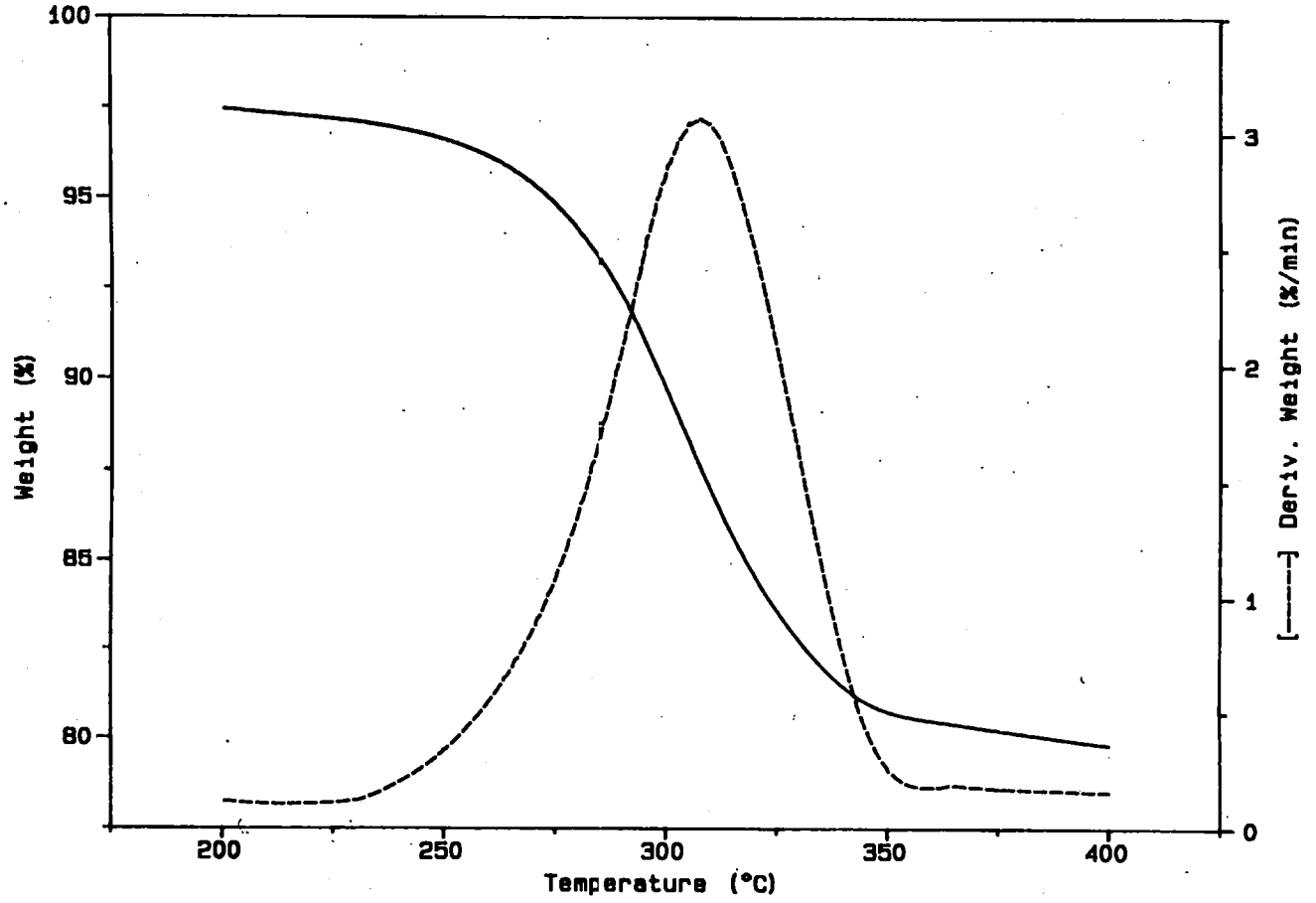

Figure 6.6 – Thermogravimetric curve for nickel(II) hydroxide.

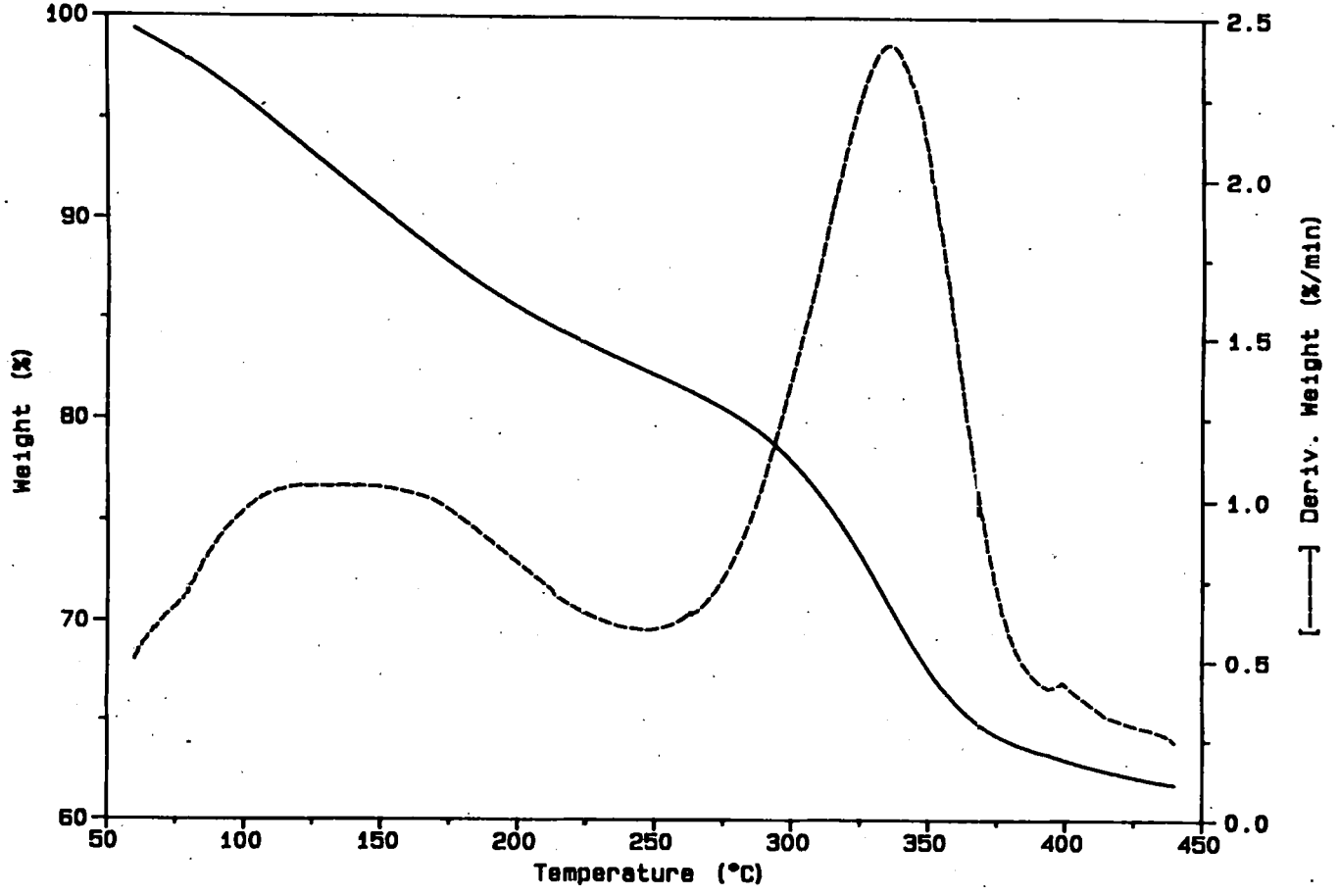

Figure 6.7 – Thermogravimetric curve for basic nickel(II) carbonate.

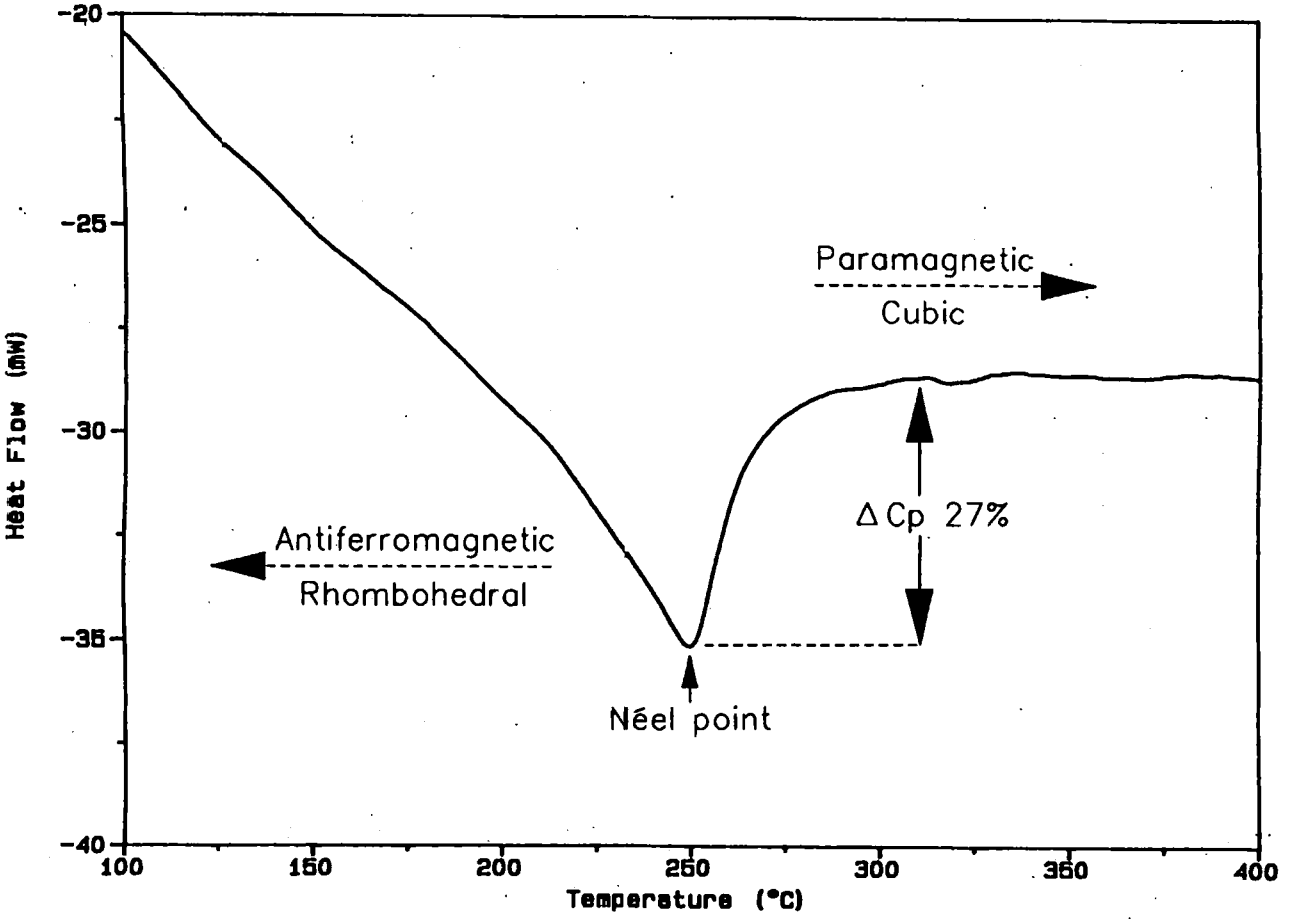

Figure 6.8 – DSC curve for nickel(II) oxide.

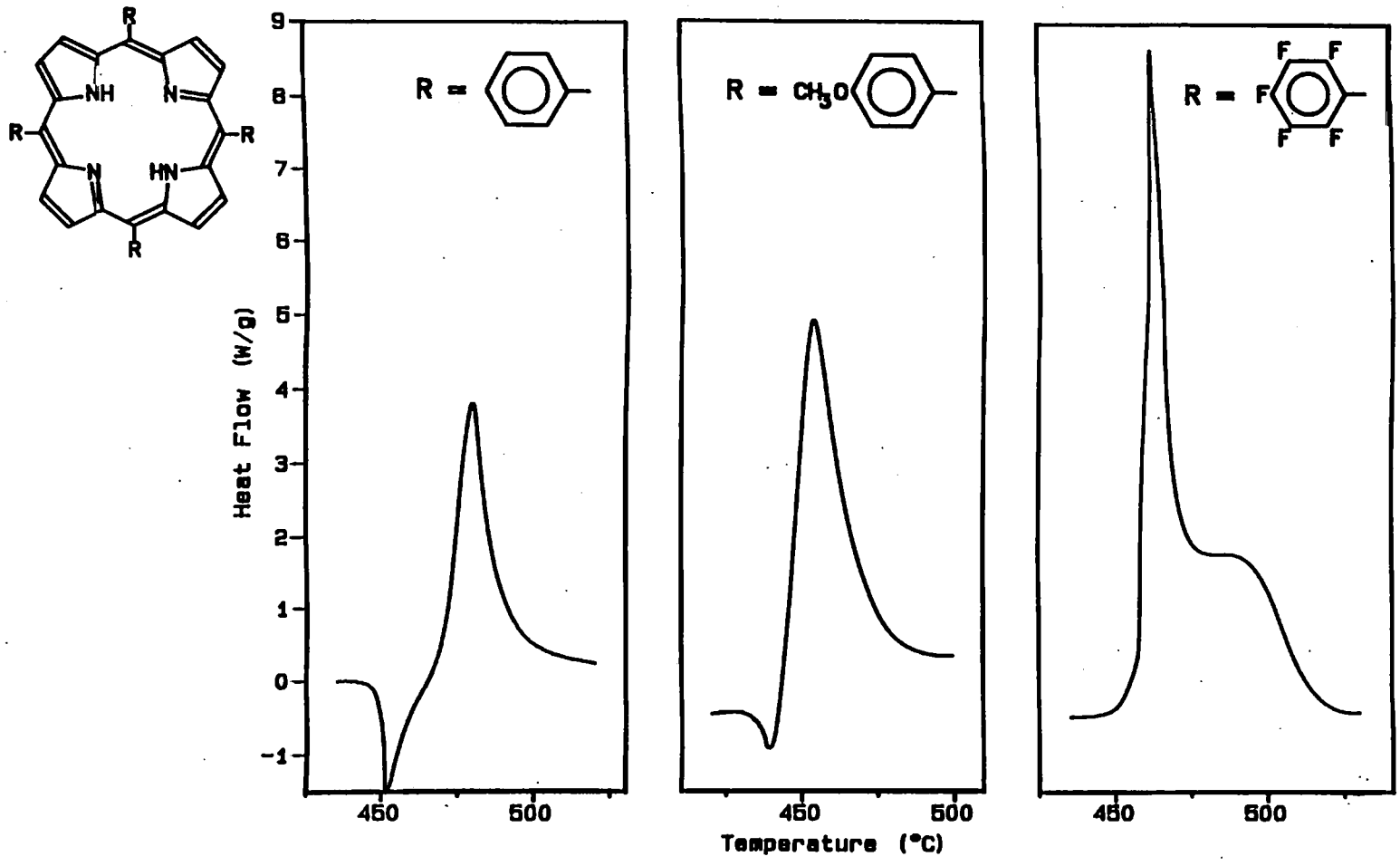

Figure 6.9 – Effect of substituent structure on the resolution between fusion and decomposition for the meso–tetra–aryl porphyrins.

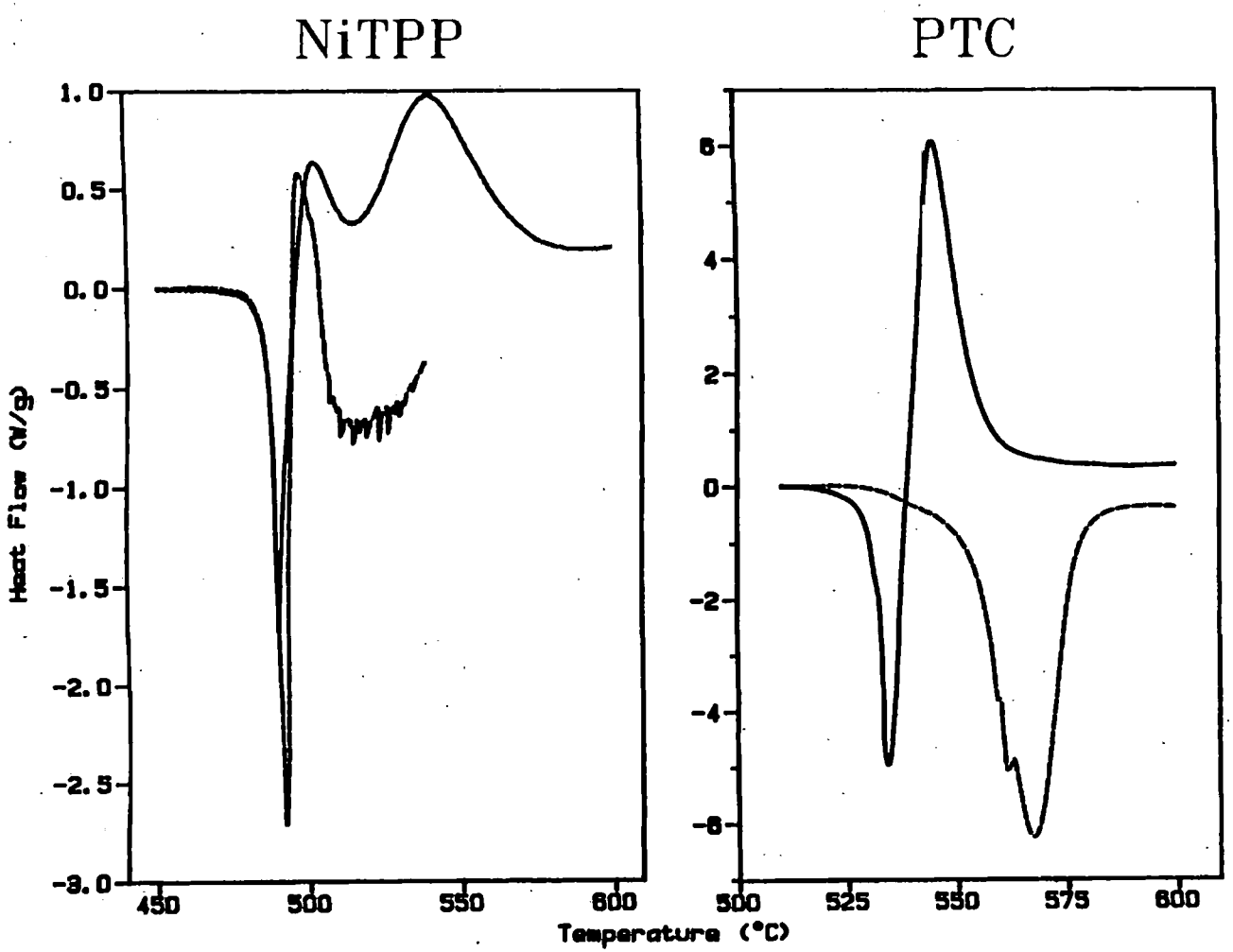

Figure 6.10 – Effect of pan type on the DSC curves for tetraphenylporphyrinato–nickel(II) and phthalocyanine.

——— Setaram hermetic -------- Du Pont non–hermetic

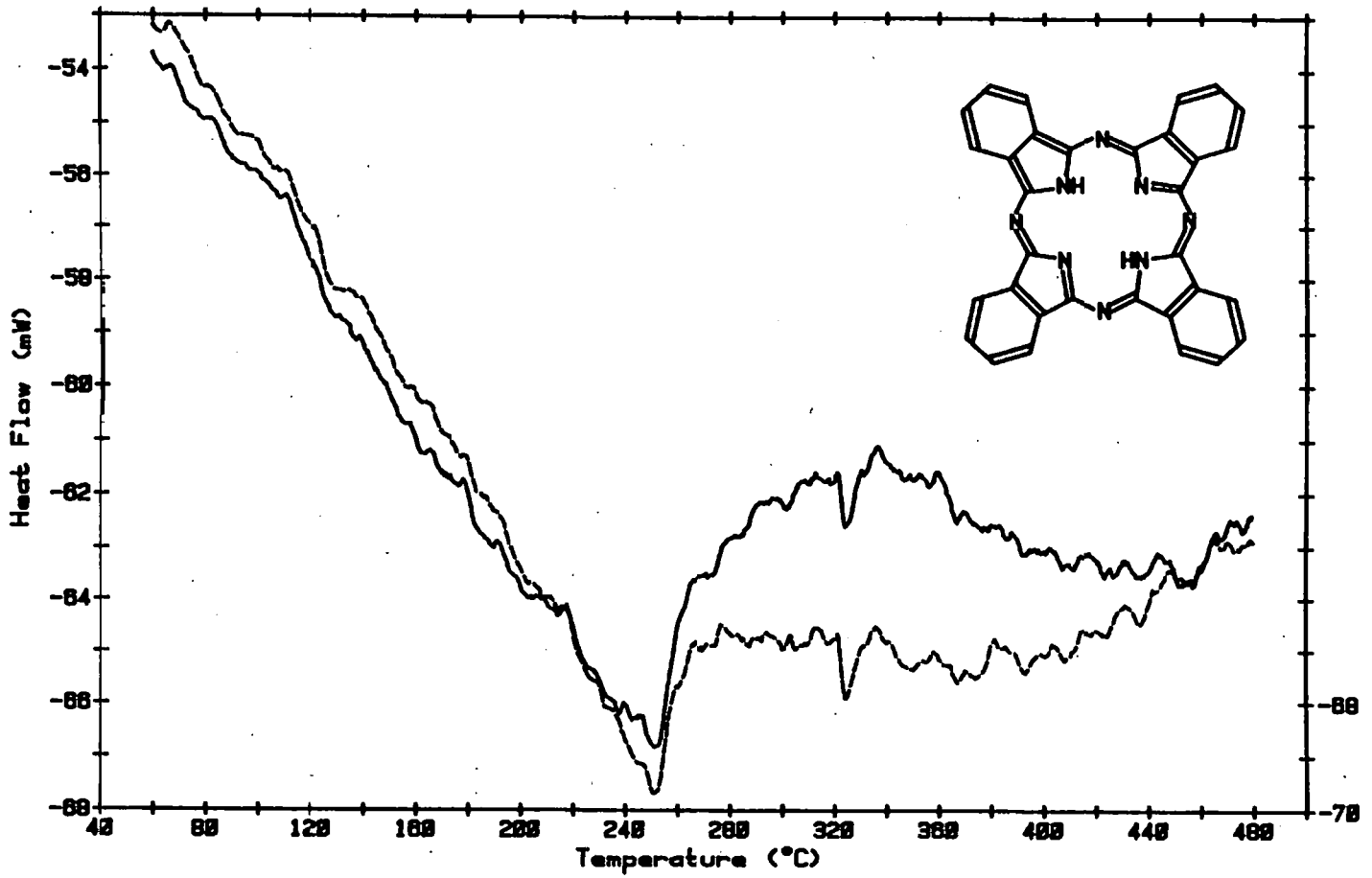

Figure 6.11 – Initial and repeat DSC curves for a PTC/NiO composite pellet.

——— 1st scan -------- 2nd scan

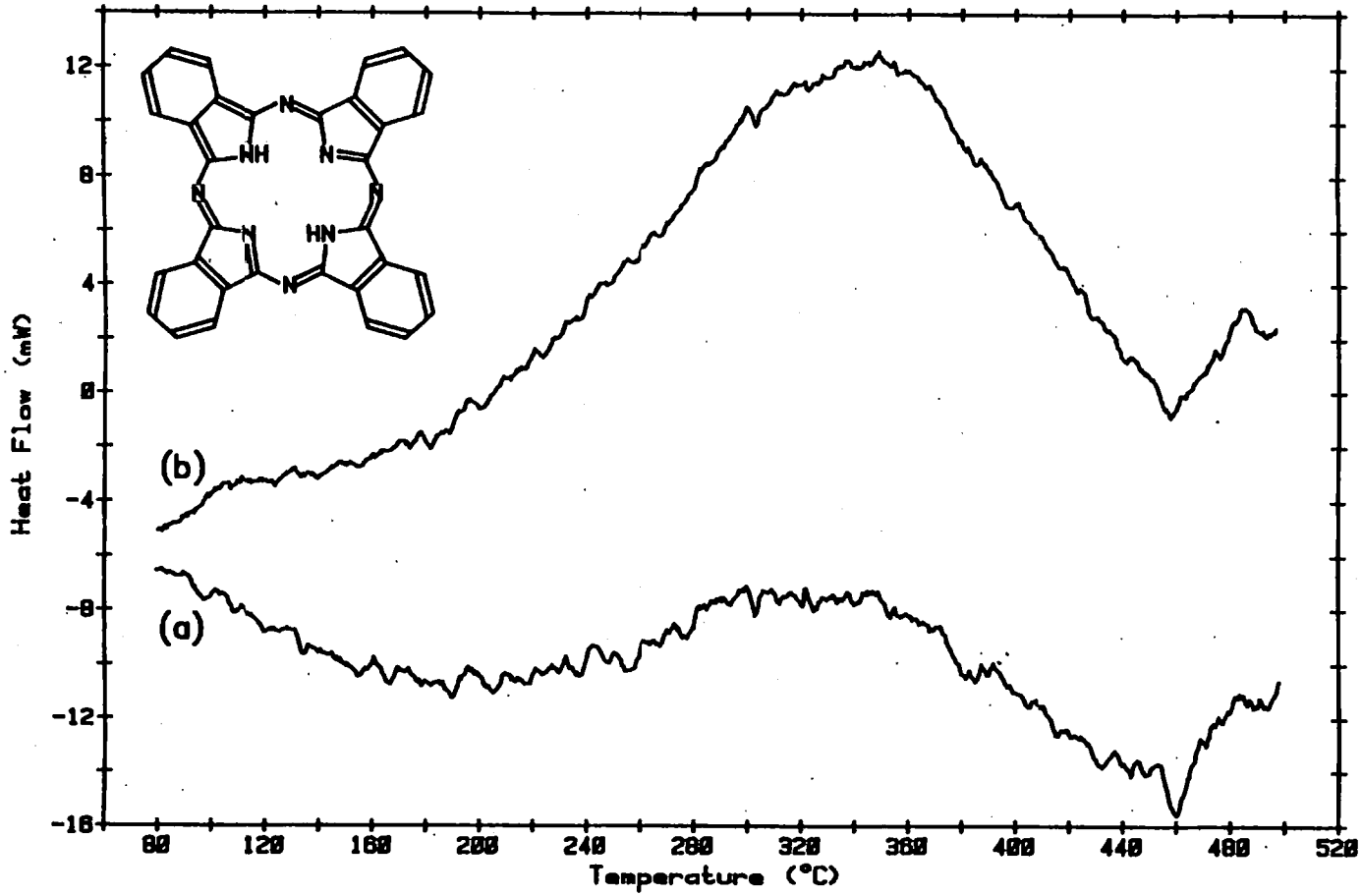

Figure 6.12 – Effect of data subtraction [1st–2nd scan] on the DSC curve for a PTC/NiO composite.

(a) Single 40 mg pellet (Y–axis = x2) (b) Sum of curves for 3x40mg pellets.

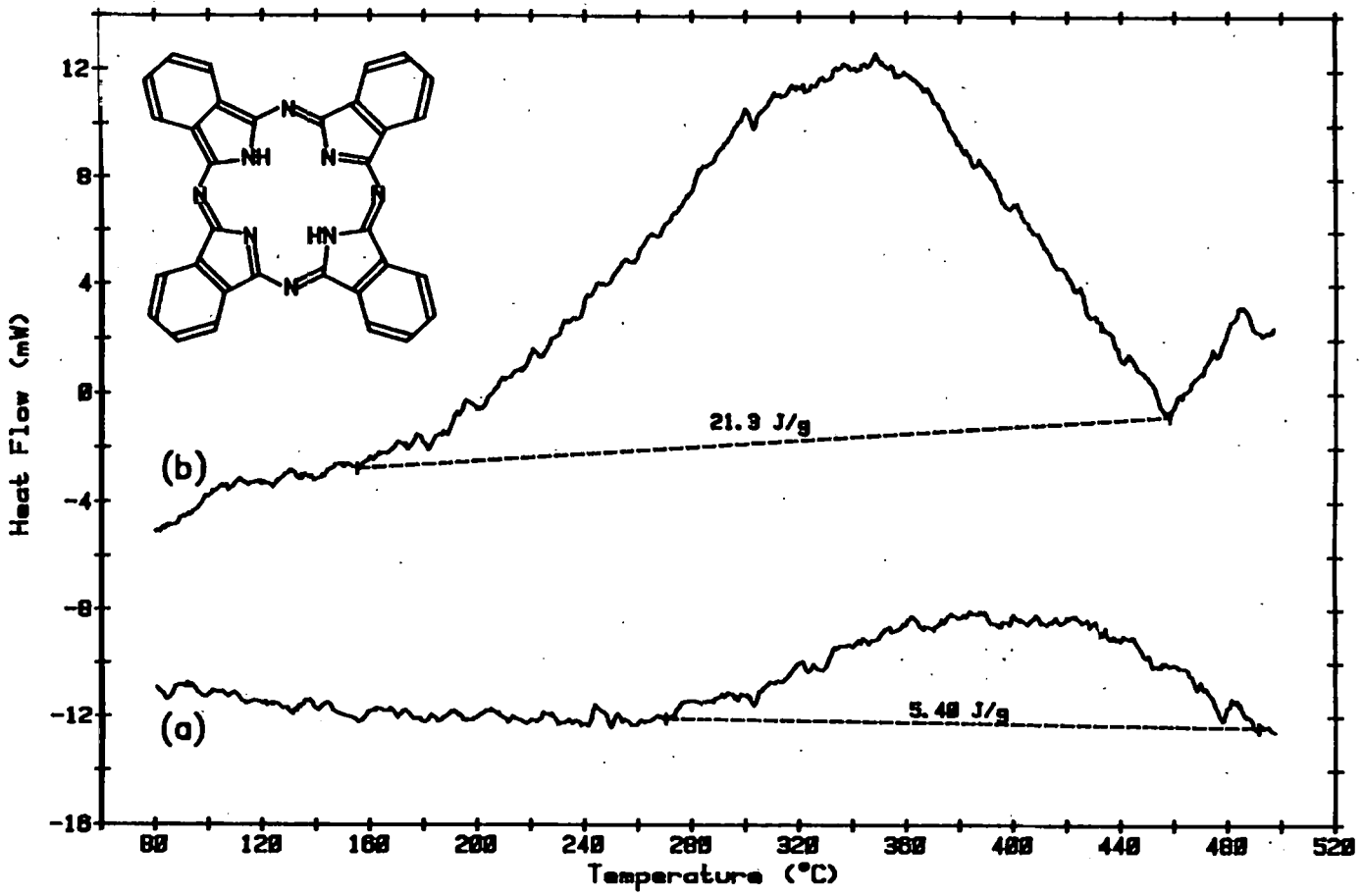

Figure 6.13 – Contribution of stress relaxation in PTC to the 'Interaction DSC curve' for a PTC/NiO composite.

(a) 2x30 mg pellets of PTC (b) 3x40mg pellets of PTC/NiO.

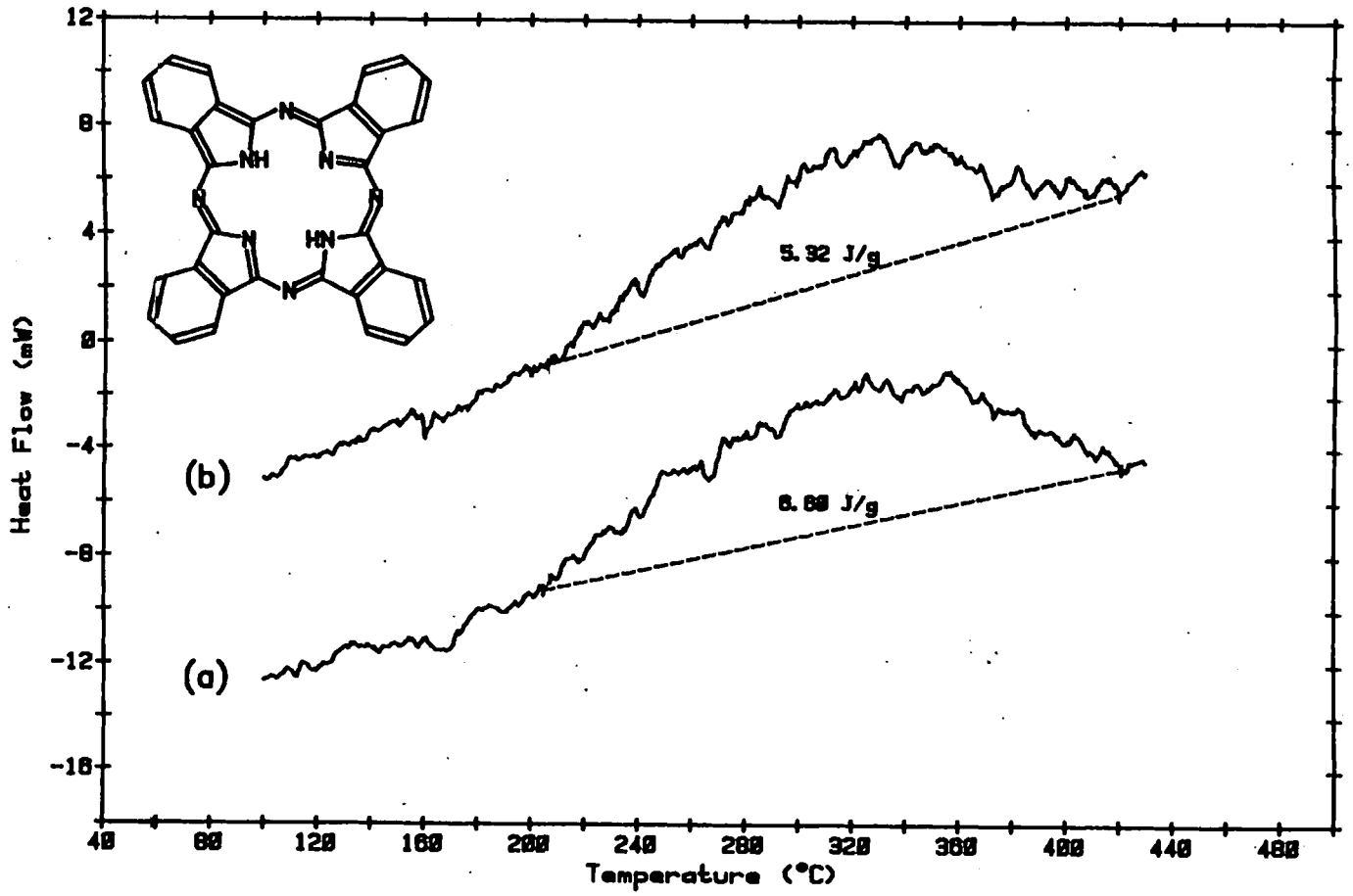

Figure 6.14 – Residual interaction DSC curves after de–activating the oxide.
Oxide treatment: (a) Equilibrated with polar solvent (b) Annealed at 300°C.

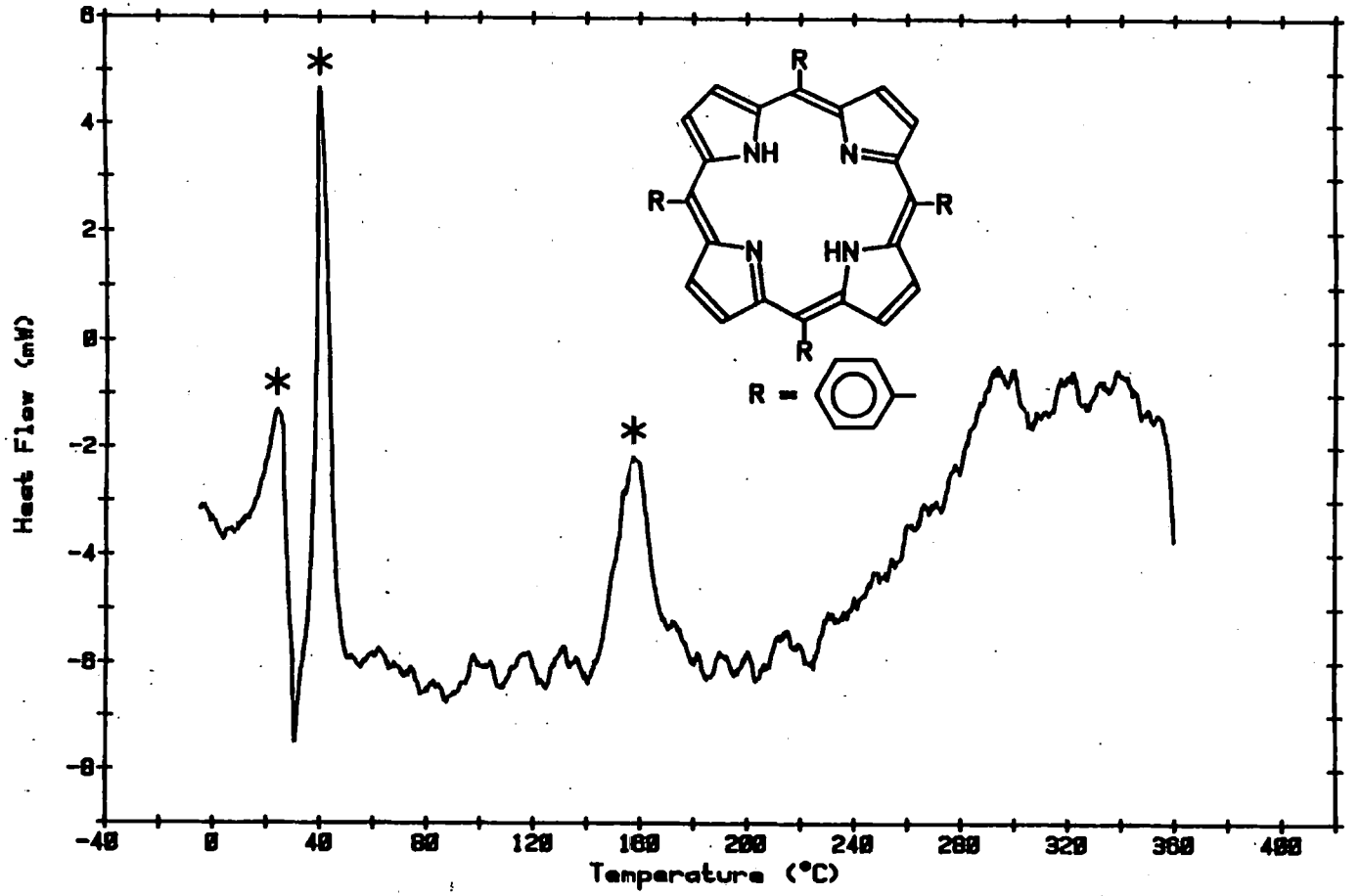

Figure 6.15 – Interaction DSC curve for TPP/annealed NiO.
(peaks marked * appeared as endotherms in the second scan)

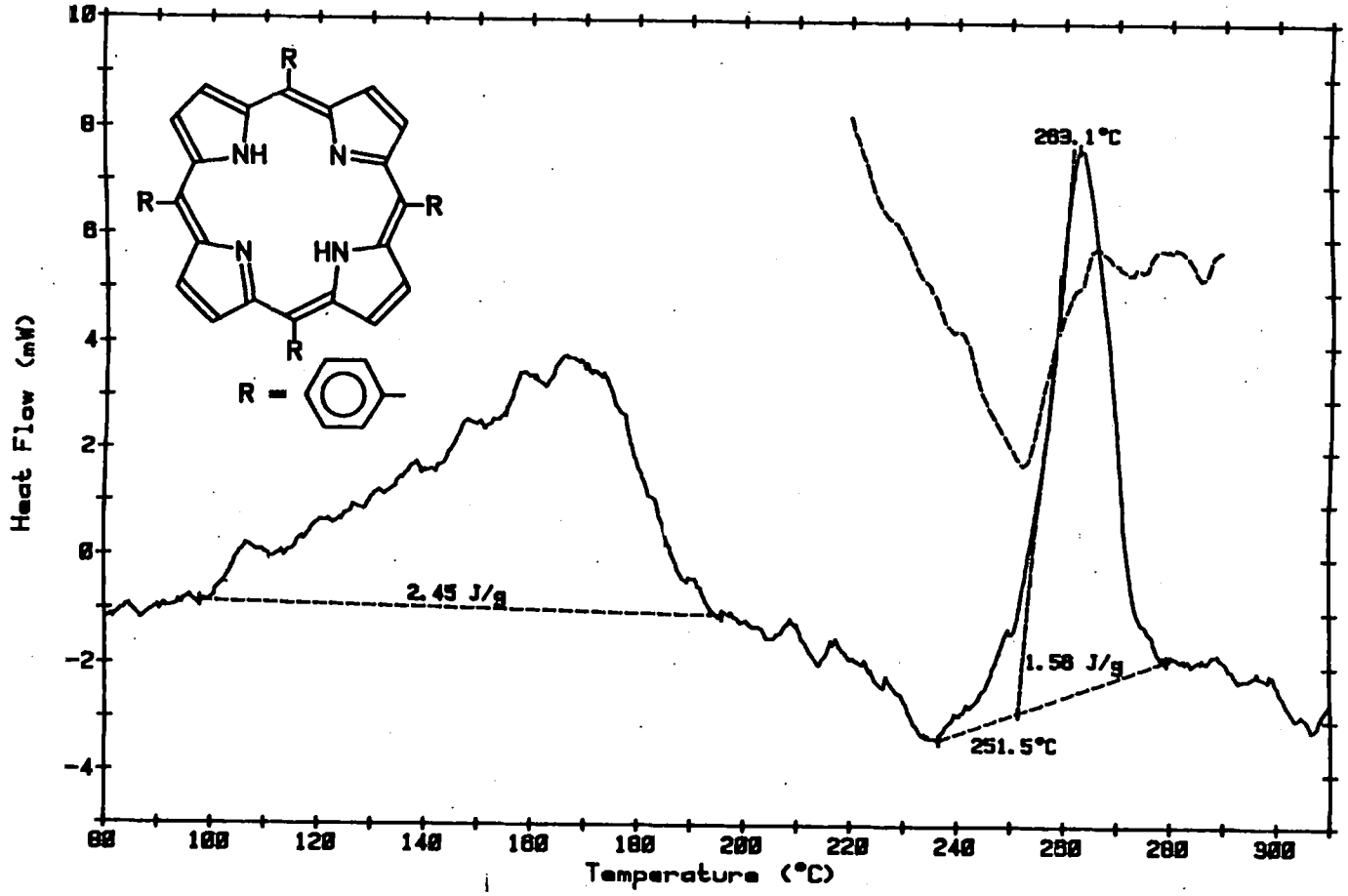

Figure 6.16 – Interaction DSC curve for TPP/un–heated NiO.

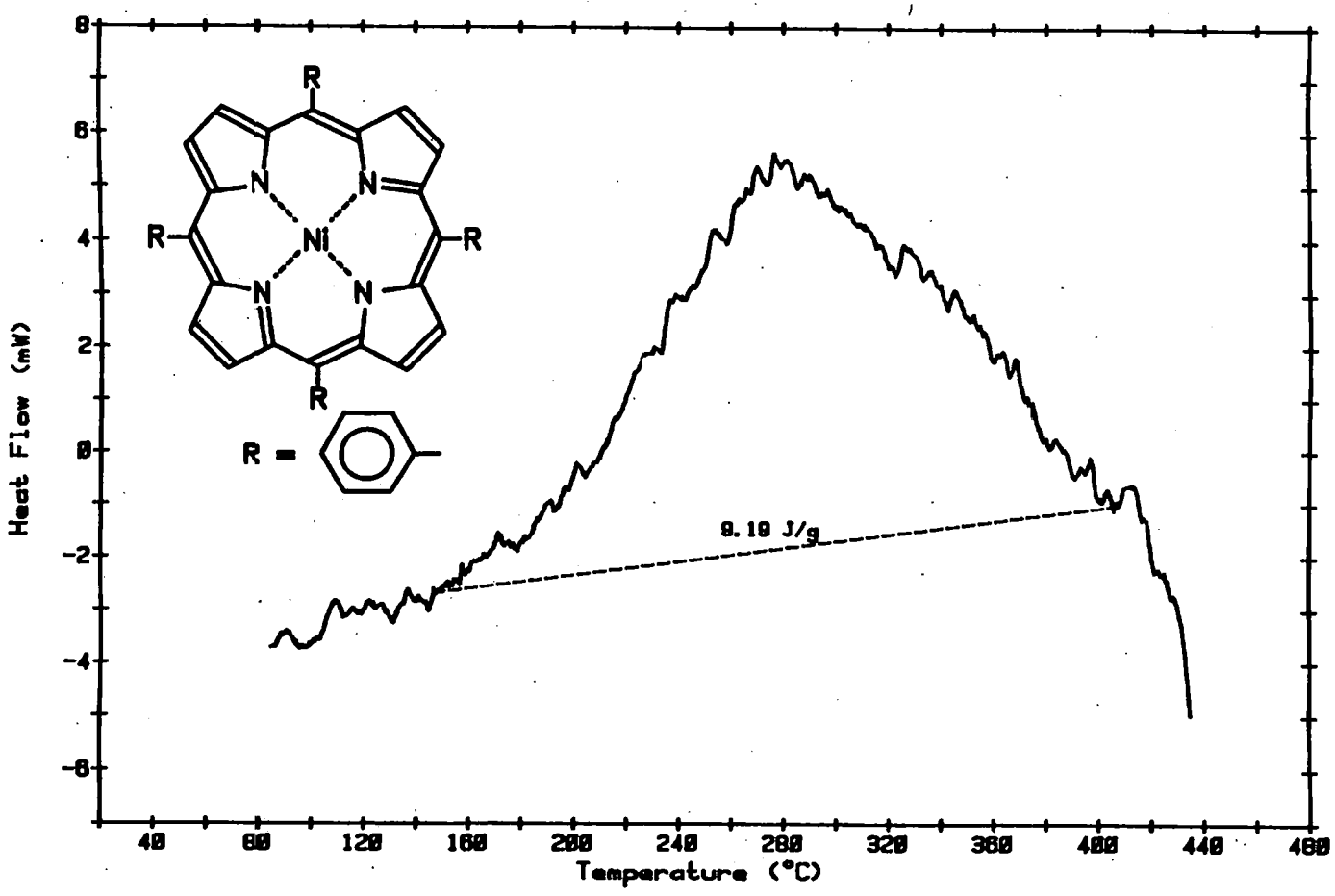

Figure 6.17 – Interaction DSC curve for NiTPP/annealed NiO.

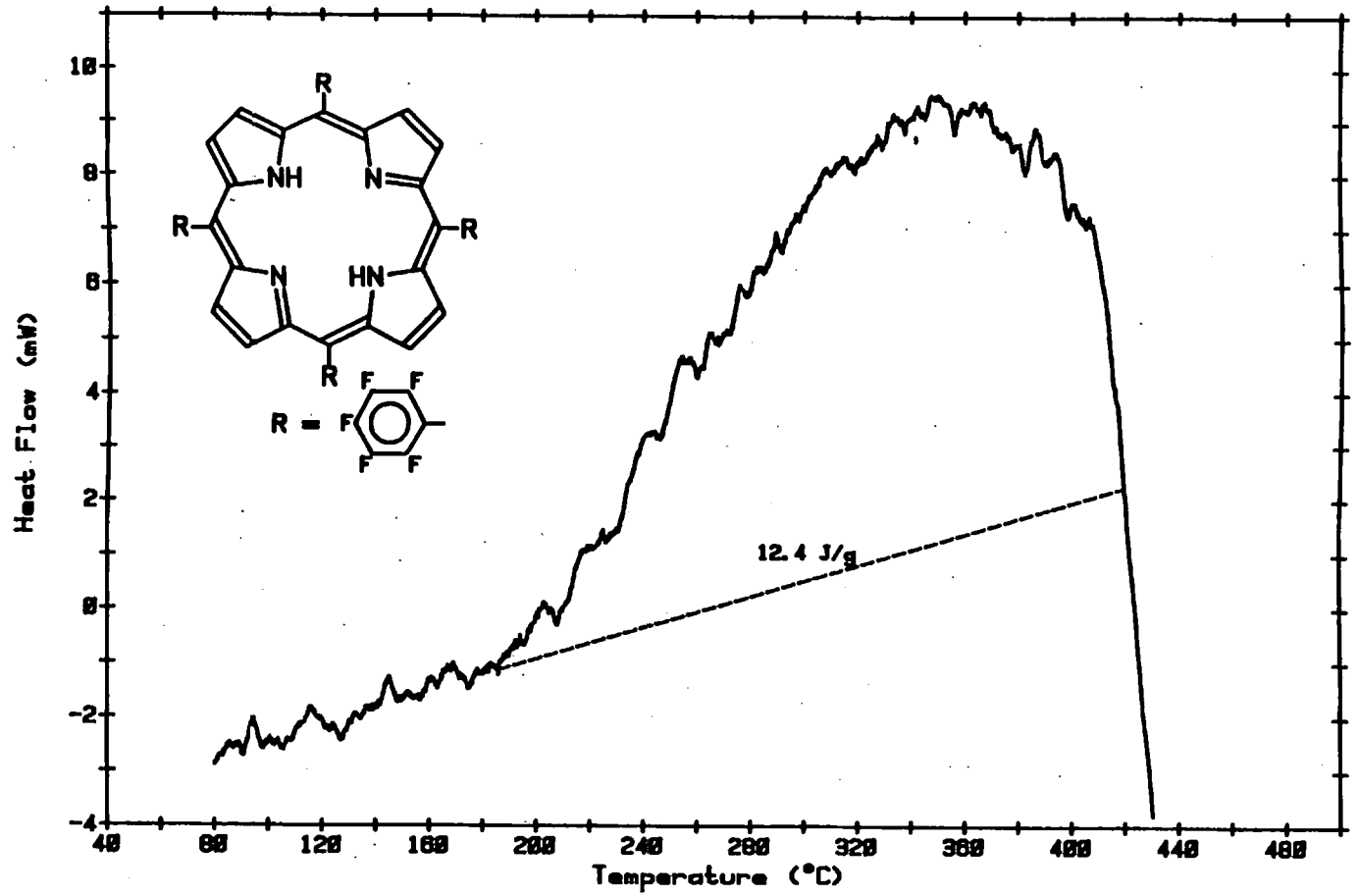

Figure 6.18 – Interaction DSC curve for T(PFP)P/un–heated NiO.

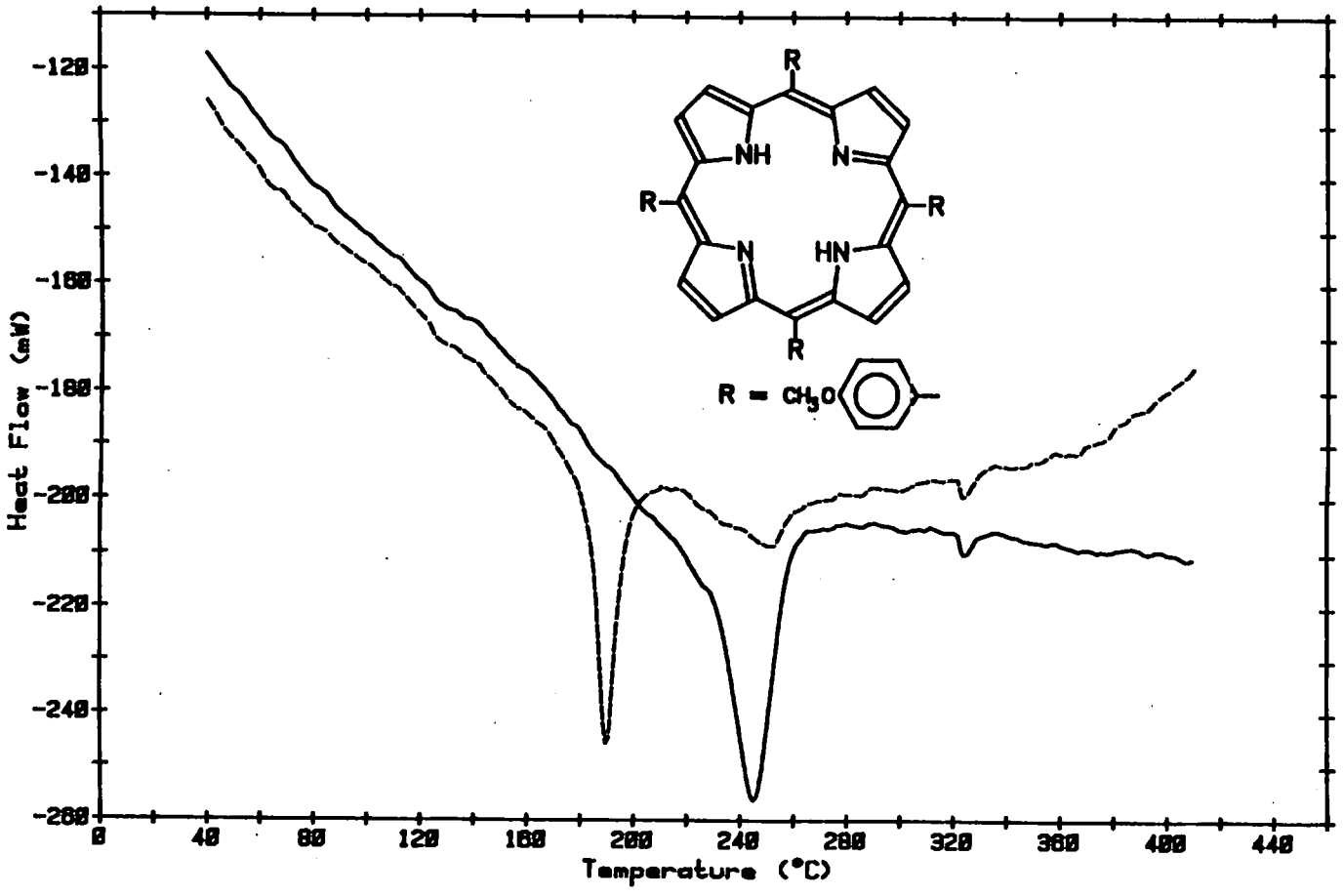

Figure 6.19 – Initial and repeat DSC curves for T(p–MP)P/un–heated NiO.
——— 1st scan --------- 2nd scan

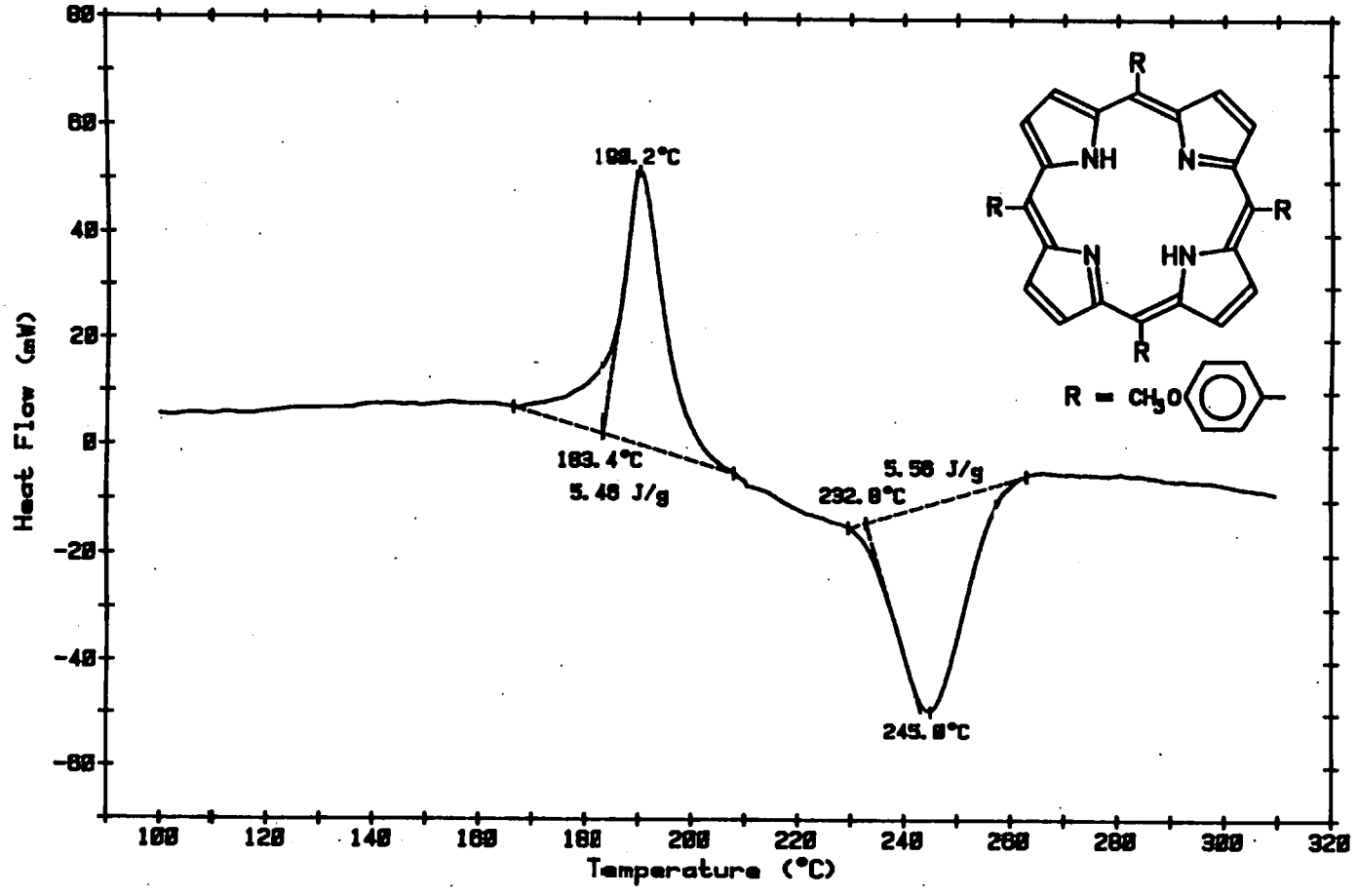

Figure 6.20 – Interaction DSC curve for T(p–MP)P/un–heated NiO.

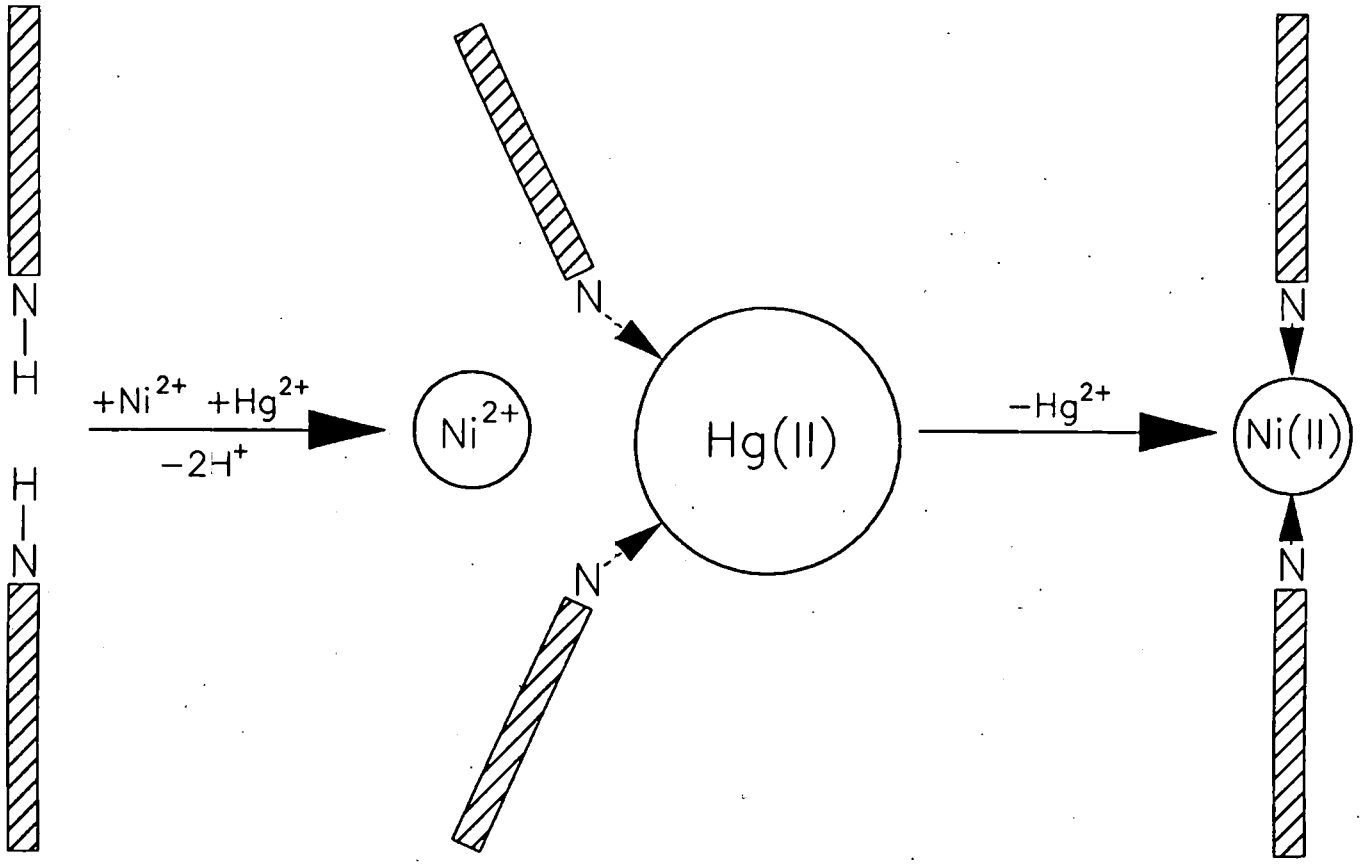

Figure 6.21 – Mechanism for accelerated formation of a nickel–porphyrin complex, via a distorted bimetallic intermediate

(the shaded bar represents a section through the porphyrin plane)

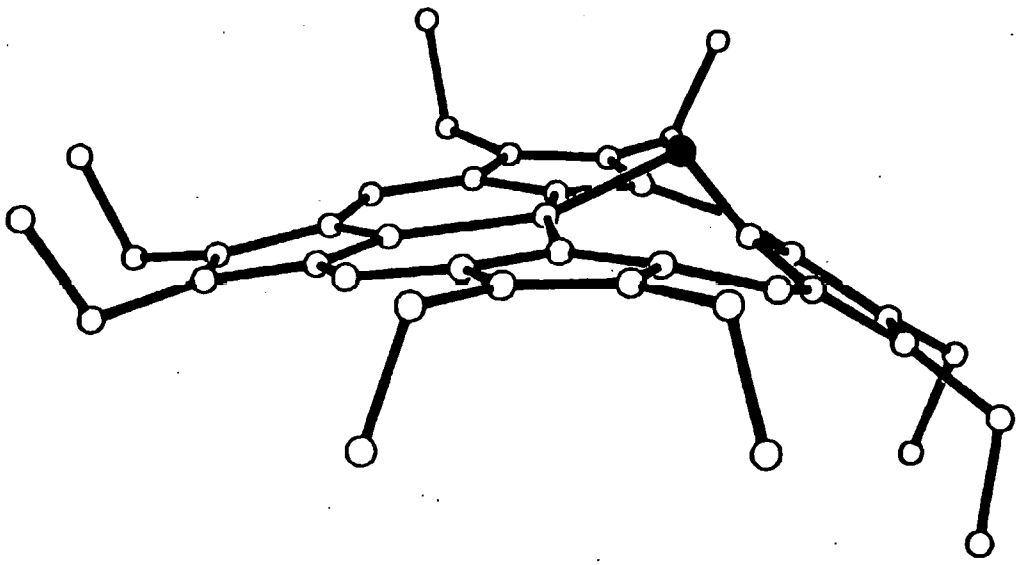

Structure of N–oxo NiOEP, showing distortion from planarity
(bridging oxygen is shown as a filled circle)
[adapted from Balch et al., J. Am. Chem. Soc. 107 (1985)]

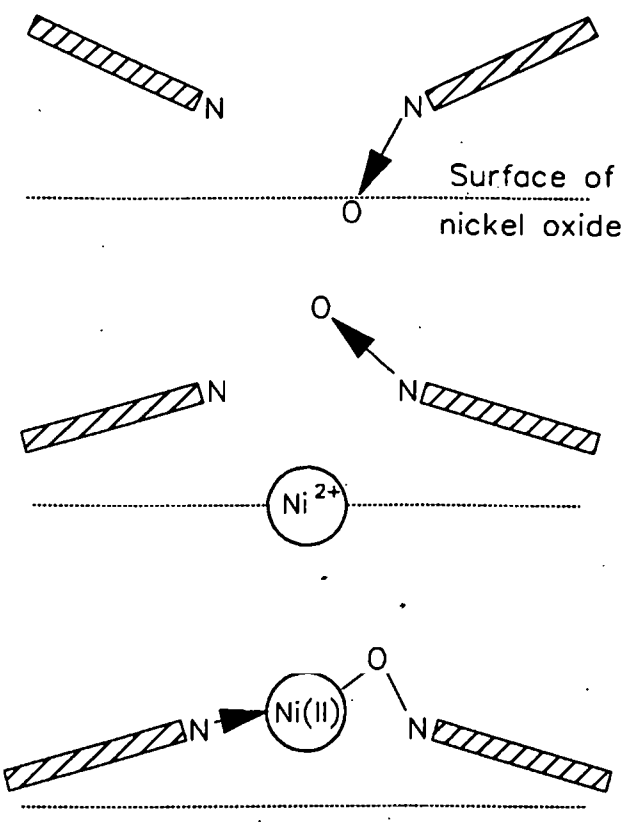

(1) Adsorption and oxidation of porphyrin on NiO surface

(2) Porphyrin 'flips' and moves to eclipse a nickel ion

(3) Nickel ion is abstracted from surface, forming N–oxo complex

Figure 6.22 – Structure of N–oxo NiOEP and a proposed mechanism for producing N–oxo porphyrins on a NiO surface.

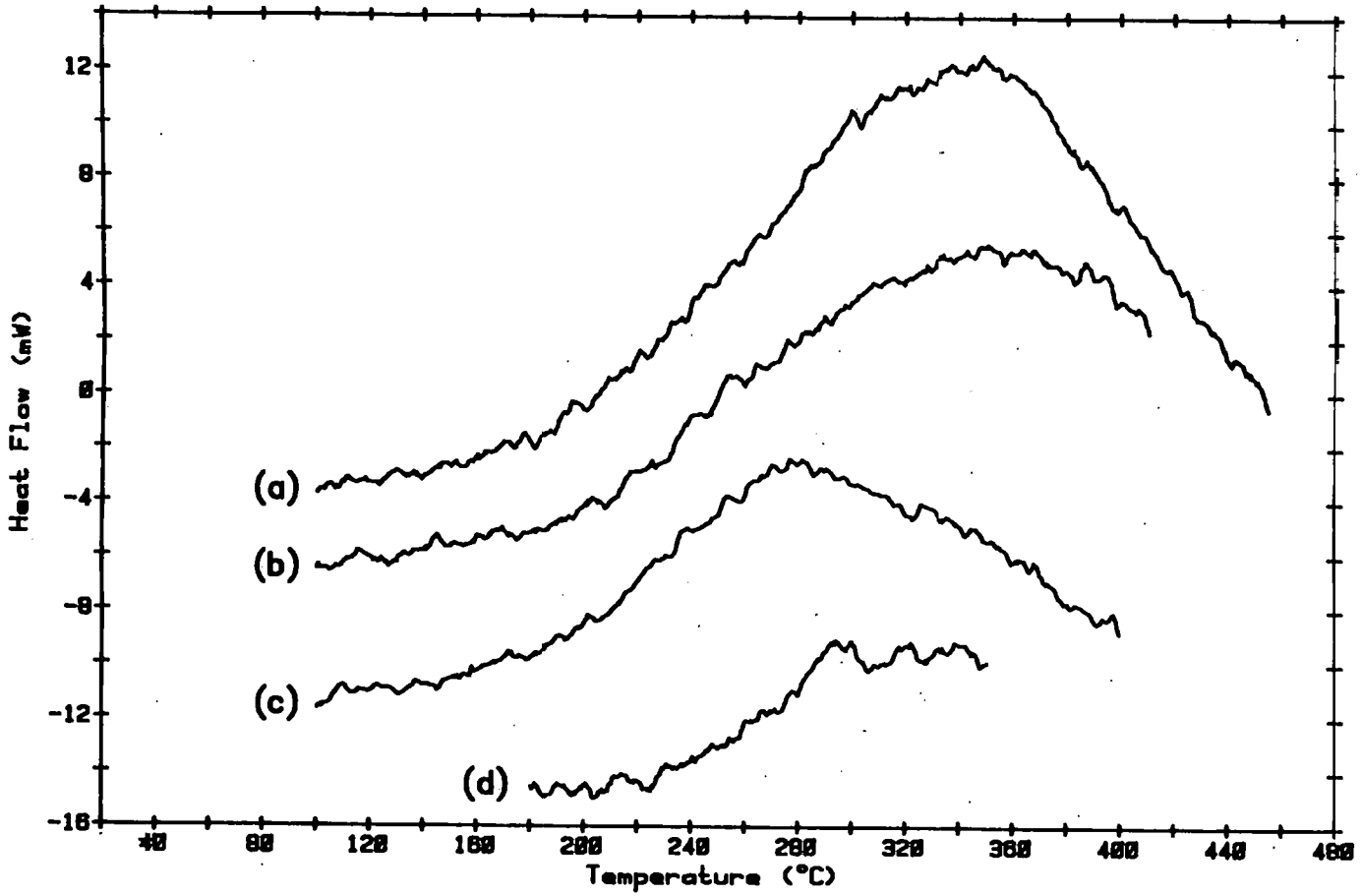

Figure 6.23 – Summary of broad interaction events detected by DSC.
(a) PTC/un–heated NiO (b) T(PFP)P/un–heated NiO
(c) NiTPP/annealed NiO (d) TPP/annealed NiO.

CHAPTER 7

CONCLUSIONS

7.1 EXPERIMENTAL FACTORS WHICH AFFECT DSC PERFORMANCE

Modern DSC systems allow even an inexperienced operator to obtain superficially good DSC data, but the simplicity of the technique is frequently its downfall. Poor quantification and erroneous results are often blamed on the technique of DSC, when the real cause is poor experimental design. The underlying principles of DSC have been widely discussed in the literature, but are perhaps not sufficiently emphasised by the instrument manufacturers because simplicity is a good selling point. The work described in this thesis highlighted the fact that DSC should not be treated as a 'black box' which will produce accurate data no matter how the sample is presented. It is essential to consider the calorimeter, the DSC specimen and its container as being interrelated components which are linked together by heat flow.

7.1.1 Heat transport in a DSC experiment

In order to achieve high sensitivity with a DSC, the proportion of heat flowing into the sample via the measured path (across the ΔT thermocouple) must be maximised relative to all the other flow paths. Thermal resistances in most parts of the DSC are fixed and only the contact resistance (R_c) and leakage resistance (R_g) are accessible to the operator. Control over R_g is limited, because the nature and pressure of the purge gas are usually chosen on chemical grounds rather than with sensitivity in mind.

The concept of the 'transportable DSC specimen' was invoked to describe the combination of the analytical specimen and its container. The operator has more scope for change in this area than in any other, but this option is rarely explored beyond the choice between hermetic and open pans. The type of sample pan and the way it couples the specimen to the heat flow sensing element of the calorimeter have a very significant effect on propagation of an event within the specimen and the way it is detected. Heat transfer between the DSC furnace and the site of a thermal event within the specimen may be broken down into three parts, all of which were shown to have important effects on DSC response:

(a) DSC furnace ⟶ sample container (Figure 7.1)

(b) sample container ⟶ sample boundary (Figure 7.2)

(c) sample boundary ⟶ reaction site (Figure 7.3)

(a) Coupling between the DSC and the transportable specimen

Parasitic heat transfer through the sample chamber atmosphere acts in parallel to the measured heat flow. Increasing the thermocouple/pan contact resistance therefore increases the relative contribution by the unmeasured parasitic component, and hence reduces calorimetric sensitivity. This fact is explicit in the theory of heat-flux DSC, but the influence of the external aspect of the sample pan is less obvious. Altering the geometry or emissivity of the pan affects the parasitic flux directly and the errors from this source were found to be surprisingly large. This observation is not simply academic - it has important consequences in common applications of DSC. For example, recommended procedures for the measurement of heat capacity [46,47,48] involve a change of sample container geometry which can bias the results by several percent. Differences in the ratio between parasitic and measured heat fluxes also explained the observation made by Baricco *et al* [90], that the DSC calibration factor derived from heat capacity measurement altered when a conductive metal was substituted for α-Al_2O_3.

The change of sensitivity with resistance of the measured conduction path was found to be the same (within experimental error) for both endothermic and exothermic events occurring in a similar temperature range. This is to be expected because the relative resistance values for the measured and parasitic paths were identical in the fusion and crystallisation experiments. This means that, even if the heat flows are reversed during the exothermic process, the relative measured and parasitic fluxes will be in the same ratio.

(b) Heat transfer to the analytical specimen

One of the simplest, yet most important, observations in this work was the dramatic improvement of peak shape achieved by using a close fitting lid on the DSC pan (Figure 3.10). The effects were consistent with the lid acting as a parallel heat flow path around the boundary of the specimen, which allowed a second interface to form on the top

surface of the specimen, as shown in Figure 7.2. The implication was that a crimped container, which makes contact with the specimen over a large area, should be used whenever the chemistry of the process being investigated allows the specimen to be enclosed.

(c) Heat transfer within the specimen

When heat has been transported to the surface of the specimen, it must then travel through the body of the specimen to the reaction site. If the solid is heterogeneous, the microstructure of the specimen becomes important in determining its effective thermal resistance and the geometry of interface development. The leading edge of the DSC peak for the γ-β transition in potassium nitrate was much more curved than its thermal conductivity had predicted. This effect was attributed distortion of the interface as it traversed the micro-crystalline specimen. The conductivities of porphyrin/nickel oxide composites were also found to be particularly sensitive to changes in their microstructure, which resulted from interactions at the interface between the two phases (Figure 7.3).

7.1.2 Consequences for the design of DSC experiments

It is evident that sample preparation and the design of the DSC experiment are particularly important when studying reactions in the solid state. The microstructure of the specimen and the shape and magnitude of the resistance profile within it determine the rate at which the transition can propagate. Consequently, these factors affect the apparent kinetics of the process as indicated by the DSC response. The thermal resistance of the specimen, and the way it changes during the DSC experiment, should be considered both as an essential part of the experimental design and as a source of error when analysing the results.

Sensitivity to small energy changes and accurate recording of a DSC event will both be optimised by minimising the following:

- thermocouple/pan contact resistance,
- pan/specimen contact resistances,
- internal resistance of the specimen,
- emissivity of the sample container.

If results from different materials are to be subjected to rigorous comparison, it is important to match the above variables rather than sample mass. The best configuration of the transportable specimen which was identified to meet these requirements was - an analytical specimen in the form of a disc, held in a polished container which makes effective thermal contact with both planar surfaces of the disc.

7.1.3 Relevance to other DSCs

All of this work was carried out using a Du Pont calorimeter, but the conclusions are equally applicable to other types of DSC based on Boersma's design. Power-compensation and Tian-Calvet systems will also be subject to matrix effects, because heat must still be transported through the body of the specimen. Calorimetric errors for these types of DSC may well be different from those measured in the Du Pont 910, because the specimen is enclosed by a boundary which forms part of the heat flow path. This will alter the form of the resistive matrix which transports heat through the specimen and hence cause different distortion of the DSC peak for a particular specimen geometry.

There appears to be scope for improvement in the design of Du Pont's DSC cell, which has remained virtually unchanged from the design discussed by Baxter in 1969 [32]. The dominant thermal resistance is at the contact surface between the sample container and the thermocouple (R_c). Decreasing this resistance would make peaks sharper, which would reduce the parasitic contribution and also improve the resolution between overlapping events. For quantitative calorimetric work, Du Pont [47] recommend placing the sample and reference pans on silver discs, which are attached to the thermocouple platforms using a paste of zinc oxide in silicone grease. This approach is rarely satisfactory, because melting and evaporation of the grease tend to degrade the quality of results. Permanently fixed broad, flat platforms would improve thermal contact and their geometry could be optimised to give accurate centring for a particular type of pan. Radiative heat transfer could be reduced by gold-plating the constantan disc and sample chamber walls, although this might create problems when the cell required cleaning.

Most of the heat-flux DSCs produced today bear a striking resemblance to Boersma's original design, published in 1955. This widespread adoption reflects both the quality of the design and the relative ease of producing it commercially. There have been repeated attempts to discredit it as not being 'real DSC' (particularly by Perkin-Elmer) but heat-flux and power-compensation instruments actually give very similar results. The fact that two such widely different physical approaches can produce the same data gives confidence that DSC in general is a robust technique.

7.2 THE USE OF DSC TO INVESTIGATE INTERACTIONS BETWEEN SOLIDS

The main objective of this work was to optimise experimental DSC conditions for the study of low energy events, occurring in large solid specimens. This was achieved and good results were demonstrated for several composites of porphyrins with nickel(II) oxide. The procedures which have been developed should be equally applicable to many other types of composite. With minor modifications, they are also compatible with other designs of DSC. The overall procedure for investigating solid-state interactions involved three parts. These may be used together or applied separately in DSC experiments other than interaction studies.

7.2.1 Sample preparation

The pellet dies normally used to form KBr discs for infrared spectroscopy are ideal for preparing DSC specimens from powdered samples. Disc-shaped specimens produced in this way make good thermal contact with the most widely used type of DSC sample pan. A hydraulic press can give very high compaction pressures within the safe operating range of these dies. Use of the maximum specified force with a 6 mm die:

- produced cohesive composites,
- did not cause detectable chemical reaction to occur,
- gave sufficient solid-solid contact to allow interactions to be detected by DSC.

7.2.2 Measurement of thermal conductivity

Published thermal conductivity data obtained by the DSC fusion onset slope method show precision of the order ± 20-50% and bias which is often > 100% of the measured value. This study has led to significant improvements in the precision and accuracy which can be achieved in measuring thermal conductivity by DSC. A measurement precision of ± 3% was achieved for chemically homogeneous materials and it is believed that systematic bias was eliminated. The accuracy of the results was limited to approximately ± 10% by the use of silica as a reference material. An accuracy of better than ± 5% should be accessible through the use of calibration materials whose physical properties are closer to those of the sample.

Peak shape analysis, for a transition propagating through the test material, was considered as a novel approach to measuring thermal conductivity. This analysis confirmed the formation of two transition interfaces in a covered DSC specimen, but was not successful in measuring λ. Anomalies in the apparent conductivity were attributed to the microscopically heterogeneous nature of the specimen. This technique may be a way of investigating interface geometry in disordered solids.

Conductivity data were obtained, using the improved fusion onset slope method, for porphyrins which had not previously been studied and were only available in small quantities. A comparative study was also carried out on binary mixtures containing porphyrins. This was used to evaluate various mathematical models for calculating effective conductivities. One of these, the Hashin and Shtrikman (H&S) treatment, was identified which is applicable to this type of composite. Comparison of the predictions of the H&S model with experimental values of λ was found to be a useful way of detecting structural changes at a solid-solid interface. The technique appeared to be fairly sensitive in cases where a gaseous reaction product caused disruption of the interface. It was particularly useful in the study involving phthalocyanine because the very limited solubility of the organic reactant and product made conventional chromatographic analysis virtually impossible.

7.2.3 Detection of small enthalpy changes

Instrumental artifacts were found to be a very significant source of error in this work. The form of any artifacts should always be investigated under conditions which are to be used for subsequent interaction studies. Conditions which accentuate artifacts include the use of a high signal gain or operation with a large ΔT offset (due to a large sample mass). Some of the spurious effects were of a similar magnitude to the interaction events, and of a form which could easily be mistaken for thermal events within the sample. It was evident that the reference used for data subtraction must be very carefully matched to the sample if the results are to be valid. Use of the fully reacted specimen as a reference proved to be very effective in rising temperature experiments. The complex DSC background, which resulted mainly from the change of heat capacity in nickel(II) oxide, was reduced to below the instrument noise level by this correction procedure. The detection limit achieved by using the double-scan procedure on a single 40 mg specimen was:

Peak heat-flux < 0.1 mW at a signal/noise (S/N) ratio = 5:1.

The S/N ratio was improved by carrying out three replicate double-scan experiments on separate specimens and combining the interaction DSC curves. This achieved:

S/N = 20:1 for $\Delta H \sim 3\ J \cdot g^{-1}$ of sample, over a 300°C interval.

7.3 INTERACTIONS BETWEEN PORPHYRINS AND NICKEL(II) OXIDE

Liquid intermediates participate in many reactions which appear to involve only solid phases. This was observed for technical grade TPP, where the DSC curve for a composite with nickel(II) oxide was dominated by events which were attributable to liquid impurities. Careful purification of the porphyrins allowed two types of DSC event to be detected which are believed to be true solid-solid interactions:

Broad event > 150°C:

This was observed for several porphyrins (Figure 6.23) and may be a general feature for all molecules of this type. The following characteristics were identified:

(a) The exothermic process began at a temperature ~ $0.55 \cdot T_{fus}/K$ for the porphyrin. This suggested (according to Tammann's rule) that interaction was initiated by mobility in the porphyrin lattice. The ranking of Tammann temperatures also correlated with steric hindrance of the porphyrin core.

(b) The onset point did <u>not</u> correspond to the temperature regions assigned to either stress-relaxation in the compacted porphyrin, or decomposition of OH^-/CO_3^{2-} functions on the oxide surface.

(c) There was no detectable change of heat-flux during the Néel transition which might be attributed to enhanced reactivity.

(d) The event was suppressed or eliminated by deactivating the nickel oxide with polar solvents, or by annealing it at 300°C in argon.

(e) The reaction occurring in this temperature region caused disruption at the interface for PTC/NiO, as shown by SEM of the fracture surface. This disruption caused λ to decrease.

<u>Sharp event for TPP/un-heated NiO</u>:
This appeared as a very specific, repeatable peak in the DSC curve of only one of the composites. Its characteristics were as follows:

(a) The onset point (first deviation from the baseline) corresponded to decomposition of OH^- and CO_3^{2-} functions associated with Ni^{2+}.

(b) The heat-flux increased rapidly at the Néel transition point. This is probably related to stress-induced nucleation caused by dimensional changes in the surface layer or the underlying oxide. Similar phenomena have been attributed to the Hedvall effect.

(c) The peak was eliminated by annealing the nickel oxide at 300°C in argon.

The effect of annealing on both of these events may be related to the degree of oxygen coverage on the oxide surface. Products attributable to oxidation of the porphyrin were not detected in the few

chromatographic analyses which were carried out, but *N*-oxo porphyrins are feasible as reaction products (as discussed in section 6.6.4).

7.4 FURTHER WORK

The studies reported in this thesis have led to improved techniques for:

(a) Measurement of thermal conductivity using small specimens.

(b) Detection of low energy interactions in heterogeneous solids.

These techniques are applicable to a wide range of problems, but especially in the study of interfacial processes such as:

- understanding the formation and behaviour of organic coatings on inorganic substrates, such as those used in electrochemical and photovoltaic devices.
- deactivation of catalysts and reactions which take place at organic/inorganic interfaces.
- growth of passivating surface films and formation of deposits.

Modelling and measurement of thermal conductivity might be used to investigate topotaxic mechanisms, which are important in understanding some solid-state reactions. For example, if one reactant phase were grown from vapour or solution onto the substrate phase, the former should be well ordered and have a relatively high conductivity. A topotaxic reaction would lead to a correspondingly well ordered product with little structural disturbance at the interface and the high conductivity would be preserved. Formation of a randomly oriented product would lead to a disordered interface structure and hence reduce the conductivity of the effective medium.

The geometry of an interface as it propagates through a DSC specimen is clearly important in determining the shape of the heat-flux curve. Mathematical comparison of DSC peak shapes for transitions occurring in ordered and disordered solids may help to understand the influence of sample microstructure on the mechanism of the transformation.

Several specific questions arose concerning interactions between porphyrins and nickel oxide which are worthy of further investigation.

- How much nickel-complex is formed from the purified porphyrins during the broad exothermic event > 150°C?
- Do the black and green forms of nickel oxide interact differently with the purified porphyrins?
- Can the events which were suppressed by annealing nickel oxide at 300°C be recovered by re-annealing at 800-900°C?
- Are *N*-oxo porphyrins or their complexes formed when the nickel oxide has a large excess of bulk/surface oxygen?

Most of these could be answered by carrying out interaction DSC experiments using nickel oxide specimens which had been annealed under various conditions. Conditions have already been established for measuring the yield of simple Ni-porphyrin complexes by HPLC, but reference materials would be required in order to adapt these for identification of the *N*-oxo compounds.

7.5 CONCLUDING REMARKS

Mark Twain observed [152] that *"There is something fascinating about science. One gets such wholesale returns of conjecture out of such a trifling investment of fact."* A corollary of this is often levelled critically at the technique of DSC - *"It tells you that something is happening, but not what it is."* Although this statement is true as far as it goes, DSC is only intended as a technique for measuring heat flow. The work described in this thesis showed that the Du Pont 910 calorimeter fulfils this role very well and is capable of very high sensitivity, even in the presence of strongly interfering events.

Critics of DSC commented during this work that some of the experiments were so far removed from analytical DSC as to make them irrelevant. This was particularly directed at the experiments involving a stack of silica and aluminium discs under the sample pan*. Although this

---

*This jaundiced view may stem from unconscious memories of Christian-Anderson's classic fairy tale, in which the Queen-mother also employed detection through a resistive laminate as a test of sensitivity.

approach may seem unorthodox, it was effective in simulating the axial resistance of the composites (which were ~ 50-100 $K \cdot W^{-1}$) for studies using the metallic glass. The results from the investigation of matrix effects gave confidence that the small events detected in the composites represented real interactions, rather than being artifacts.

Many of the problems encountered in thermal analysis result from over-interpretation of the data. Kinetic parameters derived from thermal techniques are not renowned for their accuracy and this usually arises because the change under investigation is not measured directly. For example, fractional mass losses during a TG step and partial areas under a DSC curve are both used to infer the degree of reaction (α). This approach of 'reading-across' renders both techniques subject to large errors, many of which result from the nature of the (solid) sample. In TG, entrainment of a volatile product within the solid often causes α to be under-estimated. The shape of an exothermic DSC peak was shown in this thesis to be affected by changes of thermal resistance, which altered the apparent kinetics of crystallisation and resulted in compensation behaviour.

Oswald has stressed the need for a range of complementary techniques when studying thermal decomposition reactions [153]. One of the most useful techniques in thermal studies is visual inspection, and it is sometimes possible to observe the geometry and progress of a reaction directly. Galwey *et al* have used a replication technique to identify the internal structure of nuclei formed during dehydration. In chrome-alum these nuclei were shown to be composed of clusters of laminar cracks which separated the product into regions of approximately hexagonal section [154]. Some of the problems which can arise if a thermal analysis experiment is poorly designed are illustrated by the decomposition of $Ni(SCN)_2(NH_3)_2$ [155]. The reaction takes place by loss of ammonia and begins specifically on two opposite ((001) and (00$\bar{1}$)) faces of the crystal. The two interfaces advance into the crystal at a linear rate and converge along the *c*-axis. The reaction was shown to be inhibited if two crystals contacted each other on their (001/00$\bar{1}$) faces, or if a single crystal contacted the sample holder on this face. TG analysis using a single crystal with its (001/00$\bar{1}$) faces exposed gave results which supported linear

interface advance. However, a more conventional TG experiment, using a bed of powdered sample, grossly underestimated the rate of decomposition for unconstrained $Ni(SCN)_2(NH_3)_2$.

None of the above facts relating to the geometry of reaction nuclei and interfaces could have been derived from analysis of a thermoanalytical curve. In the work for this thesis, the combination of electron microscopy with measurements of ΔH and λ (using DSC) allowed the occurrence of a gas-forming interfacial reaction to be demonstrated. Heat-flux measurements alone would have given no indication as to the nature of the interaction. When treated in isolation, a heat-flux curve does indeed offer 'wholesale returns of conjecture' but the information provided by DSC is invaluable when it is recognised as being <u>complementary</u> to other analytical techniques.

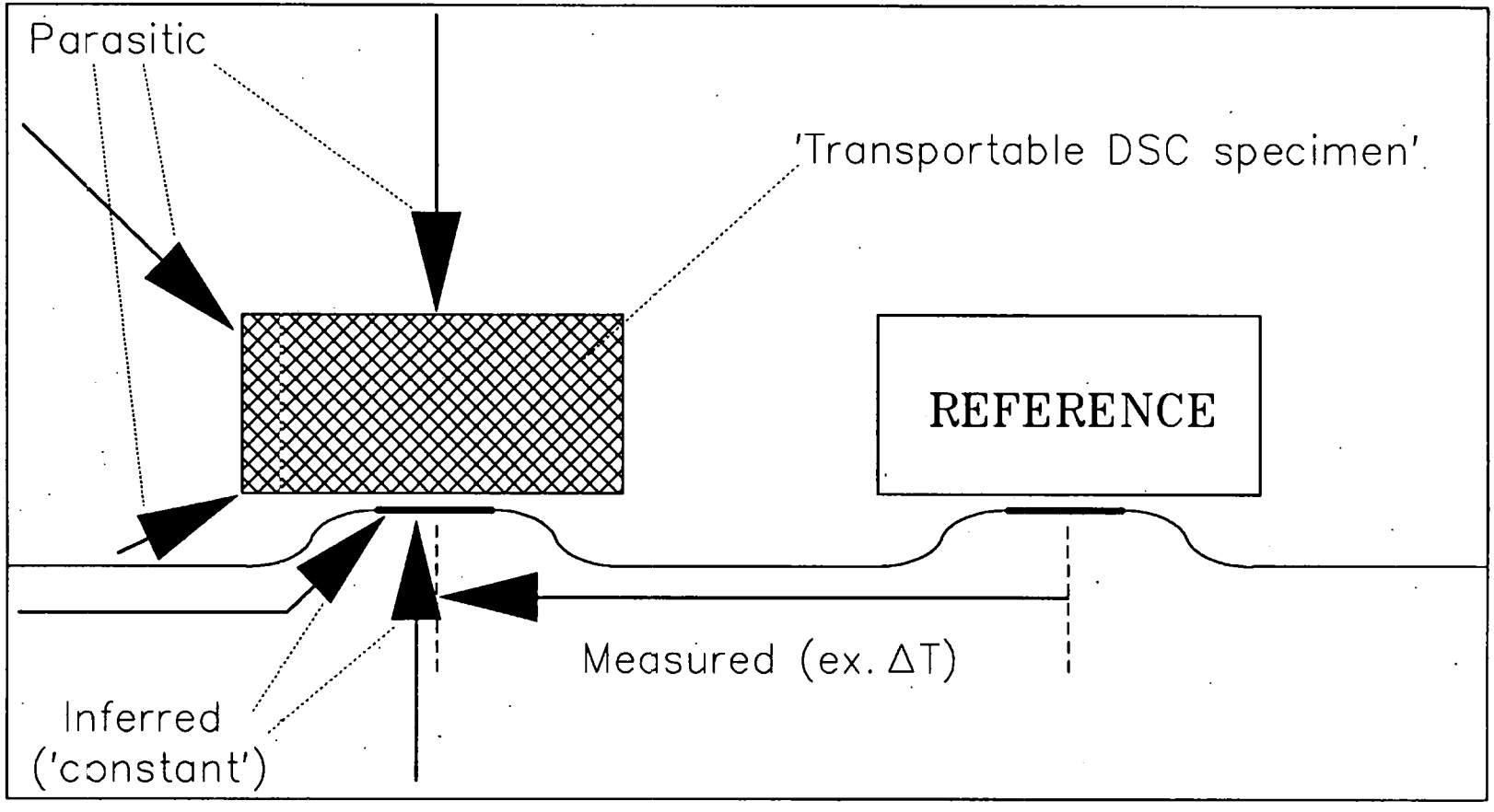

Figure 7.1 – Heat transfer paths in the DSC sample chamber.

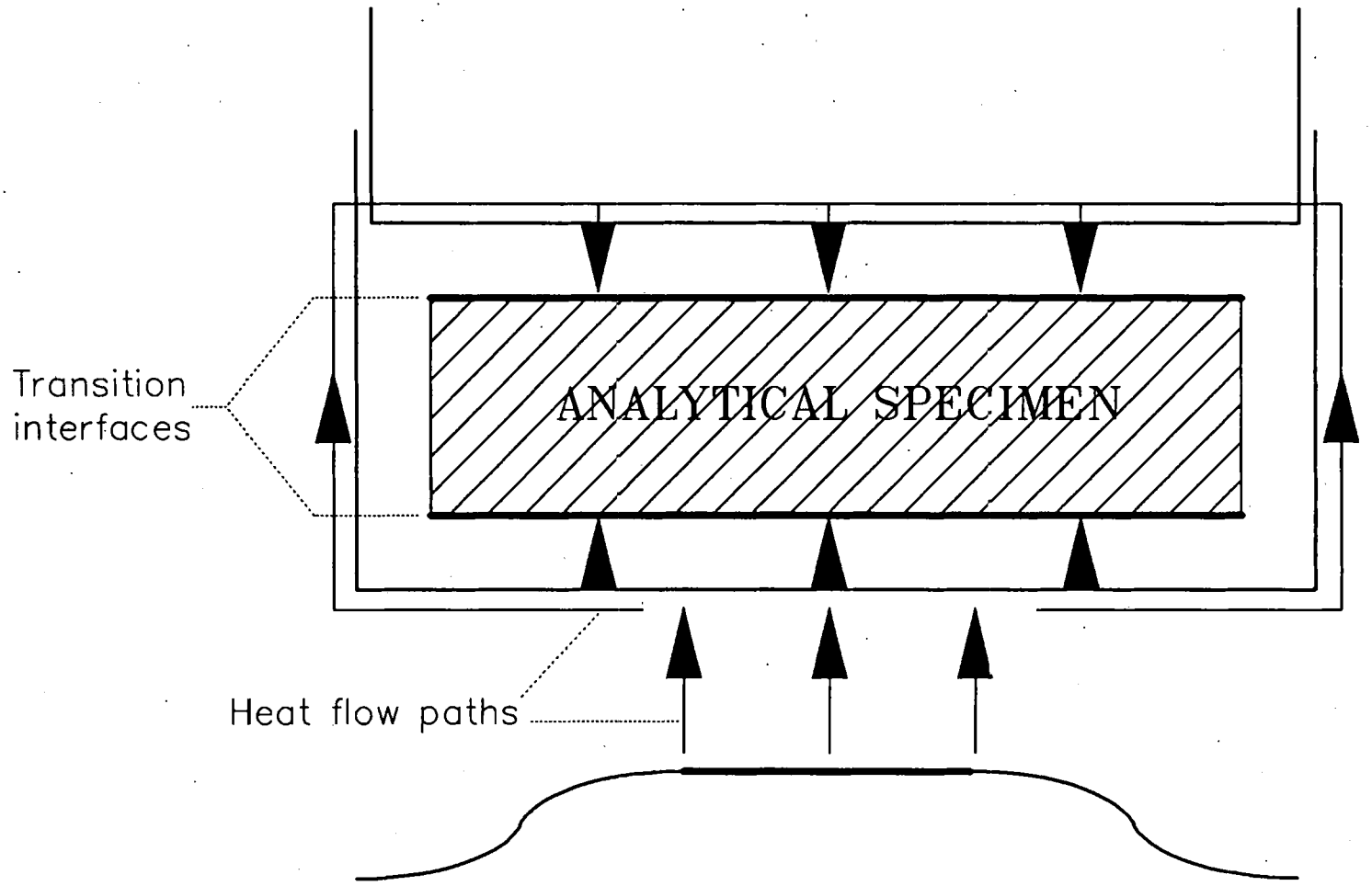

Figure 7.2 – Heat flow around the boundary of the transportable DSC specimen.

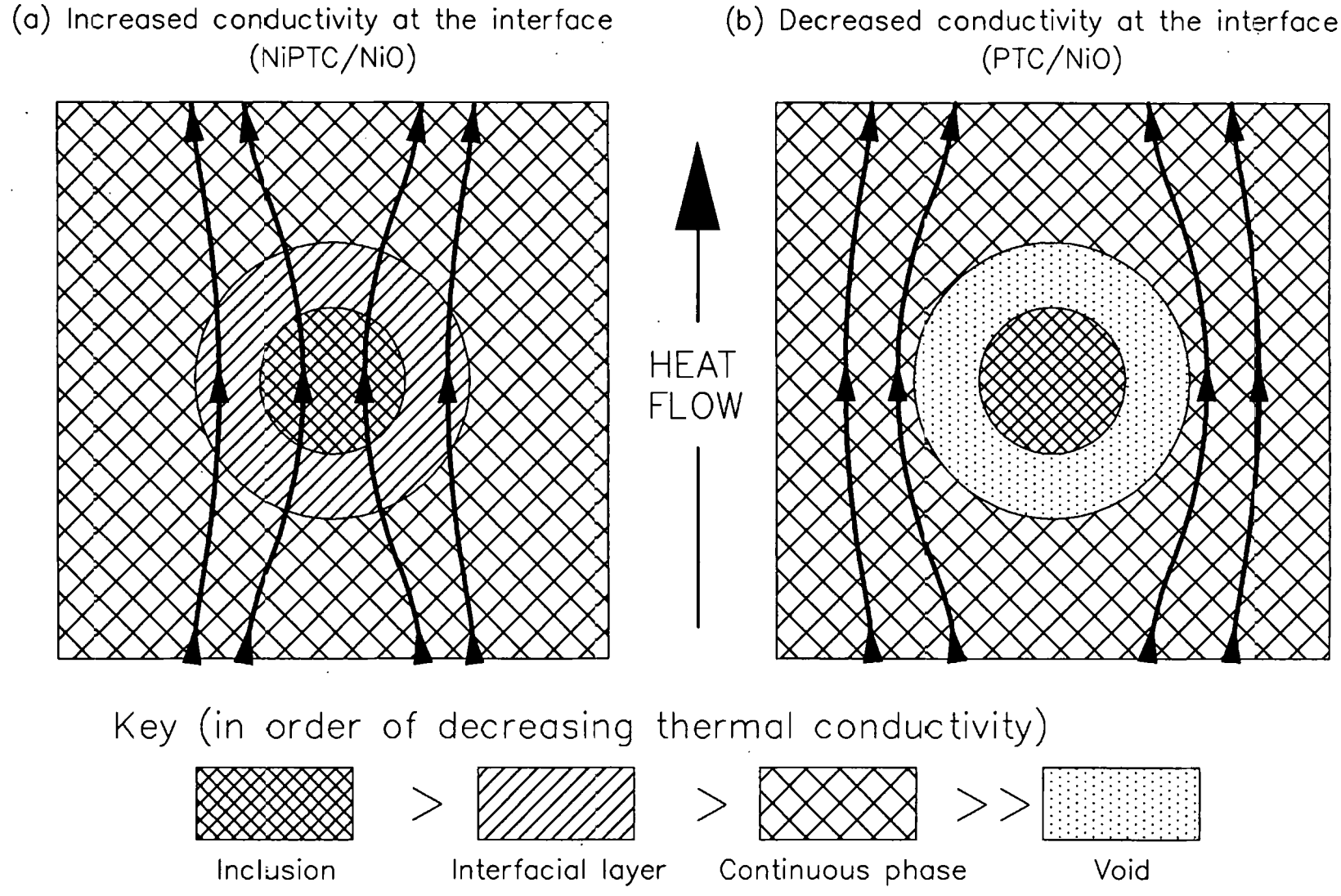

Figure 7.3 – Heat flow through a composite in the region of an inclusion.

REFERENCES

[1] 'Thermal decomposition of porphyrins'; M. Thompson, M.Sc. Thesis submitted to the Victoria University of Manchester (1981).

[2] 'Porphyrins, power and pollution'; A.D. Adler, V. Váradi and N. Wilson, Ann. N.Y. Acad. Sci. 244 685-94 (1975).

[3] 'Visible light-induced oxygen generation and cyclic water cleavage sensitised by porphyrins'; E. Borgarello, K. Kalyanasundaram, Y. Okuno and M. Grätzel, Helvetica Chimica Acta 64(6) 1937-42 (1981).

[4] 'Oxygen reduction catalysts as cathodes of button air batteries'; Japanese patent JP 59073051, 25th April 1984.

[5] 'Photochemical manufacture of epoxides'; Japanese patent JP 62263172, 16th November 1986.

[6] 'Method and apparatus for electrochemical catalytic oxidation of sulphur dioxide to sulphuric acid'; European patent EP 302224, 8th February 1989.

[7] 'Metal phthalocyanines used as catalysts in gas phase reactions'; F. Steinbach and H.J. Joswig, J. Catal. 55 272-80 (1978).

[8] 'Catalytic reduction of nitric oxide over tetraphenylporphyrin complexes'; K. Tsuji, H. Fujitsu, K. Takeshita and I. Mochida, J. Molecular Catal. 9 389-98 (1980).

[9] 'Strong interaction of metallotetraphenylporphyrins with supporting metal oxides in the catalytic decomposition of hydrogen peroxide'; I. Mochida, A. Yasutake, H. Fujitsu and K. Takeshita' J. Phys. Chem. 86 3468-71 (1982).

[10] 'The role of trace metals in petroleum'; T.F. Yen (ed.), Pub. Ann Arbor Science (1975).

[11] 'Interfacial activities and porphyrin contents of oil-shale extracts'; J.W. Moore and H.N. Dunning, Ind. & Eng. Chem. 47 1440-4 (1955).

[12] 'Analysis of a temperature-controlled scanning calorimeter'; M.J. O'Neill, Anal. Chem. 36(7) 1238-45 (1964).

[13] 'Heat flux differential scanning calorimetry - theory and practice'; J.D. Lee and P.F. Levy, Paper #38, Proc. 11th. Conf. North American Thermal Analysis Society 2 215-228 (1981).

[14] 'Calorimetric determination of purity by simulation of DSC curves'; S. Sarge, S. Bauerecker and H.K. Cammenga, Thermochim. Acta 129 309-24 (1988).

[15] 'Thermal analysis kinetics: problems and pitfalls and how to deal with them - *Special Review*'; J.H. Flynn, J. Thermal Anal. 34 367-81 (1988).

[16] 'Influence of experimental variables on curves in differential scanning calorimetry. Parts I-IV; A.A. van Dooren and B.W. Müller, Thermochim. Acta 49 151-97 (1981).

[17] 'An analysis of the factors affecting the peak shape and quantitative reliability of a heat flux DSC cell'; A. Marini, V. Berbenni, G. Flor, V. Massarotti and R. Riccardi, Thermochim. Acta 95 419-24 (1985).

[18] 'The influence of sample mass, heating rate and heat transfer coefficient on the form of DSC curves'; J.C. van Miltenburg and M.A. Cuevas-Diarte, Thermochim. Acta 156 291-7 (1989).

[19] 'Microcalorimeter with compensation by Peltier and Joule effects'; A. Tian, Bull. Soc. Chim. de France 33(4) 427-9 (1923).

[20] 'Recent progress in microcalorimetry'; E. Calvet and H. Prat. H.A. Skinner (trans.) Pergamon Press (1963).

[21] 'A new differential calorimeter with electrical compensation'; E. Calvet. Academie des Sciences. Comptes Rendus des Sciences. Series 2: Mecanique, Physique, Chimie, Sciences de la Terre, Science de l'Univers 226 1702-4 (1948).

[22] 'De l'action de la chaleur sur les argiles'; H. Le Chatelier, Bull. Societe Francais de la Minerale 10 203-11 (1887).

[23] 'Fifth report to the Alloys Research Commitee: Steel'; W.C. Roberts-Austen, Proc. Inst. Mech. Engrs. (London) 56 35-68 (1899).

[24] 'Multiple differential thermal analysis'; P.F. Kerr and J.L. Kulp, American Mineralogist 33 387-419 (1948).

[25] 'Temperature distribution during mineral inversion and its significance in differential thermal analysis'; H. Smyth, J. Am. Ceram. Soc. 34(7) 221-4 (1951).

[26] 'A theory of differential thermal analysis and new methods of measurement and interpretation'; S.L. Boersma, J. Am. Ceram. Soc. 38 281-4 (1955).

[27] 'Quantitative differential thermal analysis with an isothermal microcalorimeter'; H. de Waal, Instrument Practice 19(11) 1022-8 (1965).

[28] 'New differential scanning calorimeter. New thermochemical applications'; J. Mercier, J. Thermal Anal. 14 161-71 (1978).

[29] 'A high-performance sensor for heat-flux differential scanning calorimetry'; G. van der Plaats and T. Kehl, Paper #109, Proc. NATAS Conf. Vol. II 570-4 (1989).

[30] 'A differential scanning calorimeter for quantitative differential thermal analysis'; E.S. Watson, M.J. O'Neill, J. Justin and N. Brenner, Anal. Chem. 36(7) 1233-8 (1964).

[31] 'For better thermal analysis'; G. Lombardi. Pub. International Confederation for Thermal Analysis (1977). (Available ex. Chemical Society - Thermal Methods Group. London).

[32] 'A scanning microcalorimetry cell based on a thermoelectric disc - theory and applications'; R.A. Baxter in 'Thermal methods of analysis: Vol. 1' W.W. Wendlandt (ed.). 65-84 Acad. Press (1969).

[33] 'Calorimetry of high polymers III. A new type of adiabatic jacket and calorimeter '; A.W. Worthington, P.C. Marx and M. Dole, Review of Scientific Instruments 26(7) 698-702 (1955).

[34] 'E-curve: DSC cell heat flow function' p.10 in '912 Dual Sample DSC Operator's Manual' Du Pont PN 912027-001 (1982).

[35] 'Purge gas enhancement of peak resolution in differential scanning calorimetry'; G.-W. Jang, R. Segal and K. Rajeshwar, Anal. Chem. 59 684-7 (1987).

[36] 'Modelling differential scanning calorimetry'; C. Sandu and R.K. Singh, Thermochim. Acta. 159 267-98 (1990).

[37] 'Measurement of thermal conductivity using a modified DSC'; W.P. Brennan, B. Millar and J.C.W. Whitwell, J. Appl. Polymer Sci. 12 1800 (1968). Also in 'Differential Scanning Calorimetry'; J.L. McNaughton and C.T. Mortimer, Perkin-Elmer reprint No.L-604.

[38] 'Determination of thermal conductivity of selected materials by DSC'; F.N. Larson and C.L. Long. Presented at 26th Pittsburgh Conf. on Anal. Chem. & Appl. Spec. Cleveland, Ohio (1975).

[39] 'Determination of thermal conductivity by differential scanning calorimetry'; J. Chiu and P.G. Fair, Thermochim. Acta. 34 267-73 (1979).

[40] 'The measurement of thermal conductivity by DSC'; T. Boddington and P.G. Laye, Thermochim. Acta. 115 345-350 (1987).

[41] 'Thermal conductivity measurements on small polymeric samples using the DSC'; V.F. Mazzio. Presented at 38th Pittsburgh Conf. on Anal. Chem. & Appl. Spec. Atlantic City, N.J. (1987).

[42] 'Measurement of the thermal conductivity of solid substances by DSC'; G. Hakvoort and L.L. van Reijen, Thermochim. Acta. 93 317-20 (1985).

[43] 'A method for the determination of thermal conductivity of sheet materials by DSC'; J.H. Flynn and D.M. Levin, Thermochim. Acta. 126 93-100 (1988).

[44] 'A new differential scanning calorimetry based approach for the estimation of thermal conductivity of polymer solids and melts'; Y.P. Khanna, T.J. Taylor and G. Chomyn, Polymer Eng. & Sci. 28(16) 1035-41 (1988).

[45] 'Theoretical analysis of peak height in classical DTA, power-compensated DSC and heat-flux DSC'; Y. Saito, K. Saito and T. Atake, Thermochim. Acta 107 277-82 (1986).

[46] 'Specific heat of aircraft turbine lubricants by thermal analysis'; Standard test method D 3947-83, Annual book of ASTM standards, Vol.05.03 (1986), American Society for Testing and Materials - Philadelphia, USA.

[47] 'Measurement of specific heat capacity of liquids by differential scanning calorimetry (DSC)'; Thermal analysis application brief No.TA 83, Du Pont Company - Wilmington, USA.

[48] 'An improved technique for precise measurements of specific heat of a liquid using Du Pont 990 DSC'; H.K. Yuen and C.J. Yosel, Thermochim. Acta 33 281-291 (1979).

[49] 'Instruction manual: 910 Differential Scanning Calorimeter System'; PN 910037-000, Du Pont Company - Wilmington, USA.

[50] 'The impact of computers on thermal analysis'; B. Wunderlich, International Laboratory 12(8) 32-43 (1982).

[51] 'Rough Surfaces'; T.R. Thomas (ed.), Pub. Longman (1982).

[52] 'SAS User's Guide: Statistics'; Version 5, 575-606. Pub. SAS Institute Inc., Box 8000, Cary, N. Carolina, USA (1985).

[53] 'An algorithm for least-squares estimation of non-linear parameters'; D.W. Marquardt, J. Soc. Ind. & Appl. Mathematics 11 431-41 (1963).

[54] 'DUD, a derivative-free algorithm for non-linear least-squares'; M.L. Ralston and R.I. Jennrich, Technometrics 1 7-14 (1979).

[55] 'Thermal conductivity / temperature table for metals'; Table 3-321, in 'Perry's Chemical Engineer's Handbook. 6th edn.' R.H. Perry, D.W. Green and J.O. Maloney (eds.) McGraw-Hill (1984).

[56] 'Thermal conductivity of vitreous silica'; C.K.L. Carwile and J.H. Hoge, Nat. Bur. Stand.(US) Spec. Publ. 302 59-76 (1967).

[57] 'Calibration of the Du Pont 910 DSC cell'; W. Eysel and K.H. Breuer, Techscan 2(2) 24-7, Pub. Du Pont, Wilmington USA (1982).

[58] 'Principles of Solid State Chemisty'; P.P. Budnikov and A.M. Ginstling (K. Shaw ed. and trans.), Pub. Maclaren & Sons, London (1968).

[59] 'Measurement of exothermic reactions by differential scanning calorimetry'; M.J. O'Neill, Anal. Chem. 47(4) 630-7 (1975).

[60] 'Calibration and application of a heat-flux DSC in the study of heterogeneous catalysed reactions'; H. Dötsch and H. Fink, Thermochim. Acta 112 51-6 (1987).

[61] 'Metallic glasses'; R.W. Cahn, Contemp. Phys. 21(1) 43-75 (1980).

[62] 'Reactions in vitreous and amorphous solids'; H. Scholze in Proc. 9th Int. Symp. on Reactivity of Solids (Bristol) 160-185 and refs. therein (1972)

[63] 'Understanding the structure of metallic glasses'; P.H. Gaskell, p.35-57 in 'Summer school on amorphous metals', Wilga, Poland, 1985. Pub. World Scientific. Singapore (1986)

[64] 'Structure of glassy metallic alloys'; D.E. Polk, Acta. Metall. 20(4) 485-91 (1972).

[65] 'Geometry of the structure of monatomic liquids'; J.D. Bernal, Nature 185 68-70 (1959)

[66] 'Structure simulation of transition metal-metalloid glasses'; D.S. Boudreaux and J.M. Gregor, J. Appl. Phys. 48(1) 152-8 (1977).

[67] 'Gram-atomic volumes of metal-metalloid glass forming alloys'; D. Turnbull, Scripta. Met. 11 1131-6 (1977).

[68] 'A new structural model for transition metal-metalloid glasses'; P.H. Gaskel, Nature 276 (No. 5687) 484-5 (1978).

[69] 'Short-range structure for amorphous intertransition metal alloys'; R. Wang, Nature 278 (No. 5706) 700-3 (1979).

[70] 'Local boron environment in $Ni_{100-x}B_x$ metallic glasses - an NMR study'; P. Panissod, I. Bakonyi and R. Hasegawa, Phys. Rev. B28(5) 2374-81 (1983).

[71] 'Structural relaxation in amorphous alloys - compositional short range ordering'; T. Egami, Mater. Res. Bull. 13(6) 557-62 (1978).

[72] 'Structural relaxation in amorphous $Fe_{40}Ni_{40}P_{14}B_6$'; T. Egami, J. Mater. Sci. 13(12) 2587-99 (1978).

[73] 'Electron microscopy and electron diffraction study of crystallisation of metastable phases in amorphous Fe-B Alloys'; P. Duhaj and F. Hanic, Phys. Stat. Sol. 76(a) 467-77 (1983).

[74] 'Molecular transport in liquids and glasses'; M.H. Cohen and D. Turnbull, J. Chem. Phys. 31(5) 1164-9 (1959).

[75] 'Crystallisation of metallic glasses' ; U. Köster and U. Herold 225-59 in 'Glassy metals', Topics in Applied Physics 46, H.J. Guntherodt and H. Bech eds., Springer-Verlag, Berlin (1981).

[76] 'Thermal stability'; S. Ranganathan and S. Banerjee p147-63 in 'Metallic glasses'; T. Anantharaman (ed.). Pub. Trans. Tech. (1984).

[77] 'Kinetics of the thermal decomposition of solids'; P.W.M. Jacobs, Mater. Sci. Res. 4 37-52 (1969).

[78] 'Crystallisation kinetics of the amorphous alloy $Fe_{80}B_{20}$ studied using a thermomagnetic balance'; S. Budorov, T. Spassov and T. Markov, J. Mat. Sci. 21 2553-6 (1986).

[79] 'The application of differential thermal analysis to the study of reaction kinetics'; H.J. Borchardt and F. Daniels, J. Am. Chem. Soc. 79 41-6 (1957).

[80] 'Kinetic parameters - *Special review*'; P.D. Garn, J. Thermal Anal. 13 581-93 (1978).

[81] 'The pre-exponential factors for solid-state thermal decomposition'; H.F. Cordes, J. Phys. Chem. 72(6) 2185-9 (1968).

[82] 'Activated complex theory applied to the thermal decomposition of solids'; R.D. Shannon, Trans. Faraday Soc. 60 1902-13 (1964).

[83] 'The kinetic compensation effect'; P.D. Garn, J. Thermal Anal. 10 99-102 (1976).

[84] 'The kinetic compensation effect'; J. Zsakó, J. Thermal Anal. 9 101-8 (1976).

[85] 'Compensation effect in heterogeneous catalysis'; A.K. Galwey, Adv. Catal. 26 247-322 (1977).

[86] 'A general explanation for the compensation effect'; Wm. Curtis Connor Jr., J. Catal. 78 238-46 (1982).

[87] 'Comments on the theoretical explanation of compensation behaviour'; A.K. Galwey, J. Catal. 84 270-2 (1983).

[88] 'Further comments on a general explanation for compensation behaviour'; Wm. Curtis Connor, J. Catal. 84 273-4 (1983).

[89] 'Effect of quench rate on the structural relaxation of a metallic glass'; A.L. Greer, J. Materials Sci. 17 1117-24 (1982).

[90] 'Enthalpic study of structural relaxation and crystallisation in some metallic glasses'; M. Baricco, L. Battezzati and G. Riontino, J. Thermal Anal. 30 1259-66 (1985).

[91] 'Fundamental study of heating process in DSC. Effect of the cure enthalpy and heating rate'; J.Y. Armand, J. Bourgois and J.M. Vergnaud, Thermochim. Acta 116 301-16 (1987).

[92] 'Transport properties of two-phase materials with random structure'; G.K. Batchelor, Ann. Rev. Fluid Mech. 227-255 (1974).

[93] 'Effective medium models for the optical properties of inhomogeneous materials'; G.A. Niklasson, C.G. Granqvist and O. Hunderi, Appl. Optics 20(1) 26-30 (1981).

[94] 'Heat transmission in low conductivity materials'; A.W. Pratt, in 'Thermal conductivity. Vol.1' (R.P. Tye ed.) 301-405, Acad. Press (1969).

[95] 'Thermal conductivity VIII. A theory of thermal conductivity of porous materials'; A.L. Loeb, J. Am. Ceram. Soc. 37(2) 96-9 (1954).

[96] 'The measurement of thermal conductivity of refractory materials'; F.H. Norton and W.D. Kingery, U.S. Atomic Energy Commission report NYO-6442 (1954). From: Technical information service, Oak Ridge, Tennessee.

[97] 'Thermal conductivity IX. Experimental investigation of the effect of porosity on thermal conductivity'; J. Francl and W.D. Kingery, J. Am. Ceram. Soc. 37(2) 99-107 (1954).

[98] 'Thermal conductivity X. Data for several pure oxide materials corrected to zero porosity'; W.D. Kingery, J. Francl, R.L. Coble and T. Vasilos, *ibid* 107-10.

[99] 'Calculation of several physical constants of heterogeneous substances. Part 1: Dielectric constants and conductivities of mixed-bodies of isotropic substances.' (german); D.A.G. Bruggeman, Ann. Phys. (Leipzig) 24 636-64 (1935).

[100] 'Syntactic foam as a structural material in a marine environment'; A.R. Lyle and M.H. Collins, Paper 23, Conf. 'Polymers in a marine environment 1987', Pub. Marine Management (Holdings) Ltd. (1989).

[101] 'A variational approach to the theory of the effective magnetic permeability of multiphase materials'; Z. Hashin and S. Shtrikman, J. Appl. Phys. 33 3125-31 (1962)

[102] 'Normal total emissivity of various surfaces'; Section 10-51, in 'Perry's Chemical Engineer's Handbook. 6th edn.' R.H. Perry, D.W. Green and J.O. Maloney (eds.) McGraw-Hill (1984).

[103] 'An X-ray study of the structure of the phthalocyanines. Part 1. The metal-free, nickel, copper, and platinum compounds'; J.M. Robertson, J. Chem. Soc. 615-21 (1935).

[104] 'X-ray structural studies of hemiporphyrazine and phthalocyanine'; E.C. Bissel, Ph.D thesis, Case West. Reserve Univ., Cleveland, Ohio. Avail. Univ. Microfilms, Ann Arbor, Mich., Order No. 70-25,849. From: Diss. Abstr. Int. B 1970, 31(6) 3295-6 (1970).

[105] 'A photographic essay of porphyrins and related macrocycles'; E.F. Meyer Jr. and D.L. Cullen, in 'The porphyrins, III' D. Dolphin (ed.) 513-29, Acad. Press (1978).

[106] 'Porphyrin stereochemistry'; W.R. Scheidt, *ibid* 463-511.

[107] 'Structure of octaethylporphyrin. A comparison with other free base porphyrins'; J.W. Lauher and J.A. Ibers, J. Am. Chem. Soc. 95 5148-52 (1973).

[108] 'New crystalline phase of (octaethylporphinato)nickel(II). Effects of π–π interactions on molecular structure and resonance Raman spectra'; T.D. Brennan, W.R. Scheidt and J.A. Shelnutt, J. Am. Chem. Soc. 110 3919-24 (1988).

[109] 'The structure of crystalline tetraphenylporphine. The stereochemical nature of the porphine skeleton'; M.J. Hamor, T.A. Hamor and J.L. Hoard, J. Am. Chem. Soc. 86 1938-42 (1964).

[110] 'The crystal and molecular structure of triclinic tetraphenyl-porphyrin'; S.J. Silvers and A. Tulinsky, *ibid.* 89 3331-7 (1967).

[111] (X-ray) Powder diffraction file, 1985; Entry No. 2-0312: Metal-free phthalocyanine (monoclinic), JCPDS Int. Centre for Diffraction Data, Swarthmore, Pa. (USA).

[112] 'High pressure structure of metal-free phthalocyanine'; R.S. Kirk, Nat. Bur. Stand. (US) Spec. Publ. 301 389-92 (1967).

[113] 'Modelling in calorimetry working under isothermal conditions or in scanning mode'; J.M. Vergnaud, Thermochim. Acta 114 15-27 (1987).

[114] 'Effect of the layer of air between the calorimeter and cylindrical samples in DC experiments'; H. Liu, J.Y. Armand, J. Bouzon and J.M. Vergnaud, Thermochim. Acta 130 355-66 (1988).

[115] 'Anomalies de réactivité au point de Curie de quelques alliages et de leurs constituants'; M. Dair et H. Forestier, Proc. 4th International Symposium on the Reactivity of Solids (1960) 122-8, Pub. Elsevier (1961).

[116] 'Interpretaion of the Hedvall Effect'; I.V. Kirilyus, Eksp. Issled. Khim. Biol. 72-5 (1974).

[117] 'Studies in gas-solid reactions: Part II. An experimental study of nickel oxide reduction with hydrogen'; J. Szekely and J.W. Evans, Met. Trans. 2 1699-1710 (1971).

[118] 'Solid state reactions. A rigorous test of the Hedvall effect'; P.D. Garn and T.S. Habash, J. Phys. Chem. 83(2) 229-31 (1979).

[119] 'A note on the structure of nickel oxide at sub-normal and elevated temperatures': H.P. Rooksby, Acta Cryst. 1 226 (1948).

[120] 'X-ray studies of the system nickel-oxygen-water: 1 Nickelous oxide and hydroxide'; R.W. Cairns and E. Ott, J. Am. Chem. Soc. V 55 527-33 (1933).

[121] 'Preparation and study by electron microscopy of the development of texture with temperature of a porous exhydroxide nickel oxide': F. Fievet and M. Figlarz, J. Catalysis 39 350-6 (1975).

[122] 'Surface properties of $Ni(OH)_2$ and NiO - II. Mechanism for the decomposition of $Ni(OH)_2$ and other metal hydroxides': C.L. Cronan, F.J. Micale, M. Topic, H. Leidheiser Jr., A.C. Zettlemoyer and S. Popovic, J. Colloid & Interface Science 55(3) (1976).

[123] 'Thermogravimetric apparatus temperature calibration using melting point standards'; A.R. McGhie, J. Chiu, P.G. Fair and R.L. Blaine, Thermochim. Acta 67(2-3) 241-50 (1983).

[124] 'Thermal decomposition of iron(II), cobalt(II) and nickel(II) hydroxides': I.F. Hazel and R.J. Irving, J. Chem. Soc. (A) 669-73 (1966).

[125] 'High-temperature heat-content, heat capacity and entropy data for elements and inorganic compounds. XIII'; K.K. Kelley, U.S. Bureau of Mines (Washington) Bull. 584 p129 (1960).

[126] 'Structures of monoxides of some transition elements at low temperatures'; N.C. Tombs and H.P. Rooksby, Nature V 442-3 (1950).

[127] 'Nickel oxide'; W.J. Moore, in 'Seven Solid States' 133-62. Pub. Benjamin, New York (1967).

[128] 'Phase behaviour of cobalt, nickel and zinc phthalocyanines'; R.A. Collins and K.A. Mohammed, Thermochim. Acta. 109 397-402 (1987).

[129] 'Durene-capped porphyrins: synthesis and characterisation'; T.P. Wijesekera, S. David, J.B. Paine, B.R. James and D. Dolphin, Can. J. Chem. 66 2063-71 (1988).

[130] 'Intermolecular interaction in zinc tetraphenylporphyrin solvates'; E.V. Antina, V.P. Barannikov, A.I. V'yugin, M.Yu. Nikiforov and G.A. Krestov, Zh. Neorg. Khim, 35(2) 400-4 (1990).

[131] 'Synthesis and properties of metalloporphyrins'; J.W. Buchler, Chap. 10 p389-483 in 'The Porphyrins: Vol. V'; D. Dolphin (ed.), Pub. Acad. Press (1978)

[132] 'Heterogeneous metal-insertion: A novel reaction with porphyrins'; O. Herrmann, S.H. Mehdi and A. Corsini, Can. J. Chem. 56(8) 1084-7 (1978).

[133] 'Solid-solid reactions'; A.J.E. Welch, 297-310 (Chap. 12) in 'Chemistry of the solid state'; W.E. Garner (ed.), Pub. Butterworths (1955) and references therein.

[134] 'Thermal study of $NiC_2O_4.2H_2O$ obtained by a solid state reaction at room temperature and normal pressure'; M.E. Garcia-Clavel, M.J. Martinez-Lope and M.T. Casais-Alvarez, Thermochim. Acta 118 123-34 (1987).

[135] 'Studies in solid state reactions between basic copper carbonate with cinnamic, succinic and adipic acids'; P.S. Bassi, G.S. Chopra and B.R. Gupta, Thermochim. Acta 124 197-203 (1988).

[136] 'Routes of electron transfer'; C.E. Castro, Chap. 1 p1-27 in 'The Porphyrins: Vol. V'; D. Dolphin (ed.), Pub. Acad. Press (1978)

[137] 'Adsorption mechanism of Boscan porphyrins on MoO_3, Co_3O_4 and $CoMo/Al_2O_3$'; A. Morales and R. Galiasso, Fuel 61 13-7 (1982).

[138] 'Kinetics of metal-ion complexation with *N*-methyltetraphenyl-porphyrin. Evidence of a general mechanism of porphyrin metallation'; M.J. Bain-Ackerman and D.K. Lavallee, Inorg. Chem. 18(12) 3358-64 (1979).

[139] 'Kinetics of metalloporphyrin formation with particular reference to the metal ion assisted mechanism'; M. Tanaka, Pure & Appl. Chem. 55(1) 151-8 (1983).

[140] 'Proton transfer kinetics in solids: Tautomerism in free base porphines by ^{15}N CPMAS NMR'; H.H. Limbach, J. Hennig, R. Kendrick and C.S. Yannoni, J. Am. Chem. Soc. 106 4059-60 (1984).

[141] 'Effect of biography on stoichiometric composition and chemisorptive properties of nickel oxide'; J. Deren and J. Stoch, J. Catal. 18 249-59 (1970).

[142] 'Surface analysis of nickel oxides by X-ray photoelectron spectroscopy'; J. Finster, P. Lorenz, F. Fievet and M. Figlarz, Materials Science Monographs - Reactions of Solids 10(1) 391-6 (1982).

[143] 'Infrared spectroscopic evidence for the surface complexes of singlet oxygen'; A.A. Tsyganenko and V.N. Filimonov, Spectroscopy Letters 13(8) 583-92 (1980).

[144] 'The effect of surface oxygen on the catalytic and chemisorptive behaviour of Ni(110): ligand effects and oxide states'; S.W. Johnson and R.D. Madix, Surface Science 66 189-209 (1977).

[145] 'Porphyrin *N*-oxides': R. Bonnett and R.J. Ridge, J. Chem. Soc. Chem. Comm. 7 310-1 (1978).

[146] 'A complex containing a Ni-O unit at the center of a porphyrin. The X-ray crystal and molecular structure of the nickel(II) complex of octaethylporphyrin *N*-oxide dianion'; A.L. Balch, Y-W Chan and M.M. Olmstead, J. Am. Chem. Soc. 107 6510-14 (1985).

[147] 'Porphyrin synthesis through tripyrrins: An alternative approach'; K.M. Smith and G.W. Craig, J. Org. Chem. 48 4302-6 (1983).

[148] 'Application of differential scanning calorimetry in the study of intrazeolite metallophthalocyanines'; J.K. Balkus and J.P. Ferraris, J. Phys. Chem. 94(21) 8019-20 (1990).

[149] 'The temperature of the beginning of inner diffusion in crystals'; G. Tammann, Z. Anorg. Allg. Chem. 157 321-5 (1926).

[150] 'Chemical reactions taking place in mixtures of solid substances at high temperatures'; G. Tammann, Z. Angew. Chem. 39 869-75 (1926).

[151] 'Petroporphyrins: Structural elucidation and the application of HPLC fingerprinting to geochemical problems'; G. Eglinton, S.K. Hajibrahim, J.R. Maxwell and J.M.E. Quirke, Phys. Chem. Earth 12 (Adv. Org. Geochem. 1979) 193-203 (1980).

[152] 'Life on the Mississippi'; Mark Twain, Chapter 17 ('Cut-Offs and Stephen') Pub. Harper & Bros., New York (1917).

[153] 'Experimental requirements for the determination of kinetics and mechanism for decomposition reactions of solids'; A. Reller and H.R. Oswald, Proc. 6th Int. Conf. Thermal Anal. (ICTA) Vol.1 63-8. G.H. Wiedemann (ed.). Pub. Birkhauser Verlag (1980).

[154] 'Observations on internal structures of chrome alum dehydration nuclei'; A.K. Galwey, R. Reed and G.G.T. Guarini, Nature 283 52-4, 3rd January (1980).

[155] 'Facts and fiction in the mechanistic interpretation of thermal decomposition processes'; H.R. Oswald and E. Reller, Mater. Sci. Monogr. 10 (Reactivity of Solids 2) 964-7 (1982).

[156] 'On the preparation of metalloporphyrins'; A.D. Adler, F.R. Longo, F. Kampas and J. Kim, J. Inorg. Nucl. Chem. 32 2443-5 (1970).

APPENDIX I

SOURCE AND SPECIFICATION OF MATERIALS

DSC SAMPLE CONTAINERS	Manufacturer's part code
Du Pont	
Non-hermetic aluminium pans:	900786-901
Lids for above:	900779-901
Hermetic aluminium pans:	900796-901
Lids for above:	900790-901
Perkin-Elmer	
Lids for non-hermetic aluminium pans: (used as radiation shields)	0219-0041
Lids for hermetic stainless steel pans: (used as pans for λ measurements)	0319-1526
Setaram	
Hermetic stainless steel crucibles:	
Crucible body	08/12732
Crucible lid	08/12735
Nickel sealing ring	08/12751

METALS AND REAGENTS (grade and purity as specified by supplier)

Aldrich Chemical Co. Ltd.

Nickel(II) oxide: Gold label > 99.999%

Nickel oxide (black): Specified Ni content ~ 76.5% (= $NiO_{1.13}$)

Tin (shot): Gold label > 99.999%

Indium (powder): Gold label > 99.999%

meso-Tetraphenylporphyrin (TPP) > 99%

meso-Tetrakis(pentafluorophenyl)porphyrin (T(PFP)P) (no purity spec.)

meso-Tetrakis(*p*-methoxyphenyl)porphyrin (T(*p*-MP)P) ~ 97%

Phthalocyanine (PTC) ~ 98%

Fluka Chemicals Ltd.

Nickel(II) hydroxide: Purum grade > 97%

Nickel(II) carbonate (basic, tetrahydrate): Purum grade > 97%

Nickel(II)phthalocyanine: Pract. grade ~ 97% (ex. Ni)

Indium (wire): Puriss. grade > 99.999%

Johnson Matthey

Lead (0.25 mm sheet): Puratronic > 99.999%

Zinc (0.25 mm sheet): Puratronic > 99.999%

Prepared at Thornton Research Centre

Silver: Prepared by electrolysis of analytical grade silver(II) nitrate, believed to be > 99.99% pure.

β-Octaethylporphyrin (OEP).

meso-Tetraphenylporphyrinato-nickel(II) (NiTPP).

MISCELLANEOUS

Mould release agent: 'Crossflon-20' (dry spray fluorocarbon); ex. Henry Crossley (Packings) Ltd., Hill Mill, Temple Road, Bolton.

Evacuable pellet die (6 mm): Part No. 3070; ex. Specac Ltd., St. Mary Cray, Orpington, Kent.

Vitreous silica: 'Heralux' ex. Heraeus Silica & Metals Ltd. Bromborough, Wirral.

Chromatographic alumina: Basic, Activity 1, ex. Merck.

Chromatographic silica gel: 923 grade, 100-200 mesh, ex. W.R. Grace Ltd., Huntingdon, Cambs.

Solvents: all 'Glass distilled' grade ex. Rathburn Chemicals or A.R. grade ex. BDH Chemicals.

PHYSICAL DIMENSIONS USED FOR THE CALCULATIONS IN CHAPTER 3

The following dimensions were measured from specimens used in the experiments, except for thermal conductivity values which were taken from published data as indicated.

Sample container: (Du Pont 900786/779-901)

Pan internal diameter: 6.5 mm
Lid external diameter: 6.5 mm
Pan height: 1.7 mm
Pan mass: 12.9 ± 0.1 mg
Lid height: 1.0 mm
Lid mass: 10.4 ± 0.1 mg
Wall thickness: 0.08 mm
Thermal conductivity [55]: 240 $W \cdot m^{-1} \cdot K^{-1}$ @ 130°C

Silica discs:

Diameter: 6.0 mm
Thickness: (i) 0.26 mm) (mean values)
(ii) 0.49 mm)
Thermal conductivity [56]: 1.54 $W \cdot m^{-1} \cdot K^{-1}$ @ 154°C

Indium discs:

Diameter: 4.0 mm
Thickness: 0.25 mm (= 23 mg, which was typical of experiments giving onset slopes in the asymptote region).

APPENDIX II

PURIFICATION AND PRE-TREATMENT OF REAGENTS

NICKEL(II) OXIDE

The oxide powder was sieved to a size range of 38-75 μm and either used without further treatment, or annealed as follows. Batches of ~ 2 g of the oxide were contained in a quartz boat, forming a bed ~ 1 mm deep. This was heated for 24 hours at 300°C in a tube furnace of 2 cm internal diameter. High purity argon was passed through the furnace at a flow rate of 100 $cm^3 \cdot min^{-1}$ during this period. The oxide was allowed to cool in the flowing argon and then stored under air in a sealed vial.

PORPHYRINS

meso-Tetraphenylporphyrinato-nickel(II) (NiTPP) was prepared from nickel(II) acetate and TPP in *NN*-dimethylformamide, using the method suggested by Adler *et al* [156]. Two methods were used to purify the porphyrins. Column chromatography was the more efficient technique, but the very low solubility of some of the compounds precluded using this. Continuous extraction was used for the other porphyrins, which were mixed with a large excess of alumina to adsorb polar impurities such as pyrrylmethenes.

(a) Chromatography

OEP, TPP, NiTPP and T(PFP)P were purified by chromatography on a mixed-bed column of basic alumina and silica gel which was packed as follows. The glass column (3 cm i.d.) was filled with toluene and a slurry of silica gel in toluene added to give a bed depth of 10 cm. Dry alumina powder was then added to the column of solvent to give a further bed depth of 40 cm. (The lower bed of silica gel was included to decompose any traces of aluminium porphyrin which might have formed on the alumina). The porphyrin (~ 1 g) was dissolved in about 1 litre of boiling toluene, which was allowed to cool before applying the solution to the column. Any un-dissolved porphyrin was taken up in

more boiling toluene and transferred to the column. The adsorbent bed was washed with a further 500 cm^3 toluene and the porphyrin was then desorbed using 40% v/v dichloromethane in toluene. The eluate was evaporated down to ~ 200 cm^3, methanol was added until the onset of crystallisation was observed and the solution was allowed to cool slowly. The crystalline porphyrin was filtered off, washed with boiling methanol and dried at 140°C for 24 hours, in an oven which had been flushed with nitrogen and then evacuated.

(b) Extractive crystallisation

The other three porphyrins, which had very low solubilities in most solvents, were purified by extractive crystallisation in hot dichloromethane (T(*p*-MP)P) or chlorobenzene (PTC and NiPTC). The porphyrin (~ 2 g) was mixed with 100 g alumina, packed into a glass fibre Soxhlet thimble and covered with quartz wool. Continuous extraction was carried out just below the boiling point of the solvent, by means of a vapour-jacketed Soxhlet apparatus. Extraction of T(*p*-MP)P was complete in about 50 hours, but the phthalocyanines required more than ten days. The T(*p*-MP)P extract was evaporated to ~ 200 cm^3, and 100 cm^3 methanol added to assist crystallisation. Precipitation of the phthalocyanines from chlorobenzene was virtually quantitative, even while the solvent was boiling. The crystalline products were each transferred to a clean thimble and washed by extraction with boiling methanol for 24 hours. They were then dried as for the other porphyrins.